Searches for signals from cosmic point-like sources of high energy neutrinos in 5 years of AMANDA-II data

DISSERTATION

zur Erlangung des akademischen Grades
doctor rerum naturalium
(Dr. rer. nat.)
im Fach Physik

eingereicht an der
Mathematisch-Naturwissenschaftlichen Fakultät I
Humboldt-Universität zu Berlin

von
Herrn Dipl.-Phys. Markus Ackermann
geboren am 30.01.1977 in Dettelbach

Präsident der Humboldt-Universität zu Berlin:
Prof. Dr. Christoph Markschies

Dekan der Mathematisch-Naturwissenschaftlichen Fakultät I:
Prof. Thomas Buckhout, Ph.D.

Gutachter:

1. Prof. Dr. Hermann Kolanoski
2. Prof. Dr. Thomas Lohse
3. Prof. Dr. Lutz Köpke

eingereicht am: 04.08.2006
Tag der mündlichen Prüfung: 13.11.2006

Abstract

AMANDA-II is a neutrino telescope located in the glacial ice at the South Pole. It is optimized to detect neutrino induced muon tracks with energies larger than 100 GeV by their Čerenkov light emission. We analyzed the data collected in 1001 effective days of detector operation between the years 2000 and 2004 for a signal from point-like sources of neutrinos. Such a signal is expected from cosmic objects that accelerate hadrons to very high energies, which subsequently interact with ambient protons or photons.

The dominant event class recorded in AMANDA-II are muons produced in the interactions of cosmic rays in the atmosphere. Due to their energy loss, the muons cannot penetrate the Earth and have down-going directions. The main signature to identify a neutrino induced event is therefore its up-going direction. A sample of 4282 up-going events is extracted from the 10 billion events triggered in the period selected for this analysis.

The search for point sources is accomplished on this data sample by looking for a localized excess over the isotropic background of atmospheric neutrinos. The procedure is applied for the directions of candidate sources, like Active Galactic Nuclei, Supernova remnants and X-ray binaries. In a second step, the full northern sky is scanned for unknown sources.

Further, we investigate methods to enhance the detection chance for sources which are suspected to be highly variable neutrino emitters. We search for an excess of neutrino events in periods of high activity of a source, defined by the intensity of its electromagnetic emission in certain frequency bands. An additional test based on a sliding time window is applied to the dataset to find flares of neutrinos, which would not be visible in the time-integrated search.

Neither a localized excess nor a neutrino flare has been found in the analyzed dataset. Therefore, we calculate upper limits on the neutrino fluxes which are compatible with this observation. The average upper limit achieved for a combined $\nu_\mu + \nu_\tau$ flux with a spectrum of $d\Phi/dE \propto E^{-2}$ is $E^2 \, d\Phi/dE = 1.0 \cdot 10^{-7}$ GeV cm^{-2} s^{-1} assuming a flavor ratio of $1:1$. It represents the most stringent upper limit on neutrino fluxes from point-like sources reported so far.

Keywords:
AMANDA, point source, neutrinos, cosmic rays

Zusammenfassung

AMANDA-II ist ein Neutrino Teleskop, das sich im Eis des Gletschers befindet, der den Südpol bedeckt. Es wurde optimiert um Spuren von hochenergetischen Myonen ($E > 100$ GeV), die in Neutrino-Wechselwirkungen entstanden sind, anhand ihrer Emission von Čerenkov-Licht zu detektieren. In dieser Arbeit analysieren wir die Daten, die in 1001 Tagen effektiver Detektorlaufzeit in den Jahren 2000 bis 2004 gesammelt worden sind, um ein Signal von einer Neutrino-Punktquelle zu finden. Ein derartiges Signal wird von kosmischen Objekten erwartet, die Hadronen zu sehr hohen Energien beschleunigen, welche daraufhin mit Photonen und Protonen in der Umgebung des Objekts wechselwirken.

Die Richtungen aus denen die registrierten Myon-Spuren kommen, werden rekonstruiert. Die wichtigste Signatur um ein Myon aus einer Neutrino-Wechselwirkung zu identifizieren ist eine nach oben laufende Spur. Der dominierende Untergrund von Myonen, erzeugt in Wechselwirkungen der kosmischen Strahlung in der Atmosphäre, kann die Erde nicht durchdringen. Ein Datensatz mit 4282 aufwärtslaufenden Ereignissen wurde aus den ca. 10 Milliarden im Zeitraum dieser Analyse registrierten Ereignissen extrahiert. Diese Zahl ist konsistent mit der erwarteten Anzahl atmosphärischer Neutrinos.

In der Suche nach Punktquellen wird nach einem lokalen, statistisch signifikanten Ereignisüberschuss in diesem Datensatz gesucht. Zuerst werden Quellkandidaten wie zum Beispiel aktive galaktische Kerne, Supernovaüberreste und Röntgen-Binärsysteme untersucht. Danach wird eine Rastersuche nach unbekannten Quellen auf dem ganzen nördlichen Himmel durchgeführt. Darüberhinaus werden Methoden entwickelt um die Chancen einer Detektion von Quellen zu erhöhen von denen vermutet wird, dass ihre Neutrinoemission hochvariabel ist. Wir suchen nach einem Ereignisüberschuss in Zeiträumen in denen die Quelle aktiv ist, was wir als den Zustand definieren in welchem erhöhte elektromagnetische Emission in bestimmten Frequenzbändern sichtbar ist. Ein weiterer Test mit einem Zeitschiebefenster wird auf den Datensatz angewendet, um kurze Phasen stark erhöhter Neutrinoemission zu finden, die in der zeitintegrierten Suche unsichtbar wären.

Kein signifikanter lokaler Ereignisüberschuss, auch nicht in einer kurzen Phase, wurde im analysierten Datensatz gefunden. Deswegen berechnen wir obere Grenzen für Neutrinoflüsse, die mit dieser Beobachtung verträglich sind. Die mittlere obere Flussgrenze für ein Neutrinospektrum $d\Phi/dE \propto E^{-2}$, die mit dieser Analyse erreicht wird, ist $E^2\, d\Phi/dE = 1.0 \cdot 10^{-7}$ GeV cm^{-2} s^{-1} für den aufaddierten Fluss von $\nu_\mu + \nu_\tau$ unter der Annahme eines *Flavor*-Verhältnisses von 1 : 1. Dies entspricht der momentan niedrigsten Flussgrenze für Neutrinoflüsse von Punktquellen.

Schlagwörter:
AMANDA, Punktquelle, Neutrinos, Kosmische Strahlung

Contents

Chapter 1

Preface

“On the 11th day of November in the evening after sunset, I was contemplating the stars in a clear sky. I noticed that a new and unusual star, surpassing the other stars in brilliancy, was shining almost directly above my head; and since I had, from boyhood, known all the stars of the heavens perfectly, it was quite evident to me that there had never been any star in that place of the sky, even the smallest, to say nothing of a star so conspicuous and bright as this. … A miracle indeed, one that has never been previously seen before our time, in any age since the beginning of the world”[1]

Tycho Brahe, De Stella Nova, 1573

In ’De Stella Nova’ Tycho Brahe describes the first systematic astronomical observation of what seemed to him the birth of a new star. It took more than three centuries to find out that it was actually the death of a star, a Supernova. The core of the star collapsed while its hull was blasted away into the universe. With today’s instruments we can still see the remnants from this catastrophic event as a source emitting X-rays and radio waves, called Tycho’s Supernova remnant.

A remarkable feature of the observed radiation is that its spectrum cannot be explained by thermal emission from the hot gas in the blast wave of the explosion alone. The likely origin of the non-thermal component is synchrotron radiation, pointing to the presence of high energy particles in this and other Supernova remnants. By today, many objects besides the residues of star explosions have been discovered featuring such non-thermal radiation. They constitute what we call the “high-energy” or “non-thermal” universe.

Another evidence for the existence of particle accelerators in the universe came from the discovery of cosmic rays in the beginning of the 20th century. A continuous flux of particles from space with energies of up to 10^{20} eV impinges on the Earth atmosphere. Unfortunately, from measurements of these particles we cannot localize their origin. As charged particles they are un-traceably deflected in the interstellar magnetic fields.

An active science field – high-energy astrophysics – has formed since then trying to discover and understand the sites and processes involved in cosmic particle acceleration. The analysis of data collected in many experiments helped to draw a detailed picture of the non-thermal universe. Sources of high-energy gamma-rays with energies up to several tens of TeV have been found and their energy spectra derived. The cosmic ray flux and its composition has been measured by satellite, balloon and ground based experiments over many orders of magnitude in energy. Still many problems remain unsolved. An outstanding one is the origin of the cosmic rays.

---

[1] quoted from the translation in [Bur78]

A very peculiar elementary particle might help to solve this puzzle, the neutrino. High energy neutrinos are produced by interactions of cosmic rays in the relatively dense photon and matter clouds close to their source. Interacting only by the weak force and carrying no electromagnetic charge, they can reach the Earth on straight trajectories unharmed by matter, photons or magnetic fields. However, the same properties make them also difficult to detect. To observe the rare interactions of astrophysical neutrinos, a detector needs a huge target mass, of the order of giga-tons.

The AMANDA-II detector and its larger successor IceCube, currently under construction, have been designed to allow such a search for cosmic high energy neutrinos with energies above 100 GeV. The giga-ton target is the 3 km layer of glacial ice below the South Pole. Modules equipped with Photomultiplier tubes are deployed in holes drilled up to 2.5 km deep into the glacier. They record the Čerenkov light emitted by the charged particles that are produced in the neutrino interactions. The characteristic cone-like emission pattern of the Čerenkov light and the good time resolution of the Photomultipliers make it possible to reconstruct the direction of the incident neutrinos with an average resolution of $2°$ in AMANDA-II. For IceCube less than $1°$ is expected.

Constructed between 1995 and 2000, the AMANDA-II detector is fully operational since February 2000. In the analysis presented here, we investigate the data collected in 1001 days of effective operation between 2000 and 2004 for indications of neutrino emission from a point-like cosmic source. Due to the overwhelming background from down-going muons produced in cosmic-ray interactions in the atmosphere, this search is restricted to the northern hemisphere. Besides looking for a signal in the integrated observation time, special techniques are applied to enhance the detection chances for sources with a time variable neutrino flux.

We will describe the mechanisms and source candidates for neutrino production in astrophysical environments as well as the propagation and detection of neutrinos in chapter 2. The AMANDA-II detector will be introduced in chapter 3. The description of the simulation software to generate hypothetical signal and background follows in chapter 4. In chapter 5 it will be shown how direction and topological parameters of the recorded events are reconstructed. The reconstructed direction and the topological parameters are used in chapter 6 to separate the signal from the background and produce an event sample dominated by neutrino induced events. We will then present the strategies applied to search for point-sources of neutrinos in chapter 7 and summarize the results of this analysis in chapter 8. From these results flux upper limits on astrophysical neutrino fluxes are derived in chapter 9, after discussion of the systematic uncertainty which has to be taken into account. Finally, in chapter 10 the implications of the flux limits will be discussed and a summary of the analysis is given.

Chapter 2

A short introduction to neutrino astrophysics

2.1 Cosmic rays

In his famous balloon flights of 1912, Victor Hess detected an increase of ionizing radiation with altitude [Hes12] concluding that the origin of this radiation must be high-energy particles from space which interact in the atmosphere. Since then, hundreds of experiments have been conducted to measure the flux, the shape of the energy spectrum and the composition of these high-energy particles called cosmic rays. It was found that the main component were charged nuclei ranging from protons to the heaviest stable elements, but also electrons, positrons, anti-protons and gamma-rays have been identified.

Another component of the cosmic radiation, neutrinos, have only been observed at low energies so far: A continuous flux of MeV-Neutrinos originating from the sun has been observed in several experiments [A^+94, H^+90]. The only detection of MeV-neutrinos from outside the solar system so far was a short burst of neutrinos in coincidence with the Supernova explosion SN 1987A [H^+87, B^+87]. However, we will argue below that the existence of high-energy neutrinos among the cosmic rays is guaranteed from the observation of nuclei impinging on the atmosphere of the Earth with energies up to 10^{11} GeV.

In this section, we give a short overview of the properties of charged and neutral cosmic rays including the neutrino component and how they are connected to each other.

2.1.1 Charged cosmic rays

While electrons, positrons and anti-protons have been observed by various satellite and balloon experiments up to several GeV (for a summary of the measured spectra see [PM05]), charged hadrons from protons to heavy nuclei have been found to dominate the cosmic ray flux over many orders of magnitude in energy. Figure 2.1 shows the measured flux of cosmic rays between 0.01 GeV and 10^{11} GeV. While there is a large uncertainty in the normalization of the flux between different experiments, the slopes of the energy spectra agree well. Over many orders of magnitude, the differential flux follows a power law $d\Phi/dE \propto E^{-\gamma}$. In the high energy range, two characteristic features are visible [Hoe04]: Above the "knee", at $4{\cdot}10^6$ GeV the spectral index steepens from $\gamma \approx 2.7$ to $\gamma \approx 3.1$. Above the "ankle" ($\approx 10^{10}$ GeV) the spectrum flattens again to steeply drop at $5 \cdot 10^{10}$ GeV[1].

---

[1] The existence of a steep drop is still subject to discussions, since data from the AGASA experiment points to an extension of the energy spectrum beyond 10^{11} GeV, while the results from several other experiments indicate a cut-off (see [GS02] for references).

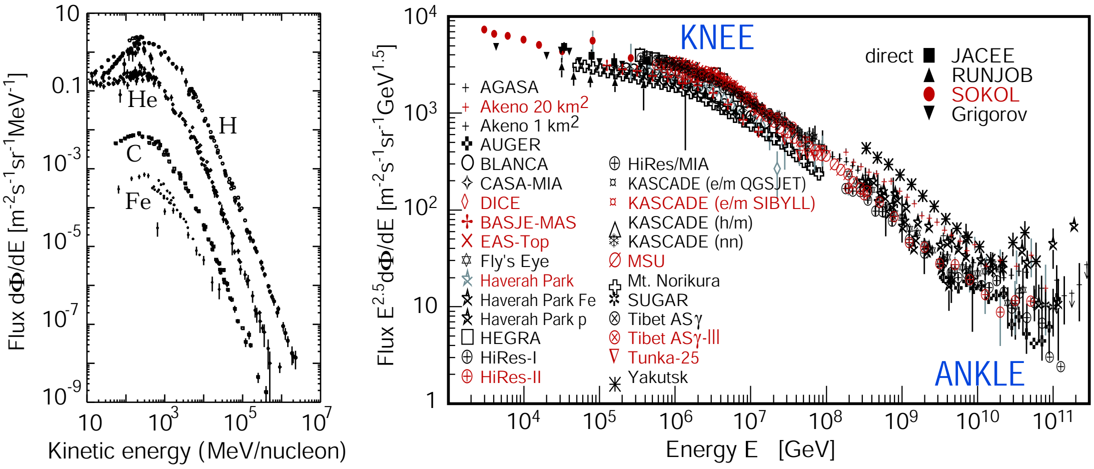

Figure 2.1: *Spectrum of the charged cosmic rays between* 0.01 *GeV and* 10^{11} *GeV. The left picture shows the flux below 10 TeV/nucleon resolving the contribution of different elements. The right picture shows the all-particle flux above 1 TeV derived from the observation of cosmic ray induced air showers in many balloon and ground based experiments. Pictures adapted from [GS02] for this thesis.*

A common explanation for the knee is that the cosmic rays with lower energies are of galactic origin [GS02, Hoe03]. Galactic sources are not expected to be able to efficiently accelerate particles above a few PeV per nuclear charge Z. The actual shape of the spectrum above the knee is then determined by the individual cut-offs in energy for the different elements, which is proportional to Z. The existence of a so called "second knee" at $5 \cdot 10^8$ GeV (i.e. a slight steepening of the spectrum at this energy) supports this theory, since it could originate from the energy cut-off for the heaviest elements. At the ankle, a second extra-galactic population of cosmic ray emitters becomes dominant which can accelerate particles to much higher energies. These sources are believed to be capable of producing particles with energies beyond 10^{11} GeV. The fact that a steep drop in the energy spectrum is still visible above $5 \cdot 10^{10}$ GeV was explained in [Gre66, ZK66] and is called the "GZK cut-off". Protons exceeding this energy interact with the 2.7 K Cosmic Microwave Background radiation producing pions via the Δ-resonance. The attenuation length of $2 \cdot 10^{11}$ GeV protons is 30 Mpc. Therefore, cosmic rays emitted from sources located at considerably larger distances do not reach the Earth without a substantial energy loss.

The spectral index of $\gamma = 2.7$ found below the knee is consistent with the assumption that the acceleration mechanism of the nuclei is Fermi acceleration (see section 2.2), which features typically a spectral index of $\gamma \approx 2.1$. Leakage of the higher energy particles from the Galaxy steepens the spectrum to the observed index of $\gamma = 2.7$.

The sources of both galactic and extra-galactic charged cosmic rays remain unknown so far. Due to the irregular magnetic fields in and outside the galaxy, the trajectories of the charged particles arriving at the Earth do not point back to their origin. To find and explain these objects is one of the main motivations for studying the neutral cosmic rays, high energy photons and neutrinos.

2.1.2 Neutral cosmic rays

Both high energy photons and neutrinos are produced when relativistic nuclei collide with nuclei or photons of the ambient medium. The details of these processes are described

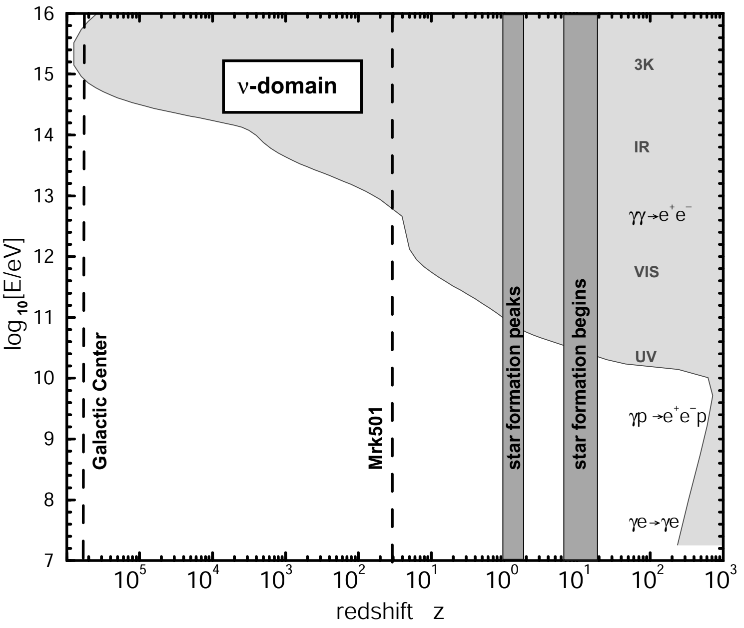

Figure 2.2: *Gamma-ray horizon of the universe. Photons from the grey shaded regions do not reach the Earth. On the right side the responsible absorption process is indicated. Figure adapted from [LM00].*

in section 2.2. The photons and neutrinos generated in the interaction carry a significant fraction of the energy of the accelerated nucleus and reach the Earth on a straight trajectory.

Several hundreds of sources emitting high energy gamma-rays ($E > 100$ MeV) have been discovered so far. A few tens of sources have been identified by Imaging Air Čerenkov Telescopes producing even photons up to TeV energies. However, the detection of high energy photons from these sources does not prove that hadrons are accelerated there. Ultra-relativistic electrons accelerated in the source can produce such photons by Inverse Compton (IC) scattering [Sch03] of the electrons off ambient photons. In the simplest of such scenarios the photons are provided by the synchrotron radiation of the same electron population (Synchrotron-Self-Compton or short SSC model). But also external photons from the source can exhibit the photon target (External-Compton or EC model). A common term to define the scenarios explaining the origin of the high energy gamma-rays based on electron acceleration and IC scattering is “leptonic models”. In contrast, models are named ”hadronic models’, if the high energy photons are assumed to be produced by the decay of pions generated in collisions of hadrons. Spectral features of the measured photon flux might distinguish between a hadronic or a leptonic origin of the photons but no feature has been found so far in the analysis of gamma-ray spectra which is unambiguously contradicting the one or the other scenario.

2.2 High energy neutrino production in astrophysical environments

The detection of cosmic high energy neutrino sources on the other hand would be a “smoking gun”: neutrinos are the unambiguous sign for hadron acceleration and interaction since they can only be produced in the decay of charged mesons. For this reason they are unique messengers providing new insight into the cosmic acceleration sites. But also a second reason makes the search for neutrino emitting objects worthwhile: gamma-rays interact with the photons of the extra-galactic and galactic background light in the process

$$\gamma + \gamma_{EBL} \longrightarrow e^{+} + e^{-} \ , \tag{2.1}$$

if their center-of-mass energy exceeds the pair production threshold. This makes the universe opaque to gamma-rays emitted from a certain distance. Figure 2.2 shows the gamma-ray horizon in units of the redshift z versus the photon energy. The distance of the Galactic Center and a nearby Active Galaxy (Mrk 501) are indicated. The early universe is invisible to gamma-ray astronomy already at TeV energies, at PeV energies even our own galaxy forms a barrier to high energy photons. In these distance and energy regions, neutrinos can provide exclusive information from acceleration processes and sites in the universe.

2.2.1 Neutrino production

In an astrophysical environment high-energy neutrinos are mainly produced from the decay of pions generated in the interactions of accelerated protons and nuclei with target protons or photons via the reactions:

$$\begin{array}{rcl} p + N & \longrightarrow & \pi^{\pm} + \pi^{0} + K^{\pm} + K^{0} + \ldots \\ p + \gamma \longrightarrow \Delta^{+} & \longrightarrow & \pi^{+} + n \\ & \longrightarrow & \pi^{0} + p \ . \end{array}$$

The charged pions subsequently decay into neutrinos and leptons while the neutral pions decay into photons:

$$\begin{array}{rcl} \pi^{+} & \longrightarrow & \mu^{+} + \nu_{\mu} \longrightarrow e^{+} + \nu_{e} + \overline{\nu}_{\mu} + \nu_{\mu} \\ \pi^{0} & \longrightarrow & \gamma + \gamma \\ \pi^{-} & \longrightarrow & \mu^{-} + \overline{\nu}_{\mu} \longrightarrow e^{-} + \overline{\nu}_{e} + \nu_{\mu} + \overline{\nu}_{\mu} \ . \end{array}$$

The contribution to the neutrino flux from higher mass mesons (like $K^{\pm}$, K^{0}) is small and can be neglected. In a thin medium (like astrophysical environments) pions and muons decay before they interact resulting in an approximate production ratio of muon neutrinos and electron neutrinos $(\nu_{\mu} + \overline{\nu}_{\mu}) : (\nu_{e} + \overline{\nu}_{e})$ of 2:1 independent of energy. It has been argued that this ratio might change for particle energies $E_{\nu} \gg 100$ TeV, in dense sources where free muon decay is suppressed (i.e. the muon looses a significant amount of energy due to interactions before it decays) [KW05].

An additional contribution to the number of electron neutrinos due to the decay of free high energy neutrons produced in the interactions above or by photo-disintegration of heavy nuclei via

$$n \ \longrightarrow \ p + e^{-} + \overline{\nu}_{e} \ ,$$

can be neglected since the energy of the produced anti-neutrino is $\approx 10^{3}$ times smaller than the energy of the parent neutron and the flux of nuclei drops steeply with energy for common acceleration scenarios [KW05].

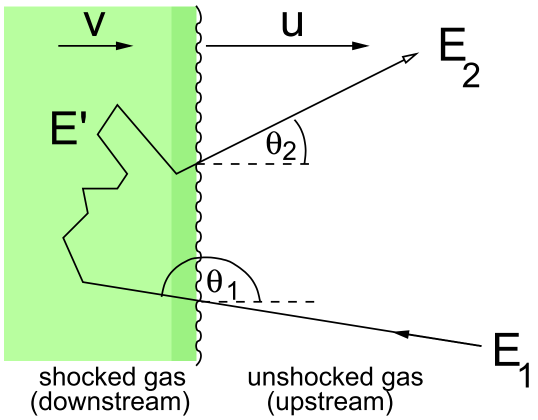

Figure 2.3: *Schematic view of Fermi acceleration across a shock front in interstellar gas. The "downstream" region corresponds to the shocked gas, the "upstream" region to the unshocked gas.*

2.2.2 Fermi acceleration

The acceleration mechanism usually considered responsible for producing the spectrum of high energy nuclei is (first order) Fermi acceleration [Fer49] through shock waves in the interstellar medium. The following description is based on [Gai90].

Figure 2.3 illustrates first order Fermi acceleration. A plane shock front, i.e. a supersonic wave, is moving at a speed $\vec{\mathbf{u}}$, much larger than the speed of sound c_s in the surrounding medium. In the laboratory frame the gas in front of the shock wave ("upstream") is at rest. The gas behind the shockwave ("downstream") moves slower than the shock front. Its speed is $\vec{\mathbf{v}} = 3/4\,\vec{\mathbf{u}}$.

Now consider a relativistic particle ($E_1 \gg m_1$) with an energy E_1 crossing the shock front under an angle θ_1 (to the shock front normal) into the "downstream" region. Its energy in the rest frame of the gas behind the shock front is:

$$E_1' = \gamma E_1 (1 - \beta \cos\theta_1) \ , \tag{2.2}$$

where $\beta = |\vec{\mathbf{v}}|/c$ is the speed of the gas and $\gamma = (1-\beta^2)^{-1/2}$. The particle is elastically "scattered" by the irregular magnetic fields in the plasma behind the shock conserving its energy ($E_2' = E_1'$). If it crosses the shock front again with an angle θ_2' its energy in the upstream rest frame becomes:

$$E_2 = \gamma E_2' (1 + \beta \cos\theta_2) = \gamma^2 E_1 (1 - \beta\cos\theta_1)(1 + \beta\cos\theta_2') \ . \tag{2.3}$$

The average net gain of energy $\langle E_2 - E_1 \rangle$ by this process can be calculated by averaging over the angles $\langle \cos\theta_1 \rangle$ and $\langle \cos\theta_2 \rangle$, taking into account the probability distribution for a particle moving at an angle θ to cross the shock front.

The velocity distribution of particles in the rest frames of the downstream and upstream gas are uniform. However, the probability that such a particle crosses the shock front again is proportional to its velocity component perpendicular to the shock front. For the average over the angle one finds $\langle \cos\theta_2' \rangle = -\langle \cos\theta_1 \rangle = \frac{2}{3}$. Using (2.3) the average energy gain per acceleration cycle becomes:

$$\frac{\langle E_2 - E_1 \rangle}{E1} = \frac{1 + \frac{4}{3}\beta + \frac{4}{9}\beta^2}{1 - \beta^2} - 1 \approx \frac{4}{3}\beta = \frac{|\vec{\mathbf{u}}|}{c} \,. \tag{2.4}$$

The energy gain is of first order in β, which distinguishes the described mechanism from the one originally described by Fermi for an acceleration in moving magnetized gas clouds. An equivalent line of argumentation can be followed for the energy gain in such clouds, but the average over the angles results in different values due to the modified geometry. The energy gain is then second order in β and therefore called second order Fermi acceleration:

$$\frac{\langle E_2 - E_1 \rangle}{E1} \approx \frac{4}{3}\beta^2 = \frac{3|\vec{\mathbf{u}}|^2}{4c^2} \,. \tag{2.5}$$

The small energy gain per acceleration cycle makes it unlikely that second order Fermi acceleration can produce particles of such high energies as the ones observed in cosmic rays under realistic astrophysical conditions.

After one acceleration cycle, the particles can escape with the probability P_{esc} or they are scattered back and the process is repeated. Taking into account the energy gain per acceleration cycle (2.4), the produced energy spectrum of particles by first order Fermi acceleration can be calculated. The number of particles N with an energy larger than E follows a power law:

$$N(\geq E) \propto 1/P_{\text{esc}} \left(\frac{E}{E_1} \right)^{-\gamma} \,, \tag{2.6}$$

with $\gamma \approx P_{\text{esc}}\, c/|\vec{\mathbf{u}}|$. An evaluation of P_{esc} results in a differential spectrum dN/dE for strong shocks of:

$$\frac{dN}{dE} \propto E^{-2-\frac{4c_s^2}{|\vec{\mathbf{u}}|^2}} \approx E^{-2.1} \,, \tag{2.7}$$

where $c_s \ll |\vec{\mathbf{u}}|$ is the velocity of sound in the interstellar gas.

2.2.3 Acceleration in electrostatic gaps

A different mechanism generating high energy nuclei which could lead to the production of neutrinos is the acceleration in electrostatic gaps [LB05], which are supposed to arise around rotating neutron stars, called Pulsars. Figure 2.4 shows a schematic view of such a Pulsar. In general the direction of the magnetic moment $\vec{\mu}$ and the rotation axis $\vec{\mathbf{\Omega}}$ of a Pulsar are not aligned. A remarkable feature is the existence of open magnetic field lines in the polar regions, along which an outflow of particles is possible.

An analytical calculation for the case that magnetic moment and rotation axis are aligned [GJ69] finds a potential drop across the Pulsar surface from the pole to the last open field line of:

$$\Delta\Phi = \frac{\Omega^2 B R^3}{2c^2} \,, \tag{2.8}$$

where $\Omega = 2\pi/t_r$ is the angular velocity, B the magnetic field at the poles and R the radius of the Pulsar surface. In the region of closed field lines, the potential drop is compensated in equilibrium by plasma surrounding the Pulsar (the so called magnetosphere). In the

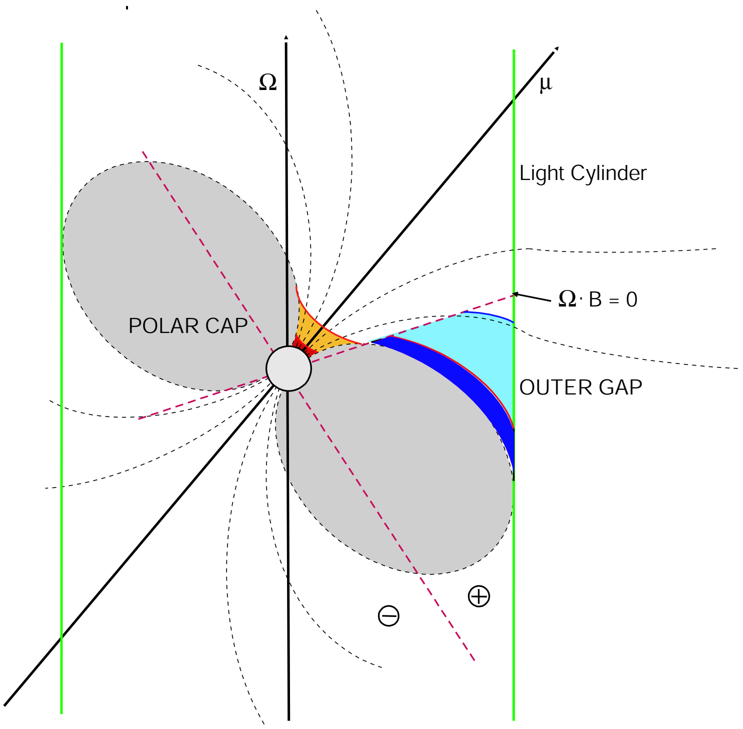

Figure 2.4: *Model of a Pulsar with misaligned rotational and magnetic moment axes. Around the polar caps open field lines exist, which allow a particle outflow along them. Discussed regions of electrostatical gaps are shown as orange and blue regions. Picture adapted from [Sch05].*

region of open field lines such an equilibrium is never fully reached due to the constant outflow of particles. Detailed calculations for misaligned rotation and magnetic moment axes [RS75, CHR85] result in electrostatic gaps, where particles could be accelerated. The proposed locations of these gaps are shown as orange and blue areas in figure 2.4. It is reasonable to assume that the potential difference across these gaps is of the order of (2.8). For the case of $\vec{\mu}\,\vec{\boldsymbol{\Omega}} < 0$, positively charged nuclei can be accelerated in the gaps. For typical parameters of Pulsars, a magnetic field of $B = 10^{12}$ G, a rotation period of $t_r = 10$ ms and a surface radius of $R = 10^6$ cm protons can reach PeV energies if the full potential drop is available.

This energy is high enough to produce pions via the Δ-resonance in photo-nuclear interactions with thermal photons available around the Pulsar (typical surface temperature of young Pulsars: $T_s = 0.1$ keV). The subsequent decay of the pions would lead to a flux of high energy neutrinos from such an object.

2.3 Galactic and extragalactic neutrino sources

2.3.1 Active Galactic Nuclei

Prime candidates for neutrino emission produced in the interactions of Fermi accelerated hadrons are Active Galactic Nuclei (AGN). The contemporary picture of an AGN is shown in figure 2.5. A super-massive black hole with a mass of $M > 10^8 M_\odot$ is located inside a very luminous galaxy. The black hole is surrounded by an accretion disk ($r \approx 10^{-3}$ pc), providing the energy for relativistic jets of matter, which are ejected perpendicularly to the disk. Further away from the black hole – in the same plane as the accretion disk –

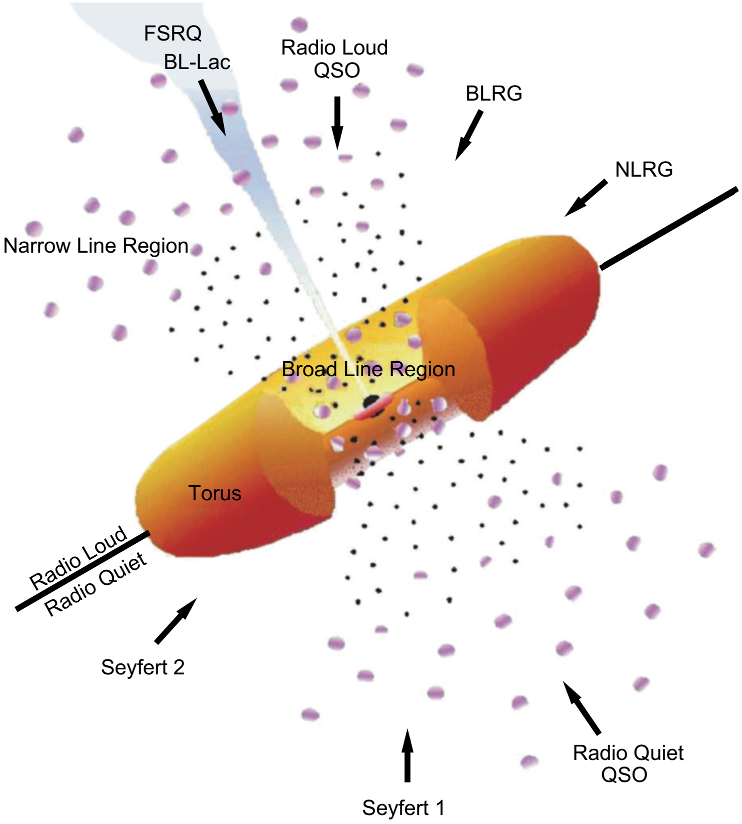

Figure 2.5: *Schematic view of the unification model for AGN. The upper half corresponds to a radio-loud AGN, the lower half to a radio-quiet AGN. A central black hole is surrounded by an accretion disk and a toroidal dust cloud. Perpendicular to it a relativistic jet can form. The different morphologies observed from these objects are caused by different viewing angles. The names of the morphological classes and the corresponding viewing angles are indicated on the picture. Picture adapted from [Tlu03].*

concentric toroidal gas clouds are found which feed the accretion disk ($r \approx 100$ pc) [Ree84].

With this model of an AGN it was possible to unify several classes of previously discovered extragalactic objects showing different morphologies. A detailed description of the problems and the results of the AGN unification is found in [UP95]. An overview of all morphological classes can be found in [A$^+$06a]. The main morphological classification parameters are the radio flux, the width of absorption lines and the intrinsic source luminosity. In the unified AGN model, radio emission from a source emanates mainly from the relativistic jet. The observed radio luminosity L is related to the intrinsic luminosity L_0 by the relativistic Doppler factor δ:

$$L = \delta^4 L_0 = \left(\gamma(1 - \beta\cos\theta_v)\right)^{-1} L_0 \ , \tag{2.9}$$

and therefore to the viewing angle θ_v under which we observe this jet (β is the bulk velocity of the jet and $\gamma = (1-\beta^2)^{-1/2}$).

Also the width of the absorption lines depends on the viewing angle. If we observe the AGN from a direction perpendicular to the jet, we observe only absorption from the slow gas clouds far away from the black hole and therefore narrow absorption lines (Narrow Line Radio Galaxies, Fanaroff-Riley-I/II Galaxies). For intermediate angles, broadened absorption lines can be seen from the fast moving clouds close to the accretion disk (Broad

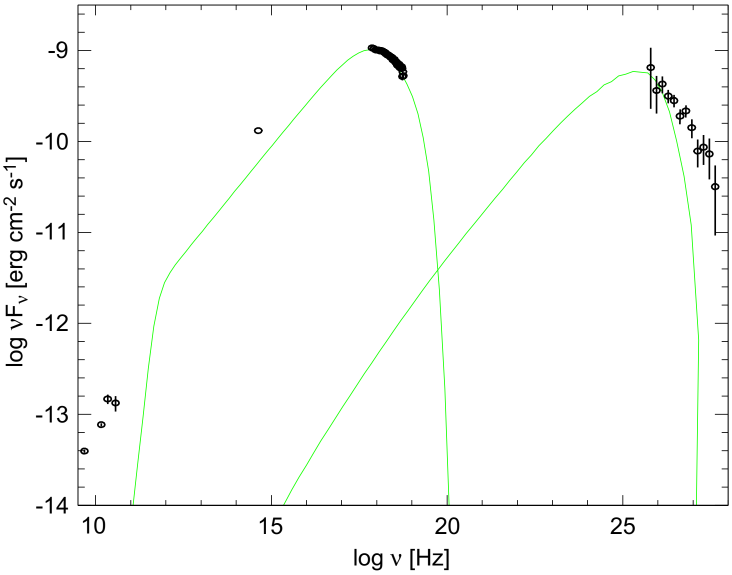

Figure 2.6: *The spectral energy distribution of Markarian 421 – a high peaked BL Lac object – in a state of high flux. The two peaked structure is typical for all Blazars. The green lines represent a fit of the spectrum with a model assuming leptonic acceleration. Picture adapted from [B$^+$05b].*

Line Radio Galaxies, Steep Spectrum Radio Quasars). Finally, if we look straight into the jet the absorption lines vanish and a flat spectrum is found (BL Lac objects, Flat Spectrum Radio Quasars). Besides the radio-loud objects, also sources with weak radio emission (no or faint jet) can be similarly unified by taking the viewing angle into account. Seyfert-II Galaxies show narrow lines, implying that the core region is obscured by the torus gas clouds from our line of sight. Seyfert-I Galaxies and Radio Weak Quasars feature broad absorption lines from the accretion disk region. The mapping of the various morphological classes to different viewing angles is illustrated in figure 2.5.

Equation (2.9) is also valid for the neutrino luminosity of a source. For a jet with $\gamma = 10$ the Doppler factor can become as large as $\delta = 20$ if the jet is closely aligned to our line of sight enhancing drastically the observable flux. That makes the BL Lac objects and Flat spectrum Radio Quasars (FSRQ) the most interesting candidates to look for neutrino emission among all AGN. Both object classes together are called Blazars and are characterized by a spectral energy distribution (SED) with two distinct peaks, the lower one ranging from infrared to X-ray energies, the higher one from MeV to TeV energies. An example of such a spectral energy distribution for Markarian 421 is shown in figure 2.6. The main difference between individual objects within the Blazar class are the radio luminosity and the position of the peaks in the SED. The peak energy provides a classification of the BL Lac objects into HBL (“high-frequency peaked BL Lac”) and LBL (“low-frequency peaked BL Lac”) as well as a classification of the FSRQs into HPQ (“high-frequency peaked Quasar”) and LPQ (“low-frequency peaked Quasar”). Moreover one can find a correlation between the radio luminosity and the peak energy in the SED, so these groups can be ordered by decreasing radio luminosity and increasing peak energy to form the “Blazar-sequence” [Ghi98]:

$$\begin{array}{c}\textbf{LPQ} \longrightarrow \textbf{HPQ} \longrightarrow \textbf{LBL} \longrightarrow \textbf{HBL}\\ \longrightarrow \quad \text{decreasing radio luminosity}\\ \longrightarrow \quad \text{increasing peak energy}\end{array}$$

Consequently, TeV gamma-rays have been observed so far only from HBLs, while many LBLs and FSRQs have been observed in the MeV to GeV band by the EGRET satellite experiment. Both leptonic [Ghi98] and hadronic [M^+03] acceleration models have been successfully applied to fit Blazar spectra.

In the case that hadrons are accelerated, one can ask the question which Blazars would be the strongest neutrino sources. In a naive approach one can just assume that if the gamma-rays are produced by π^0-decay, an approximately equal number of charged pions would be produced. The ratio of gamma-rays to neutrinos would be about 1:1 at the source in such a case [Gai90]. The highest photon energies are measured for HBLs up to several TeV. During high states (states with enhanced emission, see below) the gamma-ray flux from these objects is close to a neutrino flux which could be detected by the analysis described in this work. Following this line of reasoning we consier the 5 HBL, visible in TeV gamma-rays on the northern sky, as neutrino source candidates for this analysis (see section 7.1.2).

However, more advanced models prefer the LBLs and FSRQs as neutrino sources. The common aspect of these models is that protons are accelerated to energies of 10^{10} GeV. Due to the lack of target material, neutrino production happens by $p\gamma$-interactions with the soft photons available in the core of the AGN.

In [M^+03] electrons and protons are co-accelerated. The synchrotron radiation from the electrons produce the lower peak in the SED, while the peak at high energies is due to proton, muon and pion synchrotron radiation as well as gamma-rays from π^0-decay. An additional contribution comes from the photons radiated in the aforementioned processes which then interact with soft photons producing e^+e^--pair-cascades. In fitting the observed spectra from Blazars one finds that for HBL the proton and muon synchrotron radiation are the dominant processes producing the high energy peak in the SED. The luminosity from $p\gamma$-interactions – which would produce neutrinos – is about three to four orders of magnitude lower. For LBLs on the other hand, where higher densities of soft photons are observed, the contribution from π^0-decay is significant and the power emitted in neutrinos is comparable to the power emitted in high energy photons.

[N^+02, NS02] come to a similar conclusion employing an argument based on the cross sections for $p\gamma$-interactions and $\gamma\gamma$-interactions. To efficiently produce neutrinos the mean free path for high energy protons $l_p = (\sigma_{p\gamma} n_{\mathrm{soft}})^{-1}$ must be much smaller than the radius of the AGN core R_c (n_{soft} denotes the number density of soft photons in the core). On the other hand for high energy photons to escape from the core region, their mean free path $l_\gamma = (\sigma_{\gamma\gamma} n_{\mathrm{soft}})^{-1}$ must be larger than the size of the core. With $\sigma_{\gamma\gamma} \approx 10^{-25}$ cm^2 and $\sigma_{p\gamma} \approx 10^{-28}$ cm^2 both conditions cannot be simultaneously fulfilled. Therefore TeV-visible Blazars should not be promising neutrino emitters. A list of EGRET Blazars which are candidates for strong neutrino emission is provided in [NS02].

Three other individually selected AGN are considered in this analysis as candidate sources for neutrino emission:

3C273: the optically brightest FSRQ, which has been considered a strong neutrino source in [NMB93, SS96].

M87: the closest AGN at a redshift of $z = 0.004$ classified as a Fanaroff-Riley galaxy. Its proximity compensates for the smaller Doppler boost due to the mis-alignment of the jet with respect to the line of sight. TeV gamma-rays have been observed from this source [A^+03b]. Neutrino emission from this object has been predicted by [PDR03].

NGC1275: the closest Quasar-like Seyfert Galaxy.

A second aspect of Blazars has not been mentioned so far. Their high energy as well as their optical/x-ray emission is extremely variable. The luminosity in the low energy peak and the high energy peak of the SED is correlated during different states of activity. This is usually attributed to the fact that the observed spectrum originates from small emission regions which move along the jet (see [Boe04] for a small review on Blazar variability). Emerging new emission regions result in strong outbursts, in which the photon flux can easily change by two orders of magnitude on time scales of hours to days. This behaviour makes them interesting objects for a search for neutrino emission correlated with an active state, which will be presented in this thesis (see section 7.2).

2.3.2 X-ray binaries

X-ray binaries are systems of a compact object (a black hole or a neutron star) orbiting a massive star. Gas from the star accretes in a disk around the compact object and sometimes relativistic jets appear. The sub-class of objects where such jets have been observed is called Microquasars. They are usually considered as the down-sized galactic counterparts of AGNs: a solar mass black hole, surrounded by an accretion disk and emitting a (parsec-scale) relativistic jet [MR99]. Their temporal behaviour is quite complex. Many of the known Microquasars exhibit strong outbursts with correlated enhanced emission in several frequency-bands, while others show rather steady emission from the jet or even periodic flares.

In [LW01] a mechanism is presented how such objects could be significant sources of neutrinos. During outbursts accelerated protons should interact with X-ray photons from the accretion disk producing neutrinos in $p\gamma$-interactions. Considering the environment, neutrinos up to energies of 100 TeV are predicted in the model. The neutrino emission should be correlated to the radio emission and precede the radio flare by several hours. [D$^+$02] calculated neutrino rates for several known Microquasars. The source SS 433 – featuring persistent jets – would be a strong neutrino source according to these calculations, which should be visible in this analysis. An additional contribution to the neutrino flux was suggested by [Bed05]. Accelerated heavy nuclei in the jet could photo-disintegrate by interacting with external photons from the companion star. Neutrons would then reach the accretion disk or the star before decaying and interacting with the gas found there. The resulting neutrino flux is predicted to be of the same order of magnitude as in [D$^+$02].

Also in X-ray binaries featuring no jet, high energy neutrinos could be produced. [A$^+$03c] predict neutrinos of energies up to 1 TeV from the accreting neutron star AO 0535+26. There, protons might be accelerated in electrostatic gaps around the Pulsar and then interact in the accretion disk to produce neutrinos in pp-interactions.

For the listed reasons all known Microquasars and AO 0535+26 are considered candidate neutrino sources in this analysis.

2.3.3 Pulsars and Supernova remnants

Supernova explosions of massive stars leave behind a compact spinning neutron star or black hole and an expanding shock wave: the Supernova remnant. If pulsed radio emission can be seen from a rotating neutron star it is called a Pulsar. An illustration of such an object is given in figure 2.4. Many Pulsars are known in the Galaxy with rotation periods ranging from 1 ms to 10 s, decreasing with age due to the energy lost in magnetic dipole radiation. Charged particles can be accelerated in electrostatic gaps of the Pulsar magnetosphere (see section 2.2). Along the open magnetic field lines around its polar caps, a constant outflow of particles from the Pulsar surface creates the Pulsar wind nebula. Neutrino production in this nebula has been considered by [BP97]. Heavy nuclei are accelerated in the electrostatic gap of young Pulsars and photo-dissociate in interactions with photons from the Pulsar surface. The created neutrons propagate to the Pulsar wind nebula to decay into protons, which then interact with the surrounding medium and create gamma-rays and neutrinos up to energies of $E_\nu \approx 100$ TeV (for the Crab Pulsar). In [LB05] it is proposed that accelerated protons would directly interact with thermal X-ray photons close to the Pulsar surface to create neutrinos in $p\gamma$-interactions. Such an emission of neutrinos would be pulsed, similar to the radio signal from these sources.

High energy gamma-rays have been seen from several Pulsars and their nebulae [H^+99, A^+05b] some up to TeV energies. The most famous of those objects is the Crab Nebula, which became the "standard candle" of gamma-ray astronomy, emitting an intense constant flux of photons. In [GA03] neutrino rates are anticipated from the Crab Nebula and similar Pulsars, which could be detected by km^3-sized detectors (like IceCube) based on the assumption that the gamma-rays are produced in hadron interactions.

Besides the three Pulsar wind nebulae, considered as neutrino sources in the models above, we will also analyze two individually selected objects. The Magnetar SGR 1900+14 and the Geminga Pulsar. A Magnetar is a Pulsar with an extremely high surface magnetic field of $B \approx 10^{15}$ G and occasional very intense X-ray outbursts. [Z^+03] predict a neutrino flux from these objects resulting from $p\gamma$-interactions close to the Magnetar surface. Geminga is the closest Pulsar and a very strong source of high energy photons ($E > 100$ MeV), as measured by the EGRET satellite [H^+99].

High energy particles can be produced not only in the Pulsar magnetosphere but also in the shock wave via Fermi acceleration. These shock waves expand freely for several hundreds of years until they start to decelerate in the so called Sedov-Taylor phase. TeV gamma-ray emission has been detected from shell-type Supernova remnants, where the shock wave is observed, but no central Pulsar is found. The most remarkable result was a spatially resolved image of the TeV gamma-ray emission of the supernova remnant RX J1713.7-3946 by the H.E.S.S. telescope array [A^+04a] matching the structures of the remnant seen at lower frequencies. The spectral features of this source can be explained assuming hadron acceleration in the remnant [BV06]. While RX J1713.7-3946 is not visible for a neutrino telescope located at South Pole, another shell-type Supernova remnant detected in TeV gamma-rays [A^+01a] – Cassiopeia A – can be investigated in this analysis . Also here the spectrum is found compatible with photons originating from π_0 decay [BPV03]. Expected neutrino rates based on the observed emission of high energy gamma-rays have been calculated in [AMH02].

2.3.4 Other source candidates

Besides these generic classes of neutrino source candidates, a possible neutrino emission from the following individually selected objects is investigated here:

- The cosmic ray multiplets: An analysis of the arrival directions of the ultrahigh energy cosmic rays ($E > 4 \cdot 10^9$ GeV) detected by different air shower experiments has revealed several clusters [U^+00]. Since the deflection in intergalactic magnetic fields at these energies is small, a point source of charged cosmic rays and neutrinos might be expected in that direction. The two triplets found in [U^+00] have been included in this analysis.

- The unidentified TeV source TeV J2032+4131: A source of TeV gamma-rays was detected by the HEGRA telescopes in the Cygnus OB2 region [A+02]. Cygnus OB2 is a globular cluster of young, massive stars. The spectral properties of this source found in follow-up observations in the X-ray and radio bands indicate hadron acceleration [B+03b].
- The unidentified EGRET source 3EG J0450+1105: Most of the gamma-ray sources discovered by EGRET are still unidentified, but potentially interesting neutrino sources. 3EG J0450+1105 is the EGRET source with the highest flux of photons ($E > 100$ MeV) of $1.1 \cdot 10^{-6}$ cm^{-1} s^{-1} detected on the northern hemisphere among the unidentified objects.

2.4 The physics of neutrino detection

After this short overview of the cosmic production mechanisms and sites of high energy neutrinos we will now focus on the fundamentals of physics related to the propagation of neutrinos and their detection in a large volume detector like AMANDA-II.

On their long way to the Earth the flavor of the neutrinos oscillates. Inside the earth the particles might be absorbed or loose energy due to interactions, before they can reach the active volume[2] of a neutrino detector. The cross section for deep inelastic neutrino-nucleon scattering and the energy loss processes of the muons produced there determine the rate of events which can be measured. The Čerenkov radiation emitted by the muons can be used to detect them. Finally, interactions of charged cosmic rays in the atmosphere which produce neutrinos and muons, have to be taken into account as a background in the search for cosmic sources of neutrinos.

2.4.1 Neutrino oscillation

The flavor eigenstate of a neutrino is not its mass eigenstate. Similar to the CKM-matrix in the quark sector, the unitarian Maki-Nakagawa-Sakata (MNS) matrix U^* describes the linear combination of mass eigenstates $i = (1, 2, 3)$ that form a flavor eigenstate $\alpha = (e, \mu, \tau)$ [Kay05]:

$$|\nu_\alpha\rangle = \sum_{i=1}^{3} U^*_{\alpha i} |\nu_i\rangle \; . \tag{2.10}$$

As a consequence, the flavor of massive neutrinos oscillates during the propagation. The probability for an oscillation from flavor α to flavor β after a distance x is:

$$P(\nu_\alpha \to \nu_\beta; x) = |\langle \nu_\beta | \nu_\alpha(x) \rangle|^2 = \delta_{\alpha\beta} - \sum_{i \neq j} U^*_{\alpha i} U_{i\beta} U^*_{\beta j} U_{j\alpha} \left(1 - \exp\left(\frac{-i \Delta m^2_{ij} x}{2E} \right) \right) \; , \tag{2.11}$$

depending on the matrix elements of U^*, the mass difference Δm^2_{ij} between two mass eigenstates and the energy E of the neutrino. The factor $E/\Delta m^2_{ij}$ defines the length scale on which the oscillations take place. In the approximation of two-flavor oscillations one

---

[2] The volume in which muons produced in charged current interactions reach the detector and can be recorded.

can define the oscillation length L_{ij} as the distance between two maxima of $P(\nu_\alpha \to \nu_\alpha; x)$. In SI-units it is:

$$L_{ij} = \frac{4\pi\hbar E}{\Delta m_{ij}^2 c^3} = 2.48 \text{ m} \left(\frac{E}{\text{MeV}}\right)\left(\frac{\text{eV}^2}{\Delta m_{ij}^2}\right) . \tag{2.12}$$

The oscillation length is short compared to cosmic distances (>100 pc) even for the highest energy neutrinos. For cosmic neutrinos one can assume therefore full mixing and evaluate $P(\nu_\alpha \to \nu_\beta)$ averaging over the oscillations [AJY00]. One finds:

$$\langle P_{\alpha\beta}\rangle = \langle P(\nu_\alpha \to \nu_\beta)\rangle = \delta_{\alpha\beta} - \sum_{i\neq j} U^*_{\alpha i} U_{i\beta} U^*_{\beta j} U_{j\alpha} = \sum_i |U^*_{\alpha i}|^2 |U^*_{\beta i}|^2 . \tag{2.13}$$

The main interest of this analysis is how the flavor ratios $\Phi_s(\nu_e) : \Phi_s(\nu_\mu) : \Phi_s(\nu_\tau)$ of a neutrino flux Φ_s emitted from a distant source change during propagation of the neutrinos to the Earth. With (2.13), the flux ratio $\Phi_e(\nu_e) : \Phi_e(\nu_\mu) : \Phi_e(\nu_\tau)$ at the Earth is given by:

$$\begin{pmatrix} \Phi_e(\nu_e) \\ \Phi_e(\nu_\mu) \\ \Phi_e(\nu_\tau) \end{pmatrix} = \begin{pmatrix} \langle P_{ee}\rangle & \langle P_{\mu e}\rangle & \langle P_{\tau e}\rangle \\ \langle P_{e\mu}\rangle & \langle P_{\mu\mu}\rangle & \langle P_{\tau\mu}\rangle \\ \langle P_{e\tau}\rangle & \langle P_{\mu\tau}\rangle & \langle P_{\tau\tau}\rangle \end{pmatrix} \begin{pmatrix} \Phi_s(\nu_e) \\ \Phi_s(\nu_\mu) \\ \Phi_s(\nu_\tau) \end{pmatrix} . \tag{2.14}$$

Neutrinos which originate from pion and subsequent muon decay in a thin medium are produced with a flavor ratio of $\Phi_e(\nu_e) : \Phi_e(\nu_\mu) : \Phi_e(\nu_\tau) = 2 : 1 : 0$ (see section 2.2). For such a flux an evaluation of (2.14) results in a flavor ratio of 1:1:1 at Earth [AJY00].

2.4.2 Neutrino interactions

In the Standard Model neutrinos interact with nucleons by $W^\pm$-boson and Z-boson exchange. If a $W^\pm$-boson is exchanged the reaction is called a "Charged-Current" interaction (CC), in the case of a Z-boson it is called a "Neutral-Current" interaction (NC). In CC-interactions a charged lepton is produced, in NC-interactions a neutrino of the same flavor $l = e, \mu, \tau$ like the incident particle is found in the final state:

$$\begin{aligned} \nu_l + N &\to l + X \quad \text{(CC)} \\ \nu_l + N &\to \nu_l + X \quad \text{(NC)} . \end{aligned}$$

The letter X stands for a hadronic final state in these reactions[3]. The NC reaction does not produce a detectable charged lepton and it is therefore of minor interest for this analysis. The differential cross section for the CC-interaction $\nu_l + N \to l + X$ with an isoscalar nucleon N is given by [G+96]:

$$\frac{d^2\sigma_{CC}}{dxdy} = \frac{2G_F^2 M E_\nu}{\pi} \left(\frac{M_W^2}{Q^2 + M_W^2}\right)^2 (xq(x,Q^2) + x\overline{q}(x,Q^2)(1-y)^2) . \tag{2.15}$$

M is the mass of the nucleon, M_W the mass of the W-boson, G_F the Fermi coupling constant of the weak interaction and $-Q^2$ the invariant squared momentum transfer between

---

[3] The cross sections for neutrino-electron scattering like $\nu_l + e \to l + \nu_e$ are for $l = (\mu, \tau)$ several orders of magnitude lower than the neutrino-nucleon cross sections and therefore neutrino-electron is neglected here.

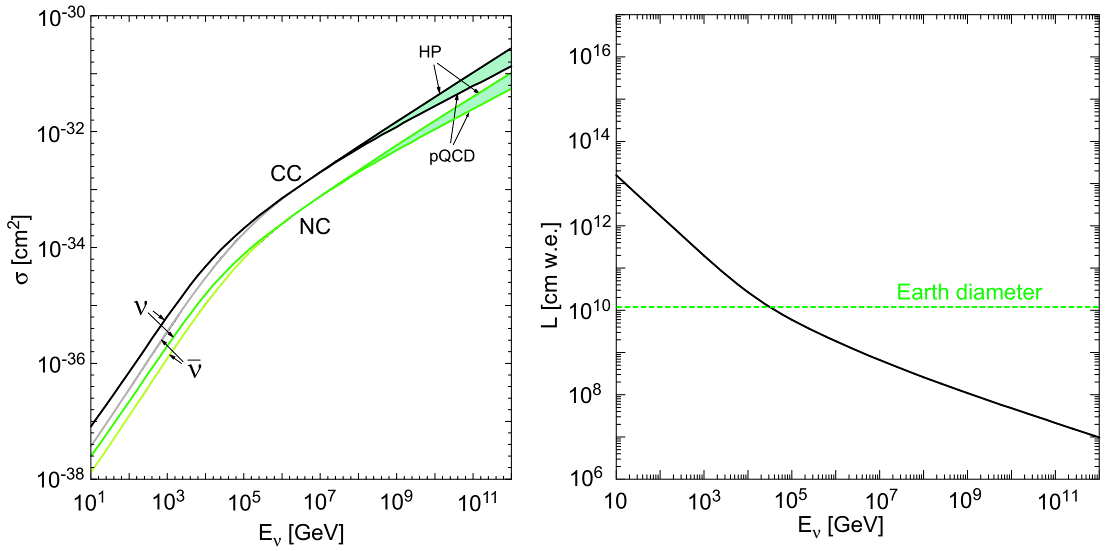

Figure 2.7: *Left: CC and NC cross sections for neutrinos and anti-neutrinos. At high energies the cross section is extrapolated introducing a large uncertainty (shaded areas). See [Kow04] for a detailed discussion of these uncertainties. Right: Mean free path of a neutrino given in units of cm w.e. (i.e. in a medium with a density equivalent to the density of water). For $E_\nu \approx 50$ TeV the mean free path becomes comparable to the diameter of the Earth indicated by the green dashed line.*

the incident neutrino and the outgoing lepton. x and y are the Bjorken scaling variables. $x = Q^2/[2M(E_\nu - E_l)]$ describes the fraction of the nucleon momentum attributed to the reacting parton. $y = 1 - E_l/E_\nu$ is the part of the neutrino energy transferred to the nucleon. Finally, $q(x, Q^2)$ and $\overline{q}(x, Q^2)$ are the parton density distributions of the nucleon, which are linear combinations of the contributions of the single quarks (the indices (v, s) denote contributions from valence and sea quarks respectively):

$$\begin{aligned} q(Q^2, x) &= \frac{u_v(x,Q^2) + d_v(x,Q^2)}{2} + \frac{u_s(x,Q^2) + d_s(x,Q^2)}{2} + \\ &\quad + s_s(x,Q^2) + b_s(x,Q^2) \\ \overline{q}(Q^2, x) &= \frac{u_s(x,Q^2) + d_s(x,Q^2)}{2} + c_s(x,Q^2) + t_s(x,Q^2)\ . \end{aligned} \tag{2.16}$$

For the cross section of the anti-neutrino, a different linear combination of quark contributions enters (2.16). The parton densities are experimentally determined in collider experiments. Tabulated versions of the functions are found for example in [B$^+$05a]. Above $E_\nu \approx 1$ PeV extrapolations have to be used.

The left picture in figure 2.7 shows the CC and NC neutrino cross sections from 10 GeV to 10^{12} GeV. Above about 10^8 GeV a considerable uncertainty is present, since the cross sections depend on the used extrapolation scheme for the parton density functions. The strong increase of the cross sections is important in two aspects for this analysis. At first, the probability for an interaction in the target volume increases for higher energies partly compensating the falling spectrum expected from a flux of astrophysical neutrinos (for example $d\Phi/dE \approx \Phi_0 E^{-2}$ from Fermi acceleration). The peak energy of the neutrinos which produce muons detectable in AMANDA-II therefore depends strongly on the spectrum, shifting from a few hundred GeV for neutrino fluxes with soft spectra to EeV energies for

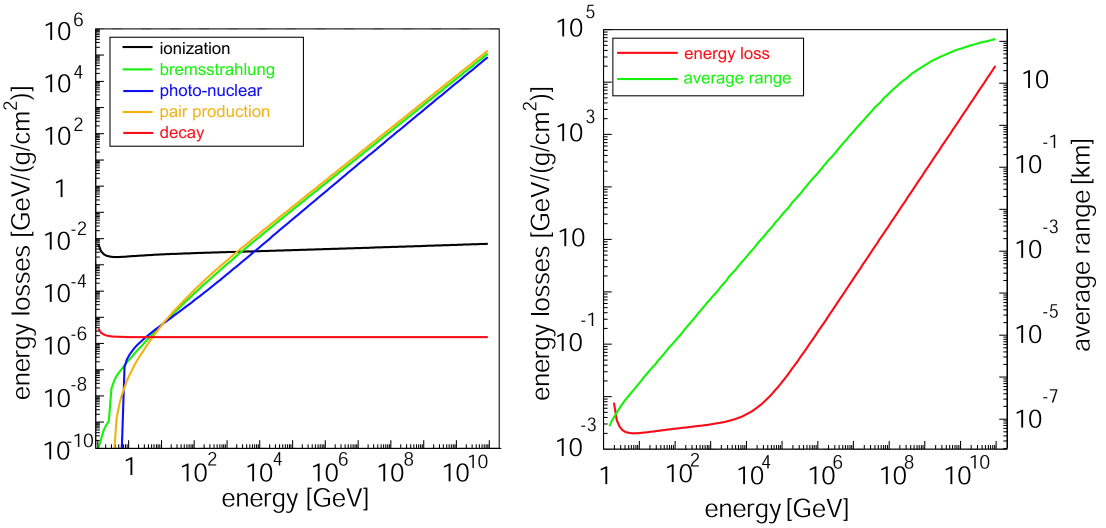

Figure 2.8: *Left: Energy loss of a muon in GeV g^{-1} cm^2. The contribution from different processes is shown. Right: Total energy loss (red) and average range (green) of a tau in a water-equivalent medium. Figures adapted from [CR01].*

fluxes with very hard spectra. Secondly, with the rise of the cross section also increases the probability that the neutrino is absorbed in the Earth before the target volume is reached. The mean free path L for neutrinos is given by

$$L = \frac{1}{N_A \, \sigma_{CC} \, \rho} \, , \tag{2.17}$$

with $N_A = 6.022 \cdot 10^{23}$ being Avogadro's number and ρ the density of the medium. The right picture in figure 2.7 shows L for neutrinos of energy E_ν. Starting from $E_\nu \approx 50$ TeV the Earth becomes increasingly opaque for neutrinos and shadows large regions of the sky. This absorption is less relevant for τ-neutrinos. The τ-lepton produced in CC-interactions decays into particles with a ν_τ in the final state. Due to the short lifetime of the τ, the energy loss during propagation is neglegible (see also figure 2.8) and a significant fraction of the energy is transferred to the secondary ν_τ. Since its energy is lower, its mean free path increases. This process, called ν_τ-regeneration, is continued until the neutrino reaches the detector. Detailed calculations on this effect can be found in [DRS00].

Besides the total cross section, the mean scattering angle $\langle\theta_{\nu l}\rangle$ between the incident neutrino and the lepton in the final state of a CC-interaction has to be considered in the search for point-like sources of astrophysical neutrinos. It gives a strict bound to the achievable angular resolution of the telescope. It can be calculated from the differential cross section and [LM00] give a parametrization of its energy dependence by:

$$\langle\theta_{\nu l}\rangle \approx 0.7^\circ \left(\frac{E_\nu}{1\ \mathrm{TeV}}\right)^{-0.7} \, . \tag{2.18}$$

It will be shown in chapter 6, that for TeV energies the angular resolution of AMANDA-II is dominated much more by limited capabilities to reconstruct the particle direction than by the neutrino-lepton scattering.

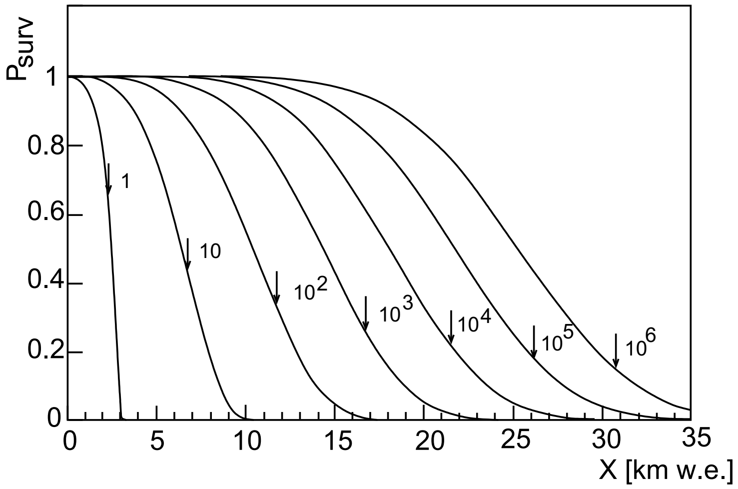

Figure 2.9: *Survival probabilities for muons of different energies (*1 *TeV –* 10^6 *TeV, indicated by the numbers besides the curves) in rock. The arrows point to the average range resulting from the approximation* (2.20). *Figure adapted from [LS91].*

2.4.3 Propagation of charged leptons

Two flavors of charged leptons produced in CC-interactions are important for this analysis, muons and taus. Electrons quickly loose energy by pair production initiating an electromagnetic cascade with a length of only a few meters. From such a compact cascade, the direction of the primary particle cannot be reconstructed. The energy loss of muons, however, is considerably smaller. A TeV muon can penetrate through kilometers of solid material like ice or rock before decaying. The lifetime of taus (below 10^8 GeV) is too short to produce tracks of significant length. But in 17.7% of the cases they decay into two neutrinos and a muon [E^+04], which can then reach the detector. We will briefly introduce the energy loss processes involved in the propagation of the muon and tau leptons. A detailed description is found in [CR01].

The left picture in figure 2.8 shows the major contributions to the average energy loss of a muon when traveling through matter: ionization, bremsstrahlung, photo-nuclear interactions, $e^\pm$-pair production, and decay. Below $E_\nu \approx 1$ TeV energy loss by ionization of the surrounding medium is dominant. For higher energies the main contribution comes from bremsstrahlung, pair production and photo-nuclear interactions. All these processes are of stochastic nature, i.e. they occur in discrete events (though energy loss by ionization can be treated as quasi-continuous below a certain threshold energy). Therefore the considerable fluctuations have to be taken into account to properly describe the muon energy loss.

A good approximation for the average range of a muon of energy E_μ is reached by assuming an energy loss dE/dx which is a linear function of the energy:

$$\frac{dE}{dx} = -a - bE \; . \tag{2.19}$$

The constant term ($a = 2.68$ MeV g^{-1} cm^2) approximates the energy losses by ionization while the linear term ($b = 4.7 \cdot 10^{-6}$ g^{-1} cm^2) sums up the fractional energy loss from the other contributions. Solving this equation one finds a range R for a muon of initial energy E_μ:

$$R = \frac{1}{b} \ln \left(1 + \frac{b}{a} E_\mu \right) . \tag{2.20}$$

Thus, the average muon range varies between $\approx$ 350 m w.e. for $E_\mu = 100$ GeV and $\approx$ 31 km w.e. for $E_\mu = 10^9$ GeV. Figure 2.9 illustrates the survival probability for a muon at a certain distance, indicating the range calculated by (2.20). The large fluctuations of the actual muon range around the mean value are clearly visible. The right picture in figure 2.8 displays the energy loss and the range of a tau neutrino. Even at $E_\tau = 10^6$ GeV the average range is only about 70 m (before it decays), the average energy loss on this distance corresponds to $\approx 0.1\%$ of the tau energy. Therefore, a potential muon produced in the τ-decay obtains a significant fraction of E_τ (depending on the kinematics of the decay).

Elastic Coulomb scattering of muons off nuclei affects the direction of the muon. The angular distribution of the scattered muon tracks (relative to the original track) after multiple scattering processes can be reasonably approximated by a Gaussian distribution. The RMS of this distribution is given by [E$^+$04]:

$$\theta_{\mathrm{RMS}} = \frac{13.6\ \mathrm{MeV}}{\beta c p} \sqrt{\frac{x}{X_0}} \left(1 + 0.038 \ln \frac{x}{X_0} \right) . \tag{2.21}$$

βc is the velocity, p the momentum and x/X_0 the traveled distance in units of the radiation length X_0. An evaluation of expression (2.21) yields $\theta_{\mathrm{RMS}} \ll \langle \theta_{\nu\mu} \rangle$, the scattering angle between muon and neutrino in the CC-interaction. For example, at 1 TeV one finds $\theta_{\mathrm{RMS}} = 0.08°$ after 2.5 km distance and $\langle \theta_{\nu\mu} \rangle = 0.7°$. Hence, the effects of multiple Coulomb scattering can be neglected in this analysis.

2.4.4 Čerenkov ight emission

A charged particle emits Čerenkov radiation, when traveling faster than the speed of light in a polarizable dielectric medium. The moving particle polarizes the surrounding atoms or molecules, which quickly fall back to their ground states emitting radiation after the particle has passed. The light emission is illustrated in figure 2.10: For a particle traveling faster than the light speed c_v/n, the light forms a coherent wavefront propagating with an angle θ_c to the incident particle trajectory.

The angle θ_c is given by the simple formula [Jac96]:

$$\cos \theta_c = \frac{1}{\beta\, n} , \tag{2.22}$$

with $\beta = v/c_v$, and n the index of refraction of the medium. The particle energy for which $\beta n = 1$ and $\theta_c = 0$ is called the Čerenkov threshold. For muons passing through ice ($n = 1.32$ at 400 nm) this threshold is approximately 160 MeV. In the energy range interesting for this analysis ($E \gg 10$ GeV) one can safely assume $\beta = 1$ and therefore a Čerenkov angle of $\theta_c \approx 41°$.

The spectral distribution of the emitted photons is given by the Frank-Tamm-Formula [Jac96]:

$$\frac{dN}{dx d\lambda} = \frac{2\pi\alpha}{\lambda^2} \left(1 - \frac{1}{\beta^2 n(\lambda)^2} \right) . \tag{2.23}$$

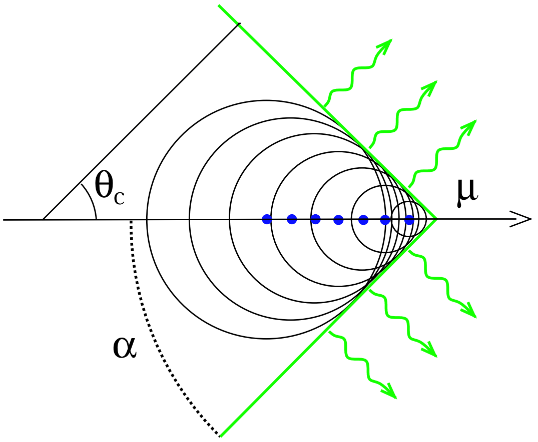

Figure 2.10: *Illustration of the formation of a coherent Čerenkov light wavefront from spherical waves emitted along the particle trajectory. The Čerenkov angle θ_c is defined as the angle between the particle trajectory and the propagation direction of the light.*

In this formula $\alpha \approx 1/137$ is the fine structure constant. Thus, for a constant index of refraction the number of photons emitted per unit length is inversely proportional to their wavelength and the Čerenkov spectrum is peaked in the ultraviolet region. From integration of (2.23) one can also determine the total number of photons expected per unit track length. In the range between 300 nm and 500 nm $2.6 \cdot 10^4$ photons are emitted by a muon in one meter. The energy loss due to the radiation of these photons is approximately 86 keV/m, neglegible compared to the dominant processes of energy loss of the muon described in section 2.4.3.

The total light yield however is much larger than the number quoted here, since high energy secondary particles and their showers produced stochastically along the track contribute to the emission as long as they are above Čerenkov threshold. Simulation studies were performed in [Wie95] to quantify the light from Čerenkov radiation of secondaries. A convenient parametrization was found from these simulations for the number of photons from

- an electromagnetic shower of energy E_s: $N_\gamma^{(e)} = 4.37\ E_s\ \frac{dN}{dx}\big|_{\text{muon}}$ m GeV^{-1};
- a hadronic shower of energy E_s: $N_\gamma^{(h)} = 3.51\ E_s\ \frac{dN}{dx}\big|_{\text{muon}}$ m GeV^{-1}.

Hence, a secondary particle with an energy of 1 GeV producing an electromagnetic shower emits the same amount of Čerenkov light as 4.37 m of muon track.

2.4.5 Atmospheric muons and neutrinos

Searches for muons induced by neutrinos from cosmic sources face an inevitable background: muons and neutrinos generated in the interactions of charged cosmic rays in the Earth atmosphere. Like in distant neutrino sources, the high energy nuclei interact with the protons and neutrons inside the atoms of the atmosphere producing jets of hadrons, which can subsequently decay into muons and neutrinos. According to their origin they are called “atmospheric” muons and neutrinos.

While the interstellar gas is a very thin target – where essentially all secondary particles decay without further interaction – the same is not true for the atmosphere. Dependent on their lifetimes τ_m, their decay length $d_m = \beta\gamma c\tau_m$ might be larger than the interaction

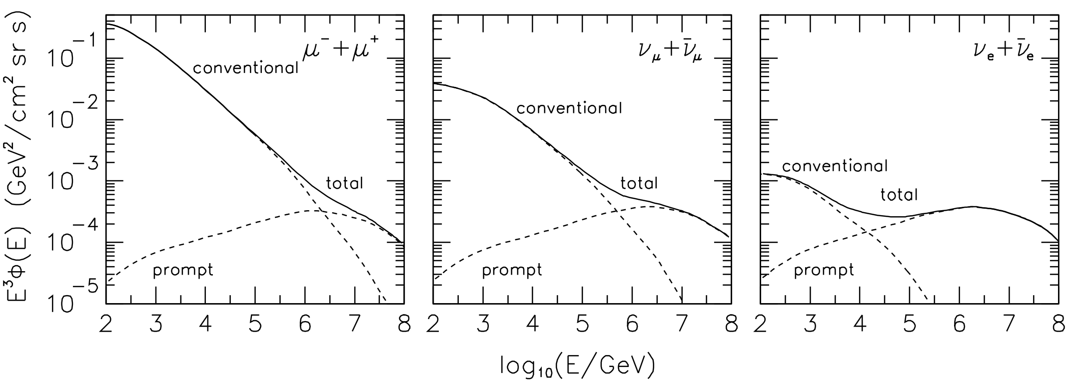

Figure 2.11: *Fluxes of atmospheric neutrinos and muons. The conventional component (from π,K decays), the prompt component (from charm decays) and their sum are displayed. Figure adapted from [TGG96].*

length λ_m. The turn-over point where $d_m = \lambda_m$ is called the critical energy ϵ_m. Above that energy interaction dominates over decay. For the most important secondaries the ϵ_m are:

$$\epsilon_\mu = 1 \text{ GeV} \quad , \quad \epsilon_{\pi^\pm} = 115 \text{ GeV} \quad , \quad \epsilon_{K^\pm} = 850 \text{ GeV} \quad . \tag{2.24}$$

Far below the critical energy for the $\pi^\pm$-decay, the spectrum of atmospheric muons follows the spectrum of the cosmic ray flux of $d\Phi/dE \propto E^{-2.7}$ (see section 2.1.1). The high interaction probability above the critical energy then steepens the spectrum to $d\Phi/dE \propto E^{-3.7}$. For atmospheric neutrinos the same steepening of the spectrum can be observed. However, due to the kinematics of the pion and kaon decays, their flux above $E_\nu = 100$ GeV is dominated by neutrinos from K-decay. Consequently the spectral break occurs around the critical energy of the kaon. The decay of muons can be neglected at the energies considered here.

Figure 2.11 displays declination averaged fluxes of atmospheric muons and of electron and muon neutrinos[4]. Above $E \approx 1$ PeV the spectrum flattens again due to the contributions of the "prompt" flux, originating from the decay of charmed mesons. These mesons have very short lifetimes and correspondingly high critical energies of $\epsilon_c > 10^7$ GeV. The flux of electron neutrinos from the atmosphere is substantially smaller than the flux of muon neutrinos. With a suppressed muon decay, the electron neutrinos are exclusively produced in the decay of K^0_L.

Accounting for the energy loss in ice, vertical downgoing atmospheric muons ($\theta = 0°$) with energies above a threshold of about $E_{\text{tr}} = 400$ GeV can reach the AMANDA-II detector located 1730 m below the surface. The threshold energy rises with the inclination angle θ and accordingly the flux of atmospheric muons drops, effectively vanishing for muon tracks nearly parallel to the surface ($\theta \approx 85°$). The integral rate of muons recorded in the AMANDA-II detector is ≈ 90 muons/s, while the rate expected from cosmic sources is in the most optimistic cases a few neutrino induced muons per year. In chapter 6 we will describe methods to separate the orders of magnitude higher flux of atmospheric muons from cosmic and atmospheric neutrinos.

---

[4] For $E > 100$ GeV the oscillation length for a flavor oscillation $\nu_\mu \to \nu_\tau$ is considerably longer than the diameter of the Earth. Therefore the flux of atmospheric ν_τ can be neglected.

Atmospheric neutrinos form a relatively isotropic background. Like neutrinos from cosmic sources they can penetrate the Earth and generate muons in CC-interactions. However, due to the small cross section for this interaction, the rate of detectable muons from these particles is much smaller than the number of atmospheric muons, a few thousand per year. In chapter 7 we will outline statistical methods to find point-like sources in the presence of this background.

2.5 Detector performance

The capabilities of a neutrino detector to measure cosmic neutrino fluxes can be quantified by several parameters. We will describe the ones frequently used throughout this work, the effective area and the sensitivity. The effective area can be seen as the aperture of an ideal neutrino telscope to which the real telescope is equivalent. The sensitivity is defined as the ability of the neutrino telescope to exclude a certain flux intensity if no signal is observed. For a description of the sensitivity it is necessary to introduce the calculation of flux upper limits. Accordingly, we will present the way flux limits are derived in this analysis before discussing the sensitivity.

2.5.1 Effective Area

The neutrino effective area A^{ν}_{eff} relates the detectable neutrino event rate R_ν to the incident neutrino flux Φ. Parameterizations of the effective area allow to calculate event rates expected from a certain neutrino flux prediction and even to compare them for different analysis techniques or experiments. Due to the energy dependent CC cross section, muon range and varying detection efficiencies, the effective area is a function of the energy. It is defined as:

$$dR_\nu(\delta) = A^{\nu}_{\text{eff}}(E,\delta)\frac{d\Phi}{dE}\,dE\ . \tag{2.25}$$

δ denotes the declination of the neutrino source in equatorial coordinates. The efficiency of a neutrino detector for recording neutrinos also depends on the direction from which the flux arrives. The detector geometry and the fraction of neutrinos absorbed in the earth vary with the declination angle[5]. Any azimuthal dependence of the effective area is averaged by the rotation of the Earth.

One can also calculate an average effective area for an integral neutrino flux above E_{min}:

$$R_\nu(\delta) = \langle A^{\nu}_{\text{eff}}\rangle(\delta, d\Phi/dE)\int_{E_{\text{min}}}^{\infty}\frac{d\Phi}{dE}\,dE\ . \tag{2.26}$$

However, such a definition introduces a dependence on the assumed spectral shape of the neutrino signal.

In this analysis the effective area at energy E is determined by evaluation of a simulation of a constant neutrino flux $d\Phi/dE = \Phi_0$ from a declination angle δ in the energy range $[E - \Delta E/2, E + \Delta E/2]$. The neutrino interactions, the response of the detector and the selection of the events are accounted for in this simulation. Figure 2.12 illustrates the procedure (details on the simulation chain will be presented in section 4.1).

---

[5] For a detector located at South Pole, the declination angle δ in equatorial coordinates and the zenith angle θ in a coordinate system fixed to the detector are simply related by $\delta = \theta - \pi/2$.

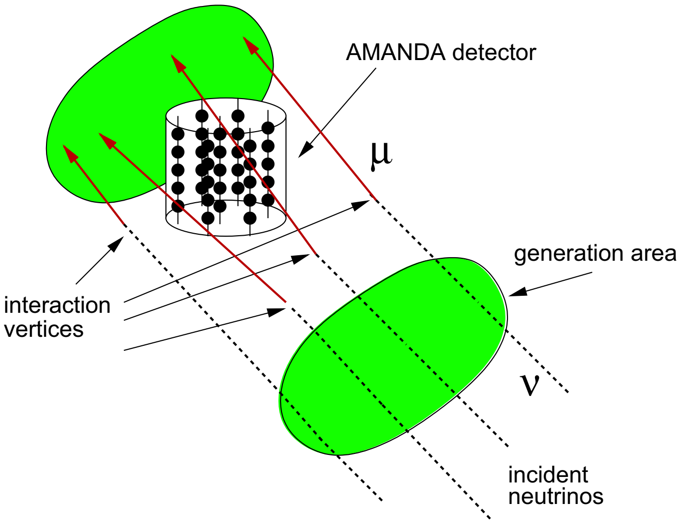

Figure 2.12: *Illustration of the simulation of a neutrino flux to determine the effective area. A constant flux is simulated in a generation plane substantially larger than the detector. The interaction vertices are randomly distributed in a cylinder of a height defined by the maximum range of the produced muons.*

The number of detected events n_{sim} in the simulated time period t_{sim} are counted and the rate $R_\nu = n_{\text{sim}}/t_{\text{sim}}$ is determined. For small intervals ΔE, one can then obtain the effective area at energy E and declination δ from (2.25):

$$A^{\nu}_{\text{eff}}(E,\delta) = \frac{R_\nu(\delta,E)}{\Phi_0\,\Delta E}\ . \tag{2.27}$$

In some cases – mainly for efficiency comparisons to other analyses or detectors – the muon effective area is an interesting quantity. Equivalent to the neutrino effective area it is defined as the relation between the detected muon rate and an incident muon flux:

$$dR_\mu(\delta) = A^{\mu}_{\text{eff}}(E,\delta)\frac{d\Phi_\mu}{dE}\,dE\ . \tag{2.28}$$

The advantage of the muon effective area is that it is independent of the neutrino cross section and the muon range. It gives a direct estimate of the effective geometrical size of a detector. The energy E is however ambiguous for muons, due to their energy loss. In this work we use the energy of the muon at the closest point of approach to the detector center when displaying a muon effective area.

2.5.2 Calculation of Flux Limits

The neutrino effective area can be used to translate a certain experimental observation into a limit on the neutrino flux: The searches for point sources that we present in this thesis depend on the comparison of observed events n to an expected number of background events b (from atmospheric muons and neutrinos). From (n,b) a limit can be calculated on how many signal events s (from a neutrino source) are compatible with this observation. The method we follow to derive the limit was proposed by Feldman and Cousins [FC98]. For hypothetical signal contributions s and background b confidence belts for the number of observed events n are created. The probability $P(n|s{+}b)$ to see n events, while expecting $s+b$ is calculated for all n. The confidence belt for a certain confidence level CL is then

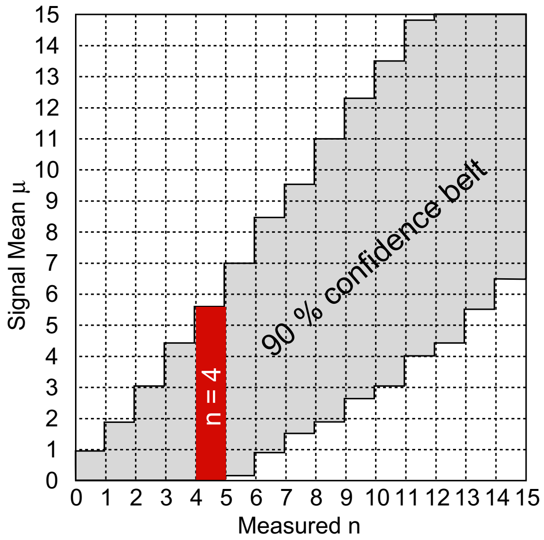

Figure 2.13: *Schematic view of the confidence belt creation corresponding to the Feldman and Cousins prescription for an expected background of* $b = 3$ *events (CL=90%). For each signal contribution* s *the interval containing 90% of the possible experimental outcomes is marked in gray. It is created using the likelihood ratio ordering rule from [FC98]. The signal range compatible with the observation of 4 events is marked by a red bar on the plot. Picture based on [FC98].*

an interval $[n_l, n_u]$ which includes a certain fraction of the expected experimental results for a given combination of (s, b), i.e it fulfills the inequality:

$$\mathrm{CL} \leq \sum_{i=n_l}^{n_u} P(i|s+b) \ . \tag{2.29}$$

The choice of $[n_l, n_u]$ is not uniquely defined by this rule, since the interval can be shifted along the probability distribution and an additional constraint is necessary to define the location of the interval. In [FC98] it is proposed to use a likelihood ratio ordering criteria. The likelihood ratio for each n is defined as:

$$\mathcal{R}_n = \frac{\mathcal{L}(n|s+b)}{\mathcal{L}_{max}(n|s_{max}+b)} = \frac{P(n|s+b)}{P(n|s_{max}+b)} \ . \tag{2.30}$$

s_{max} denotes the signal for which the maximum likelihood is reached. The n outcomes are ordered in a sequence $(n_1, n_2, \ldots)$ by decreasing likelihood ratio $\mathcal{R}_{n_1} > \mathcal{R}_{n_2} > \ldots$. The confidence belt is then defined as the smallest sequence for which the requested confidence level is reached:

$$\mathrm{CL} \leq \sum_{n_1, n_2, \ldots, n_c} P(n_i|s+b) \ . \tag{2.31}$$

Leading to a unique interval $[n_1, n_c]$ for each combination (s, b), this is also called the "unified approach". Figure 2.13 visualizes the concept of confidence belt creation. The smallest signal $s = \mu_{\mathrm{CL}}$ for which the observation n lies below the interval $[n_1, n_c]$ defines the upper limit on the signal, meaning that a mean signal μ_{CL} would have produced more than the actual number of observed events n in a fraction of all experiments defined by the confidence level. Throughout this work a confidence level of 90% is used for all stated upper limits.

In an experiment with neglegible statistical and systematic errors, the limit on the number of signal events μ_{CL} can be simply translated into a flux limit by calculating:

$$f_{\mathrm{CL}} = \frac{\mu_{\mathrm{CL}}}{R_\nu(\Phi)\; t_{\mathrm{obs}}} \;, \tag{2.32}$$

where R_ν is the event rate from (2.25) expected for a flux Φ and t_{obs} the observation time. The flux limit is then given by:

$$\Phi^{\mathrm{lim}}_{\mathrm{CL}} = f_{\mathrm{CL}}\; \Phi \;. \tag{2.33}$$

However, for the analysis presented here statistical and systematic uncertainties have to be taken into account. A method to calculate flux limits in this case will be presented in chapter 9, after the sources and the size of the systematic error have been discussed.

2.5.3 Sensitivity

Only in the case of no background, maximizing the effective area optimizes the performance for the detection or rejection of neutrino fluxes. Even a strong neutrino signal might be hidden, if a large background is present. Hence, a combined optimum has to be found, keeping on the one hand the effective area large, while keeping on the other hand the background low. To achieve this we optimize our analysis for the sensitivity, which we define as the average flux upper limit that can be set with a 90% confidence. The average in this case is taken over possible experimental outcomes. This strategy ensures that with the experimental data available, and within the parameter space of our analysis method, we get the best possible upper limits on potential neutrino fluxes.

For a mean background of b events and no signal, the number of observed events n should follow a Poisson distribution $P(n|b)$ if the experiment is repeated many times. For each observation (n, b) a limit $\mu^{\mathrm{lim}}_{90\%}(n, b)$ can be derived on how many signal events would be compatible with this observation by the method presented in section 2.5.2. To calculate the average limit we average over the probabilities for the experimental outcomes:

$$\langle \mu^{\mathrm{lim}}_{90\%} \rangle = \sum_{n=0}^{\infty} \mu^{\mathrm{lim}}_{90\%}(n, b) P(n|b) \;. \tag{2.34}$$

This average upper limit depends only on the expected background b, but not on specific experimental results. Like in section 2.5.2 one can calculate the sensitivity with respect to a neutrino flux Φ dividing $\langle \mu^{\mathrm{lim}}_{90\%} \rangle$ by the number of neutrinos expected from this flux:

$$\Phi^{\mathrm{sens}}_{90\%} = \frac{\langle \mu^{\mathrm{lim}}_{90\%} \rangle}{R_\nu(\Phi)\; t_{\mathrm{sim}}} \Phi \;. \tag{2.35}$$

The sensitivity depends on the assumed spectrum of the neutrino flux. Therefore an optimization for the best sensitivity is only valid for a specific spectrum.

Chapter 3

The AMANDA-II neutrino detector

Bringing together the pieces of information on neutrino physics presented in the last section, one can get a clear view of the principles of neutrino detection in huge volume detectors: When a neutrino interacts with a nucleus by exchange of a W-Boson, a charged lepton of the same flavor is created. After such an interaction one finds a muon in the final state for the muon (anti-)neutrino, but also for the tau (anti-)neutrino with a chance probability of 17.7%.

At the energies of interest ($E > 100$ GeV) the muon can penetrate several kilometers of dense matter before decaying. Such a high energy muon travelling through matter produces Čerenkov light. If the medium is highly transparent this light can be detected at large distance from the muon track. It can be used to record the muon track and eventually reconstruct its direction and energy loss. By this detection method, neutrino induced muon tracks are identified in the AMANDA-II detector. The dense transparent medium used is the 3 km layer of extremely clear ice on top of the Antarctic continent. The detector itself consists of 677 Optical Modules sensitive to visible and UV-light, deployed in holes drilled deep into the glacier.

In this chapter we will describe in detail the optical properties of the glacial ice surrounding the AMANDA-II neutrino detector to introduce then its instruments and electronics.

3.1 Optical properties of the South Pole glacier

3.1.1 Measurements

The main inland glacier covering several millions of square kilometers of the Antarctic continent is a structure grown over many millenia. Traces of each epoch can still be found as varying dust concentrations in the ice modifying its optical properties. The dust causes absorption and scattering of the Čerenkov photons, which has to be taken into account when a particle's direction is to be reconstructed from the arrival pattern of the light.

The optical properties have been carefully measured with in-situ light sources, which have been deployed together with the Optical Modules. These light sources are:

- Nitrogen lasers emitting UV radiation at 337 nm;
- flashing UV LEDs at 370 nm;

- flashing Blue LEDs at 470 nm;
- a frequency doubled YAG-laser at the surface emitting green light at 532 nm fed into the ice through optical fibers and diffuser balls;
- a steady UV light source emitting light at 313 nm;
- a "rainbow" module producing steady monochromatic light with adjustable wavelength between 340 nm and 560 nm.

From the analysis of measured photon arrival times for different wavelengths and different depths, a complete picture of absorption and scattering in the ice surrounding AMANDA-II can be derived [A$^+$06c]. The results of this analysis have been implemented in the Monte Carlo description of the detector.

3.1.2 Scattering

Scattering of photons off the dust particles in the ice is the predominant complication in the reconstruction of particle track directions from the patterns of Čerenkov light. The scattering length λ_s is extremely short (of the order of a few meters). However, the scattering is not isotropic but strongly forward peaked. The average scattering angle has been calculated from Mie theory by [HP98] assuming realistic dust components found in ice cores: mineral grains, acid droplets, salt crystals and soot. The mean cosine of the scattering angle was determined to be $\langle\cos\theta\rangle = 0.94$.

In such circumstances it is convenient to define an effective scattering length λ_e by:

$$\lambda_e = \frac{\lambda_s}{1 - \langle\cos\theta\rangle} \; . \tag{3.1}$$

After one effective scattering length, the center of an injected photon cloud has come to rest. Therefore the effective scattering length λ_e of anisotropic scattering can be seen as the equivalent to the geometric scattering length λ_s of isotropic scattering.

The wavelength dependence of the scattering length has also been calculated by [HP98]. It can be described as a power law with an index close to 1 (dotted lines in figure 3.2). Measurements of the scattering length have confirmed this result very well. The main variation in the scattering coefficient b_e (the inverse scattering length) originates from the fluctuations of the dust concentration with depth z.

The upper picture in figure 3.1 shows the measurements of the scattering coefficient performed with the in-situ light sources. The lower picture compares the AMANDA measurements with the results from a device called "dust-logger", measuring the scattering length with an astonishing spatial resolution of 2-3mm [B$^+$05c], which was deployed in the first hole of the new IceCube detector. Both measurements show excellent agreement.

Above the AMANDA-II detector for $z < 1400$ m the scattering length decreases dramatically. Air bubbles dominate the scattering in this region. As the depth and pressure increases air bubbles become instable and undergo a phase transition to solid air hydrate crystals [Mil69] which cause almost no scattering by themselves. However, this transition process is very slow and the air bubbles remain at all depths inside the newly drilled holes in which the Optical Modules are deployed, causing dramatically different local ice properties.

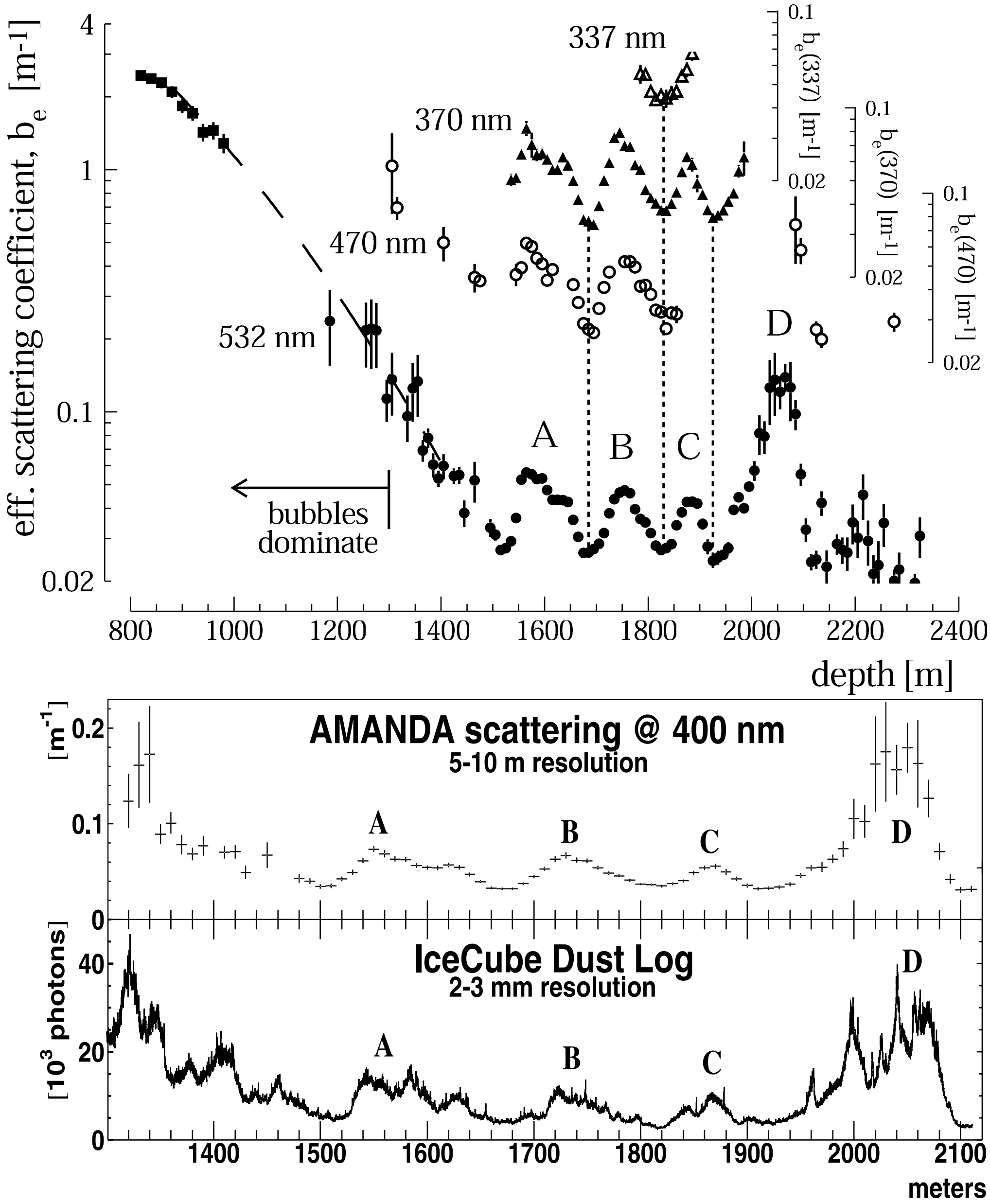

Figure 3.1: *Effective scattering coefficient of the glacial ice surrounding the AMANDA-II detector. The upper picture shows results of the measurements with in-situ light sources. Four distinct peaks (A-D) of high dust concentrations can be identified. The lower picture compares these measurements to the results from the "dust-logger" device deployed in the first IceCube hole measuring the scattering with 2-3 mm spatial resolution. Good agreement is found between the two measurements. Pictures taken from [A$^+$06c, B$^+$05c].*

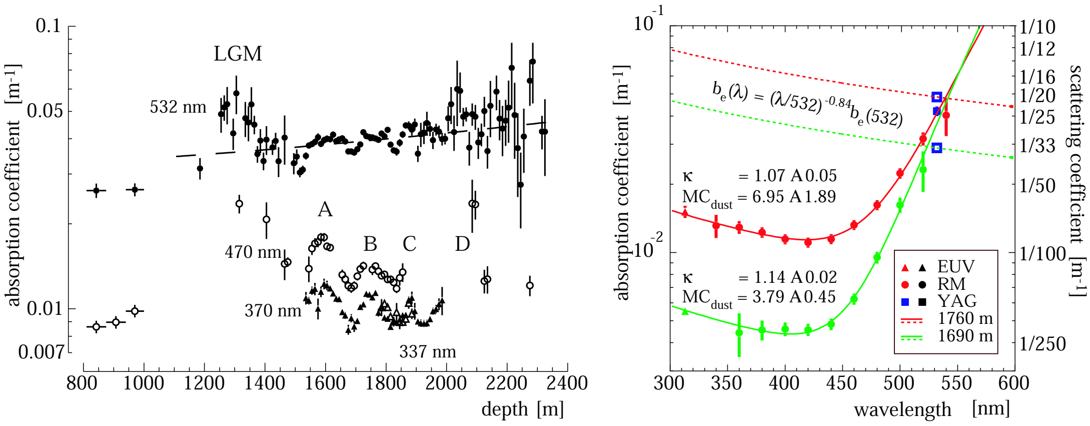

Figure 3.2: Left: *Absorptivity of the ice measured with AMANDA-II in-situ light sources. The strong increase due to molecular excitation is clearly visible at 532 nm. The structures arising from varying dust concentrations can be seen at all wavelengths.* Right: *Fit of absorptivity (solid line) measured at two different depths by the three-component-model [PB97] and wavelength dependence of the scattering coefficient (dotted line) obtained from Mie-scattering theory [HP98]. Pictures taken from [A$^+$06c].*

3.1.3 Absorption

The absorptivity of a medium λ_a^{-1} describes the fraction of light which is absorbed in the material per unit length.

Absorption in ice can be effectively described by a "three-component"-model [PB97]: At short wavelengths (below 200 nm) absorption increases exponentially due to the electronic band structure of the ice crystal. Above 500 nm the absorption is dominated by excitation of the H_2O molecules. Between 200 nm and 500 nm pure ice is extremely transparent and the main component causing absorption is the dust. In this range the absorptivity falls below 10^{-2} m^{-1}, a factor of two lower than absorptivities reached in the deep sea water [PD99] where similar experiments are constructed.

Figure 3.2 shows in the left picture depth profiles of the absorptivities derived from in-situ light sources. The strong increase of absorption for $\lambda > 500$ nm is clearly visible as well as the layer structure caused by the varying dust concentrations. The right pictures compares measured wavelength dependent values for two different depths to a fit obtained from the three component model. Good agreement is found.

Based on the measurements and fits, a global ice model was derived for the dependence of the absorptivity $\lambda_a^{-1}(z, \lambda)$ and the effective scattering coefficient $b_e(z, \lambda)$ on the depth z and wavelength λ. This model is used in the simulation of the photon propagation from the muon trajectory to the Optical Module.

3.1.4 Hole ice

The ice inside the holes in which the Optical Modules of AMANDA-II have been deployed, is very different from the bulk of the ice. The phase transition of the air bubbles to air-hydrate crystal happens on much larger time scales than the detector operation and therefore the scattering is dominated by these bubbles, leading to effective scattering lengths of less than one meter.

However, since the diameter of the holes of 60 cm is small compared to the total travel distance of the photons between point of emission and Optical Module, the main effect of the hole ice is to modify the angular photon acceptance of the modules. Photons passing at the insensitive side of the module are scattered and can reach the photocathode of the PMT. The additional arrival time delays from the scattering of the photons in the hole ice are neglegible.

Measurements of the angular acceptance have been compared to simulations of different scattering lengths λ_h [OW01]. The best fit is found for $\lambda_h = 50$ cm. The expected angular acceptance distribution for this value of λ_h is used in the photon propagation simulation.

3.2 AMANDA-II detector setup

3.2.1 Geometry

The AMANDA-II detector consists of 677 Optical Modules (OMs) deployed in 19 holes during the years 1995-2000. All OMs inside a hole are attached to a common string containing the signal and power supply cables. The detector center is 1730 m below the surface. The bulk of the OMs lies inside a cylinder of 200 m in diameter and 500 m in height around this center. Figure 3.3 shows a schematic drawing of the detector. The strings are arranged roughly in two circles which have been deployed consecutively. The inner circle is called AMANDA-B10 (deployed 1995-1996) and the full 19 string array (deployed 1998 and 2000) was named the AMANDA-II detector. Also visible on this picture is a small array at 800 m to 1000 m depth, called AMANDA-A, the predecessor of AMANDA-B/II. Due to the air bubbles present at shallow depths (see section 3.1.2) and the resulting strong light scattering it was not possible to successfully reconstruct muon tracks from the data collected by this detector.

To perform measurements of optical ice properties below and above AMANDA-II, 20 OMs on strings 11-13 were deployed above the bulk of the detector between 1150m and 1500m, while 24 OMs on the same strings were deployed below at depths between 2000m and 2350m. The spacing between adjacent Optical Modules is 10-12 m and the average inter-string distance is around 60 m. All readout and supply cables in the strings are bundled at the surface and connected to the electronic system located in the Martin Pomerantz Observatory (MAPO) about 1 km away from the Amundsen-Scott South Pole station. A close look at figure 3.3 also reveals that the center of string 17 is 500 m higher than the rest of the array. That is the result of a deployment incident: the string got stuck while lowering it into the molten hole and froze in above the designated position. This string as well as the extensions on strings 11-13 are not used for the reconstruction of particle trajectories.

3.2.2 The Optical Module

The heart of each Optical Module (OM) is an 8-inch Hamamatsu photomultiplier tube converting the incident Čerenkov photons into electric pulses. It is coupled by a transparent, refraction index adapted silicon gel to the pressure resistant glass sphere, which surrounds and protects the Optical Module. Electrical power is supplied from the surface. Besides these common aspects the OMs are quite heterogeneous with different generations deployed in the different years reflecting the understanding of limitations of the previously used technology. The various OM generations are described below.

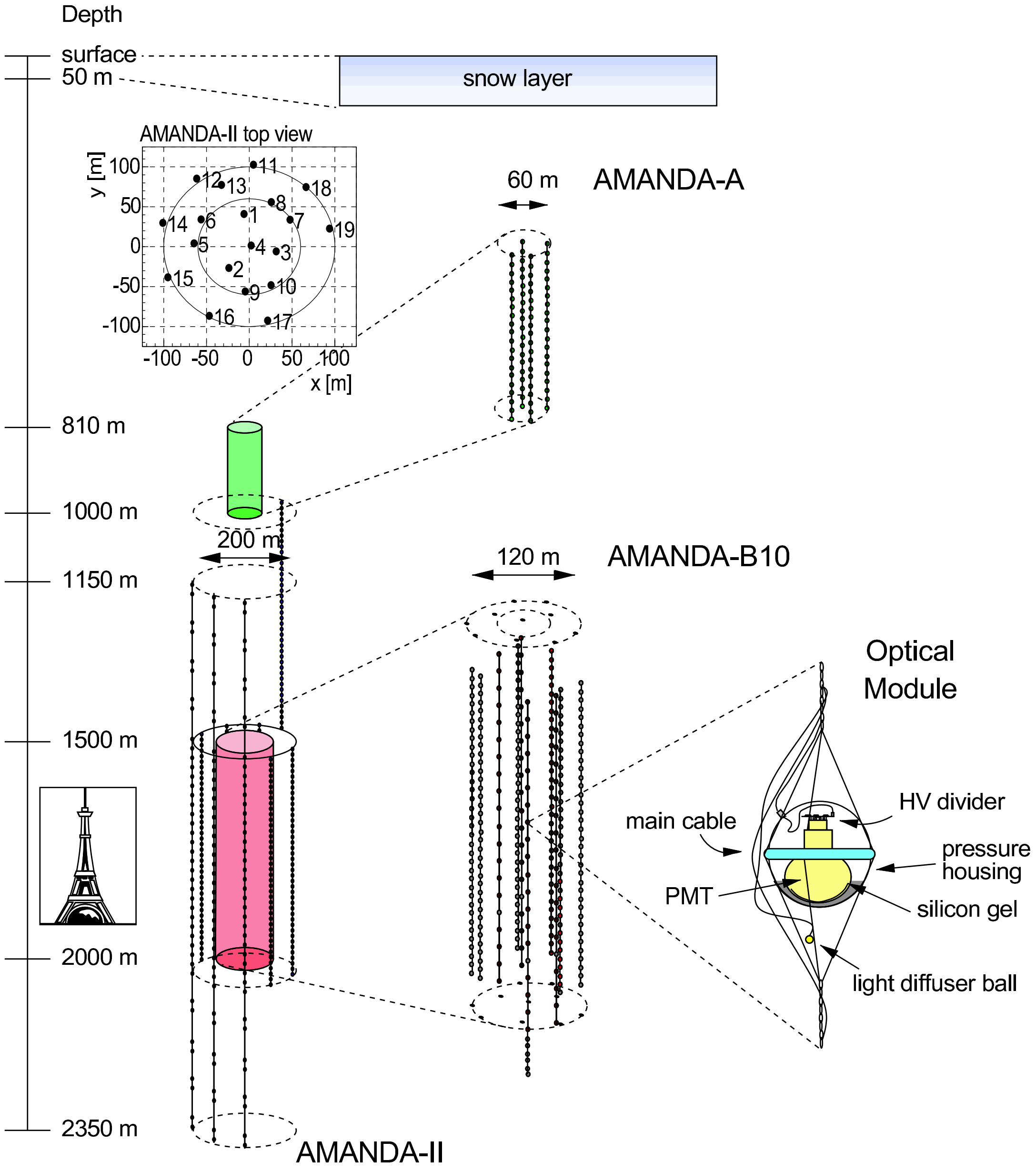

AMANDA-II and Eiffel Tower (for scale comparison, not deployed)

AMANDA-A (top)
AMANDA-B10 (bottom)

Optical Module (OM)

Figure 3.3: *Illustration of the AMANDA-II detector. The vertical axis on the left side indicates the depth below the South Pole surface level. The AMANDA-A and AMANDA-B10 detectors are shown magnified in the middle and a schematic view of a single optical module is presented on the right side. The box in the upper left part displays the location of the strings on the surface.*

Strings 1-4

High voltage power supply and transmission of the PMT pulses to the surface is performed by coaxial electrical cables insensitive to noise pick-up from induction, but suffering from high dispersion. Single photo-electron pulses are widened to 200 ns - 400 ns, so adjacent pulses cannot be distinguished. The pressure resistant glass spheres are made from a low radioactivity glass manufactured by the Billings company. Therefore the dark noise rate of these OMs is quite low (≈ 0.5 kHz). The glass becomes opaque below 350 nm reducing the OM quantum efficiency by about 25% compared to the later used glass manufactured by Benthos.

Strings 5-10

Power supply and transmission of the PMT pulses to the surface is performed by twisted pair electrical cables. This reduces dispersion to about 100 ns - 200 ns. However like in telephone cables the non-optimal shielding leads to “cross-talk”, i.e. pulses induce fake signals in adjacent cables. Benthos glass spheres are used with improved UV transparency but higher dark noise rates (≈ 1 kHz).

Strings 11-17

A LED is used to convert the electrical PMT pulse into an optical pulse, which is sent to the surface via an optical fibre. The problem of dispersion is eliminated and the pulse-width becomes around 20 ns. Optical fibers have a high failure rate from mechanical stress, so a signal transmission via twisted pair electrical cables is possible as backup solution.

Strings 18-19

Prototype strings for the IceCube optical module technology. Modules in both strings generate the high voltage inside the module itself. String 18 is equipped with Digital Optical Modules, which use waveform digitization to send the pulse as binary data via electrical cables. Analog optical signal transmission is provided as backup. Only this optical signal is currently used in the AMANDA-II data acquisition. String 19 is equipped with dAOMs, digital-analog optical modules, [Sch02] providing analog optical and electrical readout, but digital module control.

3.2.3 Data acquisition electronics

Figure 3.4 illustrates the AMANDA-II data acquisition system. Pulses are amplified by either the SWAMP (SWedish AMPlifier, for channels with electrical readout) or ORB (Optical Receiver Board, for channels with optical readout). In both cases the amplifiers produce a dual signal output, the prompt and the delayed channels. The amplification gain can be chosen independently for the two channels, the delayed output runs through a delay circuit to retard the pulse for 2 μs.

The prompt signal is fed into a discriminator which creates a rectangular pulse starting when the voltage of the pulse crosses a predefined threshold and ending when it falls below this threshold. The time of the leading and trailing edges of the rectangular pulses are measured in Time-to-Digital-Converters (TDC), while a copy of the pulse is sent to the trigger logic. When a trigger condition is found (see description below) the TDCs are

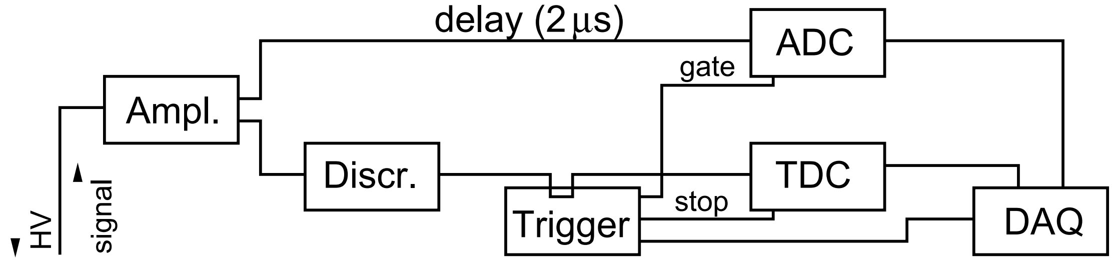

Figure 3.4: *AMANDA-II data acquisition scheme. See text for explanation.*

stopped 10 μs after the trigger. Capable of storing up to 16 edges within the last 32 μs, the TDC is read out by the data acquisition system to retrieve up to 8 pulses that arrived between -22 μs and $+10$ μs around the time of the issued trigger. The time resolution of the TDCs is approximately 1 ns.

The trigger signal also opens a recording window for the peak sensitive Amplitude-to-Digital Converters (ADC). They store the highest signal amplitude within a 10 μs window. The ADC input is the signal from the delayed channel, therefore amplitudes can be measured in the interval $[-2\ \mu\text{s}, +8\ \mu\text{s}]$ around the issued trigger.

The DAQ computer system collects all information from ADCs and TDCs, combines them with the absolute time received from a GPS clock and stores the events on disk and magnetic tape. While the readout is performed, TDCs and ADCs are not able to collect data, the detector is effectively switched off. This leads to a so called detector "dead-time". The dead-time fraction is a function of the overall rate of triggers. For AMANDA-II it is between 15% and 25%, dependent on the detector configuration.

To achieve dead-time free measurements and to allow an improved determination of pulse amplitude and charge, a second data acquisition system was introduced in 2003. The Transient-Waveform-Recorders (TWR) sample the pulse amplitudes of each individual OM every 10 ns for a 10 μs window around the trigger. Arrival time, amplitude and charge of the pulse can be simultaneously calculated from the collected data. Since two buffers are available for sample storage, pulse recording continues during readout cycles. This TWR-DAQ is not used in this work, since it was only available for the last two years of the time span (2000-2004) covered by this analysis.

3.2.4 Event Trigger

Ideally a trigger should be issued whenever a potentially interesting interaction takes place within the detector or when a particle passes through it. In practice one has to carefully set the trigger condition to balance between technical constraints and physics interests. A higher trigger rate increases the number of readout cycles and therefore the detector dead-time. Also the storage capacity on tapes and disks limits the number of events which can be processed. A too restrictive trigger on the other hand results in the loss of many potentially interesting low energy events.

As a compromise three different triggers are implemented in AMANDA-II. The main trigger is issued whenever pulses from 24 channels are recorded within a 2500 ns time window (Multiplicity Trigger). To retain low energy events coming from the center of the Earth which are potentially interesting for Dark Matter searches, the String Trigger is implemented. If 5 out of 9 channels on the same string record pulses in a given time window the array is read out. To allow cross calibration of the reconstruction of muons generated in cosmic ray air showers with a reconstruction of the shower in the SPASE-2

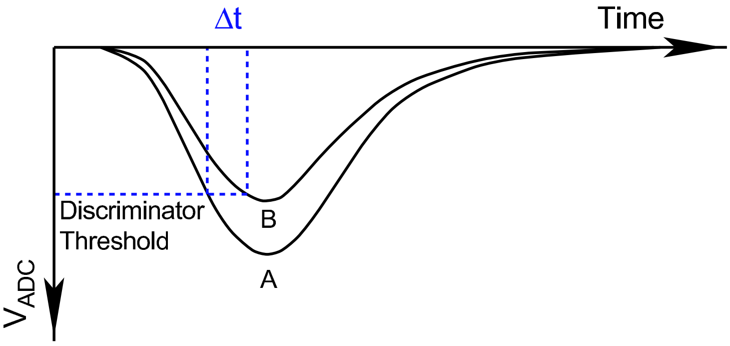

Figure 3.5: *Illustration of the amplitude dependent arrival time correction. The smaller pulse B crosses the discriminator threshold later by* Δt *than the large pulse A.*

surface array [A$^+$04b], a coincidence trigger is issued whenever an air shower is recorded in the SPASE-2 array. A rate of 80-90 events/sec is produced by these triggers and about 5 gigabyte of data are stored on magnetic tapes per day. Only the Multiplicity Trigger is used for this analysis.

3.2.5 Calibration

The event record consists of four pieces of information for every recorded hit: the time of the leading and the trailing edge (t_{LE}, t_{TE}) measured by the TDC on the surface, the maximum amplitude V_{ADC} recorded in the ADC[1] and the channel number i_{OM} at which the photon was detected. The information necessary to reconstruct event properties, however, is the arrival time of the photons at the optical module t_{OM} and the photo-electron multiplicity $N_{\mathrm{p.e.}}$, which produced the pulse. Besides that, a precise knowledge of the geometric location of the Optical Modules is essential. To obtain these quantities from the measured ones, the time, amplitude and geometry calibration is performed.

Time calibration

The time of arrival of a photon at the Optical Module can be calculated from the leading edge time by the formula:

$$t_{\mathrm{OM}} = t_{\mathrm{LE}} - t_0 - \frac{\alpha}{\sqrt{V_{\mathrm{ADC}}}} \, . \tag{3.2}$$

The time t_0 accounts for all delays introduced by the pulse propagation along the cables and in the electronics. The second term is a correction for the amplitude dependent time interval between pulse start and threshold crossing: the width of the pulse is determined by the dispersion of the cable and does not depend on its height. The consequence is that larger pulses cross a fixed discriminator threshold earlier than smaller pulses (see also figure 3.5). The beginning of the pulse can be approximated by a parabola and therefore the leading correction for this effect is of the order of $V_{\mathrm{ADC}}^{-1/2}$ [Sch02].

In the AMANDA time calibration both constants, the signal delay t_0 and the amplitude correction constant α, are measured using frequency doubled YAG-laser light pulses transmitted into the ice via optical fibers and emitted there by diffuser balls. The pulse is

---

[1] Only one amplitude value is recorded per channel. If multiple hits occurred in the same channel only the amplitude of the largest pulse is retained.

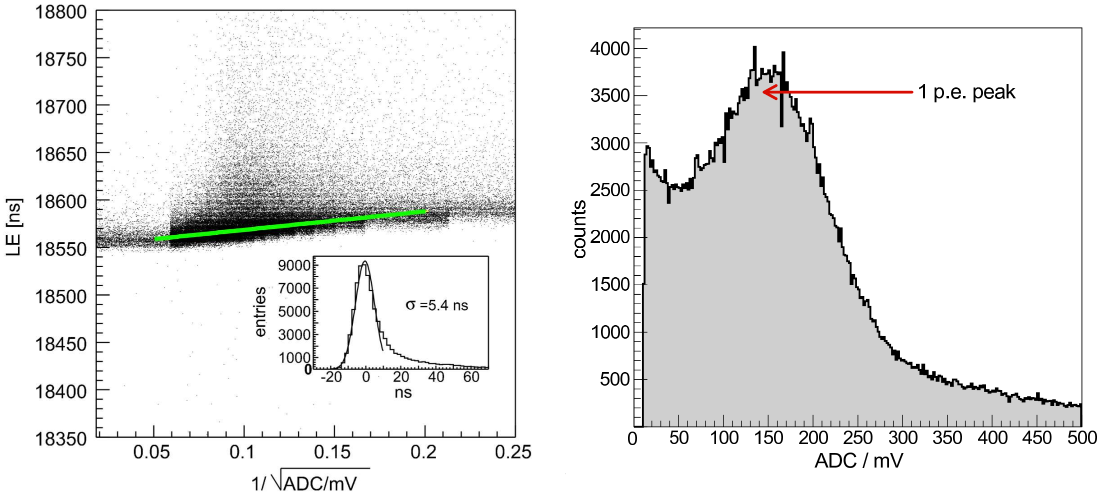

Figure 3.6: *Left: Typical output from a time calibration laser run. The leading edge time of the first hit is plotted vs. $V_{ADC}^{-1/2}$. A linear fit (green line) is performed to derive the time delay t_0 and the amplitude correction α (see text). Right: Distribution of measured pulse amplitudes from a sample Optical Module. The prominent single photo-electron peak is used for amplitude calibration.*

detected by the nearby Optical Module which is to be calibrated. To get different pulse amplitudes the intensity of the laser is varied. The left picture of figure 3.6 shows the results from such a calibration run: The measured time is plotted versus $V_{\mathrm{ADC}}^{-1/2}$. The value of t_0 can be derived from the abscissa t_0', while the amplitude correction constant α can be read from the slope of a linear fit to the curve.

To calculate the value of t_0 one subtracts from the fitted time t_0' the time when the laser pulse was emitted t_{laser}, the travel time of the light pulse inside the optical fibre t_{fiber} and the travel time of the light pulse in the ice between the diffuser ball and the Optical Module t_{ice}. t_{laser} is known from using a photodiode on the surface to trigger the data acquisition system. t_{fiber} was measured for each individual fiber from the round trip time of light reflected at the end of the fiber using an Optical Domain Time Reflectometer. Finally t_{ice} can be calculated from the known speed of light in ice and the known distance between Optical Module and diffuser ball. The time resolution for t_0 reached by this method is less than 7 ns [Bir02].

A second time calibration method uses down-going muons from cosmic ray induced air showers. This so called "muon-calibration" selects well reconstructed muon tracks to iteratively refine the t_0 constants by comparison of the time distribution of the recorded hits to their expected time distribution. It is used for channels which cannot be calibrated by the laser method due to broken optical fibers or because they are too far away from a diffuser ball. It is also applied to have an independent cross check of the laser calibration. A detailed description of this method can be found in [CH01].

Amplitude calibration

The number of photo electrons (p.e.) responsible for a pulse of amplitude V_{ADC} depends on the gain of the amplifier, the PMT gain and the signal attenuation in cables and electronics. However, the majority of the pulses in down-going muon data are 1 p.e. pulses from either dark-noise or distant tracks. They form the prominent amplitude peak visible in the V_{ADC}-distribution for a sample OM on the right picture of figure 3.6. The peak V_{1pe}

of this distribution is fitted and taken as the pulse amplitude for a single photoelectron pulse. Assuming a linear dependence of the amplitude (which is only justified for the range where saturation does not play a significant role) the approximate number of p.e. is calculated by

$$N_{pe} = \frac{V_{\mathrm{ADC}}}{V_{\mathrm{1pe}}} \; . \tag{3.3}$$

The error introduced by neglecting non-linear effects at high amplitudes does not play a role in this analysis, since the amplitude is not used for reconstruction besides the fact that hits with very low amplitudes ($N_{pe} < 0.1$) are excluded.

Geometry calibration

An important ingredient for the reconstruction is an exact knowledge (±1 m) of the geometrical location of the optical modules. Before deployment the surface position of the holes is determined by triangulation. During the drill operations the drill momentum in x-y direction is carefully monitored. Pressure sensors at the lowest and highest optical modules are used to determine the z-position in the molten hole and the string expansion during deployment. An accuracy of about 1 m in x-y and 2 m in z direction can be reached by this method [Wos00].

In a second step after deployment intra-module light sources are used to obtain a relative geometry of the Optical Modules. Strong light pulses seen from many modules are sent and with the well known refraction index the geometry is calculated from the arrival times of the light. The accuracy reached by both methods combined is about 50 cm [Wos99], resulting in an uncertainty of less than 3 ns when expected arrival times of un-scattered light are calculated.

Chapter 4

Event simulation

To study and understand the response of AMANDA-II to traversing high energy particles a detailed Monte Carlo simulation was developed. All aspects from the primary interaction to the detector electronics were modeled in software as precise as possible. Large statistics of interacting neutrinos are simulated to develop signal-background-separation techniques and assess their performance. In this chapter we describe the individual steps of the simulation chain.

4.1 Simulation of neutrino induced events

Neutrino induced events from cosmic sources are the signal which this analysis is looking for. But they are also a background for this search in the form of neutrinos produced by the interaction of cosmic rays in the atmosphere. Both classes differ only by their energy spectrum and distribution on the sky and can be simultaneously produced in a single simulation. A weighting of the Monte Carlo events is then used to obtain the results corresponding to each class.

4.1.1 Neutrino interaction

Two different programs were applied to simulate neutrino interactions in this analysis. The older one, NUSIM [Hil96] is only capable of simulating CC-interaction of muon neutrinos. The newer one ANIS [GK05] is able to do simulations of interactions of all neutrino flavors. Both packages propagate the neutrino through the Earth and account for possible absorption by CC-interaction or energy loss by NC-interaction[1] before the interaction region is reached.

In both cases neutrino events are generated with an energy distribution following an user defined power law spectrum. The direction of the events can be selected to be either fixed or isotropically distributed. After propagation through the Earth an interaction is simulated in the interaction region. For NUSIM this region corresponds to two times the approximate range of muons given by (2.20), for ANIS it was fixed to 40 km from the detector center. Actual interaction probabilities for the simulated events are assigned as weights.

NUSIM utilizes an important simplification: the scattering angle between muon and neutrino is neglected. As can be seen from (2.18) this is justified for $E_\nu \gg 1$ TeV. For lower energies however, the value of the average scattering angle approaches the angular

---

[1] Besides absorption and energy loss ANIS also handles ν_τ-regeneration in the Earth.

resolution of AMANDA-II of 1.5° – 2.5°, leading to a degradation of the overall angular resolution. In section 9.1.4 we will present an estimation of how much the signal prediction for the point source analysis is affected by this simplification of NUSIM. ANIS implements a correct treatment of the neutrino muon scattering angle.

The drawback of ANIS is that it needs a considerably higher computing time to produce one triggered event compared to NUSIM. For this reason NUSIM was still used for the bulk of muon neutrino simulations in this analysis, while ANIS is only applied for studying a signal contribution from tau neutrinos and for systematic error checks. All simulations were performed with a neutrino input spectrum of $d\Phi/dE \propto E^{-1}$. Such a spectrum provides equal statistics of generated neutrino events in each decade of energy. For analysis of other signal and background spectra the simulated sample was re-weighted accordingly.

4.1.2 Muon propagation

The muons generated in neutrino interactions lose energy by ionization, bremsstrahlung, photo-nuclear interaction and pair production before they eventually decay (see also section 2.4.3). The energy losses ΔE_μ are of stochastic nature, meaning that they happen as discrete events between periods of free propagation of the muon. The number of such events to occur per unit path length rapidly increases as the energy lost per event becomes smaller. They can then be approximately treated as a continuous energy loss.

This technique is applied in the MMC [CR01] muon propagation code used in the AMANDA simulation. All energy losses producing secondaries below $E_{\mathrm{cut}} = 0.5$ GeV are attributed to a continuous energy loss of the muon, while all other energy loss processes are treated as stochastic events. Secondaries with $\Delta E_\mu > E_{\mathrm{cut}}$ producing either electromagnetic or hadronic cascades are stored individually. Čerenkov light produced in these cascades is accounted separately in the photon propagation step in addition to the continuous contribution.

The simulated environment of MMC through which the muons are propagated consists of four horizontal layers of different material modeling the conditions found at South Pole. They are summarized in table 4.1. The snow layer refers to the top 200 m of South Pole glacial ice that is not yet fully compacted and has a lower density than the bulk of the ice [P+02a]. The real density in that layer is gradually increasing with depth and has been approximated by a layer of constant average density in the simulation.

Material	depth z [m]	density ρ [g/cm^3]
Air	< 0	$0.81 \cdot 10^{-3}$
Snow	0 – 200	0.76
Ice	200 – 2810	0.92
Standard Rock	> 2810	2.65

Table 4.1: *Material layers in MMC through which muons are propagated. $z = 0$ corresponds to the surface of the glacier. The center of the AMANDA-II detector is 1730 m below the surface.*

The NUSIM package brings its own muon propagation code to propagate muons from interactions inside the bedrock to the rock-ice boundary (PROPMU [LS91]). A comparison of both algorithms in [Hau04] resulted that the differences in event rates obtained for AMANDA-II from both codes are less than 2%. Therefore we omit here a detailed description of this alternative algorithm.

4.1.3 Photon propagation

The propagation of the Čerenkov photons emitted from the muon and its secondaries through the ice is the most complex part of the AMANDA simulation. It was shown in section 3.1, that the natural ice at South Pole exhibits strong variations of its optical properties, in wavelength as well as in depth. With current CPUs, it is impossible to do a dedicated tracking of each of the $> 10^7$ photons, emitted within the range of the detector from a high energy particle, for a large number of events.

However, the probability density p for an Optical Module located at $\vec{\mathbf{r}}_{OM}$ to detect a photon at time t_{OM} that was emitted at a certain point $\vec{\mathbf{r}}_\gamma$ along the muon track at time t_γ can be described based on a limited number of parameters. Since the optical ice properties do not change in x and y directions, the probability density can be expressed as a function of [Mio01]:

- the zenith angle of the track θ;
- the depth of the optical module z_{OM};
- the coordinates ρ and ϕ, describing the location of the optical module in a plane perpendicular to the track direction;
- the distance L from the track origin at which this plane intersects the particle trajectory;
- the difference between actual and expected[2] arrival time t_{res}.

Thus, instead of propagating each single photon of the passing particles, the software used for AMANDA-II simulation pre-calculates the probability density based on this parametrization. Two software packages are available, PHOTONICS and PTD. Their features and differences are described below.

PHOTONICS

The PHOTONICS package developed in [Mio01] pre-calculates the 6-dimensional probability density function $p(\theta, z_{OM}, \rho, \phi, L, t_{res})$ for the arrival time of detected photons and the number of photons expected per meter of track length $\mu_\gamma(\theta, z_{OM}, \rho, \phi, L)$ for a grid of values in the parameter space. The computed values of p and μ_γ are stored in tables. In the event simulation itself, the number of detected photons from the muon track and its secondaries is determined for each optical module from a Poisson distribution with the mean $\mu_\gamma(\theta, z_{OM}, \rho, \phi, L)$. The photon detection times are then assigned to the optical module following the distribution $p(\theta, z_{OM}, \rho, \phi, L, t_{res})$[3].

The pre-calculation of p and μ_γ in PHOTONICS is performed by a full scattering and absorption simulation of a Čerenkov spectrum. The photons are tracked through the bulk ice using the scattering and absorption coefficients derived from the measurements with in-situ light sources. The simulation of the Optical Module accounts for the quantum efficiency of the PMT, the optical properties of the glass-gel layer surrounding it and the ice in the re-frozen holes.

The major drawback of this approach is, that huge tables are created for a reasonable evaluation of the parameter space. Current table productions reach sizes of 10G to 50G,

---

[2] The arrival time expected from light propagation without scattering

[3] Technically this is realized as part of the AMASIM simulation described below

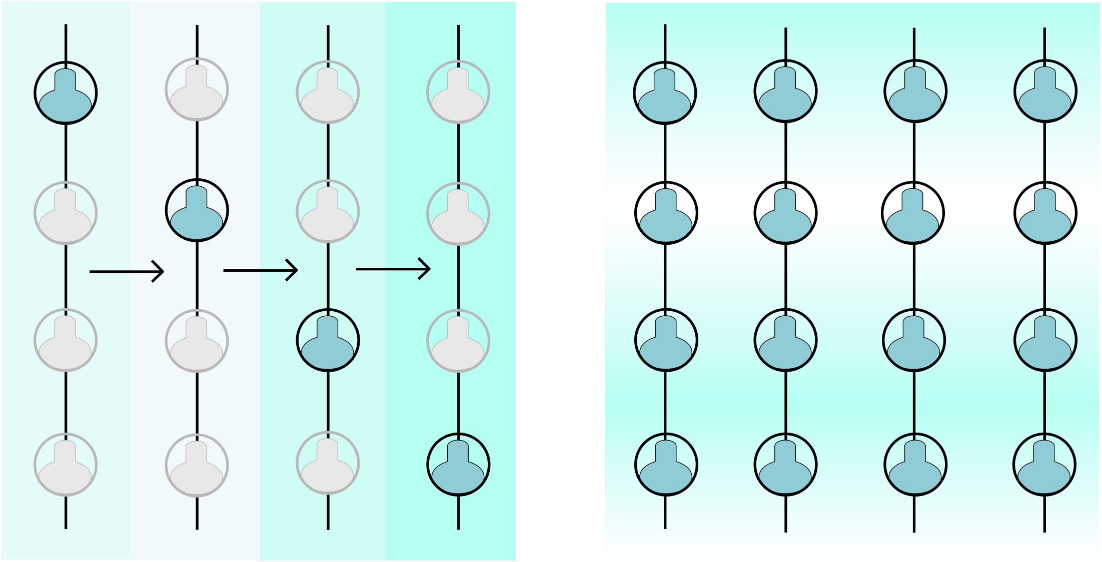

Figure 4.1: *Illustration of the difference in the ice description between PHOTONICS and PTD. In PHOTONICS (right side) each combination of particle track and Optical Module sees the true layered structure of ice between the point of photon emission and the point of photon absorption. In PTD (left side) each Optical Module sees the particle track in its own ice. Photons detected at the Optical Module have been traveled from point of emission to point of detection through homogeneous ice.*

much larger than physical computer memory available on cluster nodes. However, it was shown that an efficient processing is possible, if the events are sorted in a sophisticated way [Lan05]. Still PHOTONICS simulation consumes a considerable amount of resources and it is difficult to obtain large statistics of events. Moreover the results from PHOTONICS simulation have been only recently declared trustworthy also based on the comparisons presented in this thesis.

For those reasons the standard simulation of neutrino induced muon events used in this analysis is based on PTD, an older, simpler approximation of the ice properties which has been the standard tool for years in the AMANDA collaboration.

PTD

In PTD [Kar99] the Optical Modules are surrounded by an infinite layer of ice with constant optical properties. However, these properties may vary from module to module. Figure 4.1 illustrates this difference in ice simulation between PHOTONICS and PTD. Four classes of optical modules are distinguished in the standard PTD ice description, the "Muon Absorption Model" (MAM) [H$^+$02a]. Each class is located in an ice with different absorption and scattering properties. Also in PTD the functions p and μ_γ are determined by photon simulation, but the number of free parameters in the pre-calculated tables is reduced by two allowing much more compact tables. Instead of a full Čerenkov spectrum only photons of an average-wavelength of 420 nm are simulated.

The unavoidable errors introduced in this simplified description of the real ice properties are partly compensated by using effective ice properties instead of real ones. In MAM the scattering and absorption coefficient for each class of ice are fitted to provide the highest possible accuracy in the description of the arrival time delay of events triggered by cosmic ray induced muons [H$^+$02a].

The differences arising from the usage of the ice description of either PTD or PHOTONICS for the analysis presented in this thesis are marginal. The predictions of signal neutrinos and atmospheric neutrino background vary by less than 5% for all tested spectra (see chapter 9). This variation is included in the systematic uncertainty of the analysis. We will show comparison plots between data and Monte Carlo simulation including both ice description models. Results from the analysis are presented based on values obtained by PTD simulation.

4.1.4 AMANDA-II detector simulation

The AMASIM software package [Hun99] simulates the read-out electronics and data acquisition. Template pulse waveforms based on oscilloscope measurements of the PMT response to a photo-electron are generated for each detected photon. Their amplitude is chosen corresponding to the single photo-electron amplitude distribution provided by the PMT manufacturer. PMT dark noise pulses with Optical Module specific rates are added. If more than one hit is present in a module, the individual waveforms are summed up. For large pulses saturation effects of the amplifier are taken into account. The TDC and ADC properties as described in section 3.2.3 as well as the delay of the pulses in the cables are modeled.

While all of the features of AMANDA-II are well simulated in AMASIM, most of its problems are not: Noise introduced by the electronic components as well as cross talk in twisted pair cables is neglected. Unusual behaviour of pathological Optical Modules like high bursts or sudden drops in dark noise rate are not simulated either. And last but not least correlated noise due to bad weather conditions at the South Pole site is also not taken into account.

For these phenomena a different approach is chosen to get a consistent description of the real measurements by the Monte Carlo simulation. Pulses generated by the above effects are identified and removed from the data in a processing step called “hit cleaning”. The same procedure is applied to simulated data[4]. After removal of the hits, events from simulation and real data have to face the trigger condition described in section 3.2.4 again and are rejected if they fail. Reconstruction of event properties is performed only on hits surviving the cleaning.

4.1.5 Event weighting

It was mentioned earlier that the simulated events are subject to weighting. Instead of repeating all CPU time consuming simulation steps if hypothetical neutrino sources with different energy spectra or cosmic ray induced atmospheric neutrinos are to be simulated, a combined event sample is produced for all cases. This combined neutrino sample has a spectrum of E^{-1} and the neutrino-nucleon interaction vertices are equally distributed throughout the interaction volume. To obtain a meaningful sample each event has to be weighted with a:

Flux weight: Re-weights the number of generated events to simulated fluxes. For atmospheric neutrinos a parametrization of their flux $\Phi_{\mathrm{atm}-\nu}(E,\theta)$ by Lipari [Lip93] is used. For the simulation of a hypothetical signal a flux weight corresponding to a model prediction for the source is applied.

---

[4] Even though the effects are not simulated, their removal also rejects a small fraction of “normal” hits. Applying hit cleaning also to Monte Carlo simulation assures that the same hits are removed there.

Interaction weight: The energy, declination and neutrino type dependent probability for the simulated interaction to happen. This weight is a function of the cross section, the target density and the neutrino absorption length.

4.2 Simulation of cosmic ray induced muon background

The overwhelming majority of events recorded by AMANDA-II are cosmic ray induced muons. They exceed the number of atmospheric neutrinos by six orders of magnitude. A simulation of this background is performed using the CORSIKA [H^+98] air shower generator. It simulates air showers from cosmic ray primaries of energies up to 10^{20} eV. The muons from each air shower, that have the potential to reach the AMANDA-II detector are propagated through the ice using MMC. The Čerenkov photon propagation is performed by PTD or PHOTONICS and the detector response is simulated by AMASIM as described above.

The background simulation is used within this analysis only to compare recorded events to Monte Carlo predictions at the trigger level. The experimental data itself can be exploited to estimate the fraction of events from cosmic ray muons which remain in the data sample after the selection of neutrino induced events (see section 6.3.2). At the final event selection level the remaining data sample is strongly dominated by atmospheric neutrinos. The background for the point source analysis also can be determined from the experimental data independent of the simulation (see section 7.1.1). For these reasons only a small sample of CORSIKA generated muon events was created.

Chapter 5

Reconstruction of event properties

Simulated and experimental data are subject to the same steps of reconstruction. The goal of the reconstruction is to determine event properties from the recorded photon arrival times and amplitudes as accurately as possible, so that these properties can be used for event selection and analysis.

The most important event property for a point source analysis is certainly the event direction. Besides the direction topological parameters are used to separate neutrinos from cosmic ray induced muon background. The details of this separation process will be discussed in chapter 6. Here we introduce and explain the reconstruction methods used in this analysis.

5.1 Hit cleaning

Besides the Čerenkov light from traversing charged particles several types of noise are recorded by the AMANDA data acquisition electronics: dark noise resulting from radioactivity and thermal emission in the PMT, electronic noise picked up in the cables or generated in the amplifiers and cross-talk from neighbouring cable pairs. Moreover, a few percent (varying from year to year) of the deployed optical modules are untrustworthy, meaning that they either record too few hits or produce high levels of noise or jump intermittently between both states. To avoid biases in the reconstruction by these “fake”-hits, they are removed from the event record. For this purposes one tries to identify such hits by characteristics which distinguish them from detected Čerenkov light photons. The cleaning procedure is performed in several steps.

Bad Optical Module removal

For each year of data taking each optical module is classified as good or bad, based on the information collected in the AMANDA detector monitoring. The task was performed by different people for each year and slightly different criteria were applied. The best description of the general procedure is found in [Rib02]. An Optical Module is trusted and used for analysis if it shows reasonable:

- Dark noise rates;
- ADC rates;
- TDC rates.

Besides hits from the bad OMs also hits from modules outside the bulk of the detector are removed. For them often no reliable calibration exists or the modules are located in ice layers full of air bubbles. This applies to:

- OM 81-86 (lower extension of string 4);
- OM 307-310 & OM 337-344 (upper and lower extensions of string 11);
- OM 345-352 & OM 379-386 (upper and lower extensions of string 12);
- OM 387-394 & OM 421-428 (upper and lower extensions of string 13);
- OM 555-596 (string 17).

Table 5.1 shows the number of trustable modules, whose hits are used for reconstruction in the years 2000-2004[1], the time span of this analysis. The strong variations in the number, especially the increase in reliable modules between 2000 and 2002 was the result of two major campaigns during the austral summers 2000/2001 and 2001/2002 to identify and eliminate detector problems.

Year	# of Optical Modules
2000	491 / 481 / 468
2001	512
2002	533
2003	539
2004	534

Table 5.1: *Number of Optical Modules used for reconstruction.*

“Time Over Threshold” cleaning

Many Optical Modules with electrical signal transmission record pulses from noise picked up in the cables, generated in the amplifiers or from cross-talk induced by other pulses. A possible way to identify such pulses is to look at the time over threshold (TOT), i.e. the time between recorded leading and trailing edges: the pulse shape is often distinctly different from a photo-electron induced pulse resulting in a smaller TOT.

The left picture of figure 5.1 shows such a TOT distribution for a single optical module. Besides the main peak for photo-electron induced signals an exponentially decaying second component from noise hits is visible at short TOTs. To remove these hits a selection cut is placed individually for each year and Optical Module with electrical read-out in the valley between both peaks (between a TOT of 75 ns and 200 ns) and only hits with a TOT higher than this value are kept. For modules with optical readout a common TOT cut requiring a TOT > 5 ns was used.

Time window cleaning

Dark noise of the PMT caused by radioactive decay in the optical module or thermal emission of photoelectrons produces indistinguishable stochastic signals. However, it can

---

[1] Since several problems on different groups of channels arose during the 2000 data taking period, the year was subdivided into three periods with different bad module selections.

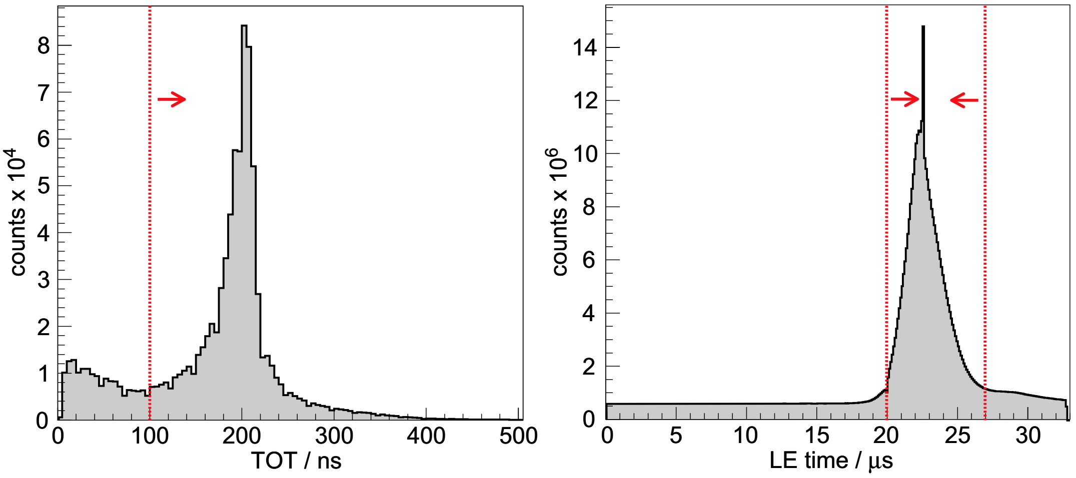

Figure 5.1: Left: *Time-over-threshold (TOT) distribution for a selected Optical Module. The noise peak at small TOT values and the peak from real PMT pulses at 200 ns are easy to distinguish.* Right: *Distribution of leading edge times for all Optical Modules superimposed. The trigger time is visible as a sharp peak (see text). In both pictures, the red lines and arrows mark the region in which hits pass the cleaning.*

be partly removed based on its temporal properties and spatial isolation. The AMANDA data acquisition records all pulses in the time interval $[-22\ \mu s, 10\ \mu s]$ around the trigger time. A particle traveling at the speed of light, crosses the AMANDA-II detector in less than 2 μs. So most of the light from single muons should arrive in a short time within the recording interval. This is used to remove parts of the dark noise. All hits outside a $[-2.5\ \mu s, 4.5\ \mu s]$ interval around the trigger time are removed from all channels. The right picture in figure 5.1 shows the time distribution of hits within the 32 μs window for all channels superimposed. The trigger time is visible as a sharp peak in that distribution (because the trigger is issued by the 24^{th} hit (see section 3.2.4), one finds a hit at the exact trigger time in every event). The time window outside which hits are removed is indicated by the red lines and arrows.

Amplitude and isolated hits cleaning

If a hit is isolated in space and time it is likely to be produced by dark noise. Therefore also hits are removed which do not have a partner hit in any of the channels within 500 ns of time or in any channel located less than 100 m away from the module.

Amplitude cleaning has a different purpose. For low amplitudes the first order amplitude correction in the timing calibration gets very large and correspondingly the uncertainty in the true arrival time of the hit (see also section 3.2.5). Moreover, sometimes it happens that ADC information for a hit is not available and no amplitude can be assigned to it, also resulting in a large uncertainty of the arrival time due to missing amplitude correction. To avoid that such hits bias the reconstruction they are removed from the event.

Cross talk cleaning

Most of the cross talk between neighbouring pairs of signal cables is removed by the TOT cleaning: the induced signal is proportional to the derivative of the original signal, resulting in a bi-polar pulse of small amplitude with a considerably shorter TOT. However especially if the cross-talk was induced by a pulse of high amplitude a simple cut in time

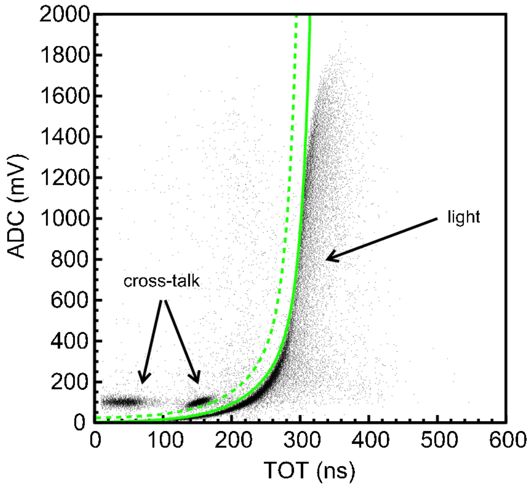

Figure 5.2: *Hit selection to remove pulses caused by cross talk. Cross-talk pulses and photo-electron induced pulses form distinct populations in the amplitude vs. time-over-threshold plot. The correlation between amplitude and time-over-threshold is fitted for the light induced photons (solid green line). The shape of this fit shifted by -20ns in TOT is used as selection cut marked by the dotted green line to remove the cross-talk hits on the left side of this line.*

over threshold cannot suppress the cross-talk without removing also a significant fraction of the hits from Čerenkov photons.

Especially cross-talk/real hit pairs which appear at modules not too far away from each other can significantly bias high level direction reconstruction, since they have a defined time relation and the potential to pull the reconstructed track into a wrong direction. Therefore a second stage of improved cross talk cleaning is applied which was developed in [Tab02].

Hits caused by photo-electrons show a non-linear correlation between amplitude (ADC) and time over threshold (TOT). Figure 5.2 illustrates this for a sample optical module. On this picture also distinct populations of hits caused by cross talk are visible. The ADC-TOT correlation of the hits caused by real photo-electrons is fitted for each optical module potentially exhibiting cross-talk (green solid line) and used as a two-dimensional selection cut shape. To avoid the loss of a significant fraction of good hits due to fluctuations in the ADC-TOT distribution, the selection cut is shifted by -20 ns in TOT. Only hits on the right side of this line are used for high level reconstruction.

5.2 First guess reconstruction

Between 2000 and 2004 about 10 billion events were triggered in the time periods selected for this analysis. A full reconstruction can be performed in $\mathcal{O}(10\text{ s})$ per event on a modern CPU. Thus, to complete such a full reconstruction of all events would consume more than 3000 CPU years. Even though this might be possible using modern computing grid technologies, it would be unreasonable since only several thousands of these events are caused by neutrinos, while the vast majority is cosmic ray induced muon background.

Therefore the reconstruction chain is divided into different levels: a large part of the muon background is easy to identify by a fast and coarse reconstruction of the event. The methods providing this identification are commonly named “first-guess” reconstructions in the

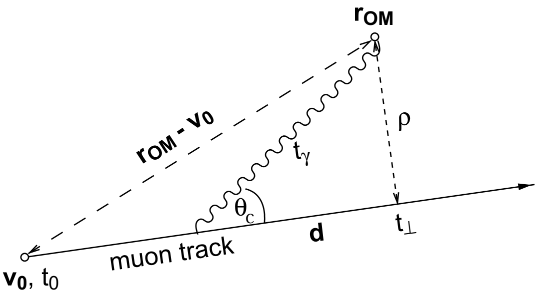

Figure 5.3: *Illustration of the geometry used for the residual time calculation. See text for details.*

AMANDA collaboration. Only events which cannot be clearly identified as background from first-guess methods are processed further in CPU time intensive likelihood and topological parameter reconstructions. The corresponding techniques are described further below. In this section we illustrate the two first guess reconstruction methods which we use for background suppression in this analysis.

5.2.1 Residual time

The fundamental variable used in all light arrival time based reconstruction algorithms is the residual time. In plain words the residual time is the difference between actual arrival time of a Čerenkov photon and its expected arrival time in a scattering-free medium. The expected arrival time is purely defined by the geometry, i.e. the relative location of the Optical Module with respect to the muon track. Let $\vec{\mathbf{v}}_0$ be the position of the muon at the time $t = t_0$ and $\vec{\mathbf{r}}_{\mathrm{OM}}$ the position of the optical module. A multi-GeV muon moves along its direction $\vec{\mathbf{d}}$ with a speed of $\beta = 1$, thus its position at time t is:

$$\vec{\mathbf{v}}(t) = \vec{\mathbf{v}}_0 + c_{\mathrm{vac}}\,(t - t_0)\,\vec{\mathbf{d}}\;. \tag{5.1}$$

We define the time $t_\perp$ as the time and ρ as the distance of closest approach of the muon to the optical module. They are easily calculated by:

$$\begin{aligned} t_\perp &= t_0 + \frac{1}{c_{\mathrm{vac}}}(\vec{\mathbf{r}}_{\mathrm{OM}} - \vec{\mathbf{v}}_0)\,\vec{\mathbf{d}} && (5.2)\\ \rho &= |(\vec{\mathbf{r}}_{\mathrm{OM}} - \vec{\mathbf{v}}_0) \times \vec{\mathbf{d}}|\;. && (5.3) \end{aligned}$$

Figure 5.3 illustrates the geometrical setup and the variables introduced here. The Čerenkov light from this muon is always emitted at the maximum Čerenkov angle $\cos\theta_c = 1/n_p$, where n_p denotes the phase index of refraction. Hence, to be detected in the Optical Module it had to be emitted a time $t_c = \rho/(c_{\mathrm{vac}}\tan\theta_c)$ before the point of closest approach is reached. The photon then propagates with a speed of $c_{\mathrm{ice}} = c_{\mathrm{vac}}/n_g$ (n_g is the group index of refraction[2]) for the time $t_\gamma = \rho/(c_{\mathrm{ice}}\sin\theta_c)$ until it arrives at the optical module. If we sum up these contributions we find the expected arrival time t_e for a photon emitted from the muon described by $(\vec{\mathbf{v}}_0, t_0, \vec{\mathbf{d}})$ at the location of the optical module $\vec{\mathbf{r}}_{\mathrm{OM}}$ as:

$$t_e = t_\perp - t_c + t_\gamma = t_\perp + \frac{\rho}{c_{\mathrm{vac}}}\left(\frac{n_g}{\sin\theta_c} - \frac{1}{n_p\sin\theta_c}\right)\;. \tag{5.4}$$

---

[2] The phase and group index of refraction are in general different for dispersive media. See [PW01] for a detailed discussion.

The difference $t_{\text{res}} = t_a - t_e$ between the actual arrival time of the photon t_a and the expected time is called the residual time for a muon track given by $(\vec{\mathbf{v}}_0, t_0, \vec{\mathbf{d}})$.

5.2.2 Direct Walk

The Direct Walk algorithm described in [Ste02] is designed to quickly find the approximate track direction of a muon passing through the detector. To accomplish this task it exploits the scattering of light in the ice: a low residual time in a given pair of optical modules is only expected if the light arrives un-scattered and therefore if the track passes close to the two Optical Modules. As a zero order hypothesis one can then assume that the muon track is the connection line between the two Optical Modules.

All such combinations of hit pairs which make good muon track candidates are collected. The condition to become a track candidate is that the two Optical Modules are separated by more than 50 m and that the residual time fulfills the inequality $|t_{\text{res}}| < 30$ ns. Afterwards, a quality selection of the track candidates is performed by evaluating how well the arrival time of other hits fit to this track candidate. This evaluation is quantified in a quality parameter Q and only candidates with $Q > 0.7Q_{\text{max}}$ survive as high quality muon track candidates. In the likely case that there is more than one high quality candidate, the number of such candidates in a 15°cone around each of the tracks is counted and the cone showing the highest multiplicity is selected. The average of the coordinates of the muon track candidates found in this cone is returned as the first guess hypothesis for the muon track.

The angular resolution[3] reached by this fit is 7.3°. 98.6% of down-going cosmic ray induced muon tracks are correctly reconstructed as down-going.

5.2.3 JAMS

A second newly developed first guess method is the JAMS pattern recognition based fit [Ste05]. It was applied in this work for the first time in AMANDA-II analysis. It is specifically designed to be effective against a class of background which is easily misinterpreted by other reconstruction algorithms as an up-going neutrino induced muon: two down-going particles which pass the detector at nearly the same time from different directions, so that they form a single event. If the lower one of these tracks slightly precedes the other, a reconstruction assuming a single muon track will likely recognize the event as an up-going particle. The JAMS fit consists of three distinct steps which are described in the following:

- search for hit clusters along a regular grid of input directions;
- track parameter reconstruction for the recognized clusters;
- quality assessment and sorting of the reconstructed tracks.

In the implementation used in AMANDA analysis JAMS selects 50 input directions $\vec{\mathbf{d}}_i$ on a regular grid and searches for clusters in x-y-ct space in a coordinate system with the z-axis defined by $\vec{\mathbf{e}}_z = \vec{\mathbf{d}}_i$. For a muon passing a pair of Optical Modules at $z_a = 0$ and $z_b = z_0$ at the same distance ρ, the expected arrival time of the light differs by $t_b = t_a + z_0/c_{\text{vac}}$. Along a muon track several Optical Modules at similar distances should be hit and thus, if the vector $\vec{\mathbf{d}}_i$ was a good approximation of a real muon track direction, a cluster should

---

[3] for simulated up-going neutrinos selected in the sample defined in chapter 6.

be found in x', y', ct' defined by $(x', y', ct') = (x, y, ct - z)$. If several tracks from different directions were responsible for the event, multiple clusters should be visible. To define the cluster, for all hit pairs (x'_i, y'_i, ct'_i) and (x'_j, y'_j, ct'_j) their distance

$$r_{ij}^2 = (x'_i - x'_j)^2 + (y'_i - y'_j)^2 + c^2(t'_i - t'_j)^2 \; . \tag{5.5}$$

is calculated and compared to a fixed maximum distance $r_{\max}$. In case one finds $r_{ij} < r_{\max}$ the number of neighbours N_i, N_j is increased by one for both hits. With $N_{\max}$ being the maximum number of neighbours found in this step, the first guess for the center (x_c, y_c, ct_c) of the largest cluster is taken as the average coordinate of all hits with $N_i \geq N_{\max} - 1$. Afterwards, the cluster center position is iteratively refined by taking into account all hits with $r_{ic} < r_{\max}$. At least 7 hits are requested to fulfill this condition in order to recognize the cluster as a valid one.

For each valid cluster the free muon track parameters (x, y, z, θ, ϕ) are calculated, which maximize a simple likelihood function made up of two Gaussian distributions of variable widths:

$$\mathcal{L} \;=\; \prod_i^{\text{all hits}} \frac{2}{\sqrt{2\pi}(\sigma_L + \sigma_R)} \begin{cases} \exp\left(-\frac{(t_{\text{res}}-t_p)^2}{2\sigma_L^2}\right) & \text{if} \quad t_{\text{res}} < t_p \\ \exp\left(-\frac{(t_{\text{res}}-t_p)^2}{2\sigma_R^2}\right) & \text{if} \quad t_{\text{res}} > t_p \end{cases} , \tag{5.6}$$

where the peak $t_p = t_p(\rho_i)$ and the left and right widths $\sigma_L = \sigma_L(\rho_i)$ and $\sigma_R = \sigma_R(\rho_i)$ are functions of the distance of the hypothetical track to the Optical Module. The advantage of this simplified likelihood is that it can be maximized much faster than the proper likelihood function introduced in section 5.3.

As the last step, the quality of the track directions reconstructed for each cluster is evaluated based on topological parameters. The topological parameters include the number of hits which come earlier or later than expected, the ratio of hits inside and outside of a cylinder with 50 m radius around the track or the distribution of the hits along the track. A quality parameter Q is calculated by feeding this information into a neural net trained on Monte Carlo simulation to separate high and low quality event reconstructions. The reconstructed tracks from all clusters are then ordered by descending Q and up to three tracks featuring the highest Q values[4] are selected.

Taking into account only the highest quality track, an angular resolution of 4.4° is reached with this fit. 98.9% of down-going cosmic ray induced muon tracks are reconstructed as down-going particles.

5.3 Likelihood based reconstruction of the event direction

The likelihood $\mathcal{L}$ for a certain track hypothesis $\vec{\alpha} = (x, y, z, \theta, \phi)$ is defined as the product of the probability density functions (p.d.f.) to find an experimental observation x_i (i.e. in the case of AMANDA-II the hit arrival time or amplitude), if the hypothesis $\vec{\alpha}$ was true:

$$\mathcal{L} = \prod_i p(x_i|\vec{\alpha}) \; . \tag{5.7}$$

---

[4] More precisely, the three tracks with the highest Q values which are separated by more then 15° from each other.

The hypothesis $\vec{\alpha}$ can then be varied in its parameter space until the track showing the maximum likelihood is found. This trajectory is taken as the best guess for the true particle direction.

Technically in AMANDA-II the parameter space is evaluated using the simplex minimization algorithm [PTVF97][5]. The main numerical problem in finding minima of functions in a multi-dimensional parameter space is that all common algorithms tend to converge towards local minima. The simplex algorithm converges slower than other minimizers which makes it relatively robust. To further avoid wrong results from local minima the algorithm is re-started n times with random track hypotheses to evaluate larger regions of the parameter space. It is then called a "n-fold iterative likelihood fit".

5.3.1 Iterative likelihood fit

The iterative likelihood reconstruction uses an approximate p.d.f. $p(t_{\text{res}}, \rho)$ developed in [Pan96] to describe the expected residual time distribution as a function of the distance ρ between the track and the module. It is given by:

$$p(t_{\text{res}}, \rho) = N_0(\rho) \frac{\tau^{-\rho/\lambda_s} \, t_{\text{res}}^{\rho/\lambda_s - 1}}{\Gamma(\rho/\lambda_s)} \exp\left(-(1/\tau + c/\lambda_a) t_{\text{res}} + \rho/\lambda_a\right) \; , \tag{5.8}$$

where N_0 is a ρ dependent normalization constant, while λ_s, λ_a and τ are ice properties related parameters [A$^+$04c]. The above likelihood does not account for the combined time jitter σ_t from calibration uncertainties and PMT response. This can be achieved by convolution of the (Gaussian) jitter distribution with the likelihood function:

$$p'(t_{\text{res}}, \rho) = \int_{-\infty}^{\infty} \frac{1}{\sqrt{2\pi}\sigma_t} \exp\left(\frac{-(t_{\text{res}} - t')^2}{2\sigma_t^2}\right) \, p(t', \rho) \, dt' \; . \tag{5.9}$$

This convolution can be solved numerically [Neu03] or analytically [JR03], but the solution is computationally demanding. Therefore in standard AMANDA-II analysis another approximation is applied [A$^+$04c]. The p.d.f. $p''(t_{\text{res}}, \rho)$ is defined in a second approximation step as a function assembled from:

- a Gaussian distribution $p''(t_{\text{res}}, \rho) \propto \exp(-t_{\text{res}}^2/2\sigma_t^2)$ for $t_{\text{res}} < 0$;
- the likelihood function defined above $p''(t_{\text{res}}, \rho) = p(t_{\text{res}}, \rho)$ for $t_{\text{res}} > \sqrt{2\pi}\sigma_t$;
- a third order polynomial providing a continuous and differentiable interpolation between $t_{\text{res}} = 0$ and $t_{\text{res}} = \sqrt{2\pi}\sigma_t$.

To incorporate the anisotropic angular efficiency of the Optical Module into the likelihood, a correction factor to the distance ρ is introduced, the effective distance ρ_{eff}, which is derived from the real perpendicular distance ρ as:

$$\rho_{\text{eff}} = a_3 \rho + a_0 + a_1 \cos\eta + a_2 (\cos\eta)^2 \; . \tag{5.10}$$

The angle η is the angle between the Photomultiplier axis and the arrival direction of un-scattered Čerenkov light. The constants $a_0, \ldots, a_3$ and the parameters λ_s, λ_a and τ are fitted from Monte Carlo simulation of cosmic ray muon and neutrino induced events.

---

[5] Finding the maximum likelihood is equivalent to finding the minimum of $-\mathcal{L}$.

The minimizer then tries to find the track hypothesis minimizing $-\mathcal{L}$ constructed from $p''(t_{\mathrm{res}}, \rho)$. For numerical reasons the actual minimization is performed on the logarithm of the likelihood, i.e. the simplex algorithm tries to find:

$$\min \left(- \sum_{i}^{\text{all hits}} \log p''(t_{\mathrm{res}}^{(i)}, \rho_i) \right) . \tag{5.11}$$

The sum is taken over all hits passing the hit cleaning steps described earlier.

When a minimum is found, the procedure is restarted 32 times with different random track directions to find a possible better minimum. The track with the highest likelihood is taken as the final reconstructed direction of the muon. The achieved angular resolution of this fit is 1.5° – 2.5° for neutrino induced muons, dependent on declination.

5.3.2 Bayesian fit

The Bayesian fit [Hil01, DH02] is a likelihood algorithm designed to test the hypothesis that the muon trajectory is down-going, i.e. caused by cosmic ray induced muons. A technique motivated by Bayesian statistics is applied: the likelihood is weighted by a prior probability representing an a-priori knowledge of the origin of the particle. The probability $P(\vec{\mu}|\mathcal{H})$ that a muon track $\vec{\mu}$ is responsible for a hit pattern $\mathcal{H}$ can by application of Bayes theorem be expressed as

$$P(\vec{\mu}|\mathcal{H}) = P(\mathcal{H}|\vec{\mu}) \frac{P(\vec{\mu})}{P(\mathcal{H})} , \tag{5.12}$$

where $P(\mathcal{H}|\vec{\mu})$ is the probability to find a hit pattern $\mathcal{H}$ under the assumption that the muon track is $\vec{\mu}$. $P(\mathcal{H}|\vec{\mu})$ is just the likelihood presented in the previous section. The probabilities $P(\vec{\mu})$, $P(\mathcal{H})$ are the priors representing the a-priori knowledge of the probabilities to have a certain track $\vec{\mu}$ or hit pattern $\mathcal{H}$. In case the prior distributions are chosen uniformly the probability $P(\vec{\mu}|\mathcal{H})$ is up to a normalization constant identical to the likelihood $\mathcal{L}$.

A polynomial fit $P(\theta)$ to the declination dependent distribution of the cosmic ray background at the depth of the AMANDA-II detector is used as the prior $P(\vec{\mu})$ to force the reconstructed direction to point down-ward in the Bayesian reconstruction. The likelihood function to be maximized becomes then:

$$\mathcal{L}_{\mathrm{Bayes}} = P(\theta)\, \mathcal{L} . \tag{5.13}$$

A comparison of the logarithm of the likelihood ratios, $\log \mathcal{L}_{\mathrm{Fit}} - \log \mathcal{L}_{\mathrm{Bayes}}$, between the standard fit and the Bayesian fit can be used to separate misreconstructed cosmic ray induced muons from true up-going neutrino induced tracks.

5.4 Reconstruction of topological event parameters

Topological properties of events can be used to further distinguish between background and neutrino events. Misreconstruction for example is likely if the particle trajectories lie outside the bulk of the detector. Two topological parameters are presented here which are used for the selection of neutrino events in this analysis, the Smoothness and the Event Resolution.

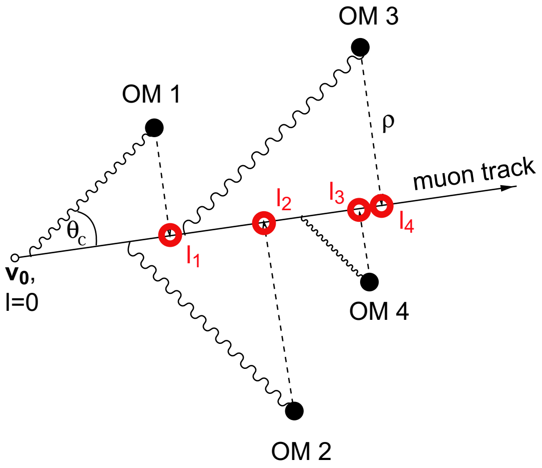

Figure 5.4: *Illustration of the projection of the recorded hits on the reconstructed track.*

5.4.1 Smoothness

The Smoothness is a parameter describing the cumulative distribution of hits along a muon track. Each hit within a radius of 50 m from the reconstructed track and with a low residual time (between -25 ns and 75 ns - the so called “direct hits”) is projected to a position l_i on the reconstructed muon track $\vec{\mu}$ (see figure 5.4). The integral number of hits from the origin of the track to the position l is then given by:

$$N(l) = \sum_{i}^{\text{direct hits}} \Theta(l - l_i) \; , \tag{5.14}$$

where $\Theta(x)$ is the Heaviside unit step function. The number of recorded hits is compared to the number of expected hits at position l. For each Optical Module inside the 50 m cylinder, the probability $P_{\text{hit}}(\rho_j)$ that the module j records a direct hit is calculated according to [A$^+$04c] for a minimally ionizing muon. This probability is summed up for the optical module’s projected positions l_j in analogy to (5.14) to get the integral number of hits expected between track start and position l:

$$N_{\text{exp}}(l) = \sum_{j}^{\text{OMs}} P_{\text{hit}}(\rho_j) \, \Theta(l - l_j) \; . \tag{5.15}$$

The Smoothness parameter S_{mooth} describes the normalized maximum deviation of $N(l)$ from $N_{\text{exp}}(l)$:

$$S_{\text{mooth}} = \frac{\text{sgn}(N(l_{\max}) - N_{\text{exp}}(l_{\max}))}{N(\infty)} \quad \max_{l} \; |N(l) - N_{\text{exp}}(l)| \; , \tag{5.16}$$

where $\text{sgn}(x)$ stands for the sign function. Therefore a high absolute value of the Smoothness (i.e. close to 1) states that either hits are missing at optical modules were hits would be expected if the track hypothesis was correct or that hits are found in modules were none would be expected, thus indicating a possible misreconstruction. The sign of the smoothness parameter distinguishes between the two cases.

5.4.2 Event Resolution

The Event Resolution is a particularly useful parameter for a point source analysis. Events which exhibit a large error in the reconstructed direction (i.e. a large separation angle $\Delta\Psi$ between true and reconstructed direction) cannot be ascribed to a neutrino source. An indicator for the individual uncertainty of the reconstructed direction is the shape and size of the (negative) likelihood valley. A method has been developed to determine these parameters in [Neu06]:

The likelihood $\mathcal{L}$ is evaluated for muon track directions (θ,ϕ) around the maximum returned by the likelihood reconstruction resulting in a set of values $\mathcal{L}_i(\theta_i, \phi_i)$. A least square fit is performed for $(a_0, b_0, b_1, c_{11}, \dots, c_{22})$ to determine the shape of a paraboloid:

$$f(\theta, \phi) = a_0 + (b_0, b_1)^T(\theta, \phi) + (\theta, \phi)^T \begin{pmatrix} c_{11} & c_{12} \\ c_{21} & c_{22} \end{pmatrix} (\theta, \phi) \ , \tag{5.17}$$

which minimizes $\sum_i (f(\theta_i, \phi_i) - \log \mathcal{L}_i(\theta_i, \phi_i))^2$. For a paraboloid curves of constant value form ellipses. The ellipse where

$$f(\theta, \phi) = \frac{1}{2} f_{\max}(\theta_m, \phi_m) \ , \tag{5.18}$$

is taken as the event specific uncertainty in the direction reconstruction, corresponding to the approximate region where the logarithm of the likelihood is larger than half of its maximum value. We define an one-dimensional resolution parameter by taking the square root of the area of the error ellipse with the radius (σ_1, σ_2):

$$R_{\mathrm{esol}} = \sqrt{\sigma_1 \sigma_2} \ , \tag{5.19}$$

and use this parameter in the event selection in chapter 6 to choose well reconstructed muon tracks.

5.4.3 Flariness

Sometimes events are recorded independently of real particles crossing the detector. Correlated electronics noise due to electromagnetic induction can produce enough hits to fulfill the trigger condition (see section 3.2.4). Such events are called “flare events” and happen frequently during times of bad, stormy weather at South Pole. Therefore one excludes these periods from data analysis based on the observation of a correlated increase in TDC count rates in the detector monitoring. However, if the fraction of flare events in the data sample is very small the increase in the correlated count rate is invisible.

Considerable effort has therefore been put in [Poh04] to develop an event based tagging of these phenomena. Eight variables called “flare indicators” have been defined there to provide this tagging. The flare indicators are normalized that their value corresponds to the logarithm of a probability. It is the probability to find such a value of the underlying indicator from a high energy particle induced event. For this analysis we use three of the indicators:

$F_{\mathbf{shortTOT}}$: the number of hits with a time-over-threshold shorter than expected from photo-electrons in channels connected by twisted pair cables.

$F_{\textbf{indB10}}$**:** the ratio of hits between strings 1-4 (coaxial cables, low electromagnetic noise pick-up) and strings 5-10 (twisted pair cables, high electromagnetic noise pick-up).

$F_{\textbf{indA2}}$**:** the ratio of hits between channels in strings 11-19 connected by optical fibers (no electromagnetic noise pick-up) and twisted pair cables (high electromagnetic noise pick-up).

Due to their normalization as logarithms of probabilities we can combine them by adding their values and define the Flariness as:

$$F_{\text{lariness}} = F_{\text{shortTOT}} + F_{\text{indB10}} + F_{\text{indA2}} \; . \tag{5.20}$$

Real particles should not show a Flariness much larger than 10. The probability for a muon track to reach such a value is 10^{-10}. Concerning that about 10 billion events were triggered in the period covered by this analysis, only one event with a Flariness of 10 is expected.

Chapter 6

Event Selection

6.1 Strategy

Only a fraction of $\mathcal{O}(10^{-6})$ of the $\approx 10^{10}$ triggered events in AMANDA-II (2000-2004) are muons induced by neutrinos. As shown in chapter 2.4.5, the unambiguous signature of a neutrino induced muon is its up-going direction. Due to the limitation of muons to penetrate dense matter like ice or rock for only a few kilometers, cosmic ray induced muons cannot reach the detector from below.

However, it was indicated in the last chapter, that the direction reconstruction can misinterpret down-going muons as up-going tracks. By selection of events based on the reconstructed direction alone, the background can only be reduced by a factor of $\mathcal{O}(10^3)$ leaving a data sample still dominated by misreconstructed cosmic ray induced muons. Therefore a second event selection step is necessary, based on event topologies and quality requirements. While more than 80% of the neutrino induced up-going muons survive the directional selection of the events, the separation of signal and background in the topological variables is less strong. To achieve an efficient suppression of the background, some fraction of the signal events has to be sacrificed.

The event selection presented here is optimized to reach the best flux upper limit setting potential, which is a function of the retained background and signal fractions. An important parameter influences the outcome of such an optimization: the assumed energy spectrum of the neutrinos from a cosmic source. Sets of selection cuts that provide a good limit setting potential for a hard spectrum might be far from optimal for a soft spectrum. To avoid the introduction of a bias towards a certain neutrino energy spectrum, the optimization was performed for a hard template spectrum ($d\Phi/dE \propto E^{-2}$) and a soft template spectrum ($d\Phi/dE \propto E^{-3}$). The term “template spectrum” is used here to express that the chosen spectra are representatives of spectra which produce the bulk of triggered events in the GeV and TeV energy regions respectively.

A selection was developed which simultaneously optimizes the upper limit setting potential for both spectra. To account for the declination dependent detector efficiencies, the event resolution and the background contamination, the optimization is performed individually for 20 declination ranges, between $\sin\delta = 0$ and $\sin\delta = 1$.

Spectra harder than $d\Phi/dE \propto E^{-2}$, even though they are proposed in certain models (for example [M$^+$03]) have not been considered in the cut optimization for several reasons. First, the energy distribution of triggered events is centered in the PeV region for such spectra. Absorption in the Earth plays a significant role, reducing dramatically the limit setting capability for high declinations. Moreover, due to the high energy of the corresponding signal neutrinos and the comparatively low energy of the cosmic ray induced muon and neutrino background a cut based on the energy of events would be more appropriate than a cut based on the direction. It would additionally permit to look at objects on the southern hemisphere close to the horizon. Therefore an optimized analysis for such hard spectra would be fundamentally different to the analysis developed here. Nevertheless we will present flux limits for sources with proposed hard spectra derived from our analysis in chapter 10.

6.2 Analysis periods

This analysis focuses on the data taken by AMANDA-II in the years between 2000 and 2004. Only the periods where a stable operation of the detector was proven were selected, especially all data collected during austral summer (early November to mid February) was rejected. This is the time where calibration and maintenance tasks on AMANDA-II are performed as well as maintenance of power systems and other equipment of the South Pole station. In this period, the detector setup is continuously changing and therefore it is impossible to reliably simulate its response. The exact periods excluded from the analysis are given in table 6.1.

Year	from day	to day
2000	1	47
2000/2001	309	44
2001/2002	293	43
2002/2003	323	43
2003/2004	315	43
2004	309	366

Table 6.1: *Periods in which collected data is excluded from this analysis due to AMANDA-II and South Pole station maintenance.*

Also in the austral winter AMANDA-II becomes occasionally instable. The main reasons are failure of electronic devices like high voltage generators or data acquisition components and electromagnetic noise induction during heavy winter storms. These periods are identified using the detector monitoring tools and rejected on a file-by-file basis (one file corresponds to approximately 10 minutes of data taking). Similar to the bad optical module selection, this task was performed for each year by different people following slightly different criteria. The common indicators for detector instability used were:

- problems reported during the detector monitoring by the shift crews in charge;
- increased number of dead or noisy Optical Modules compared to the average;
- abnormal passing rates in the first event filtering levels;
- correlated increase in the hit rates for groups of Optical Modules.

For this analysis short runs with less than 7 files were additionally rejected. A run is a continuous period of data taking lasting up to a maximum of 24 hours, if not stopped before. A manual termination of a run after a short while (less than 7 files correspond to less than one hour of data taking) indicates a problem with the detector. The total number of files rejected from 2000 to 2004 was 13254 corresponding to approximately 57 effective days of detector livetime. The remaining detector livetime for this analysis was 1001 effective days.

Technically, the selection described below was developed on the subset of data taken in the years 2000-2003 corresponding to only 807 effective days. As the data taken in 2004 became available, the already fixed selection and analysis strategies were applied to the new data and the results correspondingly updated.

6.3 Techniques

6.3.1 Background reduction by directional cuts

The first step to select neutrino induced events is to reject all events which are reconstructed with a declination angle $\delta_{\mathrm{DW}} < -20°$ by the Direct Walk first guess method (Level 1 selection), reducing the amount of background events by 97%. The main purpose of this step is to keep the amount of data low which has to be processed further, making the filtering of events more CPU time effective. The remaining events face two additional selection criteria: events which are reconstructed with a declination $\delta_{\mathrm{JAMS}} < -10°$ in the JAMS fit are removed from the sample (Level 2 selection) as well as events with a declination found in the likelihood fit of $\delta_{\mathrm{Llh}} < -10°$ (Level 3 selection).

Figure 6.1 shows the distributions of the reconstructed declinations for these three methods and indicates the selection cut. The distribution from experimental data is compared to the corresponding distributions from simulated up-going neutrinos (atmospheric neutrinos and neutrinos following an E^{-2} spectrum). The number of events reconstructed with a positive declination value still exceeds the number of expected neutrinos by several orders of magnitude and further selection steps are necessary. Also some up-going neutrino induced muons are wrongly reconstructed with $\delta < \delta_{\mathrm{cut}}$ and lost. Table 6.2 summarizes the passing rates for background dominated experimental data and simulations of up-going neutrinos of various spectra. The background is reduced to about 0.2%. The retained signal varies between 57% and 88% depending on the assumed neutrino spectrum.

Selection cut	exp. data	MC (atm-ν)	MC ($\gamma = -3$)	MC ($\gamma = -2$)	MC ($\gamma = -1$)
$\delta_{\mathrm{DW}} > -20°$	0.031	0.94	0.95	0.91	0.78
$\delta_{\mathrm{JAMS}} > -10°$	$5.9 \cdot 10^{-3}$	0.89	0.90	0.82	0.59
$\delta_{\mathrm{Llh}} > -10°$	$1.7 \cdot 10^{-3}$	0.87	0.88	0.80	0.57

Table 6.2: *Fraction of events passing the three consecutive directional selection cuts on the DirectWalk, JAMS and Likelihood reconstructions. Events that do not fulfill the condition in the first column are rejected. The fractions are tabulated for experimental data, simulated fluxes of atmospheric neutrinos and simulated fluxes of cosmic neutrinos with a power law spectrum* $d\Phi/dE \propto E^{-\gamma}$.

The lower passing rates for harder spectra result from the higher light yield of high energy events. High energy muons passing outside the detector still produce enough light to trigger the AMANDA-II array. However, due to the optical properties of the ice all photons experience multiple scattering and the photon arrival time cannot be used any more for a reliable direction reconstruction. Therefore such events could also not contribute to a search for point sources - where good direction resolution is essential - and their loss is unavoidable.

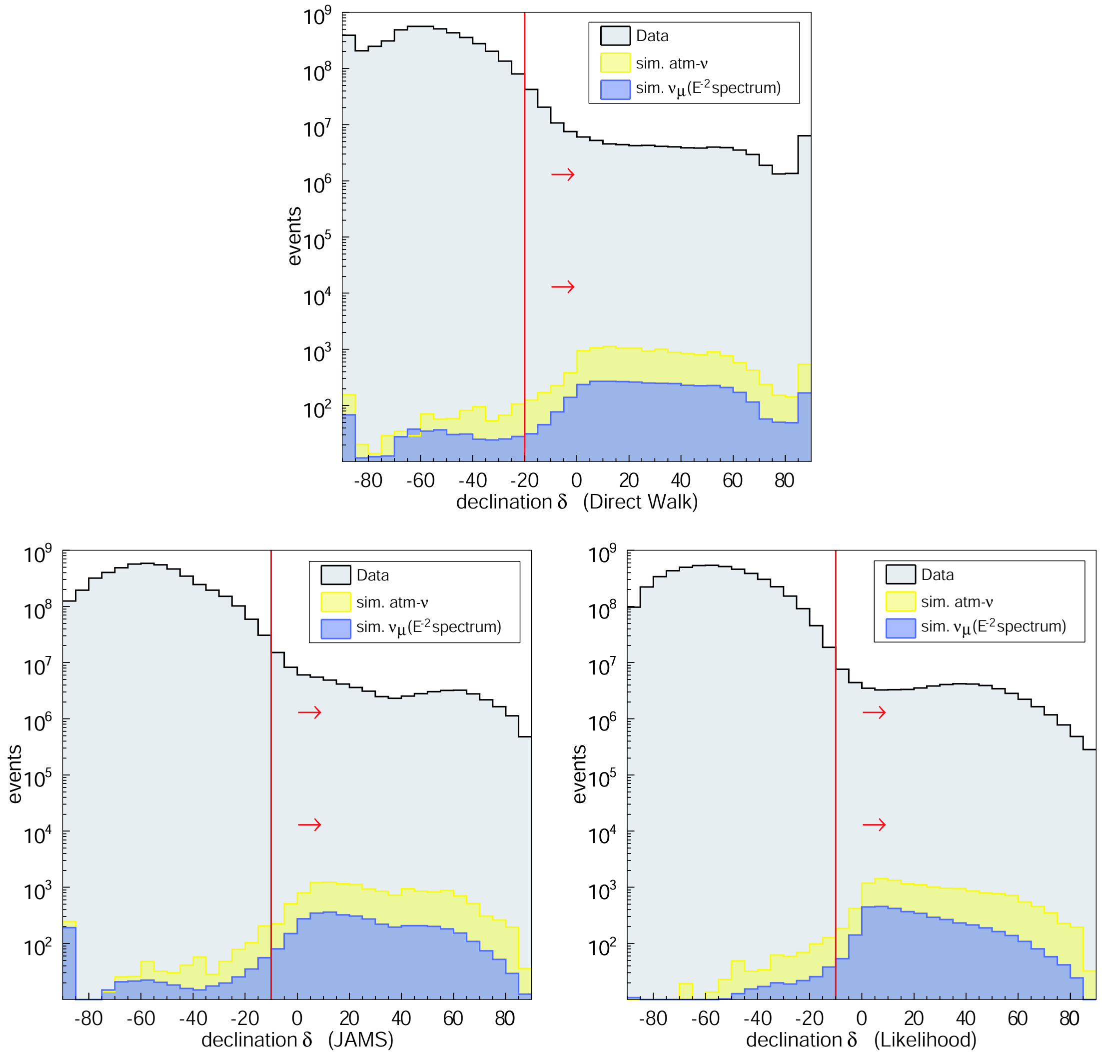

Figure 6.1: *Distribution of the reconstructed declination angles of experimental data and simulated up-going neutrinos for the two first guess fits (upper picture: Direct Walk, lower left picture: JAMS) and the likelihood reconstruction (lower right), at trigger level. The normalization of the signal flux with a spectrum proportional to* E^{-2} *is arbitrary. The red line and the red arrows mark the selection of events based on the reconstructed declination angles.*

6.3.2 Neutrino selection

The bulk of the remaining $\mathcal{O}(10^7)$ misreconstructed muon background events in the level 3 data sample are removed by imposing quality requirements on the reconstructed track. To find the optimal balance between rejecting down-going cosmic ray induced muons and retaining the signal from neutrino induced muons, the parameter space of the quality indicators introduced in section 5.4, is scanned. In the search for point sources (see section 7.1.1) also the size of the search bin influences this balance: only the fraction of events can contribute to a possible signal which are reconstructed with an angular mismatch less than the size of the search bin, while the background increases proportional to the covered solid angle of the bin. To account for that, we optimize the radius of the search bin together with the quality indicators.

For each combination $(\log \mathcal{L}_{\mathrm{Fit}} - \log \mathcal{L}_{\mathrm{Bayes}},\ S_{\mathrm{mooth}},\ R_{\mathrm{esol}},\ r_{\mathrm{bin}})$ we calculate the number of background events b within a sky bin of radius r_{bin} and the expected signal s from a

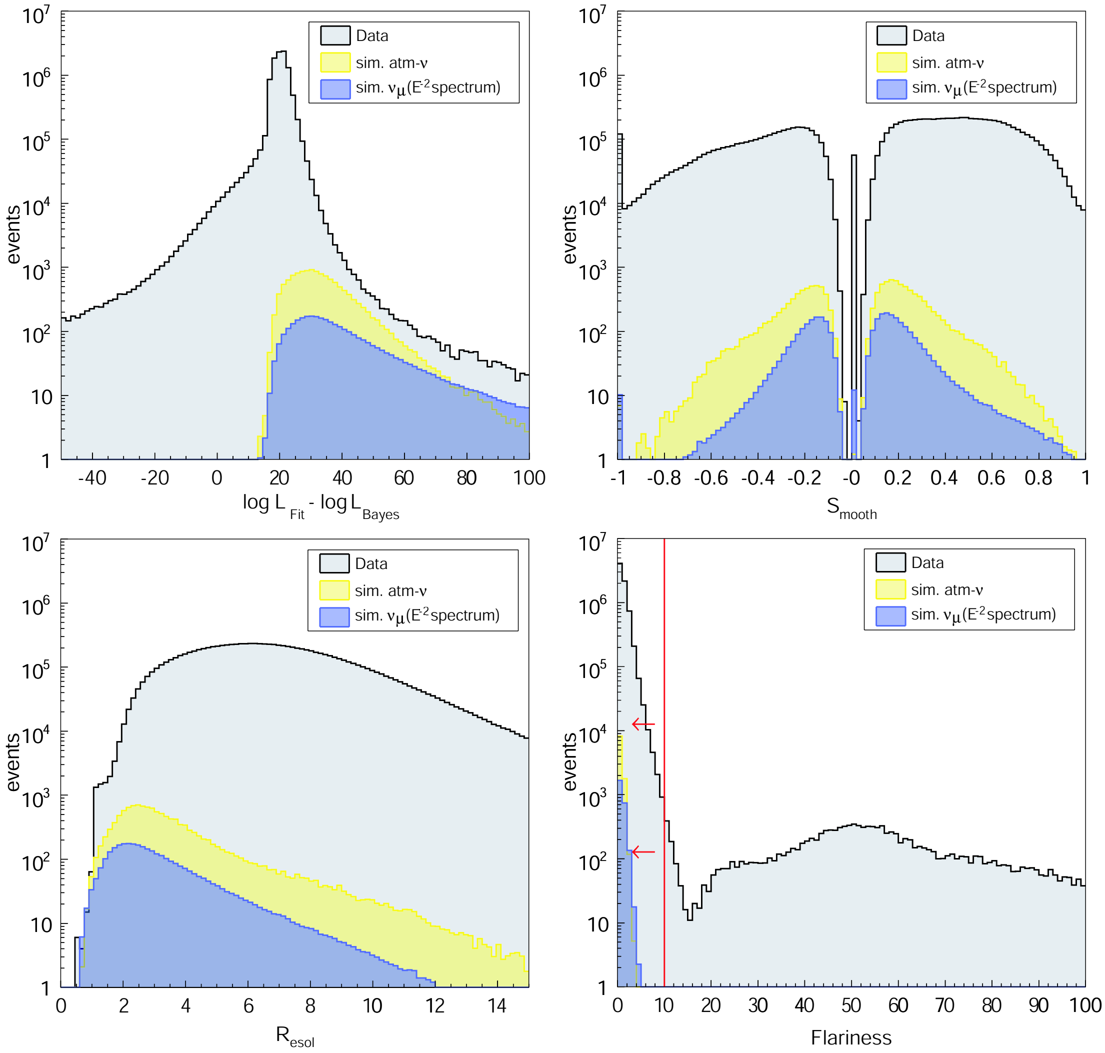

Figure 6.2: *Distributions of the topological reconstruction quality parameters for experimental data and simulated neutrino induced events after the initial directional selection. The normalization of the signal flux with a spectrum proportional to* E^{-2} *is arbitrary. The Likelihood ratio (upper left), Smoothness (upper right) and Resolution (lower left) are used to select upward-going neutrino induced muons. The selection cuts are optimized declination-wise (see text). Additionally a cut (marked by red line and arrows) is applied on the event Flariness (lower right).*

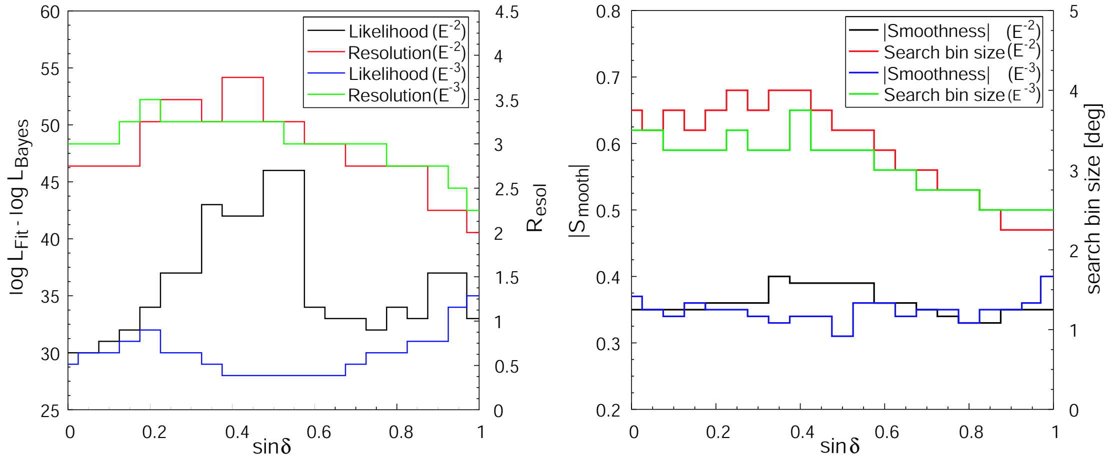

Figure 6.3: *Results from the declination-wise cut optimization for best limit setting capability. Likelihood ratio and Resolution are shown in the left picture, Smoothness and the search bin size are shown on the right side. As a first step, independent optimizations are performed for neutrino signal spectra proportional to* E^{-2} *and* E^{-3}.

hypothetical neutrino flux Φ_0. From (b, s) the average flux upper limit $\Phi^{\text{sens}}_{90\%}$ (see (2.35)) is derived. The parameter combination which provides the lowest average flux upper limit is searched. The procedure is applied to the events divided into 20 bins in $\sin\delta$ independently, to account for the changing properties of AMANDA-II events with declination. For the hypothetical neutrino flux both a spectrum with an energy dependence proportional to E^{-2} and proportional to E^{-3} are considered.

Figure 6.2 shows the distribution of the three track quality parameters considered in the optimization. Besides the optimized cuts, an additional requirement was imposed on the events: the Flariness of the event was demanded to be below 10. The distribution of the Flariness and the position of the selection cut is shown on the lower right side of figure 6.2. Since the cut position is far from any value expected for simulated neutrino induced signal events[1], the inclusion of this parameter into the cut optimization is not necessary. Even though not many non-particle events are removed due to high Flariness, the selection is extremely important since these events can mimic high quality upward going muon tracks peaked at a declination of $\delta \approx 70°$.

Figure 6.3 shows the optimal selection cut positions in the other three track quality parameters suggested by the optimization for the different declination bins and neutrino spectra proportional to E^{-2} and E^{-3}. One recognizes that the optimization procedure results in considerable fluctuations of the cut positions. A wide range of parameters produce similar upper limit setting capabilities. The position of the optimum is influenced by small statistical fluctuations. These fluctuations are unwanted since they imply rapidly changing signal and background levels between two adjacent declination bins. Therefore a manual smoothing of the selection cuts starting from the optimized cuts has been performed to reach simple, continuous cut values which provide a flux upper limit setting potential within a 10% margin around the one reached for the optimized cuts.

A common set of cut values fulfilling this condition for both neutrino spectra used in the optimization procedure could be found and is shown in figure 6.4. They are linear or constant functions in $\sin\delta$ and can be written as:

---

[1] The position of the selection cut is chosen very conservatively due to the fact that possible electronics noise is not simulated.

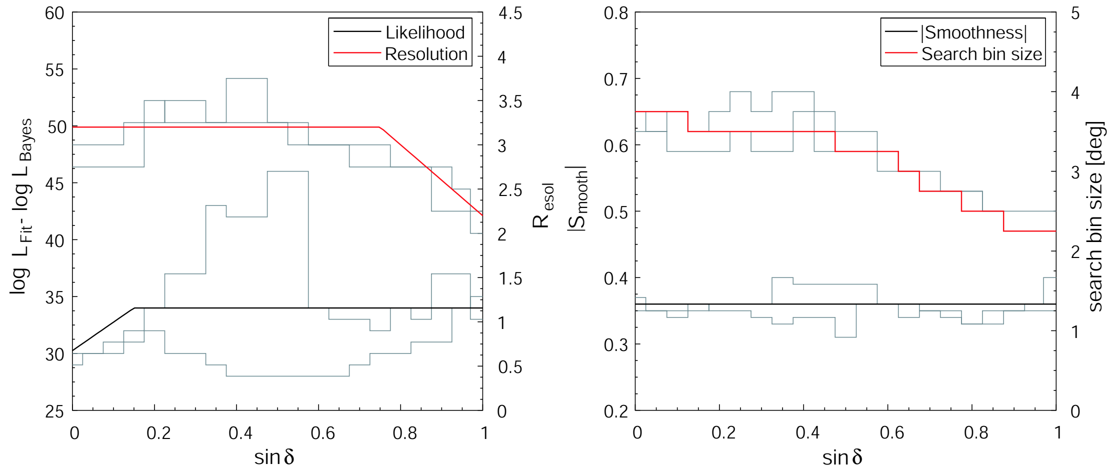

Figure 6.4: *Final parametrized cuts chosen to provide close to the optimal limit setting capability for signal spectra proportional to E^{-2} and E^{-3}. The thin grey lines indicate the results from the optimization. The Likelihood ratio and the Resolution are shown in the left picture, the Smoothness and the search bin size are shown on the right side.*

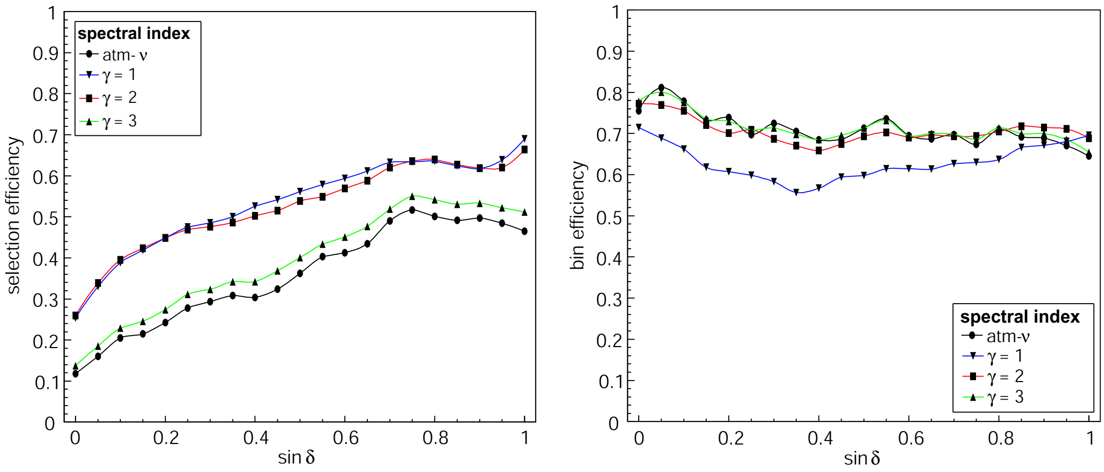

Figure 6.5: *Selection efficiency (left side) and bin efficiency (right side) achieved, applying the final cuts to different simulated neutrino spectra. The selection efficiency is the fraction of neutrino induced events passing the parametrized selection cuts. The bin efficiency is the percentage of events which are reconstructed with a directional error smaller than the optimized size of the search bin.*

$$\log L_{Fit} - \log L_{Bayes} > 34 + 25(\sin\delta - 0.15)\Theta(0.15 - \sin\delta) \tag{6.1}$$

$$|S_{\text{mooth}}| < 0.36 \tag{6.2}$$

$$R_{\text{esol}} < 3.2 - 4(\sin\delta - 0.75)\Theta(\sin\delta - 0.75)\ , \tag{6.3}$$

where $\Theta(x)$ is the Heaviside unit step function.

The selection efficiency for neutrino induced events (relative to the L3 selection) is shown on the left side of figure 6.5. It depends on the spectrum assumed for the signal, with a higher efficiency for harder spectra. On the right side of the same figure the bin efficiency is shown, i.e. the fraction of the events passing the selection cuts (6.1) - (6.3) that are reconstructed with a directional error smaller than the size of the search bin.

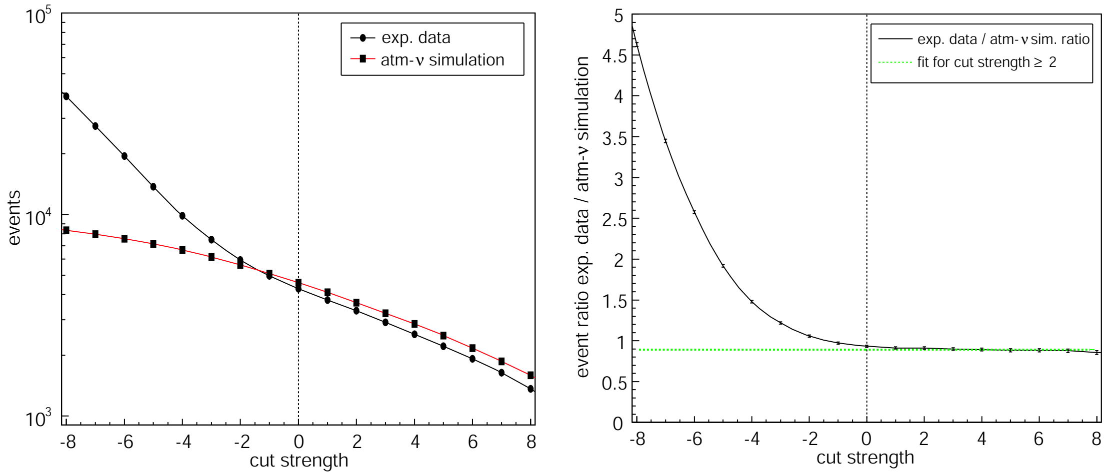

Figure 6.6: *Illustration of the method to estimate the contamination of the final data sample by mis-reconstructed cosmic ray induced muons. The event passing rate is evaluated for experimental data and simulated atmospheric neutrinos at modified cut strengths (left picture). For stronger cuts (indicated by positive numbers) the contamination becomes neglegible and the event ratio (right picture) between experimental data and Monte Carlo simulation constant (green dashed line). The muon contamination can be determined from the deviation of the event ratio to the asymptotic constant at a cut strength of* $k = 0$*, which corresponds to the position of the final cuts.*

The remaining background from cosmic ray induced muons in this sample can be estimated using a method illustrated in figure 6.6. The strength of the event selection (6.1)-(6.3) is varied by adding a positive or negative constant $k\ c_i$ to the right side of the inequalities:

$$\begin{aligned} \log L_{Fit} - \log L_{Bayes} &> 34 + 25(\sin\delta - 0.15)\Theta(0.15 - \sin\delta) + k\ c_0 \quad (6.4)\\ |S_{\text{mooth}}| &< 0.36 + k\ c_1 \quad (6.5)\\ R_{\text{esol}} &< 3.2 - 4(\sin\delta - 0.75)\Theta(\sin\delta - 0.75) + k\ c_2\ . \quad (6.6) \end{aligned}$$

The c_i are the individual scales for the variation of the cut parameter, while k is a common multiplicative factor which we call the “cut strength”. Then the number of experimentally observed events and simulated atmospheric neutrinos passing the new selection are counted and their ratio is plotted versus the cut strength k. For strong cuts it is assumed that the muon background vanishes and the ratio r becomes constant[2]. For weak cuts the sample becomes dominated by the cosmic ray induced muons and the ratio rises quickly. The remaining muon background at the actual cut position $k = 0$ can be determined from the difference of the ratio there ($r_0 = 0.93$) to its asymptotic value for strong cuts $r = 0.89$ indicated by the green line. From these numbers we conclude that the contamination from cosmic ray induced muons in this sample is less than 5%. We will call the data sample obtained by this selection in the following a pure atmospheric neutrino sample for simplicity.

If distributions of observables are compared between the final data sample and a simulation of the events generated by the flux of atmospheric neutrinos, good agreement is reached. A selection of such distributions is presented in figure 6.7.

---

[2] Due to the large theoretical [GH02] and experimental uncertainties (both approximately 25%) in the simulation of the total atmospheric neutrino flux, the ratio may deviate from 1 even for a pure atmospheric neutrino sample.

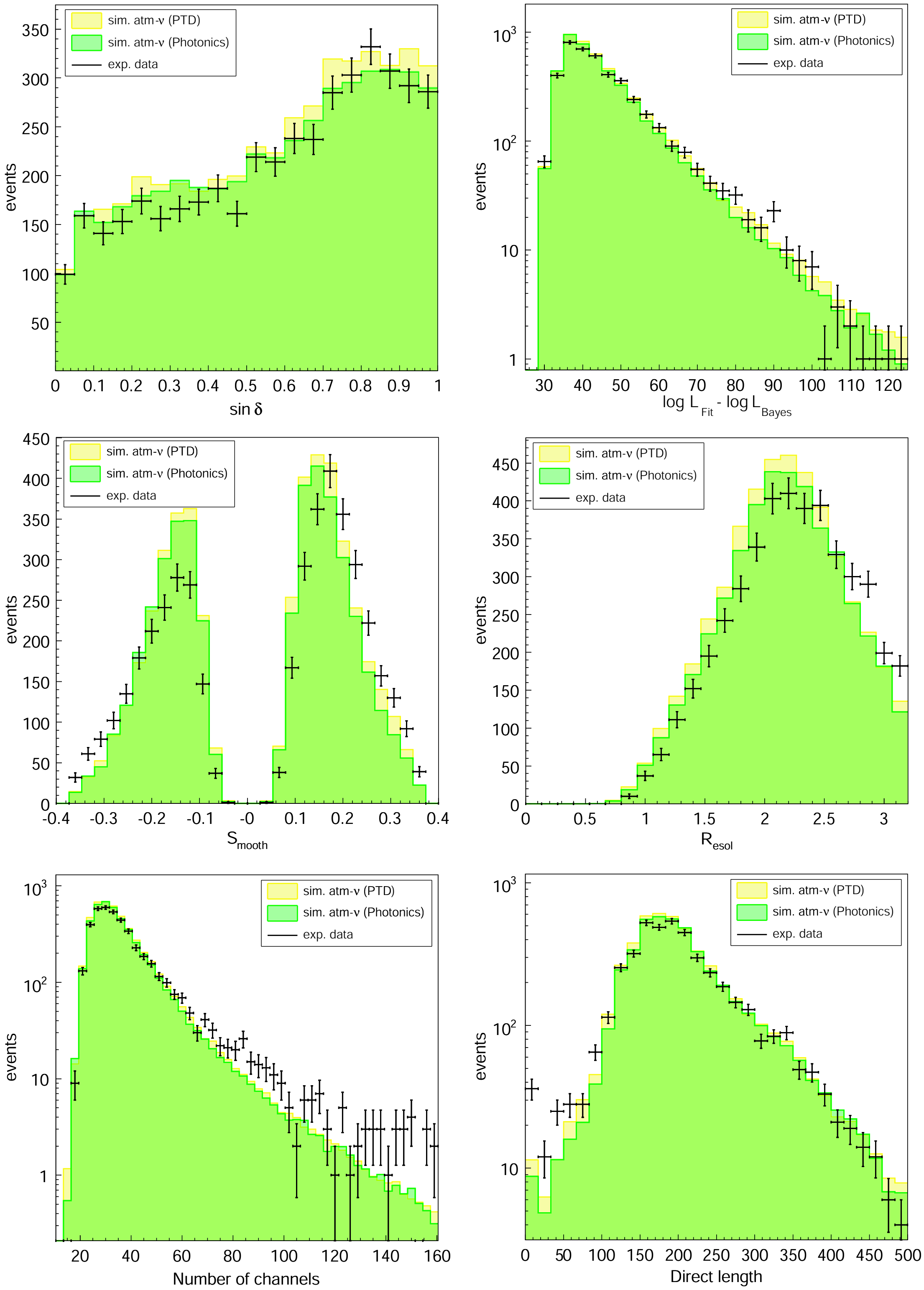

Figure 6.7: *Comparison of distributions of observables between events in the final sample and simulations of atmospheric neutrinos (with PHOTONICS and PTD photon propagation). From upper left to lower right, the reconstructed declination, the Likelihood difference, the Smoothness, the Event Resolution, the number of hit channels and the track length are presented. The track length is defined as the distance between the projections of the first and the last direct hit onto the track.*

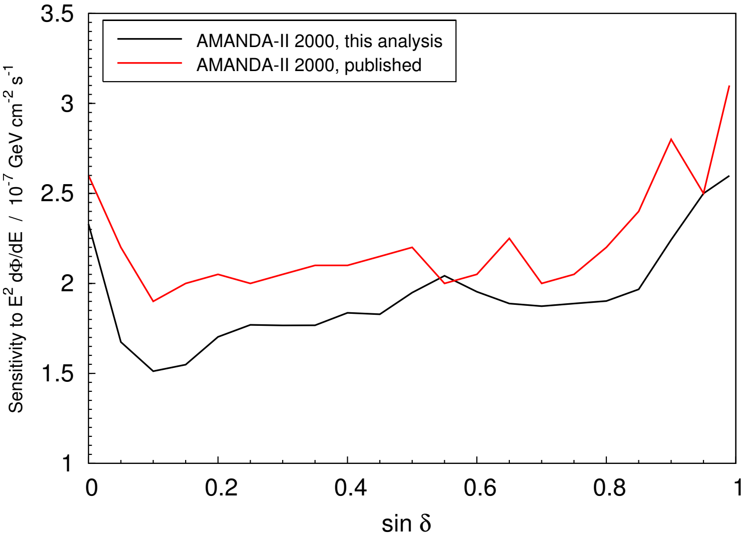

Figure 6.8: *Comparison of the upper limit setting capability of this analysis to the AMANDA-II point source analysis published in [A⁺04d]. The comparison is based on the subset of data taken in the year 2000 (the period analyzed in [A⁺04d]) to compare the effects of the event selection unbiased by the much larger live-time of this analysis. An average improvement of 15% in upper limit setting capability is reached.*

A total of 4282 events with positive reconstructed declinations have been selected compared to 4591^{+321}_{-963} simulated atmospheric neutrinos using the flux parametrization of Lipari [LS91]. The quoted systematic uncertainty is discussed in section 9.1 and includes only the experimental systematic error.

In former AMANDA-II point source analysis advanced statistical classification algorithms have been used like a feed-forward neural net [Hau04] or a support vector machine [Con03] to separate signal from background instead of one-dimensional cut values. A livetime independent comparison of the performance of this analysis with the point source analysis [A$^+$04d] by their upper limit setting capability is shown in figure 6.8. An average improvement of ≈ 15% is visible. Initial tests with a neural net did not result in significant further improvement for this analysis. Therefore no statistical classification algorithm has been applied.

6.4 Performance

6.4.1 Angular resolution

The angular resolution of AMANDA-II can be estimated from simulation of neutrino induced events. The distribution of the difference between reconstructed and true particle directions - the point spread function - is shown in figure 6.9 in its two-dimensional representation ($\Delta\theta$,$\Delta\phi$) as well as an one-dimensional distribution of the separation angle $\Delta\Psi$. It is clearly visible that the point spread function considerably narrows for tracks arriving at large declination angles. This effect results from the cylindrical geometry of the detector being more than twice as high as wide.

As an AMANDA-II convention we define the resolution as the $\Delta\Psi$ value which includes at least 50% of the events, indicated by the red line in the figure. Figure 6.10 shows how the angular resolution depends on the energy and declination angle of the muons. The resolution significantly deteriorates for high particle energies, probably due to detector

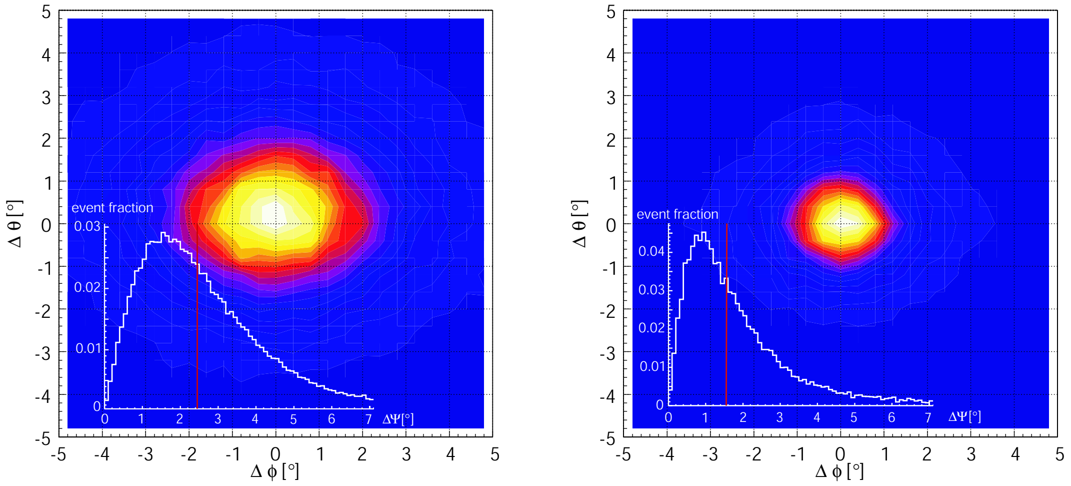

Figure 6.9: *Point spread function of the AMANDA-II detector at declinations of* $\delta = 10°$ *(left) and* $\delta = 80°$ *(right) derived from simulation. The angular resolution is defined as the minimum angle between true and reconstructed event direction* $\Delta\Psi_0$*, such that* $\Delta\Psi < \Delta\Psi_0$ *for at least 50% of the events in the final sample (marked by the red line).*

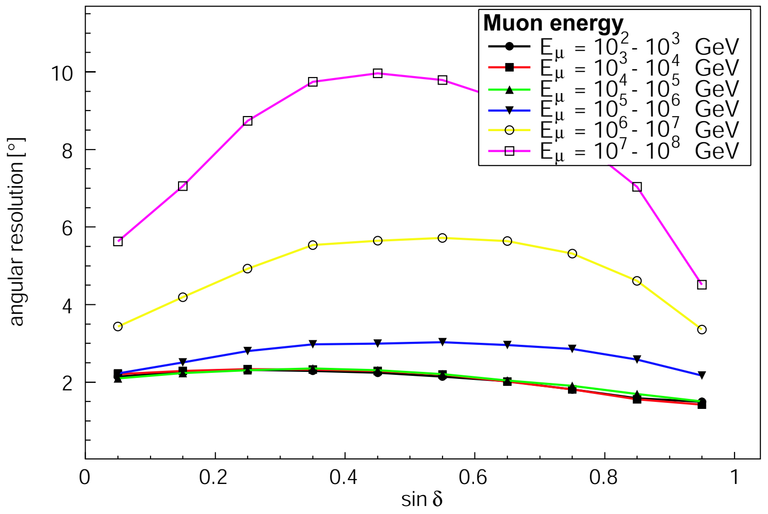

Figure 6.10: *Resolution of the AMANDA-II detector as function of declination for different muon energies (at the point of closest approach to the detector center).*

saturation effects. For a neutrino spectrum proportional to E^{-2} the resolution is found to range between 2.5° for horizontal tracks and 1.5° for vertical tracks.

A simulation independent test of the angular resolution was performed within the collaboration by evaluating the directional reconstruction of events registered in coincidence with the SPASE air shower array [A$^+$04b]. The analysis delivered compatible results.

6.4.2 Energy distribution

The energy distribution of events for different signal spectra is important to define boundaries for the validity range of the flux limits derived in the point source analysis. A flux limit can be set only in an energy range where events would be expected in the detector. We define this energy range as the central interval containing 90% of the expected events for a certain signal spectrum.

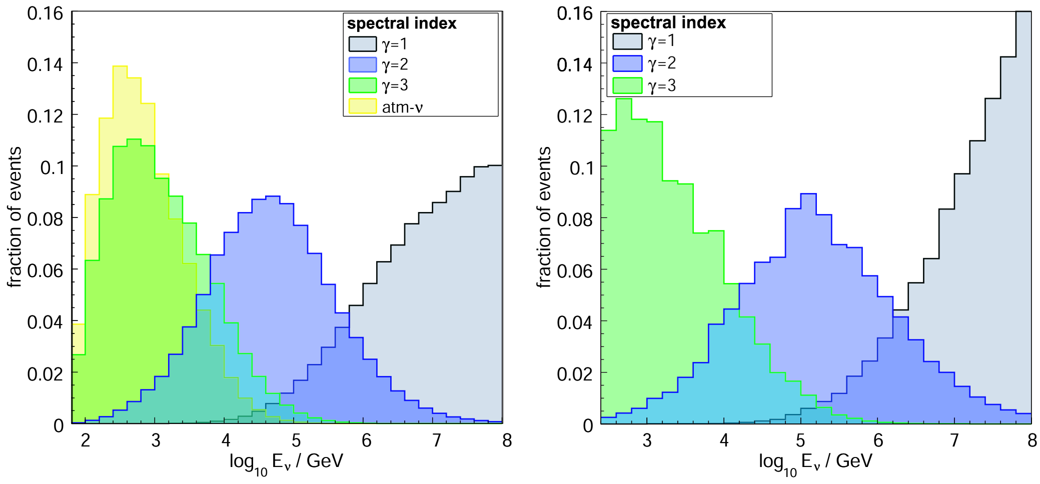

Figure 6.11: *Neutrino energy distribution of ν_μ (left) and ν_τ (right) induced events in the final sample predicted by the simulation for cosmic and atmospheric neutrino fluxes.*

Figure 6.11 shows the normalized neutrino energy distribution of the simulated events passing the selection criteria for a few signal spectra. The peak of the distribution is in the GeV region for a neutrino spectrum proportional to E^{-3}, while it resides several orders of magnitude higher for a spectrum proportional to E^{-1}. The intervals containing 90% of the events are summarized in table 6.3.

Spectrum	E_{min} [GeV]	E_{max} [GeV]
$E^{-1}(E < 10^8$ GeV)	$1.6 \cdot 10^5$	$7.9 \cdot 10^7$
E^{-2}	$1.6 \cdot 10^3$	$1.6 \cdot 10^6$
E^{-3}	130	$3.2 \cdot 10^4$
atm-ν	100	$7.9 \cdot 10^3$

Table 6.3: *Neutrino energy intervals $[E_{min}, E_{max}]$ containing 90% of the events in the final selection for different signal spectra.*

6.4.3 Sensitivity

The reached average flux upper limit setting capability is the primary benchmark of the selection (see section 2.5.3). Figure 6.12 shows the sensitivity as a function of declination assuming a neutrino spectrum proportional to E^{-2} for a ν_μ, a ν_τ and a combined $\nu_\mu + \nu_\tau$ signal. The sensitivity to ν_τ is nearly an order of magnitude worse, since only 17.7% of the tau decays produce muons in the final state and additionally the average fraction of energy transfered from the tau neutrino to the muon is lower. The tau contribution however is important for the combined $\nu_\mu + \nu_\tau$ limit which can constrain astrophysical fluxes stronger than the muon neutrino limit in current scenarios of astrophysical fluxes assuming a flavor ratio of ν_μ:ν_τ=1:1 (see section 2.4.1). A comparison of the sensitivity to point sources of muon neutrinos to the corresponding published value from the AMANDA-II 2000 point source analysis [A+04d] results in an average improvement of a factor of 3.8 from this analysis.

Figure 6.13 shows the corresponding sensitivities for differential neutrino fluxes with spectra proportional to E^{-3} and E^{-1}. For the soft spectrum the sensitivity improves for high

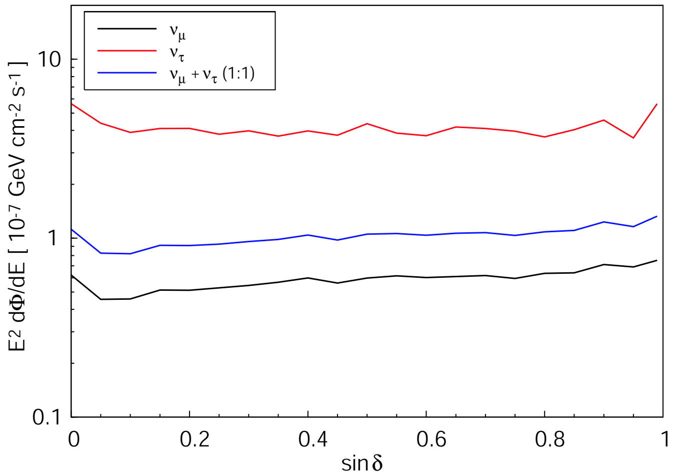

Figure 6.12: *Sensitivity to ν_μ, ν_τ and $\nu_\mu + \nu_\tau$ fluxes achieved in this work for a neutrino spectrum proportional to E^{-2}. The average upper limit is shown as a limit to the normalization constant Φ_0 of the differential flux $d\Phi/dE = \Phi_0 E^{-2}$.*

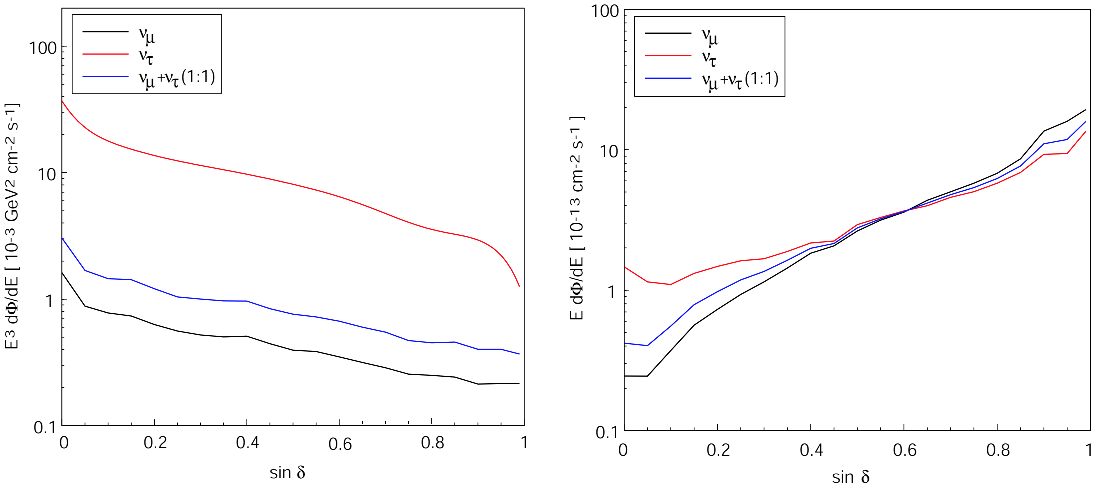

Figure 6.13: *Sensitivity to ν_μ, ν_τ and $\nu_\mu + \nu_\tau$ fluxes for neutrino spectra proportional to E^{-3} (left) and E^{-1} (right) achieved in this work.*

declinations, where both trigger and selection efficiency are better than at low declinations. For the hard spectrum the opposite can be seen. At high declinations a considerable fraction of the high energy neutrino events are absorbed in the Earth before reaching the detector. Indeed, the tau neutrino signal dominates the sensitivity in this declination region. Due to ν_τ-regeneration (see section 2.4.3), they are capable of traversing the Earth even at the very high energies.

6.4.4 Effective area

The influence of ν_τ-regeneration is also reflected in the effective areas (see section 2.5.1) for muon and tau neutrinos reached by this analysis. Figure 6.15 shows them as functions of declination and energy. The effective areas rise quickly with energy due to the increasing neutrino-nucleon scattering cross section and muon range until Earth absorption effects become dominant. While the muon effective area is dramatically reduced for high declinations and high energies, the Earth absorption plays a weaker role in the tau channel. A summary of averaged muon neutrino effective areas $\langle A^{\nu}_{eff} \rangle$ for different declinations and signal spectrum assumptions is presented in table 6.4.

	Effective area in cm^2 for $d\Phi/dE \propto$			
Declination δ	E^{-1}	E^{-2}	E^{-3}	$E^{-3.7}$
5°	$6.4 \cdot 10^4$	15	$3.2 \cdot 10^{-2}$	$3.1 \cdot 10^{-3}$
25°	$1.3 \cdot 10^4$	12	$5.5 \cdot 10^{-2}$	$5.9 \cdot 10^{-3}$
50°	$4.4 \cdot 10^3$	12	$1.0 \cdot 10^{-1}$	$1.5 \cdot 10^{-2}$
75°	$1.3 \cdot 10^3$	8.7	$1.1 \cdot 10^{-1}$	$1.6 \cdot 10^{-2}$

Table 6.4: *Averaged muon neutrino effective area for various signal spectra.*

Besides the neutrino effective area, the muon effective area is an interesting parameter to characterize the performance of detector and analysis. As was pointed out in section 2.5.1 it shows the effective detector size (i.e. accounting for detection efficiency) disentangled from neutrino-nucleon cross sections and muon ranges. Figure 6.14 displays the muon effective area as a function of declination and the muon energy at its point of closest approach to the center of the detector. A peak muon effective area of about $4 \cdot 10^4$ m^2 is reached.

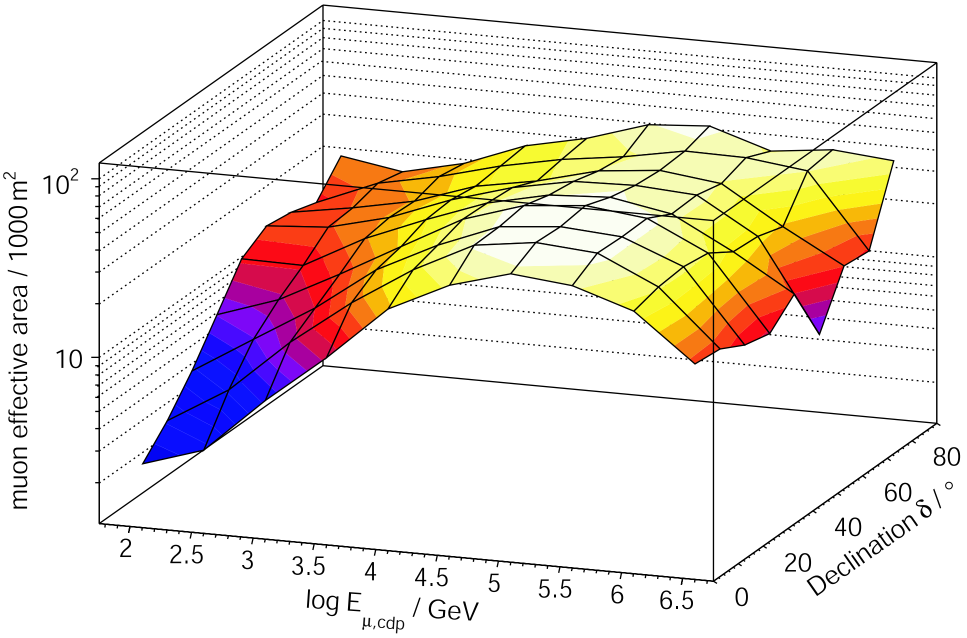

Figure 6.14: *Muon effective area for the presented event selection as a function of muon energy (at the point of closest approach to the detector center) and declination. In the calculation of the effective area we account for the bin efficiency.*

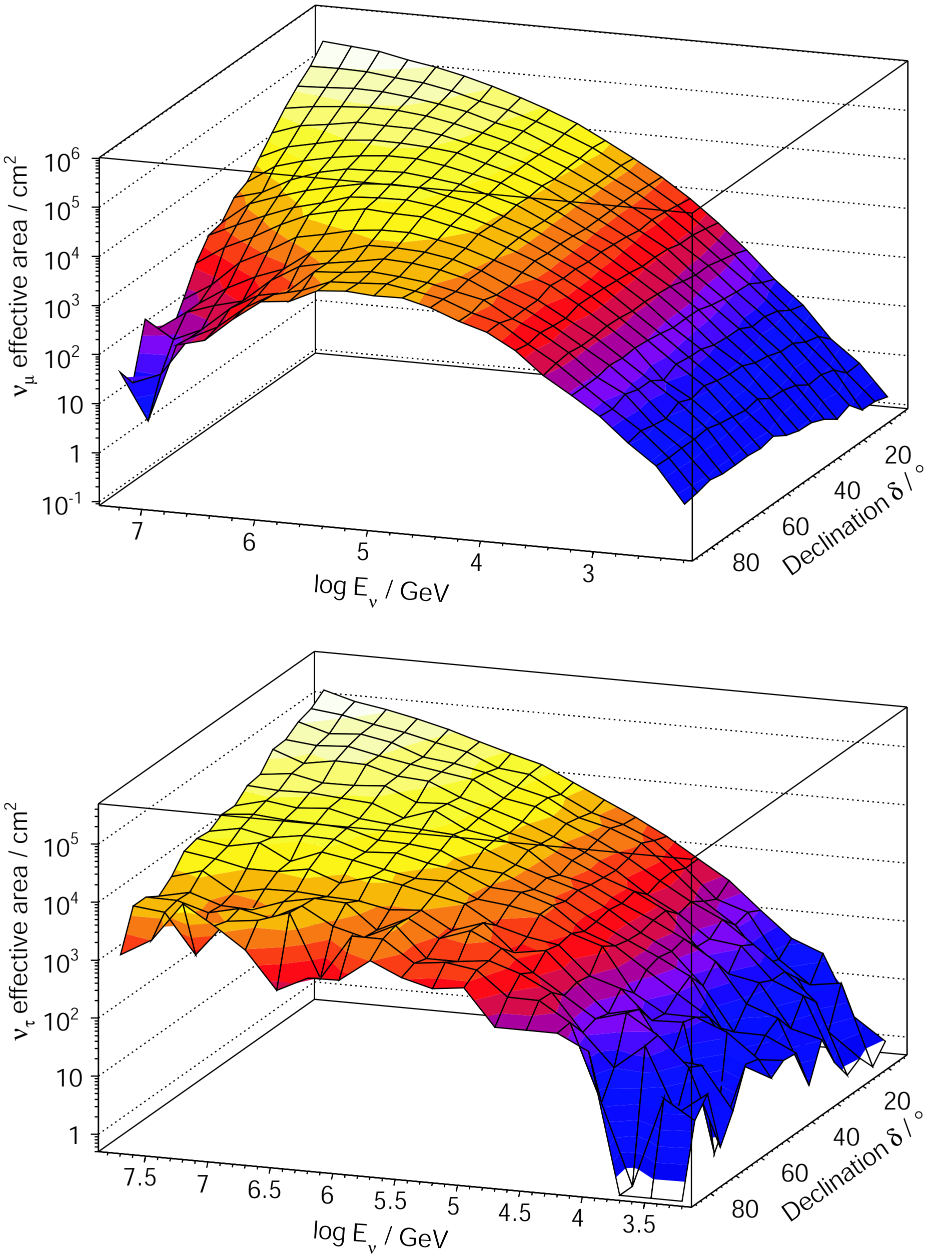

Figure 6.15: *Muon neutrino (upper picture) and tau neutrino (lower picture) effective areas for the presented event selection as functions of energy and declination. In a point source search, only the fraction of events inside the search bin (see section 7.1.1) contributes to the signal, therefore we account for the bin efficiency of 70%-80% (see figure 6.5) in the calculation of the effective area.*

Chapter 7

Search strategies for the discovery of neutrino point sources

7.1 Strategies based on spatial information

A signal from a neutrino point source manifests itself as a local excess of events on the uniform background b of atmospheric neutrinos and misreconstructed muons. In the case that such an excess is not present, a limit on the maximum neutrino flux can be set which is compatible with this observation.

To get the optimal upper limit on the average neutrino flux from a candidate source, the best strategy is to integrate as much observation time as possible. The expected number of signal events s is proportional to the average source flux Φ and the observation time t. The average event upper limit $\langle \mu_{CL} \rangle$, i.e. the number of signal events which can be excluded at a certain confidence level (see section 2.5.3), however, increases signficantly slower than linear with the number of background events b [FC98]. Therefore, assuming a constant background rate, the flux upper limit $\Phi_{\mathrm{Limit}} \propto \langle \mu_{CL} \rangle / s$ improves the more observation time is added.

In several cases integration of all available observation time is also the best way to search for an excess of events: if a candidate source is expected to emit a constant or nearly constant flux of neutrinos, or if there is no model for the time pattern of neutrino emission at all. In those cases one assumes that the source flux is constant and therefore the number of expected signal neutrinos proportional to the exposure time t. In the Gaussian limit, the significance of s observed signal events on top of an expected background of b events is proportional to the signal divided by the standard deviation of the background $s/\sqrt{b}$. Since s and b increase linearly with time, the significance grows with the square root of the observation time $\sqrt{t}$.

In the described scenarios, events are therefore selected on the basis of the reconstructed track direction only (information on arrival time is not used). Several of such direction based strategies to search for neutrino sources and to set flux limits are presented in the following sections.

7.1.1 The binned search

A relatively simple but still very powerful method to separate a localized excess from a uniform background is the usage of a circular search bin. The reconstructed directions of neutrino induced muons from a point like emitter are smeared out corresponding to the

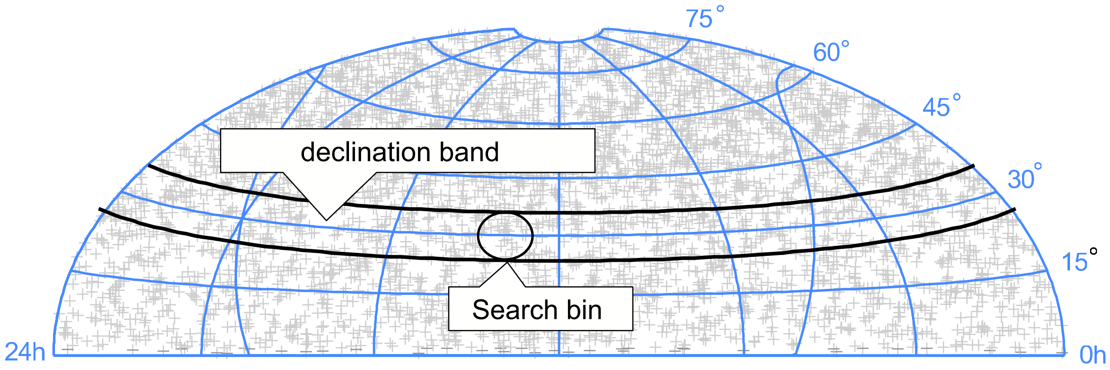

Figure 7.1: *Schematic visualization of the search for neutrino point sources with circular sky bins: Events within a certain angle around a hypothetical source position are counted and their density is compared to the average event density derived from all events in the declination band.*

point spread function of the detector introduced in section 6.4.1. Around the sky position $\mathbf{d}_S = (\delta_S, \alpha_S)$ of a hypothetical neutrino emitter, a region within a space angle Ψ_0 is defined as "on-source". All events N_S with reconstructed arrival directions $\mathbf{d}_\nu$ that fulfill the condition:

$$\vec{\mathbf{d}}_S\,\vec{\mathbf{d}}_\nu \;= \cos\Psi \;<\; \cos\Psi_0 \;, \tag{7.1}$$

are counted. This number is compared to the expected number of background events μ_b from atmospheric neutrinos and misreconstructed muons for this region. A probability is calculated that the observation of N_S events in a single search bin is caused by a fluctuation of the background, properly accounting for the fact that multiple observations are performed. If this probability is not extremely low, an upper limit on the signal contribution to the events inside the search bin is derived.

The expected background density can be estimated from the data outside the "on-source" region. Due to the changing detection and reconstruction efficiencies, the event densities in the analysis sample vary with declination. As a consequence only the declination region which contains the search bin $[\delta_S - \Psi_0, \delta_S + \Psi_0]$ should be used for the background calculation. In right ascension, the event density is uniform, since existing azimuthal efficiency variations are washed out by the rotation of the earth. The expected background inside the search bin can therefore be calculated as:

$$\mu_b \;=\; \frac{A_{\text{search bin}}}{A_{\text{decl. band}}}\,N_{bg,band} \;=\; \frac{1-\cos(\Psi_0)}{\sin(\delta_S+\Psi_0)-\sin(\delta_S-\Psi_0)}N_{bg,band}\;, \tag{7.2}$$

where $A_{\text{search bin}}$, $A_{\text{decl. band}}$ denote the solid angle of the search bin and the declination band respectively. Implicitly this method assumes that the contribution from neutrino sources in the declination band is neglegible. This is a fairly safe assumption since no neutrino source at all was so far discovered. Further, the existence of many weak sources, which have a too low flux to be detected individually, is disfavored by the results of the angular correlation search (see section 8.4). Moreover, it is a conservative approach in the sense that undetected sources present in the declination band would result in a too large μ_b and therefore decrease any excess significance. With the statistics provided by the 2000-2004 analysis sample the statistical uncertainty on the estimation of μ_b by this method becomes 5%-8%. Being derived directly from the data rather than simulation the systematic error on μ_b is neglegible.

Figure 7.1 visualizes the concept of the binned search described here. From a statistical point of view it is favorable to apply this method to the most promising candidates for neutrino emission first, before doing a full sky scan. This will be explained in the next sections together with the methods to derive excess significances and flux limits from N_S and μ_b.

An alternative approach to the binned search has been developed within the IceCube collaboration in [Neu03]: Each event is assigned an individual resolution determined with the event resolution estimator described in section 5.4.2. The reconstructed direction of the muon track is then replaced by a likelihood for the true direction in the (δ,α)-space containing a Gaussian term with a variance proportional to the resolution parameter. The likelihood product of all events is evaluated at the position $(\delta_S,\ \alpha_S)$ of a hypothetical neutrino source and compared to the likelihood distribution of randomized events at this spot to derive the significance of a possible excess. This method delivers comparable results to the binned search used throughout this analysis (compare [Hau04] and [Neu03]). To cross-check results it was applied to the 2000-2003 subset of data within this analysis sample. The results gained from the two different approaches were compatible.

7.1.2 Scan of a list of candidate sources

Statistical advantage of candidate definition

As shown in section 2.3 there are many ideas about which galactic or extragalactic objects should emit detectable fluxes of neutrinos. If, as a first step, the search is restricted to these candidates it makes the result statistically more powerful, since the so called 'trial factor' is considerably lower than in a full sky search.

The trial factor describes the reduction of the significance of a single observation in the case multiple equivalent observations are performed: let $P(i,b)$ denote the probability to observe i events on an expected background of b and let n denote the actual number of observed events. The significance $\mathcal{S}_{n,b}$ is the chance probability that this outcome is due to a fluctuation of the background. For a single observation we have:

$$\mathcal{S}_{n,b} = P(\geq n|b) = 1 - \sum_{i=0}^{n-1} P(i,b)\ . \tag{7.3}$$

It is convenient to express the significance $\mathcal{S}_{n,b}$, which corresponds to a probability, in units of standard deviations of a normal distribution σ. Its value in this unit is defined by solving the following equation for x:

$$\mathcal{S}_{n,b} = \int_{x\sigma}^{\infty} \left(\sqrt{2\pi}\sigma\right)^{-1} \exp\left(-x^2/2\sigma^2\right)\ . \tag{7.4}$$

The chance probability for a background fluctuation is expressed in terms of the chance probability of a normally distributed variable to be found with a value x standard deviations above the mean[1].

If m multiple independent experiments are performed (like looking at more than one source), one has to consider the probability that a certain background fluctuation can occur in any of these trials. The significance then becomes:

---

[1] Please note that a lower value of $S_{n,b}$ means a higher significance, since it represents a probability. In case it is expressed in units of σ, a higher σ-value corresponds to the higher significance.

$$\mathcal{S}^{(m)}_{n,b} = 1 - \left(\sum_{i=0}^{n-1} P(i,b) \right)^m > \mathcal{S}_{n,b} \; . \tag{7.5}$$

Thus, in multiple independent experiments, one needs to observe more events than in a single experiment to exclude a background fluctuation at the same confidence level. The factor by which it is reduced is called the "trial factor". We call the quantity $S_{n,b}$, which does not account for the trial factor, the "excess parameter" of the observation in the case of multiple experiments.

For m experiments which are not independent, e.g. sources so close together that the search bins are overlapping, the trial factor can not be analytically computed and one has to rely on simulations to estimate it. This will be important in the case of the grid search mentioned later. However in the case of small overlap – which we can assume for the relatively short list of candidate sources – the significance of m independent observations is a good and conservative estimate of the real significance.

Significance and Flux limit evaluation

In the case of the binned search the probability $P(n,b)$ to observe n events inside the "on-source" region, having counted b events in the declination band, is described by binomial statistics. The background is uniformly distributed and in the case of no signal contribution the probability for an event to be recorded in the search bin is given by the ratio of the solid angles of the bin and the declination band. Therefore $P(n|b)$ can be written as:

$$P(n|b) = \binom{b}{n} \left(\frac{A_{\text{search bin}}}{A_{\text{decl. band}}} \right)^n \left(1 - \frac{A_{\text{search bin}}}{A_{\text{decl. band}}} \right)^{b-n} \; . \tag{7.6}$$

To calculate the significance of the experimental result (n,b), we now follow the considerations of the last section. First the excess parameter (7.3) is derived from $P(n|b)$, then the significance accounting for the multiple observations $\mathcal{S}^{(m)}_{n,b}$ is estimated assuming that the "on-source" bins of the 34 neutrino candidates are non-overlapping and the trials therefore independent.

Following a common agreement in particle physics and astro-physics we would call an excess with a significance $> 3\sigma$ an indication for a neutrino source and an excess with a significance $> 5\sigma$ a source detection. Thus, the chance probabilities that an indication or detection are caused by a fluctuation of the background are 0.003 and $6 \cdot 10^{-7}$, respectively.

In the case that no excess is found we calculate an upper limit on the signal contribution to the events which is still compatible with the experimental result (n,b) as introduced in section 2.5.2.

Candidate selection

The selection of sources to be included in the candidate list has to be a good compromise between keeping the chances to find a signal high and the trial factor low. Therefore only the most promising candidates from each class of sources have been selected and included in the catalogue. Only sources on the northern hemisphere have been selected, since the sensitivity declines rapidly for negative declinations.

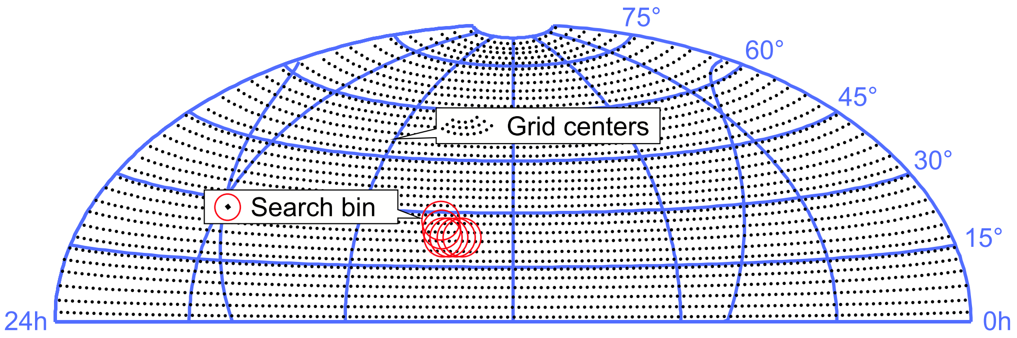

Figure 7.2: *Illustration of the scan of the northern hemisphere for a signal from a point source with a binned search on a predefined grid. The distance between adjacent grid centers is much smaller than the resolution of the detector and the search bin size. Therefore the contents of the search bins are highly correlated.*

Several objects have been chosen from the main classes of neutrino candidate sources: Blazars seen in TeV or GeV gamma-rays, Pulsars, Supernova remnants and Microquasars. Besides them, individual sources which have promising predictions of neutrino fluxes have been added to the list. A discussion of the sources considered and of existing predictions of neutrino fluxes was done in section 2.3. Table 7.1 shows the names of the selected candidates, their positions on the sky in equatorial coordinates and references where possible neutrino emission from these sources is discussed.

7.1.3 Grid search on the northern sky

The statistical advantages of a candidate catalog are partly compensated by the introduction of a model dependency into the analysis: Sources which are not suspected to be emitters of neutrinos are excluded from the very beginning.

The catalog is defined based on considerations derived from the electromagnetic spectral properties of the candidates at different wavelengths. But parts of the electromagnetic spectrum could be hidden due to photon-absorbing matter along the line of sight. Just recently the H.E.S.S. Čerenkov telescope reported the detection of a source of TeV gamma-rays, which has no obvious counterpart in any other region of the spectrum [A$^+$05d]. The mentioned gamma-ray source is not in the field of view of AMANDA, but similar sources on both hemispheres would most likely remain undetected since gamma-ray telescopes with their small field of view can cover only a small fraction of the sky. Such objects would be prime candidates for neutrino emission but missing in the catalog. Hence, it is justified to perform a second unbiased search with less statistical power due to the considerably higher trial factor.

In the frame of this thesis such an unbiased search is realized by a scan of the northern sky on a grid with steps of 0.5° in declination and right ascension. The method is identical to the binned search assuming a hypothetical neutrino source on each grid center. For each point, the number of events in the search bin is compared to the background and the excess parameter (7.3) is calculated. Figure 7.2 illustrates such a grid scan.

While limits can be derived for each grid center in an analog way to the candidate sources, the significance of the observation has to be computed differently, since the search bins are strongly overlapping. An analytical calculation or even approximation of the trial factor becomes impossible. A Monte Carlo technique is used instead, which is described below. Obviously, the trial factor increases with the density of grid points, but also the average misalignment of a bin to an unknown source diminishes, reducing the loss of potential

Source name	RA/h	Dec/°	redshift z	References	other names
TeV Blazars					
Markarian 421	11.1	38.2	0.033	[M$^+$03]	
1ES 1426+428	14.5	42.7	0.13	[H$^+$02b]	H 1426+428
Markarian 501	16.9	39.8	0.033	[Man98]	
1ES 1959+650	20.0	65.1	0.048	[Boe05, HH05]	
1ES 2344+514	23.8	51.7	0.044	[C$^+$98]	
GeV Blazars					
QSO 0219+428	2.4	42.9	0.44	[NS02]	3C 66A, 3EG J0222+4253
QSO 0235+164	2.6	16.6	0.94	[NS02]	3EG J0237+1635
QSO 0528+134	5.5	13.4	2.07	[NS02]	3EG J0530+1323
QSO 0716+714	7.4	71.3	0.30	[NS02, M$^+$03]	3EG J0721+7120
QSO 0954+556	9.9	55.0	0.91	[NS02]	3EG J0952+5501
3C273	12.5	2.1	0.16	[Man93, SS96]	3EG J1229+0210
QSO 1611+343	16.2	34.4	1.40	[NS02]	3EG J1614+3424
QSO 1633+382	16.6	38.2	1.81	[NS02]	3EG J1635+3813
other AGN					
NGC 1275	3.3	41.5	0.018		
M87	12.5	12.4	0.0042	[PDR03]	
Microquasars & Neutron star binaries					
LSI +61 303	2.7	61.2		[D$^+$02]	
CI Cam	4.3	56.0		[D$^+$02]	XTE J0421+560
GRO J0422+32	4.4	32.9		[D$^+$02]	
AO 0535+26	5.7	26.3		[A$^+$03c]	
XTE J1118+480	11.3	48.0		[D$^+$02]	
SS433	19.2	5.0		[D$^+$02]	
GRS 1915+105	19.3	10.9		[D$^+$02]	
Cygnus X-1	20.0	35.2		[D$^+$02, Bed05]	
Cygnus X-3	20.5	41.0		[D$^+$02, Bed05]	
Supernova Remnants & Pulsars					
PSR J0205+6449	2.1	64.8		[Bed03, BP97]	
Crab Nebula	5.6	22.0		[Bed03, BP97, GA03, LB06]	
Geminga	6.6	17.9		[H$^+$99]	
SGR 1900+14	19.1	9.3		[Z$^+$03]	GRB 980827
PSR 1951+32	19.9	32.9		[Bed03]	
Cassiopeia A	23.4	58.8		[A$^+$00b, AMH02, BPV03]	
AGASA UHECR Multiplets					
Multiplet 1	1.3	20.4		[U$^+$00]	
Multiplet 2	11.3	56.9		[U$^+$00]	
Unidentified high energy gamma-ray sources					
3EG J0450+1105	4.8	11.4		[H$^+$99]	
TeV J2032+4131	20.5	41.5		[A$^+$02]	Cygnus OB2

Table 7.1: *Catalog of candidate neutrino sources. Name, position, redshift for extragalactic sources, references and alternative names are listed.*

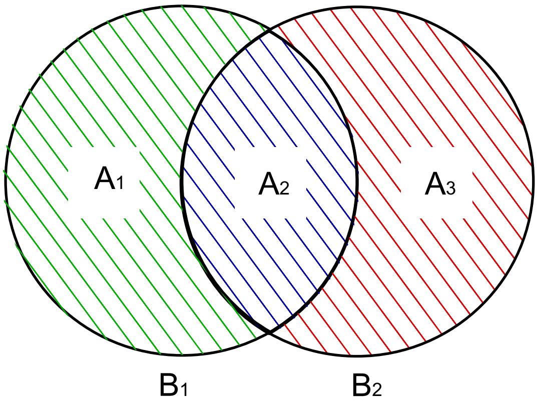

Figure 7.3: *Schematic view of two overlapping bins B_1 and B_2. The bins can be divided into 3 non-overlapping regions A_1,A_2 and A_3.*

signal events. These two effects are partly compensating and an optimal density of grid points can be found.

Significance evaluation

If the distance of the grid centers get smaller than the size of the search bins, they overlap and the corresponding measurements are therefore correlated. The probability to see an excess parameter higher than $\mathcal{S}_{n,b}$ in any of the m measurements (where m is equal to the number of grid points) is then not any more given by (7.5). In an analytical calculation of $\mathcal{S}_{n,b}^{(m)}$, one would have to identify for every solid angle element $d\Omega$ the set of search bins covering it and then sum over all possible configurations which would result in a larger excess parameter than the observed one in any of the search bins.

For $m = 2$ the situation is illustrated in figure 7.3. Three different regions can be identified, region A_1 belonging to bin B_1, region A_2 belonging to B_1 and B_2 and region A_3 belonging to bin B_2 only. Let (n_1, n_2, n_3) denote the number of observed events and (b_1, b_2, b_3) the number of expected events in the regions (A_1, A_2, A_3). If n events were observed in one of the two bins, the significance of the observation $\mathcal{S}_{n,b}^{(2)}$ is given by the sum over the probabilities P of all configurations with n or more events in either bin B_1 or B_2:

$$\mathcal{S}_{n,b}^{(2)} = 1 - \sum_{n_1,n_2,n_3}^{\substack{n_2+n_3<n \\ n_1+n_2<n}} P(n_1, b_1)\, P(n_2, b_2)\, P(n_3, b_3)\ . \tag{7.7}$$

For $m \gg 1000$ as in the case of the grid search this expression becomes arbitrarily complicated, and it is tedious to evaluate it. Instead a simulation based approach is chosen to calculate the significance of an observation. The search bin which shows the highest excess parameter $\mathcal{S}_{max}$ is identified. Then samples of randomized experimental outcomes are created by replacing the right ascension value of the event coordinates with uniformly distributed random numbers. By randomization of the right ascension coordinates instead of both coordinates, one accounts for the declination dependent variations of the background densities due to changing detector efficiencies and event selection criteria. These properties are reproduced in the toy experiments, while every event correlation from a possible contained point source signal is effectively eliminated.

For each of these samples the grid scan is repeated and the maximum excess parameter $\mathcal{S}_{rand,max}$ found is compared to $\mathcal{S}_{max}$. The number of cases k with a higher significance

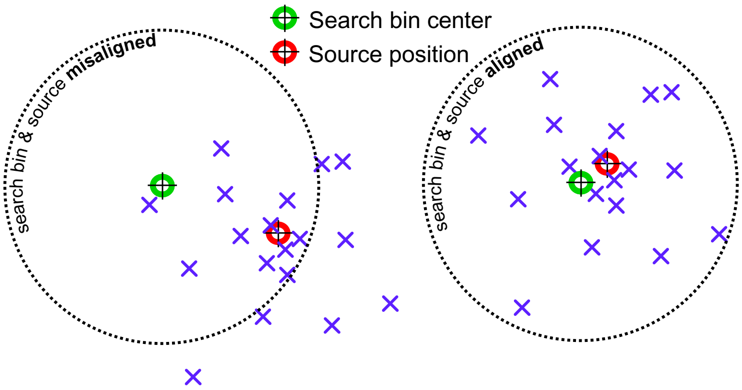

Figure 7.4: *Example of signal loss in a scan with sparse grid centers: for the coarser search grid (left side) the average misalignment between source position (red cross) and closest grid center (green cross) is higher. This leads to a higher fraction of the signal events (blue crosses) outside the search bin (dashed black circle) than in the case of a finer spaced search grid (right side of the picture).*

than the experimentally observed one are counted. If $k \gg 1$ the fraction of toy experiments with $\mathcal{S}_{rand,max} > \mathcal{S}_{max}$ provides a reasonably good estimate of the significance.

Optimal grid spacing

The question remains, what is the optimal spacing of the grid to get the best significance for a potential point source on the sky map. Decreasing the distance between adjacent grid centers will increase the trial factor since more evaluations are necessary to cover the full hemisphere. On the other hand the average misalignment between the sky position of a point source and the closest grid center will drop. Figure 7.4 demonstrates this effect.

Which effect is dominant can be quantified using toy experimental outcomes with randomized event coordinates like the ones described above: from the 3000 created random event samples the distribution of their maximum excess parameters is derived. The excess parameter $\mathcal{S}_{3\sigma}$ which is needed to achieve a significance of 3σ is read from that distribution. The upper picture in figure 7.5 indicates that value for a 1° grid spacing by a black line. This procedure is repeated for a set of different grid spacings $(g_1, \ldots, g_n)$.

Then the excess parameter distribution is calculated for randomized data samples where some of the background events are replaced by events from a simulated point source of average signal strength $\langle n_s \rangle$. The angular resolution is taken into account by smearing the signal according to a two dimensional Gaussian distribution with the width of the angular resolution (declination dependent between 1.5° and 2.5°). By counting the fraction of these simulations which show a higher excess parameter than $\mathcal{S}_{3\sigma}$, we find the probability that a source of signal strength $\langle n_s \rangle$ would have been detected in a grid search on a 3σ level.

The grid spacing which maximizes this detection probability is the optimum for the scan. A comparison of excess parameter distributions with and without a simulated point source and the corresponding detection probability for different average source strengths $\langle n_s \rangle$ and grid spacings g_i can be found in figure 7.5. The position of the point source on the sky is chosen randomly in these simulations to avoid biases towards grid center locations.

The detection probability decreases for increasing distance between grid points. The optimum is reached when the grid spacing becomes small compared to the search bin sizes and the detector resolution. For finer grids the function flattens and no additional

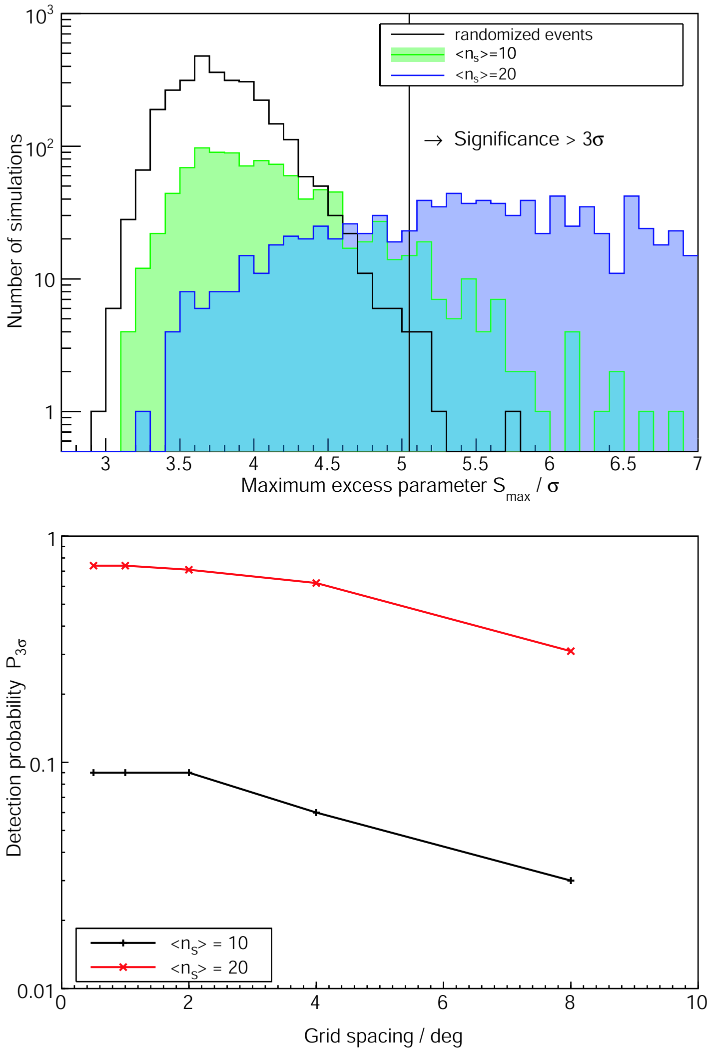

Figure 7.5: *Distribution of the maximum excess parameter (upper picture) on a grid of* 1° *spacing for a background simulation (randomized events), a simulated point source contributing with a mean number of* $\langle n_s \rangle = 10$ *signal events and a point source contributing with* $\langle n_s \rangle = 20$ *events. The black line shows the excess parameter for which a significance of* 3σ *is reached. The detection probability for the simulated sources at this significance level can be derived from the plot by counting the number of simulations on the right side of the black line. On the lower picture the* 3σ *detection probability as a function of the grid spacing is shown for simulated point sources contributing with* $\langle n_s \rangle = 10$ *and* $\langle n_s \rangle = 20$ *signal events, respectively.*

improvement is reached if the number of grid points is further increased. Therefore we use a grid spacing of 0.5° in declination as well as in right ascension for this analysis. It provides optimal detection probability for unknown sources.

7.1.4 Search for angular correlations

If the point sources are too weak to be observed individually with the methods presented above, it might still be possible to observe a cumulative signal in the case that the number of such sources is sufficiently large. One way to achieve this is to overlay their search bins and sum the observed events and the expected background. This method is known as source stacking. However, it is not trivial to decide how many and which candidates to overlay. A dedicated analysis defining generic classes and catalogs of sources within each class based on their spectral energy distribution was performed within the IceCube collaboration in [A$^+$06a]. Upper limits on the combined neutrino flux from each of the defined classes are published in [A$^+$06b].

Here we present only a more generic analysis which is sensitive to multiple weak sources, the search for angular correlations: counting the event pairs $N(\theta_{ij})$ with a separation angle θ_{ij} between each combination (i, j) of two events, there should be an excess of pairs at small θ_{ij} above the expectation from atmospheric neutrinos, if several of these sources are present. For a uniform distribution of events in the full sky the expected number of pairs separated by an angle θ would be proportional to the surface area of the unit sphere between the angles θ and $\theta + d\theta$ and therefore uniform in $\cos\theta$:

$$N(\theta)d\theta = 2\pi N_0 \sin\theta d\theta = -2\pi N_0 (d\cos\theta)\ . \tag{7.8}$$

However, due to the declination dependent variations in the selection efficiency and the restriction of this analysis to events from the northern hemisphere, the number of pairs declines for $\theta \to \pi$. The expected shape of the distribution can be found by simulating event sets with randomized right ascension coordinate, a technique introduced in section 7.1.3 (10000 event sets were simulated).

An excess of pairs is expected at small angles in the presence of weak point sources. We therefore count these pairs in bins of θ^2 ($d\cos\theta \approx d\theta^2$ for $\theta \ll \pi/2$). For this analysis the range between $0° < \theta < 30°$ is used. The choice of the upper boundary is arbitrary, but variations showed that the outcome of the statistical test described below changes only marginally as long as the range is much larger than the width of the point spread function of the detector. The bin size $\Delta\theta^2$ was chosen corresponding to the angular resolution of the detector of 1.5° – 2.5° to be $\sqrt{\Delta\theta^2} = 2°$. The mean and the variance of the number of event pairs were calculated for each bin. The variance σ^2 is within the simulation statistics in good agreement with the expectations from Poisson statistics ($\sigma^2 = N$).

To evaluate how potential point sources influence this distribution of pairs, a number N_S of sources was distributed randomly over the sky. The amount of signal events n_i from each source i was chosen to be Poisson distributed around a common mean μ_S. For each signal event a randomly chosen event from the randomized sample was removed. It was replaced by an event distributed around the position of the hypothetical source according to a Gaussian point spread function with declination dependent RMS of 1.3° ($\delta = 90°$) to 2.3° ($\delta = 0°$).

All signal simulations where performed for a mean number μ_S of 10 events. Such sources would in more than 95% of the cases result in observations of ≤ 20 events in the search

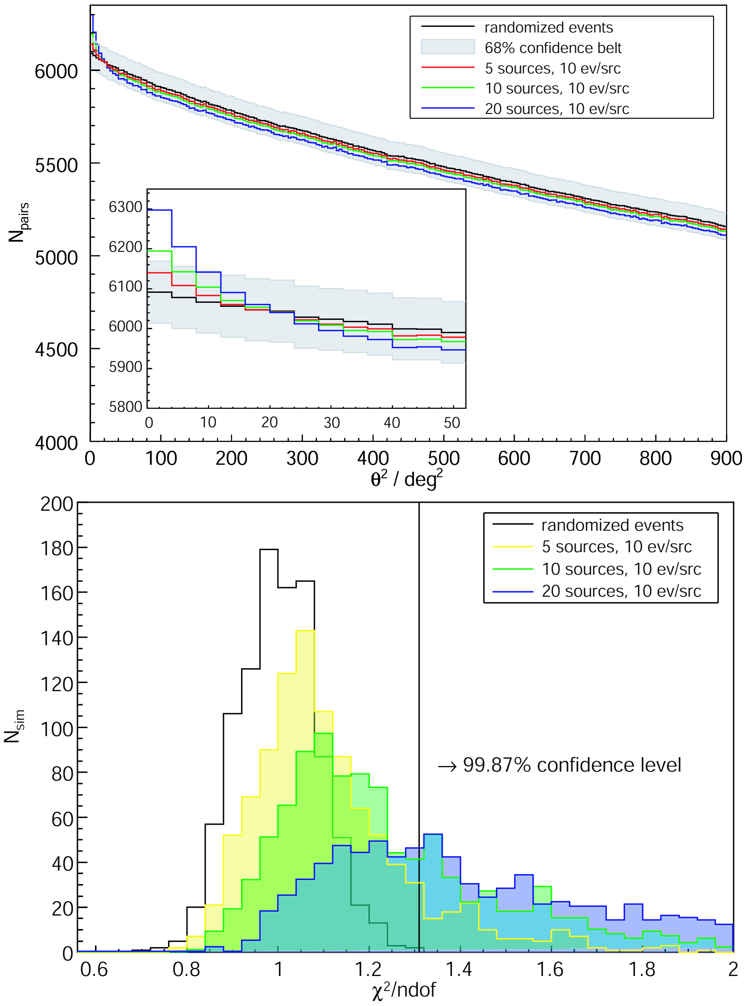

Figure 7.6: *Distribution of the mean number of event pairs in θ^2 for pure background (randomized) data samples and for samples including $N_S = (5, 10, 20)$ simulated point sources (upper picture). The means were calculated from 1000 simulations. For the background sample also the 1σ-range is given. The sources contributed on average 10 events/source and were distributed randomly over the sky. Lower picture: reduced χ^2-distribution (223 d.o.f) from the comparison of the simulation results to the expectations for a randomized data sample. The line indicates the χ^2-value above which the hypothesis that the θ^2-distribution originates from a randomized data sample can be rejected at 3σ confidence level.*

bins of the grid scan (assuming a 70% bin efficiency and an expected background[2] of 6.5). 20 events for an expected background of 6.5 translates into an excess parameter of 4.9σ, which has a significance considerably less than 3σ. Hence, these sources would be individually too weak to be detected.

Three scenarios where compared, varying the assumed number of sources: $N_S = 5$, $N_S = 10$ and $N_S = 20$. For each case 1000 simulation samples were produced and a χ^2-test was performed, comparing the resulting θ^2-distributions to the distribution expected from a pure atmospheric neutrino hypothesis.

The upper picture of figure 7.6 shows the mean θ^2-distributions for the different scenarios as well as the 1σ-range of the pure atmospheric neutrino sample. The peak at small

---

[2] Such a background and bin efficiency corresponds to typically observed values in the binned search

angles for the signal simulations is clearly visible, but also a deficit for larger angles. Since the total number of pairs in the sample is fixed, the clustering of events for small θ^2 is compensated by a decrease of the number of pairs in the other parts of the distribution.

The lower picture shows the distribution of reduced χ^2 values in each scenario for 1000 simulations. A value larger than 1.31 (223 degrees of freedom) occurs with a probability smaller than 0.0013 in the case of a pure atmospheric neutrino sample resulting in a rejection of the H_0-hypothesis at a 3σ confidence level. As can be seen a considerable fraction of the signal simulations deliver χ^2 values larger than 1.31. This fraction represents the detection probability (at 3σ level), being the fraction of experiments in which we could reject the background hypothesis. Table 7.2 summarizes the detection probabilities for the simulations performed.

Simulation parameters	Detection probability
5 sources, 10 events/source	0.11
10 sources, 10 events/source	0.32
20 sources, 10 events/source	0.65

Table 7.2: *Detection probability at 3σ confidence level for various simulated source contributions.*

Note that the detection probability depends not only on the number of sources, but also on their strength and their distribution on the sky. Rather than finding evidence or excluding certain source contribution scenarios, the aim of this test is mainly to reject or confirm the hypothesis, that the events are purely atmospheric neutrinos. There are certainly more powerful statistical tests to find unidentified weak sources. However, due to the large angular range, this χ^2-test is also sensitive to possible detector related event correlations on larger angular scales, which would point to instabilities in the detector operation. The results of this test, applied to the final data sample, can be found in the next chapter.

An alternative approach to find angular correlations was developed by [Hue06], who calculated the multipole moments for the event distribution in the data sample. A discussion on the limit setting potential of a correlation analysis to certain source distribution/strength scenarios is found there.

7.2 Strategies based on spatial and temporal information

In section 2.3 it was argued that certain classes of sources show strong variability in their electromagnetic emission with a behaviour commonly called “flaring”. Among the neutrino emission candidates several AGN and Microquasars are observed to exhibit such intense flares in different regions of the electromagnetic spectrum.

In case the intensity of neutrino emission is correlated to the intensity of electromagnetic emission, the search methods presented above are not optimal, since a large fraction of the neutrino signal may be produced during relatively short outbursts. In the observation time between the flares mainly background from atmospheric neutrinos would be accumulated. Ideally one selects only the periods in which the source is flaring in order to optimize the signal-to-noise ratio. The selection would be based on the region of the electromagnetic spectrum which is closest related to neutrino emission. This region is usually the MeV to TeV gamma-rays, which are produced simultaneously with neutrinos in the decay of pions.

However, quasi-continuous observations of the sources in the whole MeV-TeV frequency band would be necessary to select the periods of flaring activity efficiently. Otherwise chances are high that flares are missed, degrading the chance for a neutrino detection. With the decomissioning of the Compton Gamma Ray Observatory [NAS05] in the year 2000, there is no scientific instrument currently in operation, which could observe gamma-rays between a few MeV and several tens of GeV. Above 100 GeV photon energy Imaging Air Shower Cherenkov Telescopes (IACTs) are able to measure gamma fluxes, but they have a very limited field of view ($\leq 5°$ for current telescopes [B^+03a, Mag97]). Also they can only observe during moonless nights and favourable weather conditions. Therefore very limited data is available for individual sources in this wavelength range and a selection of high state periods based on it is inefficient at the moment. Two options have been considered here to overcome this problem:

Selection of periods based on a different frequency band: typical flares are visible in more than one frequency band. For BLLac objects a correlation between X-ray and high energy gamma-ray emission is indicated by observations. Theoretical arguments suggest that in Microquasars neutrino emission precedes observed radio outbursts by a few hours [LW01]. For some sources nearly continuous observations are performed in the radio and/or X-ray bands by several experiments. Data on the measured radio or X-ray flux, the so called “light curve” has been used to determine the periods of high activity.

Analysis of the neutrino event time series: based on the assumption that the majority of the signal is emitted in short periods of high activity, the time series of neutrino events from the direction of a variable source is analyzed to look for short periods with significantly high event multiplicities. Only the knowledge about the variability of a source candidate and its time scale is necessary in that case, while no continuous and simultaneous observation of the electromagnetic variability is needed.

In the following sections we highlight these two complementary methods to search for variable neutrino emission and end the chapter with a compilation of the neutrino source candidates which have been considered variable and analyzed in this way.

The strategies described have only been applied to the subset of data taken in 2000-2003 corresponding to 807 effective days of detector operation (in contrast to the 1001 effective days for the time integrated searches described above). New strategies for the analysis of event time series and photon-neutrino correlations for the IceCube detector are currently under development within the collaboration and the 2004 data set will be used as a a test sample for these methods.

7.2.1 Search for neutrinos in high state periods of variable sources

BLLac type objects

Several BLLac-type objects (HBLs) are observed to be highly variable in TeV gamma-ray emission. Flares in gamma-rays are usually accompanied by simultaneous flares in the X-ray band. TeV photon observations of individual sources by IACTs are limited to a few tens of hours per year, due to environmental and observational constraints. However, the X-ray band is (quasi-)continuously monitored by the All Sky Monitor (ASM) on board of the NASA satellite “Rossi X-ray Timing Explorer” (RXTE) [NAS02] since 1995. The data from this satellite is freely available via a web interface [Lev04].

Figure 7.7 shows the light curves measured by RXTE/ASM of the three closest TeV-variable BLLac-type objects in our sample of candidate sources, Markarian 421, Markar-

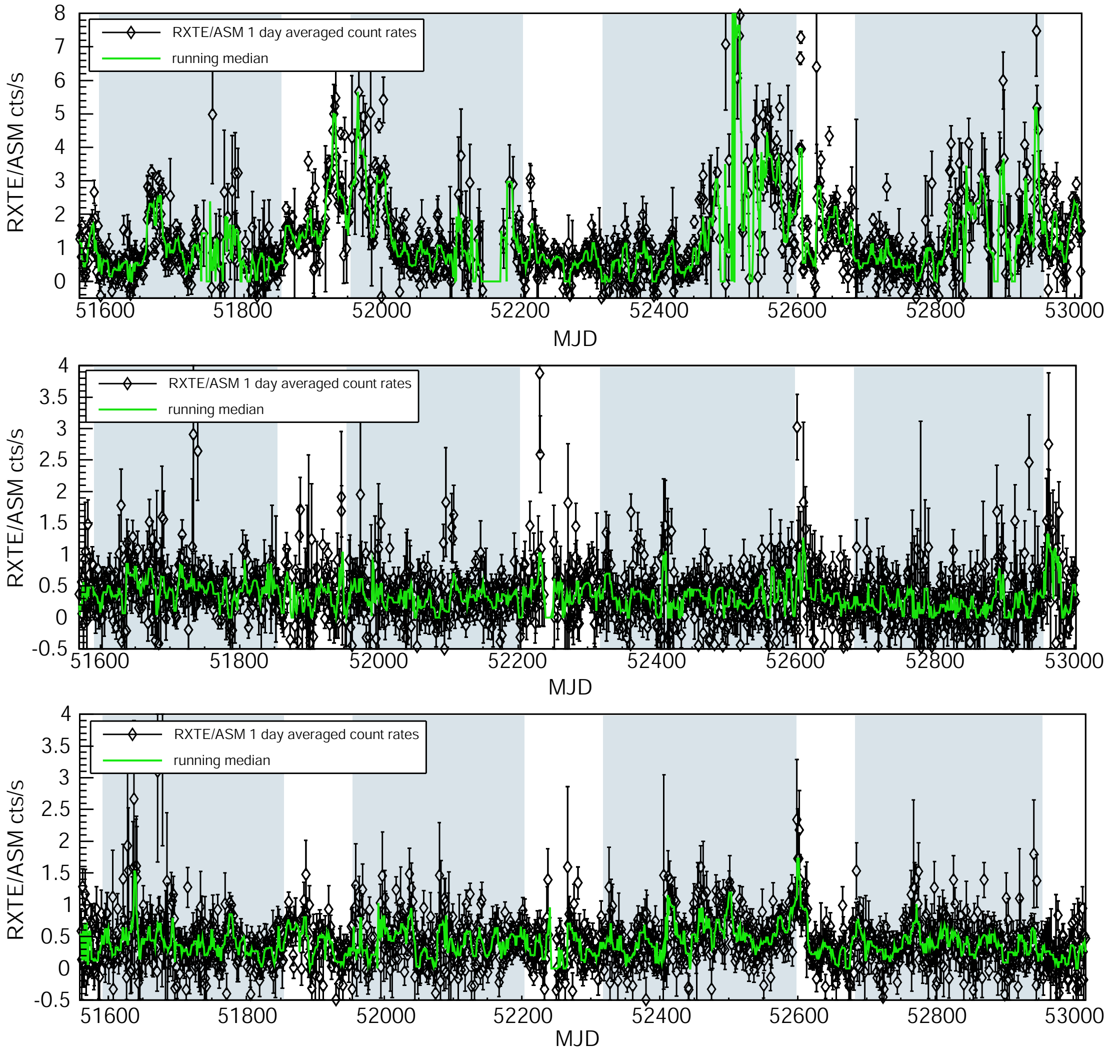

Figure 7.7: *RXTE/ASM X-ray light curves for the BLLac objects Markarian 421 (upper picture), Markarian 501 (middle picture) and 1ES1959+650 (lower picture). The grey areas show the time covered by the AMANDA-II dataset. The green curve displays the 7-day running median of the X-ray flux.*

ian 501 and 1ES 1959+650 for the period between 2000 and 2003. A median filter is applied to smooth the curves and reduce statistical fluctuations. As one can see, only for Markarian 421 structures are visible showing distinctively states of high and low activity. For Markarian 501 no gamma-ray flare was reported in this period, however a former flare in 1997 had been observed simultaneously in TeV gamma-rays and with RXTE/ASM [C$^+$97]. In the case of 1ES1959+650 several strong TeV flares were discovered in 2002 (MJD 52410-52500) [K$^+$04]. While there is no obvious increase visible in the RXTE/ASM light curve, correlated X-ray emission has been observed in a dedicated campaign with the more sensitive Proportional Counter Array (PCA) on the RXTE satellite. Thus, we conclude that a selection of high activity periods based on the RXTE/ASM light curves is only possible for Markarian 421. Markarian 501 and 1ES1959+650 show no obvious enhancements of X-ray emission during the period covered by the AMANDA dataset.

To test the hypothesis that there is neutrino emission from Markarian 421 in coincidence with high activity of the source in the X-ray band, one has to assume a certain type of correlation between the neutrino and the X-ray flux. For simplicity we assume here that this correlation is linear. To distinguish between periods of high and low activity of the

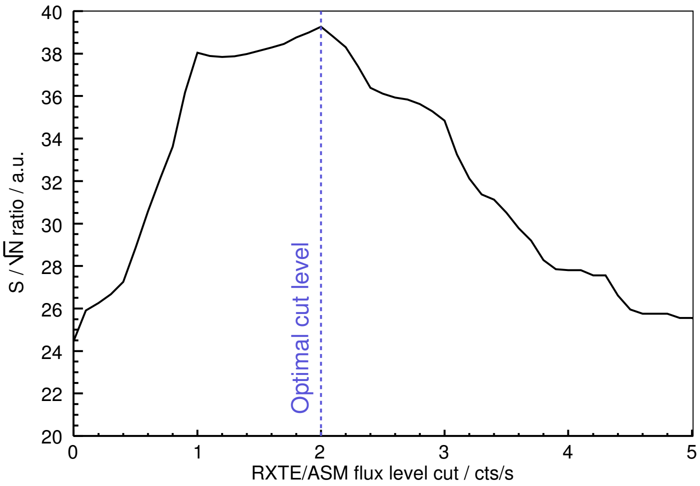

Figure 7.8: *Signal-to-noise ratio* $s/\sqrt{b}$ *for Markarian 421 in arbitrary units dependent on the X-ray flux threshold to define active states.*

source, a threshold is set on the X-ray flux. The number of neutrino events from the direction of Markarian 421 falling into time intervals of increased X-ray flux are counted and compared to the number of neutrinos expected from background.

The value of the threshold is arbitrary and should be optimized to deliver a maximum chance to detect a signal. In the approximation of Gaussian statistics the highest significance for the observation of a signal is reached if the ratio between signal s and the standard deviation $\sigma_b = \sqrt{b}$ of the background b becomes maximal. The selection of periods should therefore be governed by the attempt to maximize $s/\sqrt{b}$ for a proportionality between neutrino and X-ray flux (the hypothesis we test). The value of s is given by the integrated X-ray flux in the current selection, b can be obtained from integration of the atmospheric neutrino rate over the selected periods of high source activity.

The result of such an optimization is displayed in figure 7.8. The atmospheric neutrino rate is assumed to be constant and therefore $b \propto \sum_i \Delta t_i$, where $\sum_i \Delta t_i$ is the sum of the time intervals of enhanced X-ray flux. Instead of the raw flux values the outcome of the 7-day median filter to the X-ray flux is used to eliminate short term fluctuations. The best signal-to-noise ratio $s/\sqrt{b}$ is reached for a flux level of 2 cts/s.

This flux level is used to discriminate between active and inactive states for the hypothesis test. Figure 7.9 shows the selected periods on top of the Markarian 421 X-ray light curve. They cover a total of 141 effective days of AMANDA live time in the years 2000 to 2003.

Microquasars

Microquasars are in general not observed as strong TeV gamma-ray emitters[3] and therefore one cannot rely on the method based on TeV to X-ray correlation adopted for the BLLac type Blazar Markarian 421 in the last section. However strong outbursts at radio frequencies have been observed from some of these sources. It has been argued in section 2.3 that it is likely that neutrino emission is enhanced around these outbursts, more specifically that neutrinos precede these radio flares by a few hours.

Based on these arguments, a selection of "active states" analogous to the case of the

---

[3] Only recently the H.E.S.S and MAGIC IACTs reported weak TeV gamma-ray signals from Microquasars [A$^+$05c, A$^+$06d]

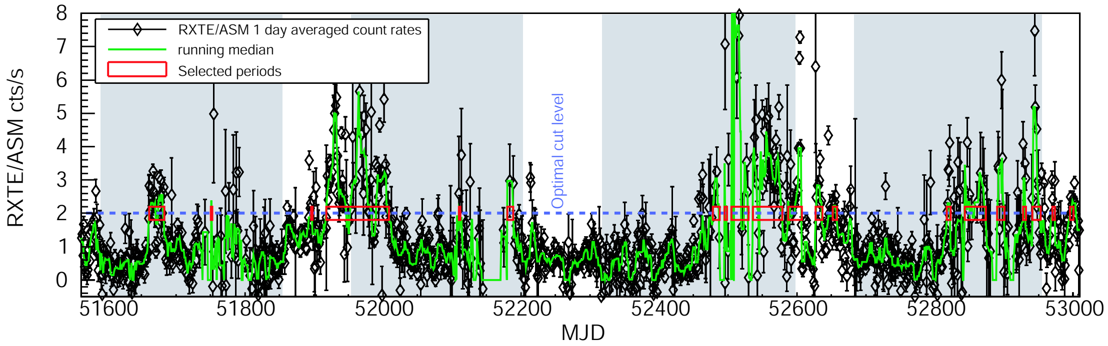

Figure 7.9: *RXTE/ASM X-ray light curve of Markarian 421 with the position of the optimized X-ray flux threshold overlaid. Periods which show a X-ray flux higher than the threshold are marked by the red boxes. These periods are tested for an excess of neutrino events compared to the expected background.*

Blazars can be performed. Instead of the X-ray light curve the radio light curve is used. At radio frequencies the RYLE telescope has a continuous monitoring program of several galactic radio sources. It provides long-term measurements at a frequency of $f = 15$ GHz [Poo04].

Scanning the catalog of candidate sources defined in section 7.1.2 one finds 7 Microquasars. To qualify for an analysis selecting flare states, these sources must match certain conditions:

- they have to be variable;
- continuous radio data must be available;
- the variability must be visible in the time period covered by this analysis.

Table 7.3 summarizes the properties of the Microquasars with respect to these aspects:

Source	Variability	Radio data available	Flares visible
SS 433	no	–	–
GRS 1915+105	yes	yes	complex radio spectrum / light curve
GRO J0422+32	yes	no	–
Cygnus X-1	yes	yes	very weak flares
Cygnus X-3	yes	yes	yes
XTE J1118+480	yes	no	–
LS I +61deg 303	periodic	yes	yes

Table 7.3: *Properties of the Microquasars in the catalog of candidate source important for a selection of flare states.*

So only Cygnus X-3 and LS I +61deg 303 are suitable candidates for this analysis. However, since LS I +61deg 303 shows periodic flares [GPT99], a dedicated analysis exploiting the periodicity is potentially more powerful and therefore the source is omitted in this approach.

A selection of flare states of Cygnus X-3 is performed using the method described in the last section. To account for the possibility that neutrinos precede the radio flare by a few

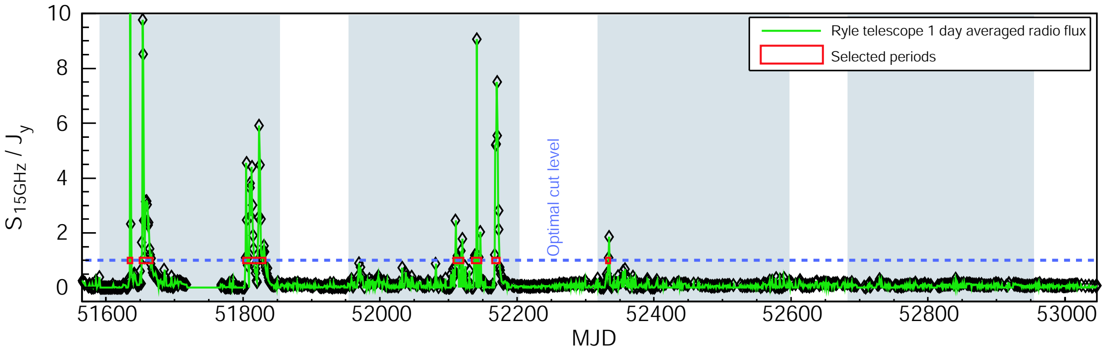

Figure 7.10: *RYLE Telescope 1-day averaged radio flux at 15 GHz from Cygnus X-3. Periods which show a radio flux higher than the threshold are marked by the red boxes. These periods are tested for an excess of neutrino events compared to the expected background.*

hours, 3 days have been added in front of each period of high radio flux. The optimal radio flux threshold to distinguish between high and low states has been found to be 1 Jy. Figure 7.10 shows the 1-day averaged radio light curve of Cygnus X-3 with the selected periods of high radio emission from this source. The livetime of the AMANDA-II detector within these periods is 114 days.

Extended neutrino data sample

In the case that no positive detection of a neutrino signal is achieved by this method for the two sources tested, a limit can be set on the neutrino flux in periods of high X-ray/radio flux compatible with this observation. The optimization of the data sample for best limit setting capability (sensitivity) presented in chapter 6 assumed a detector livetime of 807 effective days. This optimization does not deliver the optimal sensitivity for the much shorter livetime in the selected high state periods of 141 and 114 effective days respectively.

Therefore a re-optimization of the cuts was performed for this analysis using identical tools and strategies like the ones described in chapter 6. Since the livetime in flare states and the declination of Markarian 421 and Cygnus X-3 are very similar (38.2° vs. 41.0°) only one re-optimized data sample has been created, tuned to deliver the best limit setting capability in 125 days of livetime for a source located at 40° declination. Table 7.4 summarizes the event selection cuts and table 7.5 the basic properties of the re-optimized data sample for the two sources considered in this analysis.

	Re-optimized sample	Standard sample
Livetime used in optimization (days)	125	807
Search bin size	3.75	3.25/3.00
Likelihood ratio cut	31	34
Smoothness cut	0.35	0.36
Event resolution cut	3.5	3.25

Table 7.4: *Event selection cuts in the data sample re-optimized for the analysis of selected periods of high source activity, compared to the event selection cuts in the standard data sample used in the time-integrated analysis.*

	Re-optimized sample		Standard sample	
	Mrk 421	Cyg X-3	Mrk 421	Cyg X-3
Signal event ratio (sample/standard sample)	1.18	1.21	1	1
Exp. background in search bin *(flare periods)*	1.7	1.5	0.97	0.71
Exp. background in search bin *(2000-2003)*	9.9	10.3	5.6	5.0
Sensitivity to ν_μ-flux *(flare periods)* [GeV cm^{-2} s^{-1}]	$2.2 \cdot 10^{-7}$	$2.6 \cdot 10^{-7}$	$2.4 \cdot 10^{-7}$	$2.9 \cdot 10^{-7}$
Sensitivity to ν_μ-flux *(2000-2003)* [GeV cm^{-2} s^{-1}]	$0.7 \cdot 10^{-7}$	$0.7 \cdot 10^{-7}$	$0.7 \cdot 10^{-7}$	$0.7 \cdot 10^{-7}$

Table 7.5: *Properties of the data sample re-optimized for the analysis of selected periods of high source activity, compared to the standard data sample used in the time integrated analysis. "Flare periods" refers to the 141 effective days (Markarian 421) and 114 effective days (Cygnus X-3) which have been selected for showing high electromagnetic emission in the X-ray/radio frequency bands. A differential flux of $d\Phi/dE \propto E^{-2}$ was assumed for the signal event rates and the sensitivities quoted here.*

The selection cuts are relaxed providing a higher signal efficiency in comparison to the standard data sample. At the same time, the background rate from atmospheric neutrinos and cosmic ray induced muons increases. The sensitivity to a neutrino flux – comparing only the periods of high activity – is slightly better than in the standard sample.

7.2.2 Search for neutrino flares

For the majority of strongly variable sources either no continuous record of electromagnetic emission or no model linking them to neutrino emission exist. Still it is a reasonable hypothesis that if a source is known to be variable in several frequency bands it is also possible to have neutrino emission of variable strength from this source. Consequently one can search for statistical excesses in the time series of events that arrive from the direction of an electromagnetic-variable candidate source.

If neutrinos are emitted in short bursts, such bursts might not show a significant excess in the number of observed events in the 5-year integrated binned search due to the atmospheric neutrino background accumulated in the whole period. However, they remain significant in a dedicated analysis searching clusters in the time series of the events. This is illustrated in figure 7.11 for a hypothetical observation of 8 events on a background of 5.0 events expected in 4 years of AMANDA-II operation. 5 of these events are generated by a simulated flare of 20 days duration. While the Poisson probability to see 8 or more events at 5.0 expected background is relatively high ($P(8|5.0) = 0.13$), the chance probability to have a cluster of 5 events within 20 days at any time within the 4 years of operation is approximately $P(5|20 \text{ days}) = 2 \cdot 10^{-5}$ (evaluated by a simulation of random time series, see below).

In this simple example it is neglected that the prospects and the performance (i.e. the ability to distinguish neutrino flares from random fluctuations of the background) of such

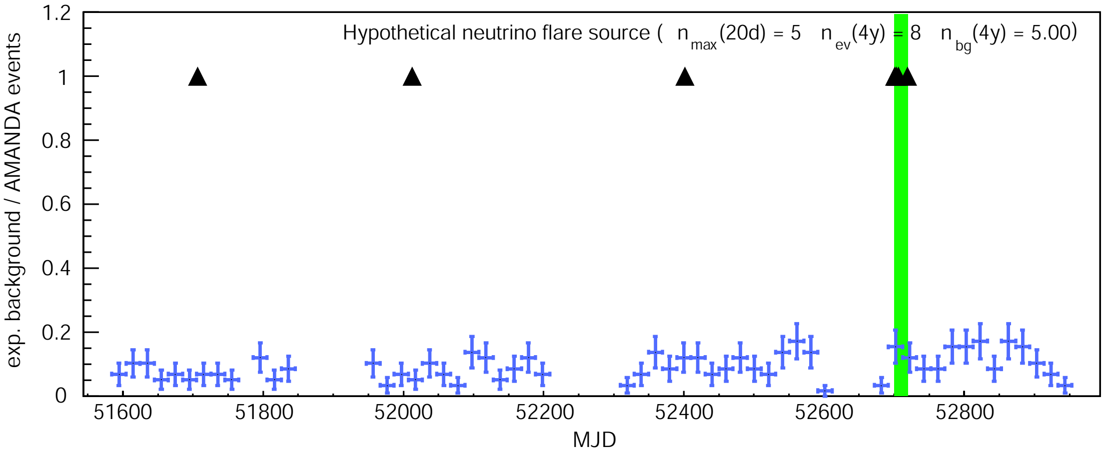

Figure 7.11: *Time-series of events from a hypothetical neutrino flare. From the 8 recorded events (black triangles) 5 fall in a window of 20 days (green box). The expected background is 5.0 events for 2000-2003. It is shown as blue error bars in bins of 20 days duration. In a time integrated analysis, the Poisson probability to see 8 or more events on this background is 0.13. The probability to see 5 events in 20 days is* $2 \cdot 10^{-5}$.

a time series analysis depend on several factors:

- the shape and the duration of the neutrino flares;
- the efficiency of the event cluster search method;
- the average background in the data sample;
- the limit obtained by the 5-year time integrated analysis.

Toy simulation studies

The influence of these parameters can be quantified using a toy simulation of neutrino flares and atmospheric neutrino background. A time series of b events is generated randomly extracting event times from the full data sample. b follows a Poisson distribution around the expected mean background μ_b from atmospheric neutrinos. This method implicitly accounts for variations in the background due to detector livetime variations. On top of this background, k flares of length l and signal strength μ_s (contributing s events with a frequency governed by Poisson statistics) are simulated, by randomly inserting these s events in the time series in a time interval of duration l.

The results from this simulation are then used to develop the statistical test to be applied in the flare analysis. The time series approach is purely detection oriented, meaning that no numerically better flux limits can be derived from a non-observation of a significant event cluster. Therefore, the parameter defining the power of a certain method is the detection probability $P_{det}(f, l, s, \sigma)$ for a flare of defined flux f, length l, shape s at a significance level σ. This detection probability can be easily determined in the simulation by comparing large numbers of simulations with and without signal. An illustration of this method is given in figure 7.12.

The significance level necessary to call an event cluster at least an “indication” for a signal is 3σ. We use this value in the following and always specify the detection probability at 3σ significance level.

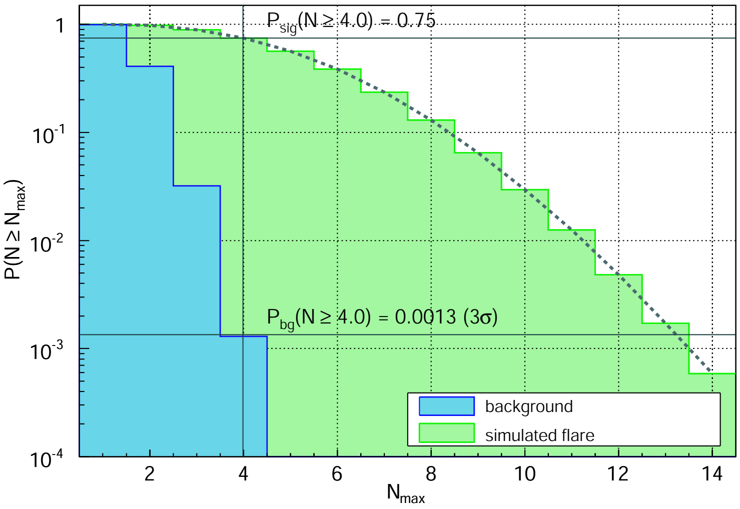

Figure 7.12: *Probabilities to find $N \geq N_{max}$ events within 20 days for uniformly distributed background samples with $\mu_b = 5.0$ (blue) and samples with an added simulated neutrino flare of signal strength $\mu_s = 5.0$ (green). The detection probability of a flare can be derived from the plot: The black vertical line marks the value of $N_{max}^{(3\sigma)}$ for which a fluctuation of the background can be excluded at 3σ confidence level. 75% of the simulated flares show a cluster with $N \geq N_{max}^{(3\sigma)}$ events within 20 days. Therefore, the 3σ detection probability for such a flare is 75%.*

The possible neutrino flux in a flare is restricted by the time integrated analysis. The upper limits from the 5-year analysis exclude at 90% confidence level a higher flux than this limit, stating that a corresponding neutrino flux would have produced more than the observed number of events in 90% of all experiments. So any “hidden” neutrino burst likely has a 5-year average flux considerably lower than this limit. A suitable choice for a flux in a toy simulation is one which would have produced more than the observed number of events in only 50% of the cases, equivalent to a Feldman-Cousins upper limit at 50% confidence level. This flux is used througout the toy simulation.

Length and shape of the expected flares are a-priori unknown. Three different shapes have been used in the toy simulation. A sudden increase of the flux with an exponential decay, a Gaussian flux curve and a uniform distribution of the signal events within the flare. In all cases the length of the flare was defined corresponding to the interval containing 90% of the expected signal events.

Certain (weak) restrictions also apply to the possible length of flares. Flares with a duration on the sub-day scale would have to emit a neutrino flux difficult to accommodate with current understanding of its generation mechanisms to produce a detectable multiplicity of events in AMANDA-II. On the other hand flares with a duration considerably larger than 50 days cannot result in a significant detection for neutrino fluxes, which are still allowed by the time integrated analysis. For the example above there is a 1% probability that 5 events occur in 100 days due to a random fluctuation of the background. In the simulation we probe the detection probability of flares lasting between 0.5% (4 days) and 5.5% (45 days) of the total detector livetime.

Data sample and evaluation method

As in the case of the selection of high state periods, the question remains if the standard data sample optimized for the best sensitivity to neutrino fluxes in 807 effective days of

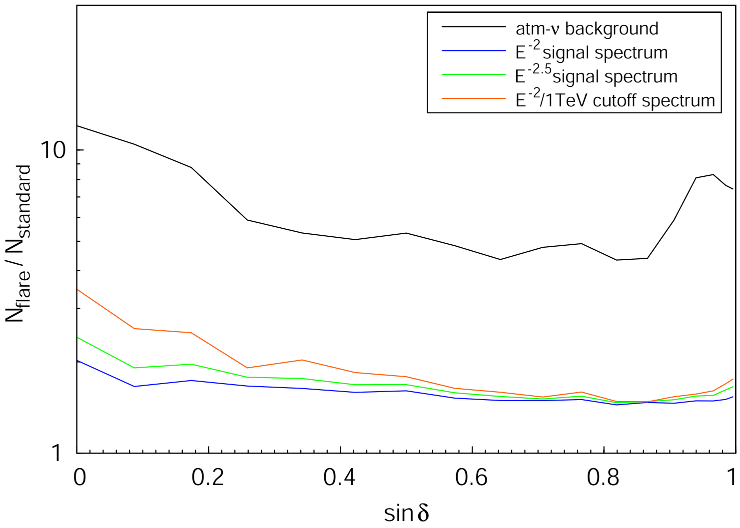

Figure 7.13: *Characteristics of the dedicated data sample optimized for best sensitivity to neutrino fluxes in 50 days of livetime. The black curve shows the declination dependent ratio of background events between this data sample and the standard data sample developed for the 5-year time integrated search. The red green and blue curves show the same ratio for a simulated signal with a differential flux* $d\Phi/dE$ *proportional to* E^{-2}, $E^{-2.5}$ *and* E^{-2} *with a 1 TeV energy cutoff respectively.*

livetime is the optimal sample. Since we are looking for short time phenomena, looser event selection cuts might be better suited to the problem, retaining more signal events at the expense of an increased background rate. To check this conjecture a second sample was created optimized for best sensitivity in 50 days. Figure 7.13 shows the ratios of expected signal events and background between this sample and the standard sample. Different assumptions on the energy spectrum of the signal are included in the comparison. An average gain factor of 1.6 is achieved for the signal strength, while the background is higher by about a factor of 6 in the dedicated data sample (compared to the standard data sample).

Besides the choice of the data sample, several choices exist for the statistical test itself, i.e. how to define event clusters. We restrict ourselves here to compare two methods. The first approach is similar to the binned search in space. A sliding window of fixed length l_W is used and the window with the highest significance is looked for. The second approach is derived from the pair correlation search. The distribution of time differences Δt_{ij} between each event pair is compared to the expected time difference distribution of the backround.

For each combination of search method and data sample the detection probability dependent on the length of the flare was derived from the simulation. For the sliding window a fixed length of $l_W = 20$ d was chosen in this comparison. The results are shown in figure 7.14 for a hypothetical source at the position of Cygnus X-3.

The highest detection probability can be reached for the standard data sample and the sliding window approach. The pair correlation test is severely limited by the low statistics while its power improves for the larger sample. Nevertheless it doesn't reach the performance of the sliding window. Assuming different shapes for the flares (uniform, exponential, Gaussian) does not change this general result. It is also declination independent.

Search window size

The free parameter in the sliding window search is the window length l_W. The simulation was used to compare detection probabilities for different combinations of window lengths and flare durations. The result can be viewed in figure 7.15. No clear optimum is visible here. Shorter windows perform better for shorter flare durations but the detection probability degrades quickly for longer flares.

So the window length should be adapted to the expected flare durations, which are however widely unknown. A trend can be identified for the duration of (electromagnetic) flares by looking at existing light curves. Galactic objects usually exhibit flares on a shorter timescale (hours-weeks) than extragalactic objects (days-months). This is also visible in the comparison of the flares of Markarian 421 and Cygnus X-3 in the light curves presented above. We therefore define different window durations for galactic and extragalactic objects:

- 20 days for galactic objects;
- 40 days for extra-galactic objects.

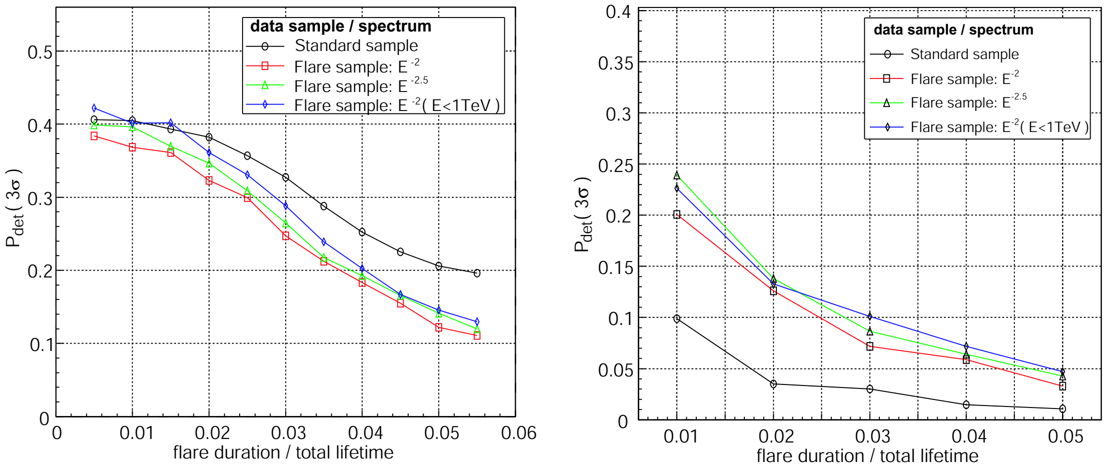

Figure 7.14: *Detection probability for simulated flares from the direction of Cygnus X-3 of different lengths with the sliding window technique (left picture) and the pair correlation test (right picture). The black curve refers to the standard data sample. The blue, green and red curves refer to the dedicated sample optimized for best sensitivity in 50 days of livetime and different hypotheses on the signal spectrum. The detection probability is given at the* 3σ *significance level. The simulated length of the flare is displayed on the x-axis as fraction of the total detector livetime of 807 effective days (0.01* $\simeq$ *8 effective days).*

7.2.3 Source candidates for the flare search

The detection probabilities above are calculated for the case that only a single source is tested. If the sliding window search is applied to many sources a trial factor has to be accounted for. Since the observations are independent, this trial factor reduces the significance of the observation of a flare as described in (7.5).

Therefore the number of sources in this test should be small and the test should only be applied to the most promising candidates. Only sources from the previously presented catalog of potential neutrino emitters have been selected which show a strong indication

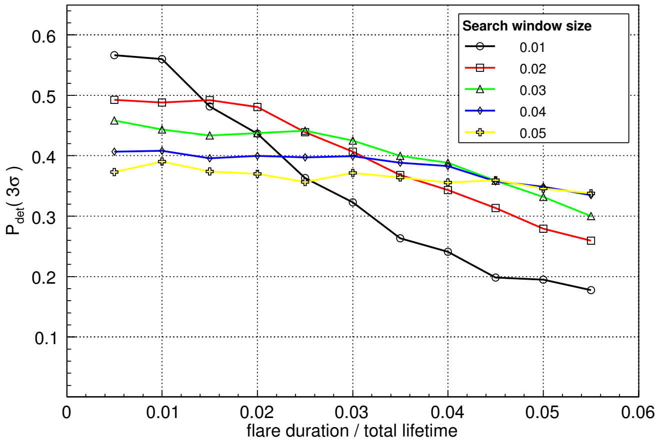

Figure 7.15: *Detection probability for simulated flares of different lengths with sliding windows of fixed size. Different colors represent different window durations. The simulated length of the flare and the window size are displayed as fractions of the total detector livetime of 807 effective days (0.01 $\simeq$ 8 effective days).*

of variability. To this list unidentified sources observed in high energy gamma-rays by the EGRET instrument were added, in case an extremely high variability was reported.

For all sources visible to EGRET in this selection, we follow a definition of variability presented by [N^+03]. A variability index δ is defined there as well as the 68% confidence interval $[\delta_{min}, \delta_{max}]$ for its value. We define two thresholds: Sources which are not in our candidate catalog are required to exhibit a $\delta_{min} > 0.7$ in accordance with the definition of the "highest variability sources" in [N^+03]. For sources already in the catalog this criterion is relaxed to a mean variability $\delta > 0.7$. This results in the selection of the established GeV Blazars QSO 0235+164 and QSO 1156+295 as well as the unidentified EGRET sources 3EG J0450+1105, 3EG J1227+4302, 3EG J1828+0142 and 3EG J1928+01733.

All Microquasars among the list of neutrino candidate sources are tested in the flare search with the exception of SS433 (features persistent jets [HJ81]), CI Cam (Microquasar classification unclear [MR04]) and LSI +61 303 (periodic [GPT99]). From the TeV-visible Blazars on the northern hemisphere only Markarian 421 and 1ES 1959+650 were selected showing strong flaring activity between 2000-2003 in the X-ray and TeV frequency bands. Supernova remnants and Pulsars are not suspected to show strong variability and are therefore omitted. Table 7.6 summarizes the sources selected for the flare search.

Source name	RA/h	Dec/°	References	other names
TeV Blazars				
Markarian 421	11.1	38.2	[B$^+$05b]	
1ES 1959+650	20.0	65.1	[K$^+$04]	
GeV Blazars				
QSO 0219+428	2.4	42.9	[N$^+$03]	3C 66A, 3EG J0222+4253
QSO 0235+164	2.6	16.6	[N$^+$03]	3EG J0237+1635
Microquasars & Neutron star binaries				
GRO J0422+32	4.4	32.9	[LW01]	
XTE J1118+480	11.3	48.0	[LW01]	
GRS 1915+105	19.3	10.9	[LW01]	
Cygnus X-1	20.0	35.2	[LW01]	
Cygnus X-3	20.5	41.0	[LW01]	
Unidentified high energy gamma-ray sources				
3EG J0450+1105	4.8	11.4	[N$^+$03]	
3EG J1227+4302	12.5	43.0	[N$^+$03]	
3EG J1828+0142	18.5	1.7	[N$^+$03]	
3EG J1928+1733	19.5	17.5	[N$^+$03]	

Table 7.6: *Sources considered in the sliding window search for neutrino flares.*

Chapter 8

Results from the searches for neutrino point sources

8.1 The sky plot

Once the event selection is finalized and the analysis strategies are set, the directional information of the neutrino events in the data sample are "un-blinded". The statistical tests previously defined are applied to eventually find the first cosmic neutrino sources or in case of no detection to set upper limits on the neutrino fluxes compatible with the observation. Figure 8.1 shows the directions of the 4282 neutrino events selected with positive declinations in the years 2000-2004 in an equal area (Hammer-Aitoff) projection.

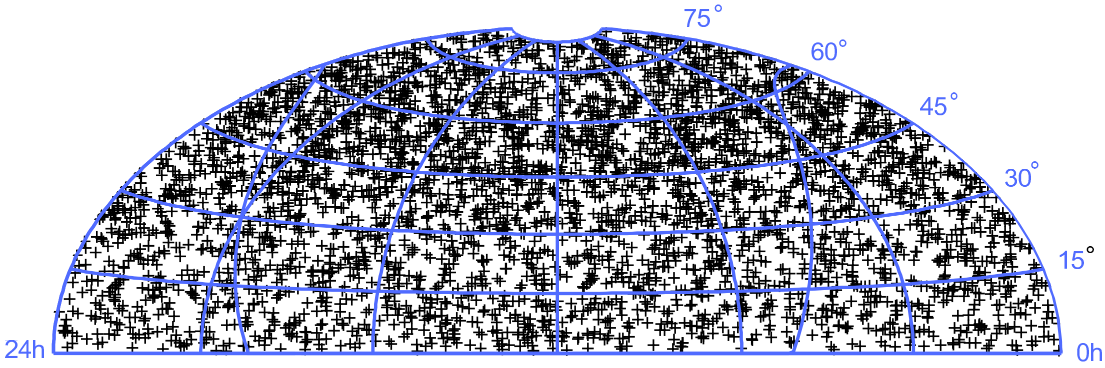

Figure 8.1: *Sky map of the 4282 neutrino events selected with positive declinations displayed in Hammer-Aitoff equal area projection.*

The event density increases with declination as the detector angular resolution gets better. This improved angular resolution allows smaller search bins and therefore relaxed selection cuts leading to higher event densities on the sky map while keeping the level of background inside the search bin approximately constant. The results from the statistical tests introduced in the last section are now reported starting with the scan of the catalog of predefined neutrino sources.

8.2 Selected candidate sources

Observations

A total of 194 events is found in the search bins around the positions of the 34 candidate sources in the catalog. That is compatible with the total expected background from atmospheric neutrinos of 208.3 ± 14 events. The maximum number of events found inside the search bin around a single source is for the Crab Nebula with 10 events compared to an expected background of 6.74. The highest excess parameter $\mathcal{S}$ is obtained for 3C273 with 8 observed events over 4.72 expected background. Already in a single observation the probability is 10.4% that the observed result is a fluctuation of the background. We therefore omit the calculation of the real significance of the excess accounting for trial factors. The signal hypothesis is already discarded by the probability stated above.

We also conclude that no excess was found which would be incompatible with a fluctuation of the background. Table 8.1 summarizes the results from this analysis for all 34 sources in the catalog. For each source the number of observed events, the expected background and the corresponding excess parameter is given. A flux upper limit is calculated for each source based on the observations presented here in section 9.4, after systematic errors of the analysis have been discussed.

Excess parameter distribution

Important cross checks for this analysis are to demonstrate that the observed fluctuations are indeed compatible with what is expected from a sample of atmospheric neutrino events. In that case the observed fluctuations should not depend on the actual position of the sources, and be in agreement with fluctuations of events isotropically distributed in right ascension. Therefore we compared the distributions of the excess parameters of the 34 candidate sources to the corresponding distributions for two cases:

- 100 sets of 34 randomly distributed sources;
- 100 event samples with events randomized in right ascension.

The result of the tests are displayed in figure 8.2. Both distributions are compatible within the errors. There is no indication of phenomena other than fluctuations of the atmospheric neutrino background.

8.3 Grid search on the northern hemisphere

Observations

To test the hypothesis that neutrinos are emitted from objects that are not included in the catalog of 34 candidate sources, a grid scan of the full northern hemisphere is performed in steps of 0.5° as described in section 7.1.3. For each grid center the excess parameter $\mathcal{S}$ is calculated based on the number of events found in the search bin and the events expected from atmospheric background. An “excess”-map of the northern sky is created and the highest excess obtained on this map is compared to simulations of events randomized in right ascension to determine its significance.

Figure 8.3 displays this map in Hammer-Aitoff and linear projections. On the second map the sky positions of the candidate sources are shown. The highest excess is found

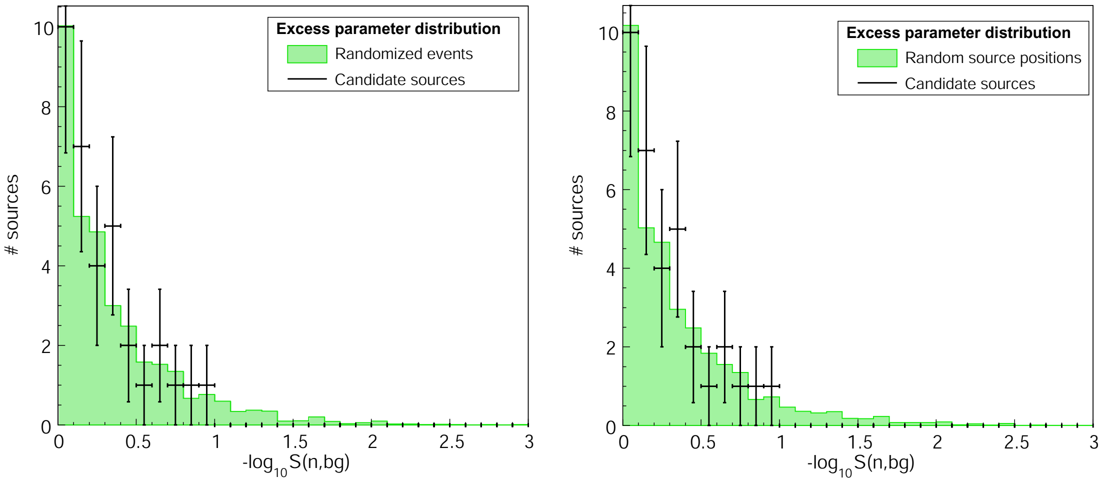

Figure 8.2: *Distribution of the excess parameter $\mathcal{S}$ for samples of events randomized in right ascension (left picture) and samples with random candidate source positions (right picture). The distribution of $\mathcal{S}$ for the real source positions and event directions is shown as black error bars on top of each of the two histograms.*

at a declination of $\delta = 4°$ and a right ascension of $\alpha = 12.6$ h. The value of the excess parameter on this spot is 3.74σ. 17 events are found compared to an expected background of 5.76. A test with 1000 simulations of randomized event samples shows that 69% of these samples have a maximum excess parameter equal to or higher than 3.74σ. Therefore it can be concluded that the observed accumulation of events is expected from fluctuations of the atmospheric neutrino background. The direction of the maximum excess found in the data is compatible with an unidentified gamma-ray source, 3EG J1236+457, detected by EGRET. It should be considered to include this source in the list of candidates for future tests on independent data samples.

Excess parameter distribution

Like in the search for a signal from candidate neutrino emitters the distribution of the excess parameter in comparison to samples of events randomized in right ascension is an important cross check. A comparison of the two excess parameter distributions is shown in figure 8.4. The data is compared to the average from 100 randomized samples. Good agreement is visible. A negative excess is defined here as the probability $P(\leq n, b)$ to see less than or equal to n events on an expected background b (in units of σ). The artefacts visible as peaks in the region of negative excess parameters as well as the asymmetric shape are due to the discreteness of the binomial probability $P(\leq n, b)$ and its asymmetric shape for small b. They are also visible in the randomized samples.

No indication is found for a distribution of excess parameters incompatible with the hypothesis of a background uniformly distributed in right ascension.

Source name	RA/h	Dec/°	search bin size	N_{obs}	N_{bg}	$-\log_{10}\mathcal{S}$
TeV Blazars						
Markarian 421	11.1	38.2	3.25	6	7.37	0.13
1ES 1426+428	14.5	42.7	2.75	5	5.52	0.19
Markarian 501	16.9	39.8	3.00	8	6.39	0.51
1ES 1959+650	20.0	65.1	2.25	5	4.77	0.29
1ES 2344+514	23.8	51.7	2.50	4	6.18	0.06
GeV Blazars						
QSO 0219+428	2.4	42.9	2.75	5	5.52	0.19
QSO 0235+164	2.6	16.6	3.50	7	6.12	0.38
QSO 0528+134	5.5	13.4	3.50	4	6.08	0.07
QSO 0716+714	7.4	71.3	2.25	1	4.20	0.01
QSO 0954+556	9.9	55.0	2.50	2	6.26	0.01
3C273	12.5	2.1	3.75	8	4.72	0.98
QSO 1611+343	16.2	34.4	3.25	6	6.96	0.16
QSO 1633+382	16.6	38.2	3.25	9	7.37	0.50
other AGN						
NGC 1275	3.3	41.5	3.00	4	6.75	0.04
M87	12.5	12.4	3.50	6	6.08	0.25
Microquasars & Neutron star binaries						
LSI +61 303	2.7	61.2	2.25	5	4.81	0.28
CI Cam	4.3	56.0	2.50	9	6.34	0.72
GRO J0422+32	4.4	32.9	3.25	9	6.72	0.63
AO 0535+26	5.7	26.3	3.50	7	6.48	0.33
XTE J1118+480	11.3	48.0	2.75	3	7.05	0.01
SS433	19.2	5.0	3.75	4	6.14	0.06
GRS 1915+105	19.3	10.9	3.50	7	6.07	0.39
Cygnus X-1	20.0	35.2	3.25	8	7.01	0.39
Cygnus X-3	20.5	41.0	3.00	7	6.48	0.33
Supernova Remnants & Pulsars						
PSR J0205+6449	2.1	64.8	2.25	1	4.68	0.00
Crab Nebula	5.6	22.0	3.50	10	6.74	0.84
Geminga	6.6	17.9	3.50	3	6.23	0.02
SGR 1900+14	19.1	9.3	3.50	5	5.65	0.18
PSR 1951+32	19.9	32.9	3.25	4	6.72	0.04
Cassiopeia A	23.4	58.8	2.50	5	6.00	0.15
AGASA UHECR Multiplets						
Multiplet 1	1.3	20.4	3.50	5	6.29	0.12
Multiplet 2	11.3	56.9	2.50	7	5.91	0.42
Unidentified high energy gamma-ray sources						
3EG J0450+1105	4.8	11.4	3.50	8	5.94	0.61
TeV J2032+4131	20.5	41.5	3.00	7	6.75	0.29

Table 8.1: *Results from the search for an excess of neutrino events from the directions of the candidate sources. From left to right are listed the name of the candidate source, its sky position, the radius of the search bin, the number of observed events, the expected background in the search bin and the logarithm of the probability to see such an excess $\mathcal{S}$ (excess parameter).*

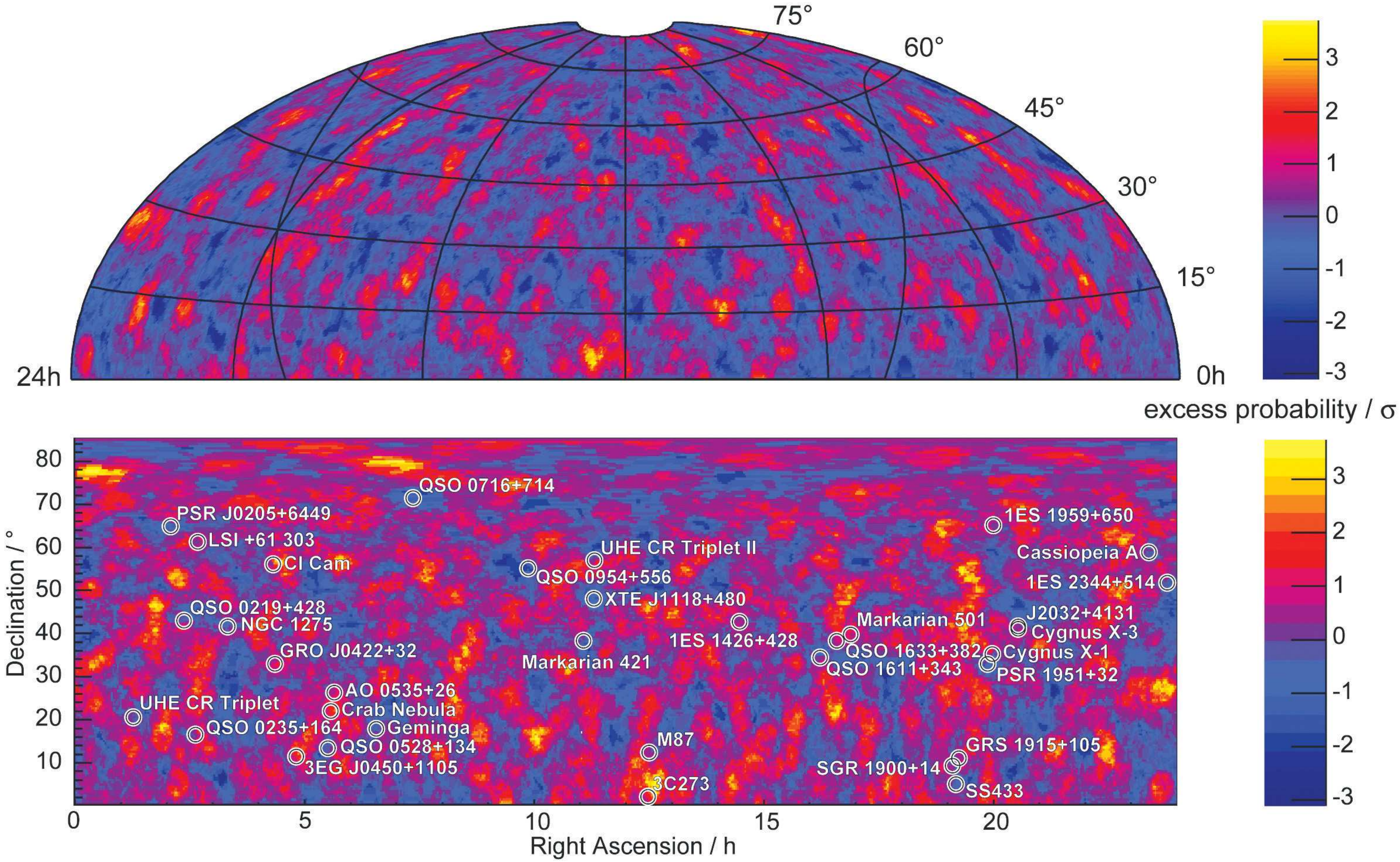

Figure 8.3: *Maps of the excess parameter distribution on the sky in Hammer-Aitoff and linear projections. The curved line on the upper map symbolizes the galactic plane. The circles with source names display the sky positions of the sources in the candidate catalog.*

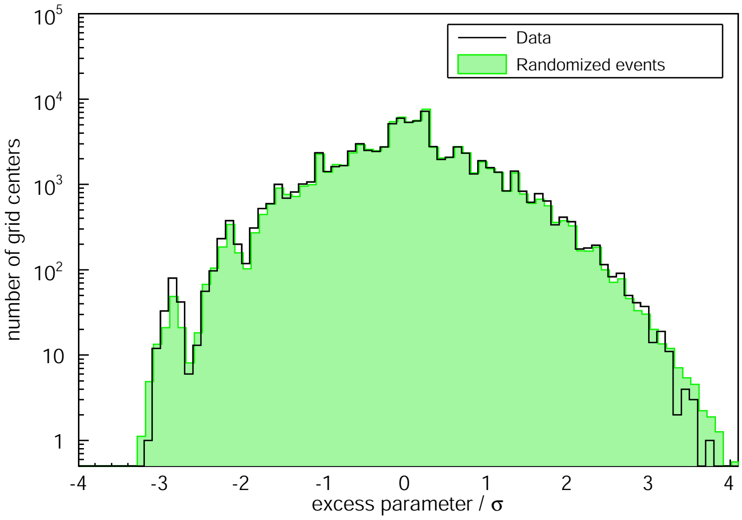

Figure 8.4: *Distribution of the excess parameter $\mathcal{S}$ for all search grid centers (black line). It matches very well the distribution of $\mathcal{S}$ gained from samples of events randomized in right ascension. The peaks at negative $\mathcal{S}$ are artefacts due to the discreteness of binomial statistics.*

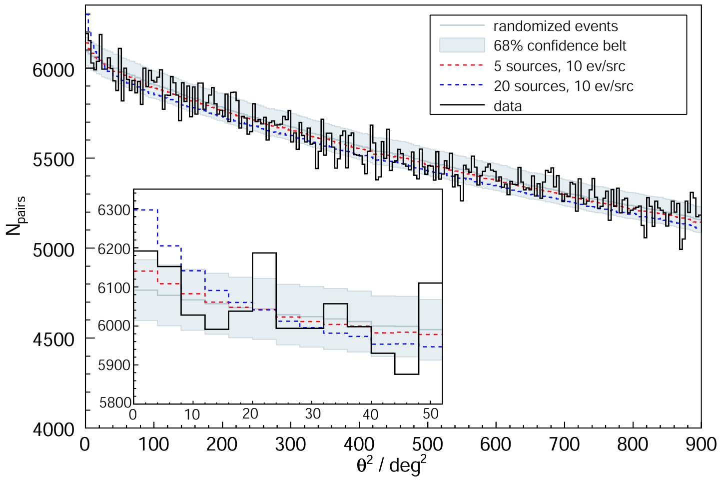

Figure 8.5: *Distribution of the squared angle between event pairs θ^2 for the data in comparison to samples with $N_S = 5$ and $N_S = 20$ simulated sources. The expected number of event pairs gained from simulation of randomized events and its standard deviation are shown in grey. They describe the expectations for a pure atmospheric neutrino sample.*

8.4 Angular correlation studies

To exclude (or find indications for) the possibility that many small sources – individually too weak to produce significant excesses – are hidden in the data sample, a test on correlations of the angle between combinations of event pairs has been performed. The χ^2-test was introduced in section 7.1.4 and its performance investigated. Figure 8.5 shows the expected distribution of the squared angle θ^2 between combinations of event pairs for a sample of pure atmospheric neutrino background and in the presence of several weak sources. The actual squared angle distribution of the data is superimposed in black.

The reduced χ^2-value obtained from comparing data to atmospheric neutrino background is (223 degrees of freedom):

$$\frac{\chi^2}{\text{n.d.o.f}} = 0.91 \,.$$

The probability to have such an or higher reduced χ^2-value is $P_{\chi^2} = 0.81$. Therefore the hypothesis that the data sample is a pure atmospheric neutrino sample cannot be rejected. No indications for a contribution from weak neutrino sources was found. Also no indication for a correlation on larger scales was discovered, which might point to detector operation instabilities.

8.5 Selection of high state periods of variable sources

For variable sources the chances to find a neutrino emission might be increased by the selection of active periods of the source. As discussed in section 7.2.1 such a selection can be performed analyzing the light curves of the electromagnetic emission of a source in a certain spectral band. Two sources, Markarian 421 and Cygnus X-3, were selected for this type of analysis. The active periods were defined and a dedicated data sample was created, optimized for a shorter detector livetime.

A comparison of the arrival times of neutrino events, recorded in the 3.75° bins around the sources, to the selected 141 effective days of high activity is shown in figure 8.6. For Markarian 421 one finds 1 out of 7 events in coincidence with a period of high state of the source. The atmospheric neutrino background is expected to contribute 1.63 events in these intervals. Hence, the observation shows no indication for a cosmic neutrino signal correlated to the states of high X-ray emission of the source. 114 effective days of AMANDA-II livetime have been selected for which Cygnus X-3 showed a high radio flux. 2 out of 13 neutrino events recorded fall into these periods. The expectation from

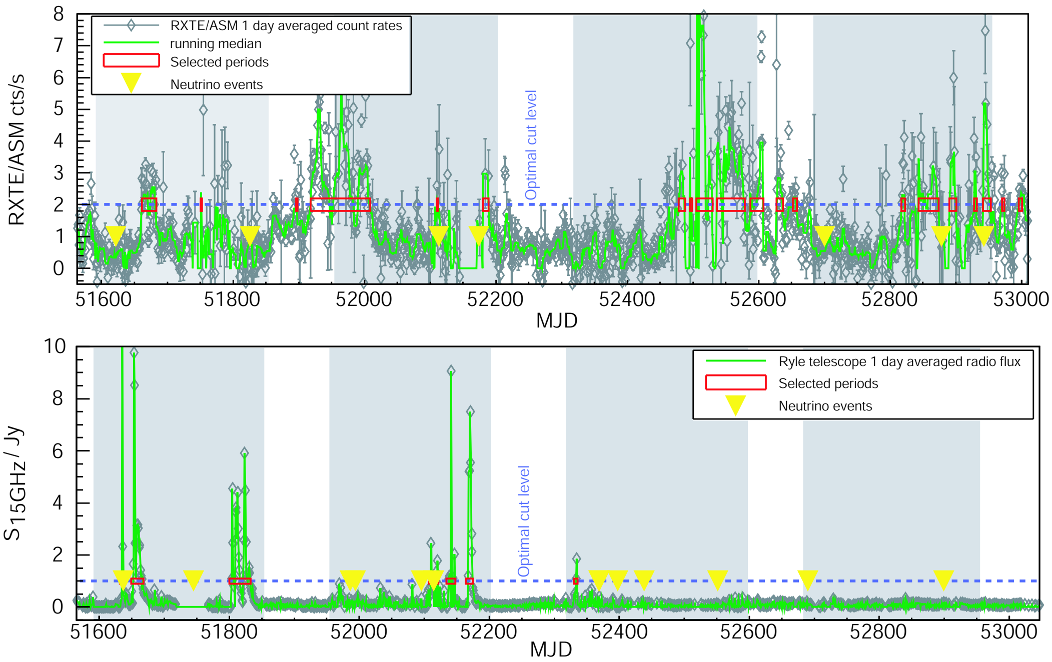

Figure 8.6: *X-ray light curve of Markarian 421 (upper picture) and radio light curve of Cygnus X-3 (lower picture) with AMANDA-II event arrival times superimposed. The arrival times correspond to the peaks of the yellow triangles. The time intervals selected as periods of high source activity are shown in red.*

atmospheric neutrinos is 1.39 events. So we conclude that also for this source no evident contribution from a cosmic neutrino signal can be seen. Upper limits to the neutrino flux compatible with this experimental result will be presented for both sources in section 9.4.

8.6 Sliding window search for neutrino flares

A sliding window search was developed (see section 7.2.2) for sources, where a selection of high states based on EM-emission light curves is impossible due to a lack of available data, or to have a model independent approach to detect neutrino flares.

13 sources known to exhibit strong variability in their electromagnetic emission have been tested, if a cluster of neutrino events can be found within a time span of 20 days (galactic sources) or 40 days (extragalactic sources), which is not expected from atmospheric neutrino background. A graphical display of the results for a few sources is presented in figure 8.7. The arrival time of the neutrino events is indicated by black triangles, the expected background binned in periods equal to the size of the sliding search window is represented by the blue error bars. The green box marks the position of the sliding window at which the highest multiplicity of neutrino events is found.

No multiplicity of events larger than 2 was found in a single search window for any of the sources analyzed. Table 8.2 summarizes the results. For each source it is indicated if a doublet was found or not and the probability for such a doublet, to occur from random fluctuations of the background. The lowest probability found is 0.32, therefore all doublets can be expected to originate from atmospheric neutrinos. No indication for a neutrino flare from the sources investigated was found.

Source name	RA/h	Dec/°	sliding window duration	doublet found	$P^{\mathrm{atm}-\nu}_{\mathrm{doublet}}$
			TeV Blazars		
Markarian 421	11.1	38.2	40 days	no	
1ES 1959+650	20.0	65.1	40 days	yes	0.34
			GeV Blazars		
QSO 0219+428	2.4	42.9	40 days	no	
QSO 0235+164	2.6	16.6	40 days	yes	0.52
			Microquasars & Neutron star binaries		
GRO J0422+32	4.4	32.9	20 days	no	
XTE J1118+480	11.3	48.0	20 days	no	
GRS 1915+105	19.3	10.9	20 days	yes	0.32
Cygnus X-1	20.0	35.2	20 days	no	
Cygnus X-3	20.5	41.0	20 days	no	
			Unidentified high energy gamma-ray sources		
3EG J0450+1105	4.8	11.4	40 days	yes	0.47
3EG J1227+4302	12.5	43.0	40 days	yes	0.43
3EG J1828+0142	18.5	1.7	20 days	no	
3EG J1928+1733	19.5	17.5	20 days	yes	0.35

Table 8.2: *Results from the search for a neutrino flare with sliding windows. It is shown the source name, the source position, the used search window size and if an event doublet was observed or not. The chance probability that such a doublet results from a fluctuation of the atmospheric neutrino background* $P^{atm-\nu}_{doublet}$ *is quoted in the last column.*

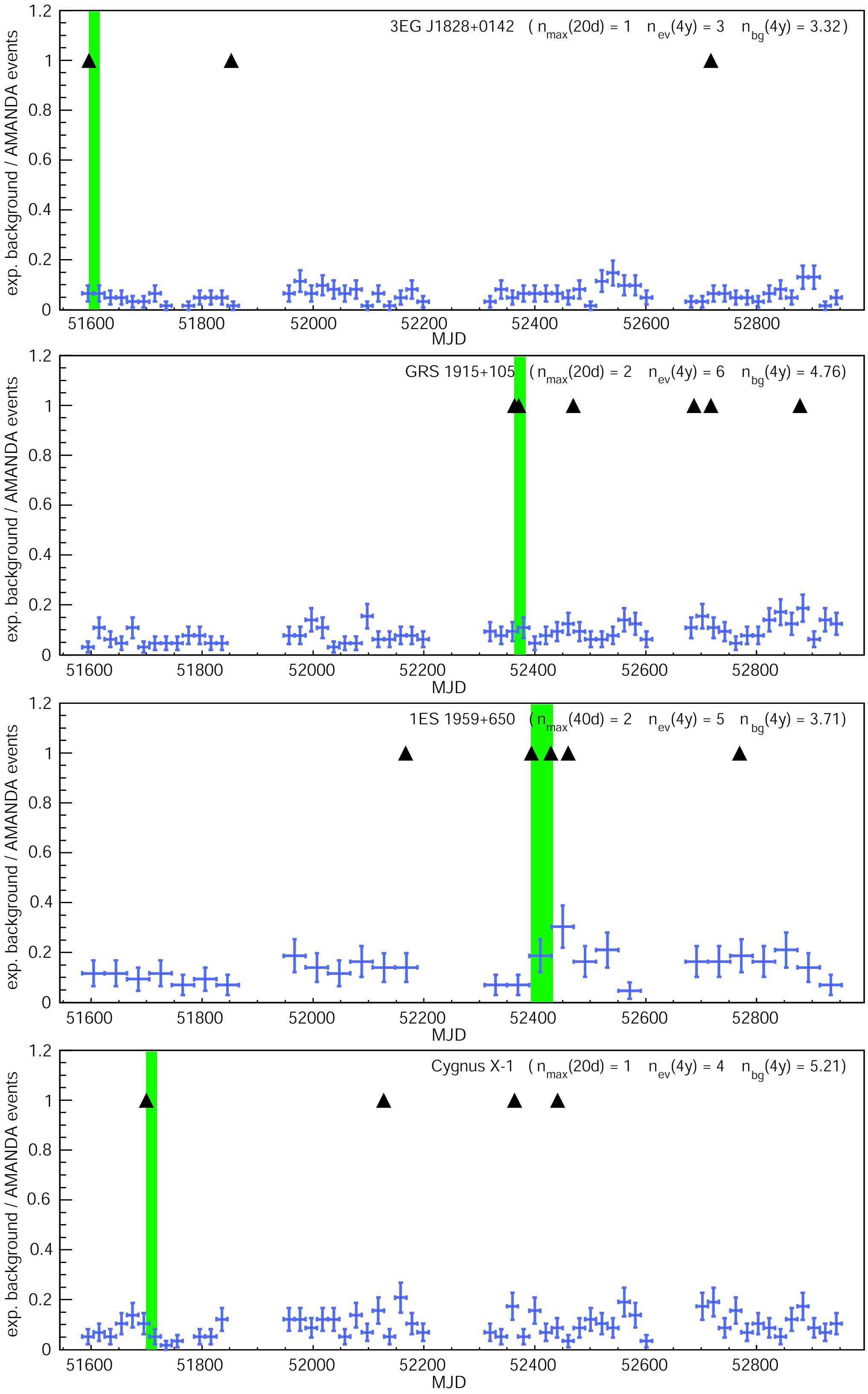

Figure 8.7: *Selected results from the search for neutrino flares. For each tested source the green region shows the 20-day/40-day time window found containing the highest multiplicity of events. The peaks of the black triangles point to the arrival times of the AMANDA-II events. The blue error bars correspond to the rate of background events expected during a time period corresponding to the size of the search window.*

8.7 Observations for the Blazar 1ES 1959+650

Even though the search for a neutrino flare did not yield a significant detection the arrival times of the neutrino events from the TeV Blazar 1ES 1959+650 show a remarkable feature: 3 out of 5 neutrinos arrived in 66 days between MJD 52394 (May 2002) and MJD 52460 (July 2002). Within this period, on MJD 52410, the WHIPPLE Gamma-ray telescope observed extremely strong flaring of this source with the measured flux above 600 GeV reaching several times the flux from Crab Nebula [H$^+$03]. This observation triggered an extensive multi-wavelength campaign. The source was observed by several instruments in the radio, optical, X-ray and high energy gamma-ray frequency bands between MJD 52410 and MJD 52500. The results from this campaign are published in [K$^+$04]. During this observation period several intense flares in TeV gamma-rays were observed by WHIPPLE as well as by the HEGRA telescope [A$^+$03a]. Neither before MJD 52410, nor from MJD 52500 on until today any other outbursts were observed in regular scheduled observations of this source.

The most peculiar of these flares was observed by WHIPPLE on MJD 52429 which reached a flux of > 4 Crab and had no visible counterpart in X-rays. This singular phenomenon became known as the "orphan" flare of 1ES 1959+650. It is difficult to accommodate with simple Synchrotron-Self-Compton models [K$^+$04] and a mechanism involving hadron acceleration has been suggested to explain this phenomenology [Boe05].

Figure 8.8 superimposes the time of the neutrino events recorded in AMANDA-II from the direction of 1ES 1959+650 on the results of the multi-wavelength campaign [K$^+$04]. The first event at MJD 52394.0 precedes the campaign by a few days. The second event arrives at MJD 52429.0 only ≈ 7 h before the "orphan" flare was detected. The third event at MJD 52460.3 coincides with a smaller flare detected by WHIPPLE which shows a flux of about 1 Crab.

The close correlation in time between the neutrino events and TeV flares triggered a vivid discussion if current hadronic models of gamma-ray emission deliver a flux high enough, so that events would likely be detected in AMANDA-II [HH05, RBP05] with different conclusions. From the experimental point of view no answer can be given if these neutrinos are due to source emission or atmospheric neutrino background, since no hypothesis was defined a-priori for this phenomenology, on which a frequentist significance test could be performed. An unbiased estimate of the involved trial factors is impossible. Future observations of similar phenomena with predefined statistical tests are necessary to find an answer, if such flares exhibit hadronic acceleration and if neutrinos are produced abundantly enough to be visible in AMANDA-II.

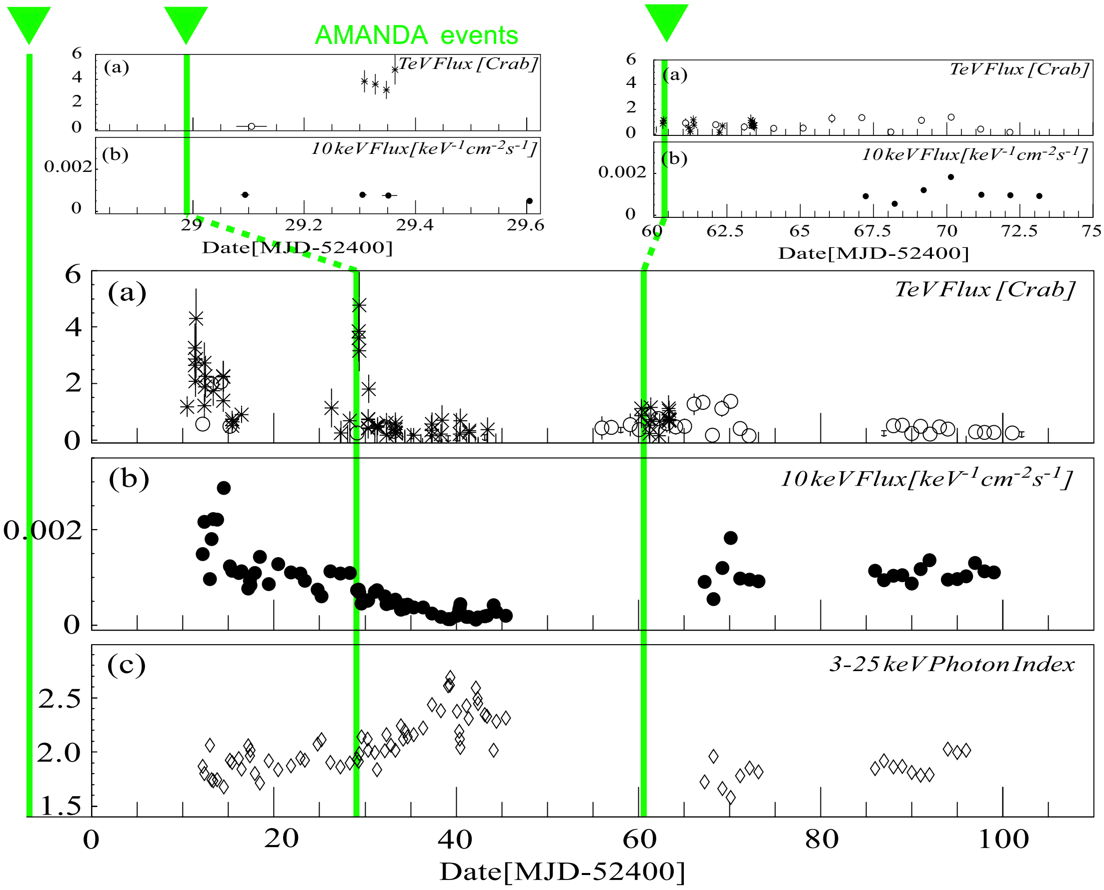

Figure 8.8: *Multi-wavelength observations of 1ES 1959+650 after MJD 52410 (Picture taken from [K^+04]). TeV photon fluxes measured by the WHIPPLE telescope are indicated by stars, measurements from HEGRA by open circles. The X-ray flux (full circles) and photon index (diamonds) was measured by the Proportional Counter Array on board of the RXTE satellite. The light curves recorded during the flares at MJD 52429 and MJD 52460 are displayed magnified in the upper part of the picture. The arrival time of the neutrino events seen from the direction of 1ES1959+650 by AMANDA-II is indicated by the green triangles and lines.*

Chapter 9

Flux limits in the presence of systematic uncertainties

9.1 Sources of systematic uncertainties

For an underground neutrino telescope there are two groups of effects which lead to the introduction of systematic biases into the measurement. The first is the limited accuracy to which detector operation parameters can be determined. Being frozen more than a kilometer deep in the ice, the Optical Modules are inaccessible once deployed. Moreover, the environment deep in the glacier is completely different compared to any laboratory simulation. Temperatures around -30° Celsius at pressures up to 200 bar cannot be artificially created at the surface (or only at unacceptable costs). Changes in the Optical Module response in the ice compared to the surface have to be evaluated using the limited calibration equipment described in section 3.1, which was deployed in the ice together with the string. Also "natural beams" – cosmic ray induced muons and neutrinos – with their rather well known properties are used to find constraints on the uncertainty to which we know the response of each of the 677 AMANDA-II Optical Modules to arriving photons.

The second possible bias for flux measurements is the simulation of the interaction physics and of the detector response. Foremost, no simulation can be more accurate than the degree to which the underlying physics is known. The neutrino-nucleon cross sections as well as the cross sections contributing to the energy loss of the muon have considerable uncertainties at the energies of interest. Secondly, due to the huge size and complexity of the AMANDA-II environment, one is forced to introduce simplified parameterizations in the simulation even beyond the state of knowledge. Especially the propagation of the photons in the inhomogeneous ice of the south pole glacier is too complex to be modeled in every detail. Here the available computing resources define the limit for the level of accuracy in the simulation.

The purpose of this section is to introduce and quantify the different sources of the systematic error for this analysis. As will be explained later, only the systematic error on the predicted number of events for a certain neutrino flux enters the limit calculation. This uncertainty usually depends on the assumed energy spectrum of the neutrino flux. Therefore, if applicable, uncertainty intervals for the neutrino rate are given for different energy spectra. All errors are assumed to be uncorrelated, so the total error can be determined by the geometrical sum of the components. This is a conservative approach, since in case of a correlation of the errors the real systematic uncertainty would be smaller than the error presented here.

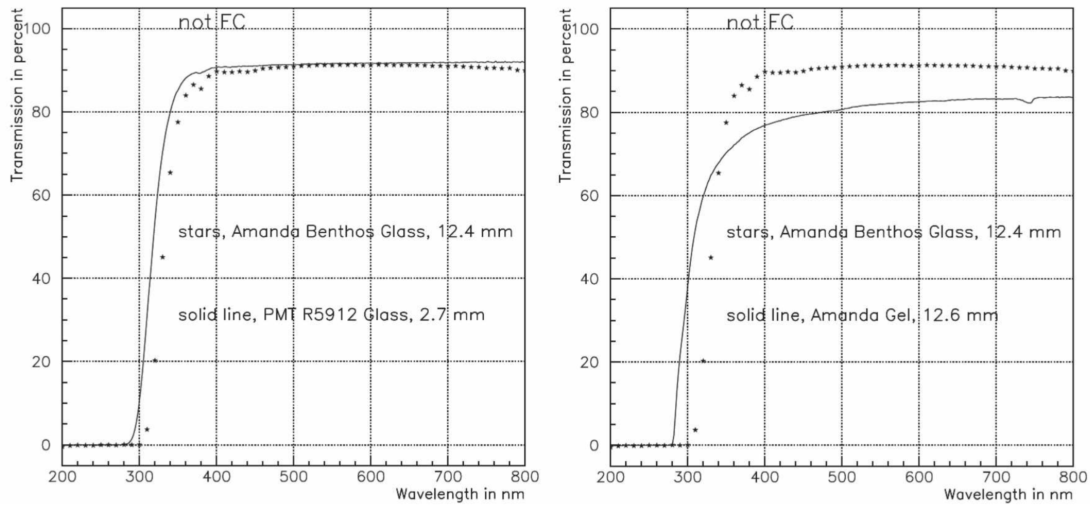

Figure 9.1: **Left**: *Wavelength dependent transmissivity of the Benthos borosilicate glass pressure spheres used for Optical Modules in strings 5-20 in the AMANDA-II detector compared to the transmissivity of the PMT glass.* **Right**: *Transmissivity of the Benthos glass compared to the transmissivity of a gel sample extracted from an unused Optical Module. Pictures taken from [Sud01].*

9.1.1 Efficiency of the Optical Module

The total light collection efficiency of the Optical Module is governed by the quantum efficiency of the Photomultiplier and by the transmissivities of the surrounding components (pressure vessel and gel). Data on the quantum efficiency of the Hamamatsu PMT is provided by the company. The wavelength dependent transmissivity of the glass spheres and the gel were measured in the laboratory at room temperature in [Sud01]. Figure 9.1 shows some results of these tests. Extensive measurements of gel samples from different production cycles have recently been performed by the IceCube collaboration during the assembly of the IceCube Digital Optical Modules, which use the same gel [Voi05].

The transmissivity of the gel showed variations of up to 10% in these measurements which were done on gel samples of 10 mm thickness. In the assembled Optical Module the thickness of the gel layer can vary by a few mm increasing the uncertainty on the transmissivity [Sud01]. Additionally, during cold room tests at $-45°$ Celsius the gel was observed to become milky, however no loss in transmissivity was observed [Nah05]. Compared to these large variations, the uncertainty on the glass transmission and PMT quantum efficiency can be neglected and it can be stated that the main uncertainty for the Optical Module transmissivity originates from the gel.

All these tests are performed for environmental conditions which do not match the ones found in the South Pole glacier. The real efficiency might differ from the values obtained in the laboratory. Hence, the systematic uncertainty has to be re-evaluated using in-ice calibration equipment and natural calibration beams, like cosmic ray induced muons and atmospheric neutrinos. Earlier works based on light seen in the upward looking modules and the distribution of the number of hit channels for cosmic ray induced muons [BW00, OW01] conservatively estimate a ±30% uncertainty on the Optical Module efficiency.

A newer analysis dedicated to infer the fluctuations of the sensitivity of the Optical Modules (in comparison to their average) was performed in [Lan05]. It uses a selection of well reconstructed downward going muons to find a relative variation of 11% between the modules. This result is roughly in agreement with the number found in the laboratory

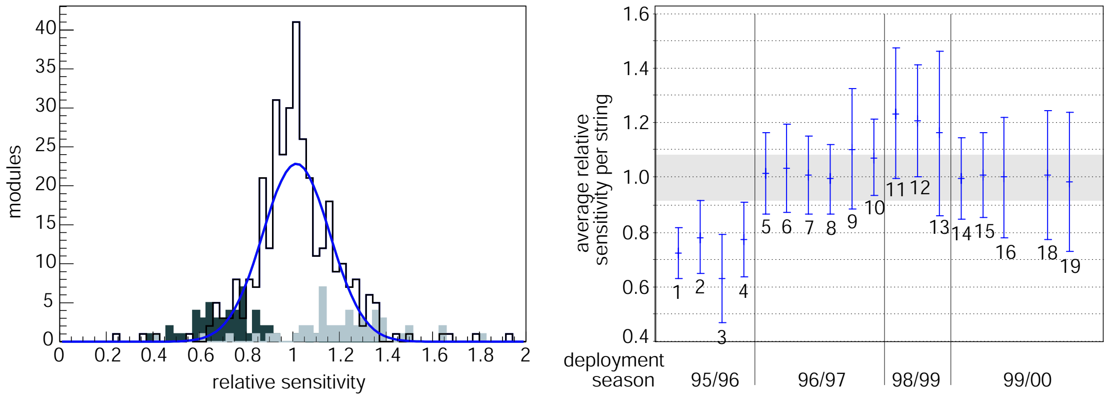

Figure 9.2: *Left: OM photon collection efficiencies divided by the average efficiency derived in [Lan05] from 2001 data. Right: String-wise average of the individual OM sensitivities and corresponding string deployment years. Strings 1-4 have lower sensitivities due to the different glass type used for the OM pressure spheres on these strings.*

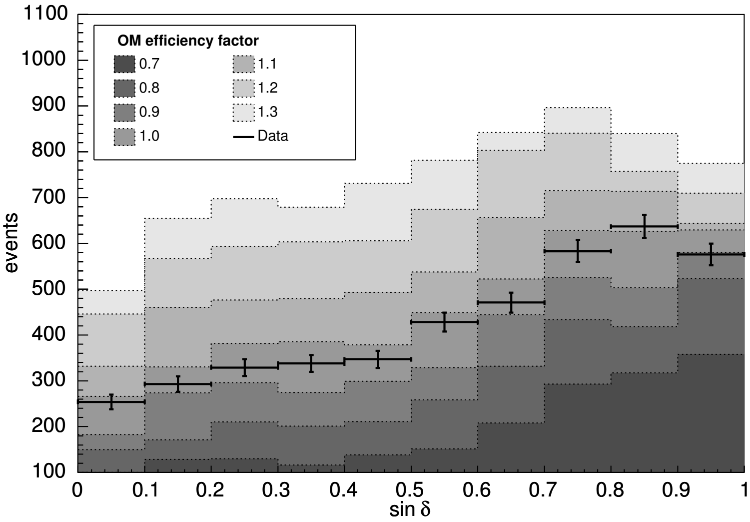

Figure 9.3: *Declination distribution of the final event sample in comparison to atmospheric neutrino simulations with varied OM photon collection efficiencies. The efficiency is given relative to the nominal OM efficiency used for standard simulation.*

measurements stated above. Figure 9.2 shows the efficiencies of the individual Optical Modules derived there relative to their average efficiency and the string to string variation. The average is taken over all modules at a certain depth. The average itself and its uncertainty remain undefined in this method.

Strings 1-4 show a much lower collection efficiency. The pressure spheres for these strings were produced by a different manufacturer (Billings). The direct measurements in [Sud01] mentioned above show that the type of glass used in the Billings spheres absorbs UV light much stronger than the standard glass (Benthos). Integration of the spectral efficiency convoluted with the Čerenkov spectrum results in an effective sensitivity of 76 ± 2 % relative to the OMs housed in standard pressure vessels. This is in very good agreement with the results in 9.2.

We found that a test on the declination distribution of atmospheric neutrinos can be used, to determine the in-ice average sensitivity of the Optical Modules more accurately then before. Figure 9.3 shows the atmospheric neutrino declination distributions expected from simulation using different average OM efficiencies between 70% and 130%. The percentages characterize the simulated efficiency of the Optical Module relative to the efficiency in the standard simulation. This standard simulation incorporates the best knowledge from laboratory measurements for glass, gel and boundary layer transmissivities as well as the OM quantum efficiency.

The ratio of vertical to horizontal events changes significantly with increased OM efficiency. The origin of this effect is a combination of AMANDA-II geometry and trigger logic. A lower OM efficiency leads to a lower multiplicity of hit channels. An event is only recorded by the trigger if it has a multiplicity > 24 channels. Vertical events generally have higher multiplicities since the extension of the detector in the vertical is bigger than in the horizontal. The number of horizontal events is therefore more sensitive to a change in OM efficiency than the number of vertical events.

One can utilize this variation in the declination distribution to determine the range of OM efficiencies which is compatible with the properties of the real events. Different OM sensitivities are simulated. The resulting declination distributions are compared to the data sample selected in chapter 6 (which is strongly dominated by atmospheric neutrinos) using a Kolmogorov-Smirnov test [PTVF97]. The upper picture in figure 9.4 shows the probability that real and simulated data originate from the same distribution for different values of the OM efficiency, interpolated by a polynomial. The 1σ-confidence interval is taken as the systematic uncertainty on the OM light collection efficiency. It corresponds to $[0.9, 1.03]$ of the efficiency of the standard simulation. The lower picture in figure 9.4 shows how the variation of the OM sensitivity affects the event rates for different input spectra.

The result is stable with respect to other sources of systematic uncertainties, which have neglegible effects on the declination distribution of the events. The same test can be performed varying the ice model, the treatment of inconsistencies between data and Monte Carlo and the input model for the atmospheric neutrino flux. Table 9.1 shows the resulting Kolmogorov-Smirnov test probabilities if such other parameters are varied. The declination distribution stays compatible in this case confirming the validity of the method.

	Probability
standard simulation	0.89
different ice description	0.46
Honda Atm-ν flux	0.91
Bartol Atm-ν flux	0.65
scaled variables (see below)	0.99

Table 9.1: *Kolmogorov-Smirnov probabilities for the compatibility of the measured and simulated declination distributions. Probabilities for different variations of input parameters to the simulation are quoted.*

Table 9.2 summarizes the relative signal event rate changes in the uncertainty interval of the OM efficiency. The effect on the rates is very strong for an atmospheric neutrino spectrum but diminishes for harder spectra.

	Spectrum			
OM efficiency	Atmospheric	E^{-3}	$E^{-2.5}$	E^{-2}
90%	-19%	-17%	-13%	-9%
103%	+6%	+5%	+3%	+2%

Table 9.2: *Relative change of predicted neutrino rates for different OM light collection efficiencies. 100% corresponds to the OM efficiency in the standard simulation. 90% and 103% are the two boundaries of the uncertainty interval of the OM sensitivity.*

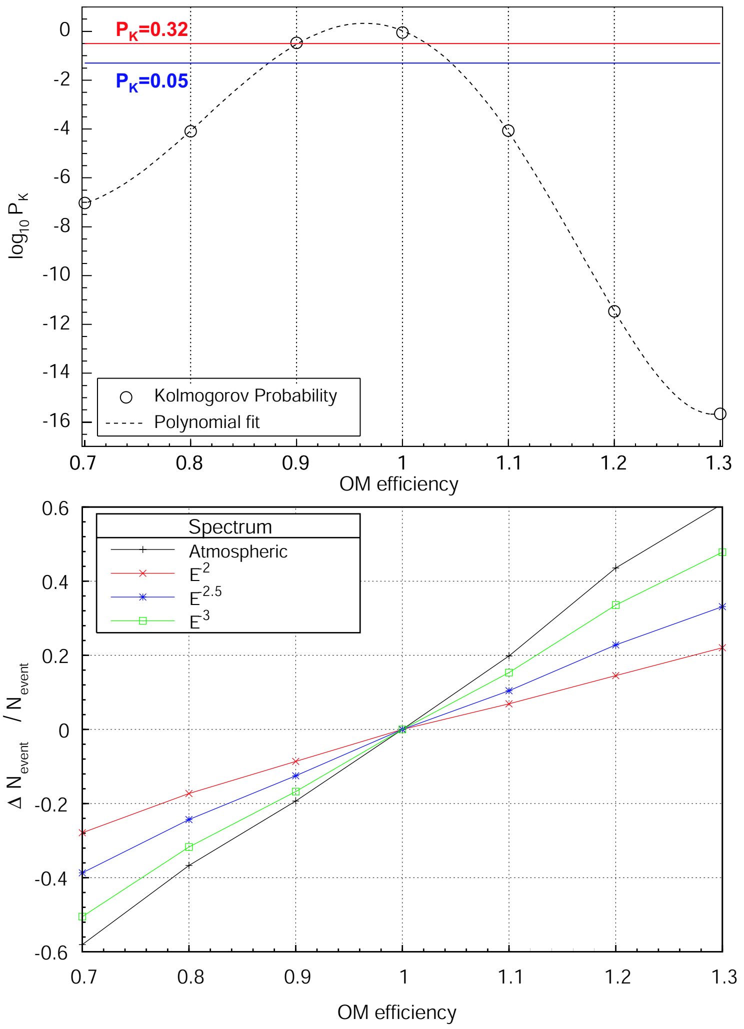

Figure 9.4: *Probability that data and Monte Carlo declination distributions are compatible as determined by a Kolmogorov-Smirnov test (upper picture). The data points are interpolated by a polynomial fit. Lower picture: relative change of the event rate due to variations of the OM efficiency in the simulation. Comparison of different neutrino spectra.*

9.1.2 Accuracy of the time calibration

The arrival time of the photon, and to a lesser extent also its amplitude, are the crucial information to reconstruct the direction of a passing particle. However, the signal readout introduces delays which have to be subtracted before an analysis can be preformed. These delays are measured in the laser calibration and consist of a constant delay t_0 and an amplitude dependent delay α (see section 3.2.5). An extensive simulation study was done in [Bir00] to infer how the accuracy of this calibration process influences the measured background and signal rates and their angular resolution. Random as well as depth dependent and string dependent errors were considered. It was found that an uncertainty of > 20 ns is necessary to obtain significant changes in rate and/or resolution. For the α parameter a 100% random error did not result in a visible change.

The uncertainty in the measurement of the t_0 values for AMANDA is found to be ≤ 7 ns [A$^+$00a] and 30% for the α-parameter [Bir00]. Therefore, the resulting systematic error on the expected number of signal events from timing calibration can be safely assumed to be neglegible. Besides the timing properties the signal amplitudes have to be calibrated to eliminate the effects of different PMT and amplifier gains. This analysis, however, does not make use of amplitude information and consequently there is no systematic error connected to them.

9.1.3 Simulation of the neutrino propagation and interaction

The number of muons passing through the AMANDA-II detector for a given flux of neutrinos depends on the rate of neutrino absorption between source and target and the probability of conversion in the target. The target in the AMANDA-II case is the column of ice and bedrock in the direction of the incoming neutrino from which muons can reach the detector. The rest of the Earth acts as an absorption layer.

In the event simulation, the neutrino propagation and interaction are performed using the generators ANIS and NUSIM described in section 4.1.1. For a given direction of the incoming neutrino, absorption and conversion rate are functions of the density and the cross section only. Consequently, the systematic bias possibly introduced in the simulation of this process can be evaluated by varying density and cross section within their respective uncertainties.

The density of the surrounding ice is well known [P$^+$02a], and its uncertainty ($< 1\%$) can be neglected. For the simulation of the Earth the Preliminary Earth Model by [DA81] is used to describe the density variations within the Earth crust, mantle and core. The conversion region is treated as "Standard Rock" with a density of 2650 kg/m^3.

Very little is known about the actual rock density in the target region. No direct geophysical measurements were performed at South Pole to determine the rock composition and density. Typical rocks are found to have densities between 2300 kg/m^3 and 2800 kg/m^3 [Low97]. Based on this information we assume a 10% uncertainty on the rock density within this analysis. Figure 9.5 shows how the expected signal in the AMANDA-II detector from a given neutrino flux varies with changes in the rock density. The assumed spectrum of the neutrino flux has an E^{-2} energy dependence. For a 10% uncertainty the event rates change between 2% (horizontal events) and 7% (vertical events) dependent on the declination. For soft spectra the effects of the uncertainty in the density of the surrounding rock becomes neglegible. Low energy (< 1 TeV) muon tracks are only a few kilometers long and the vast majority of the muons is produced by neutrino interactions in the ice.

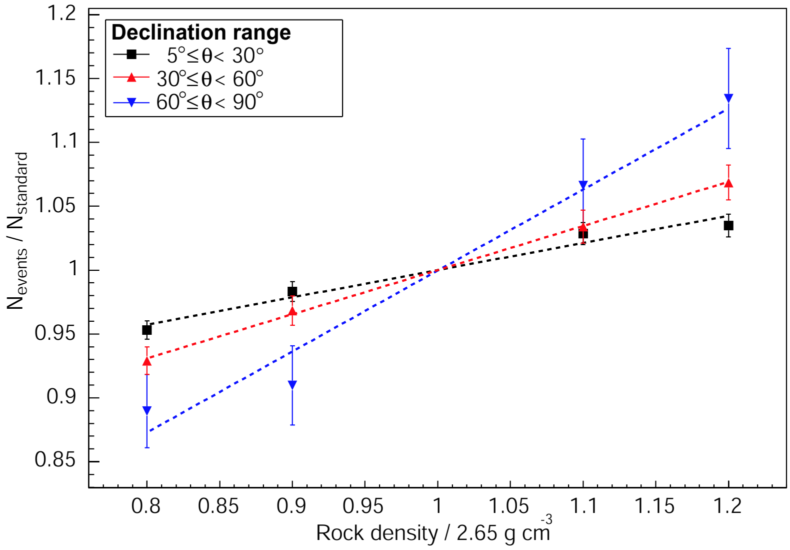

Figure 9.5: *Influence of the rock density on the number of signal neutrinos expected in AMANDA. Three declination regions are distinguished.*

The muons of interest are generated in charged current deep inelastic neutrino-nucleon scattering. An overview on the neutrino cross sections was given in section 2.4.2. A useful parametrization of the cross section is (2.15) in terms of the Parton Density Functions (PDFs), which describe the momentum distribution inside the proton.

The CTEQ collaboration [$\mathrm{B^+05a}$] regularly updates and publishes tabulated values of the PDFs on the basis of different measurements. The current tables are called 'CTEQ6'. In this version a special set of error analysis tables was published. Since the errors in the internal parameters of the CTEQ structure functions are correlated, the parameters have to be transformed into an independent set in order to do an error analysis on derived observables. In [$\mathrm{P^+02b}$] a method was introduced to perform this transformation and it was applied to the CTEQ tables in the MSbar factorization scheme. Each of the 20 independent parameters i has been varied according to its error and two tables T_i^+, T_i^- have been created corresponding to a positive and a negative variation. The uncertainty of an observable X dependent on the CTEQ function set can be calculated by simple error propagation [$\mathrm{P^+02b}$]:

$$\sigma_X = \frac{1}{2}\left(\sum_{i=1}^{N_p}\left(X(T_i^+) - X(T_i^-)\right)^2\right)^{1/2} . \tag{9.1}$$

For the neutrino cross section this means that its uncertainty can be calculated by integrating the double differential cross section (2.15) using the structure functions from the error analysis tables. The results have to be inserted in the error propagation formula above.

In this work the integration was performed numerically using the VEGAS Monte Carlo algorithm in [$\mathrm{G^+06}$]. For comparison different factorization schemes and older sets of the structure functions were included in the calculation. Figure 9.6 shows the resulting cross sections for different table sets and factorization models. Figure 9.7 shows the relative deviations of the cross sections from the one used in the ANIS neutrino generator for neutrino and anti-neutrino interactions respectively. The uncertainty band from the CTEQ6 error analysis is also included in this plot.

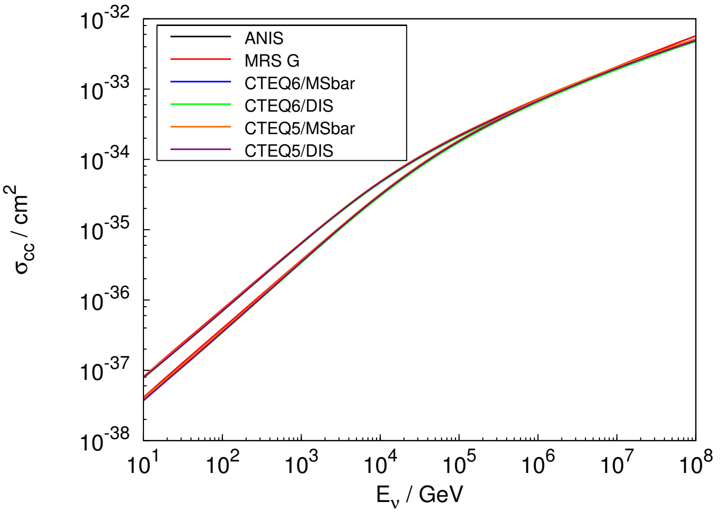

Figure 9.6: *Neutrino cross sections calculated from various parameterizations of the parton density functions.*

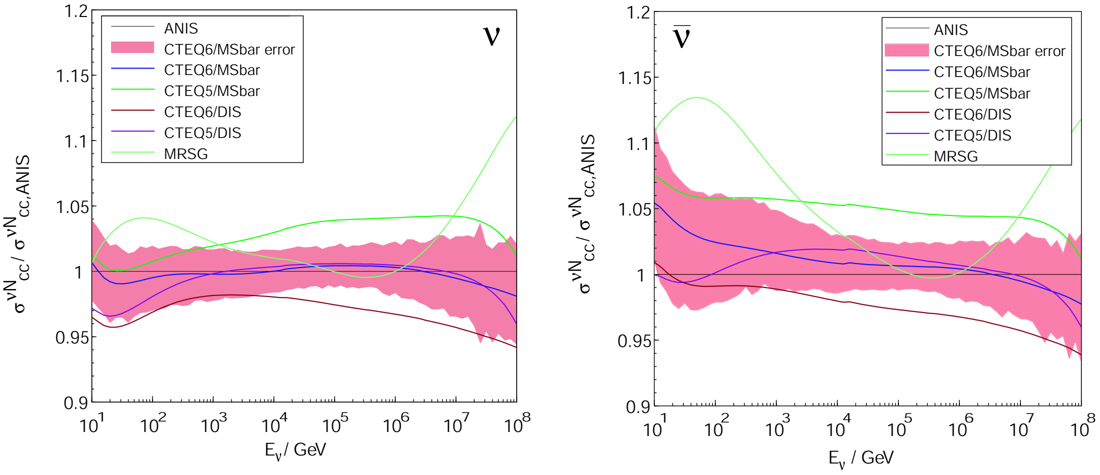

Figure 9.7: *Deviation of the neutrino cross sections calculated from different parameterizations of the parton distribution function relative to the cross section used in the ANIS neutrino generator. The red band gives the uncertainty region obtained based on the CTEQ6 error analysis tables.*

On the basis of this plot we conclude that the uncertainty on the neutrino cross section between 100 GeV and 1 PeV is approximately 3%[1]. Assuming that the neutrino rate is a linear function of the cross section the resulting uncertainty in the neutrino rate is also 3%. In combination with the uncertainty on the rock density we find the values tabulated in table 9.3 for the systematic error of the neutrino propagation and interaction stage of the simulation.

---

[1] In the PeV regime the error is dominated by the used extrapolation technique of the measured PDF's reaching ≈25% at 10^{10} GeV (see section 2.4.2 and [Kow04]).

	Signal spectrum	
Declination angle δ	E^{-2}	E^{-3} & Atmospheric
$0° < \delta < 30°$	4%	3%
$30° < \delta < 60°$	5%	3%
$60° < \delta < 90°$	8%	3%

Table 9.3: *Systematic uncertainty caused by the simulation of neutrino propagation and interaction for different spectra.*

9.1.4 Simulation of the muon-neutrino scattering angle

In the NUSIM neutrino generator, muons produced in charged current interactions are always collinear to the direction of the incoming neutrino. This disregards the - usually small - scattering angle between the muon and the neutrino. A parametrization of the mean scattering angle calculated from the relevant cross section was shown in (2.18). For a hard spectrum with the bulk of the events in the multi-TeV region this angle is much smaller than the bin size for the point source search ($2.25° - 3.75°$) and therefore neglegible.

However, for softer spectra this scattering angle leads to some broadening of the point spread function and the actual signal fraction contained inside the search bin is lower than the value expected from simulation. In contrast to the NUSIM neutrino generator, an accurate treatment of the individual muon neutrino angle is implemented in ANIS. Therefore it can be used to evaluate, what fraction of signal is lost by neglecting the non-zero scattering angle.

Figure 9.8 shows the overestimation of events in the signal bin versus search bin size for hard (E^{-2}, $E^{-2.5}$) and soft (E^{-3}, atmospheric) spectra. The bin sizes in this analysis cover the range from 2.25°(vertical tracks) to 3.75°(horizontal tracks). The resulting uncertainty for this analysis is summarized in table 9.4.

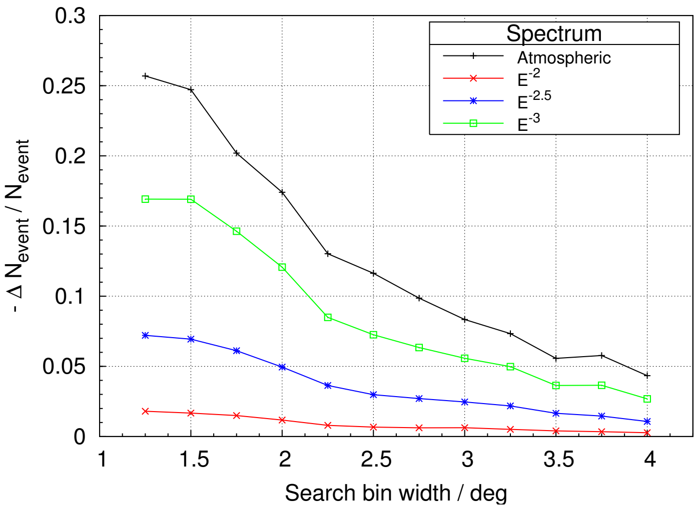

Figure 9.8: *Signal efficiency overestimation if muons and neutrinos are assumed collinear as a function of the binsize for different signal spectra.*

	Signal spectrum		
Bin size	E^{-2}	E^{-3}	Atmospheric
2.25°	$< 1\%$	8 %	13%
2.5°	$< 1\%$	7 %	12%
2.75°	$< 1\%$	6 %	10%
3.0°	$< 1\%$	5 %	8%
3.25°	$< 1\%$	5 %	7%
3.5°	$< 1\%$	4 %	6%
3.75°	$< 1\%$	4 %	6%

Table 9.4: *Systematic overestimation of event rate caused by the negligence of the muon neutrino scattering angle for different spectra.*

9.1.5 Simulation of the muon propagation

The second stage of the AMANDA-II simulation chain is the propagation of the muons through the ice and rock around the AMANDA-II detector, simulating the generation of secondaries, the energy loss and the eventual decay of the muon. Details on the features and limits of the muon propagation in the AMANDA simulation framework were presented in section 4.1.2. The simulated energy loss processes are ionization, bremsstrahlung, pair-production, photo-nuclear interactions and decay. The cross sections for these processes are well known in the GeV and TeV regime. The uncertainty of the parameterizations is about 1-2% [BSK00].

To calculate an upper limit on how these uncertainties affect the rate of triggered signal neutrinos we performed a simulation varying all cross sections by a certain factor. The result is shown in figure 9.9. A simultaneous variation of all cross sections by 2% affects the rate only by approximately 1% (indicated by the dotted lines in figure 9.9). The systematic uncertainty introduced in the muon propagation simulation can therefore be disregarded.

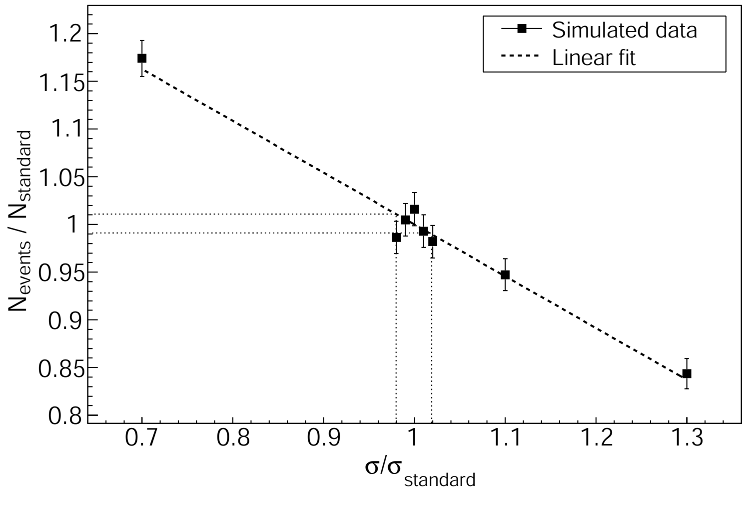

Figure 9.9: *Relative change in number of triggered signal events (E^{-2}-spectrum) for different cross sections in the muon propagation. The numbers on the horizontal axis denote the factor which is applied to the standard cross sections in the simulation of the muon propagation to estimate this change. The dotted lines show the systematic error range for the cross sections and the number of triggered events.*

9.1.6 Simulation of the optical properties of the South Pole glacier

The most challenging part in the simulation of the AMANDA-II neutrino telescope is to model the propagation of Čerenkov photons through the South Pole glacier. It possesses a layered structure which has to be reflected in the simulation. The two current approaches to do this are the PTD and PHOTONICS photon propagation packages. They mainly differ in the complexity of the ice description. Details of the photon propagation were described in section 4.1.3.

It is hard to give a reliable estimate on the influences of the ice properties. The correct method would be to vary all the input parameters to the ice model within their respective errors. But for each variation a new set of photon propagation tables has to be calculated. Since each of these table sets is about 20G in size and takes several tens of thousands CPU hours computing time, this is a huge effort which requires significant resources. Lacking those tables at the moment, we can give only a simple estimate by comparing the differences in the signal rate between PHOTONICS and PTD simulations. However, we think that this estimate is still valuable, due to the fact that the approaches of the two packages to describe the ice are fundamentally different.

Figure 9.10 shows on the left side a comparison of the declination distribution between data and simulation using either PHOTONICS or PTD photon propagation. On the right side the expected point spread function from PHOTONICS and PTD is displayed. Both distributions agree very well. Several other distributions with similar agreement were presented in figure 6.7. Integrating the declination distribution to compare the expected rates and taking the difference as a measure of the systematic uncertainty, yields the values presented in table 9.5.

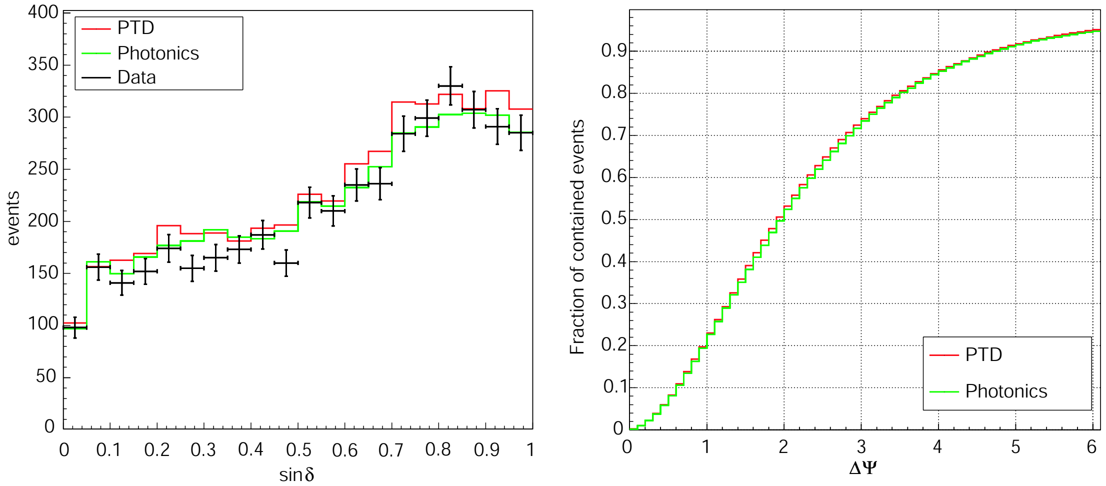

Figure 9.10: *Comparison of the declination angle distribution (left) and cumulative point spread function (right) found in the simulation of atmospheric neutrinos with different photon propagation packages. On the left plot additionally the declination distribution of the final data sample is displayed as black error bars.*

Signal spectrum		
E^{-2}	E^{-3}	Atmospheric
2%	5%	5%

Table 9.5: *Systematic uncertainty introduced by the simulation of the photon propagation in the South Pole glacier.*

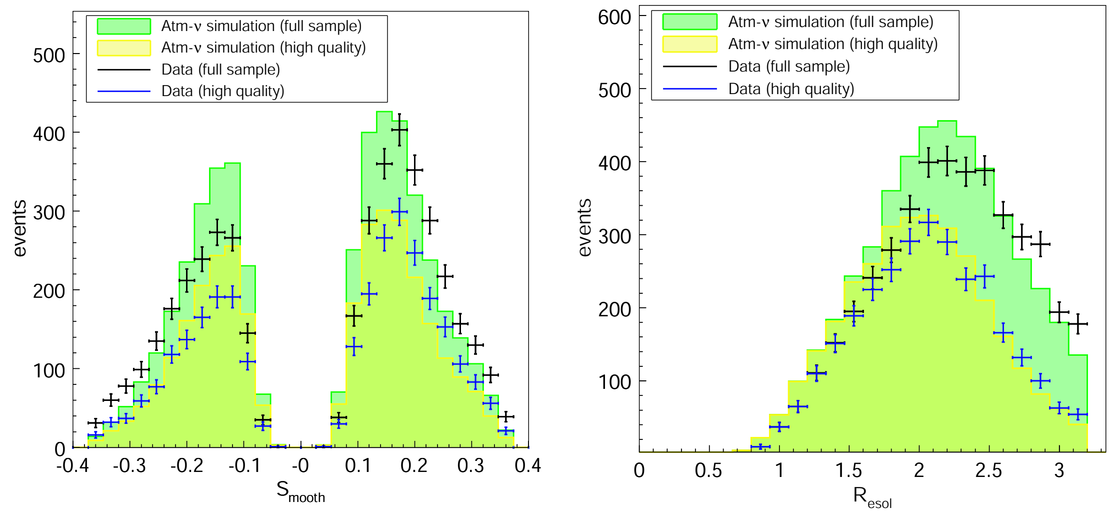

Figure 9.11: *Hit smoothness and event resolution in the final event sample and in atmospheric neutrino simulation. For the yellow histogram (simulation) and the blue error bars (data), a higher quality was required compared to the default sample (green/black) to further reduce the fraction of wrongly reconstructed muons in the sample.*

9.1.7 Bias from event reconstruction

The event reconstruction might also introduce systematic errors. Even though the reconstruction of simulated and real events is identical, the simulated events could miss features which affect the reconstruction of the real data. Such features might lead to a mismatch between Monte Carlo and experimental data in the distributions of derived event parameters. The event selection based on these parameters would then behave differently in simulation compared to real data. Typical candidates for such un-simulated features are residual x-talk hits, which are not eliminated by the cleaning procedures or short time variations in the Optical Module noise rates.

Indeed slight mismatches in the hit smoothness and event resolution distributions are observed when comparing the final neutrino candidate sample to the results from atmospheric neutrino simulations. As one possibility, these mismatches could originate from the $<5\%$ fraction of wrongly reconstructed downgoing muons, which remain in the sample. On the other hand it can not be excluded that the difference is the result of a systematic bias in the reconstruction. The first case would not result in a systematic error, since the background is estimated from the data itself and no assumption on the type of events is made. The second case would introduce an error since cuts on these variables select a different fraction of events in simulation and in real data.

A possible test to distinguish between the two options is to require a higher event quality to reduce the fraction of misreconstructed events and see if the mismatch vanishes. The results of such a test for the hit smoothness and event resolution distributions are shown in figure 9.11. Additional cuts on the reconstructed declination angle, the direct track length and the likelihood of the reconstruction were applied to increase the purity of the sample (for a description of the variables see section 6.3.2). For the event resolution some improvement for the higher quality sample can be seen. For the hit smoothness the sample purity seems not to affect the degree of the mismatch.

However, to infer an upper limit for the systematic bias we disregard these observations and treat both variables as if they would be systematically shifted by the reconstruction. To estimate how this affects the rates of signal neutrinos we assume that the variables in

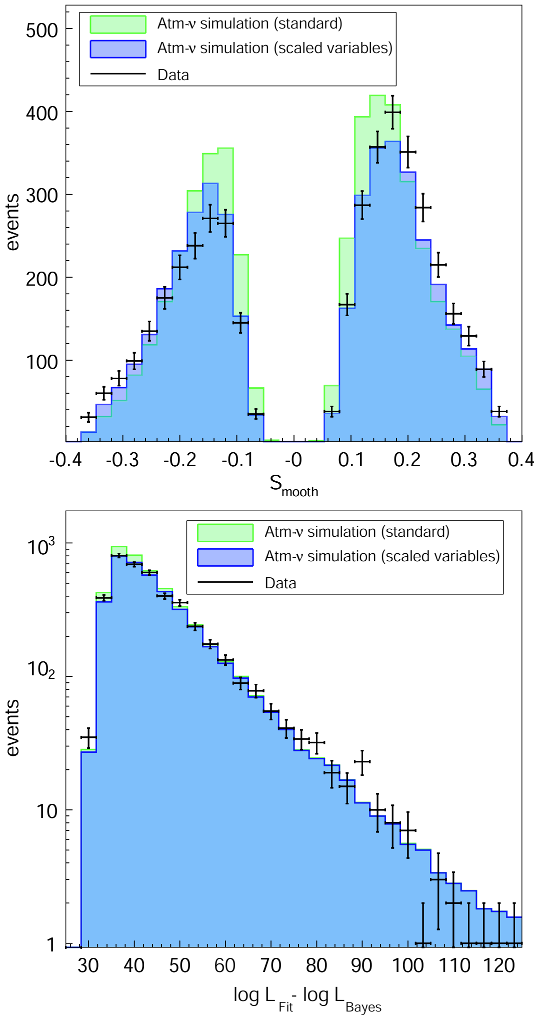

Figure 9.12: *Distributions of key variables after scaling and event selection based on the scaled variables (see text).*

Monte Carlo and data differ by the following scaling factor:

$$(S_{\text{mooth}})_{data} = 1.1\ (S_{\text{mooth}})_{MC} \tag{9.2}$$

$$(R_{\text{esol}})_{data} = 1.07\ (R_{\text{esol}})_{MC} \tag{9.3}$$

Figure 9.12 shows a comparison between data and the scaled variables after the event selection was repeated based on the scaled variables and a very good matching. Other key variables are also shown there. They are widely unaffected by the scaling. The difference in the number of expected signal events passing the selection cuts with and without scaling is quoted as the systematic error from reconstruction bias. Table 9.6 summarizes these values for different energy spectra.

Signal spectrum		
E^{-2}	E^{-3}	Atmospheric
$\pm{}^{0}_{7}\,\%$	$\pm{}^{0}_{8}\,\%$	$\pm{}^{0}_{9}\,\%$

Table 9.6: *Systematic uncertainty from event reconstruction biases.*

9.2 Sum of systematic uncertainties

As we have seen different sources of systematic uncertainties have to be taken into account. Under the assumption that these errors are independent, we can quote the total uncertainty as the geometrical sum of the individual contributions. Table 9.7 summarizes all contributions and quotes the total uncertainty. It is distinguished between a hard signal spectrum (E^{-2}), a soft signal spectrum (E^{-3}) and an atmospheric spectrum. If the error depends also on the declination of events, as a conservative approach, the systematic uncertainty from the declination bin with the maximum value is taken.

	Spectrum		
Source of systematic bias	E^{-2}	E^{-3}	Atmospheric
Optical module efficiency	$\pm{}^{2}_{9}\,\%$	$\pm{}^{5}_{17}\,\%$	$\pm{}^{6}_{19}\,\%$
Time calibration	$\pm\,1\,\%$	$\pm\,1\,\%$	$\pm\,1\,\%$
Neutrino interaction	$\pm\,8\,\%$	$\pm\,3\,\%$	$\pm\,3\,\%$
Neutrino-muon angle	$\pm{}^{0}_{1}\,\%$	$\pm{}^{0}_{8}\,\%$	$\pm{}^{0}_{13}\,\%$
Muon propagation	$\pm\,1\,\%$	$\pm\,1\,\%$	$\pm\,1\,\%$
Photon propagation	$\pm\,2\,\%$	$\pm\,5\,\%$	$\pm\,5\,\%$
Reconstruction Bias	$\pm{}^{0}_{7}\,\%$	$\pm{}^{0}_{8}\,\%$	$\pm{}^{0}_{9}\,\%$
Sum	$\pm{}^{9}_{14}\,\%$	$\pm{}^{6}_{21}\,\%$	$\pm{}^{7}_{25}\,\%$

Table 9.7: *Summary of the systematic uncertainties in this analysis.*

In figure 9.13 the declination distribution of the neutrino candidate events is compared to the simulation predictions for atmospheric neutrinos including the systematic error band[2]. Note that for the distribution of atmospheric neutrinos, there is an additional uncertainty due to the limited knowledge on the total primary cosmic ray flux and the cosmic ray interactions in the atmosphere which does not affect the searches for cosmic sources. The expected number of atmospheric neutrinos in AMANDA-II is therefore shown for two different predictions of the neutrino flux. These calculations were performed by Lipari [Lip93] and Honda [H$^+$95] respectively and mark the extremes of the current flux models. Within the errors the data is perfectly consistent with the atmospheric neutrino hypothesis.

9.3 Treatment of systematic uncertainties in the limit calculation

Flux limits derived using the Feldman-Cousins approach [FC98] do not account for any systematic or statistical error on the background b or the expected signal events s from a source. Both quantities are treated as exactly known. However, if the systematic error is not neglegible this leads in many cases to too strong flux limits and is therefore not correct. In [C$^+$03] a method is suggested to extend the Feldman-Cousins limit derivation for the cases that b and s have errors. We will use this method to derive flux upper limits on true 90% confidence level for the individual candidate sources and for the full northern sky.

---

[2] The systematic error for the neutrino-muon angle was not taken into account in this plot, since it is important only for binned point source searches.

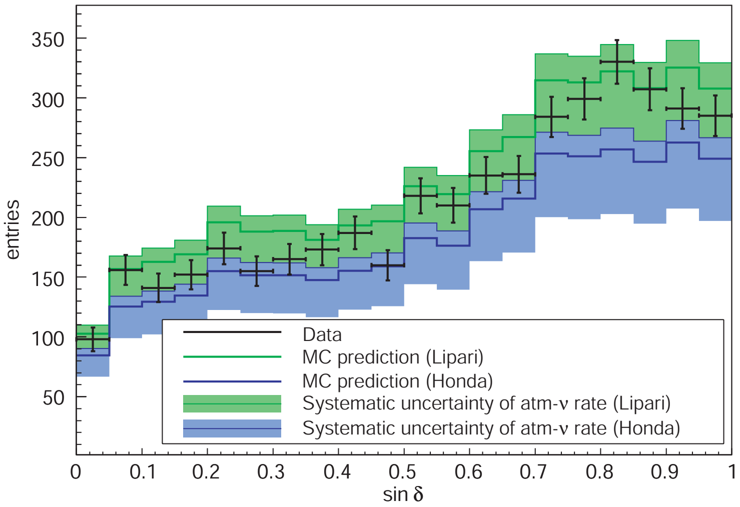

Figure 9.13: *Declination distribution of the events in the final event sample. It is shown in comparison to the predictions from simulation using atmospheric neutrino flux parametrizations calculated by Honda [H$^+$95] (blue) and Lipari [Lip93] (green). The systematic error is displayed as a band in the corresponding color.*

The expected number of events for a certain neutrino flux is predicted by Monte Carlo simulation. The systematic uncertainty involved in this prediction and the sources contributing to it were expounded above. For a differential flux of $d\Phi/dE \propto E^{-2}$ it was found to be $+9/-14\%$.

9.3.1 Statistical uncertainty on the expected background

The background is determined from the data sample by counting the events in the declination band around the hypothetical source and subsequent rescaling from the declination band area to the search bin area. The important assumption that enters in this calculation is that the background rate shows no variation in right ascension. Several tests [Lan05, Hue06] showed no indications contradicting this assumption within the available statistics.

However, since only a few hundred events are present in a single declination band, the statistical error involved in this background determination method is relatively large and has to be taken into account. Figure 9.14 shows the relative statistical error versus declination for the neutrino source candidates. For most parts of the sky it is about 5%, but it rises for higher declinations.

Thus, we assume conservatively an 8% statistical error on the background corresponding to the worst value found for any of the neutrino source candidates.

9.3.2 Confidence interval creation including systematic errors

A so called "semi-Bayesian" approach is introduced in [C$^+$03] to include systematic errors in the calculation of confidence belts and limits. As demonstrated in equation (2.29) the confidence belt for an observation is created by summing over the probabilities $P(n|s,b)$ to see n events for a certain signal s and a known background b in an interval $[n_l, n_u]$ until the chosen confidence level is reached. Feldman and Cousins provide a rule to select a unique interval $[n_l, n_u]$.

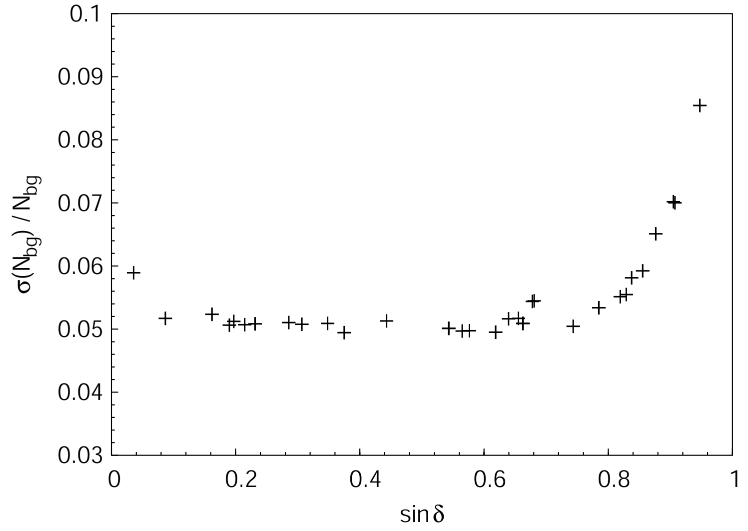

Figure 9.14: *Relative statistical error of the atmospheric neutrino background vs. declination for the neutrino source candidates.*

The idea of the semi-Bayesian approach is to average the probabilities $P(n|s,b)$ over the allowed range of the systematic uncertainty:

$$\hat{P}(n|b,s) \;=\; \int_{-\infty}^{\infty}\int_{-\infty}^{\infty} P(n|s',b')\; w_b(b')\; w_s(s')\; db'\; ds' \;, \tag{9.4}$$

where $w_b(b')$, $w_s(s')$ are the probability density functions for the background to be b and the signal expectancy to be s respectively.

The error on the background is purely statistical, therefore $w_b(b')$ can be well approximated by a normal distribution around the expected background $b_{\rm exp}$. The exact shape of $w_s(s')$ is unknown but since the errors are asymmetric one cannot simply assume a Gaussian error centered around the expected signal from Monte Carlo simulations. However, the effects of an error of $\approx 15\%$ lead only to a small correction of the limit. That justifies the introduction of the following approximation to get an effective treatment of the systematic error:

Instead using the signal prediction from Monte Carlo, the central value of the error interval is taken as the expected neutrino signal $s_{\rm exp}$ from a certain neutrino flux, i.e.

$$s_{\rm exp} \;=\; \frac{1}{2}\left[(s_{\rm MC}+\sigma_s^+) + (s_{\rm MC}-\sigma_s^-)\right] \;, \tag{9.5}$$

where $s_{\rm MC}$ is the prediction from Monte Carlo simulation and σ_s^+ and σ_s^- denote the upper and lower error range for the signal. The error around this central value is obviously symmetric and a Gaussian shape is assumed. We can then write the probability densities for background and signal as:

$$w_b(b') \;=\; \frac{1}{\sqrt{2\pi}\sigma_b}\exp\left(-\frac{(b'-b_{\rm exp})^2}{2\sigma_b^2}\right) \tag{9.6}$$

$$w_s(s') \;=\; \frac{1}{\sqrt{2\pi}\sigma_s}\exp\left(-\frac{(s'-s_{\rm exp})^2}{2\sigma_s^2}\right) \;, \tag{9.7}$$

and use the software POLE presented in [C$^+$03] to accomplish the integration (9.4) and calculate the corresponding event upper limit μ_{90} at 90% confidence level from which flux limits can easily be derived. The results are summarized in the next section.

9.4 Flux limits

Following an agreement within the AMANDA Collaboration we present upper limits at 90% confidence level. The flux limit is derived from the event upper limit by counting the expected number of observed events N_Φ in the simulation of a template differential flux (see also section 2.5.2):

$$\frac{d\Phi}{dE} = \Phi_0 f(E) \ , \tag{9.8}$$

with an arbitrary normalization Φ_0 and a spectral shape given by $f(E)$. The normalization constant to the flux limit Φ_0^{lim} is then determined by dividing the event upper limit with the number of events observed in the simulation for the template flux:

$$\frac{d\Phi_{\mathrm{limit}}}{dE} = \frac{\mu_{90}}{N_\Phi} f(E) \ . \tag{9.9}$$

Obviously the flux limit depends on the spectrum $f(E)$ and has to be recalculated for different $f(E)$. In this summary we give limits for a spectrum proportional to E^{-2}, the spectral index expected from Fermi acceleration. In the following discussion in chapter 10, we present also limits for selected sources based on different spectra which are favoured by neutrino emission models for these sources.

Predefined source catalog

Table 9.8 summarizes the upper limits found for the catalog of candidate sources. The limits are presented there as limits on the normalization constant Φ_0 for a differential flux of:

$$E^2 \frac{d\Phi}{dE} = \Phi_0 \ 10^{-8} \ \ \mathrm{GeV\ cm^{-2}\ s^{-1}} \ . \tag{9.10}$$

Limits are given for the flux of muon neutrinos, the flux of tau neutrinos and the combined flux in both channels. For the case of a neutrino flavor ratio ν_μ:ν_τ of 1:1 which is by current knowledge the most likely scenario for the energy range considered (see section 2.4.1), the combined channel flux limit represents the most stringent one to the total neutrino flux.

Another important information is the energy range in which a limit is valid. Figure 6.11 in section 6.4.2 shows the energy distribution of events for different spectra. 90% of the events seen in the detector for a spectrum proportional to E^{-2} are found between 1.6 TeV and 1.6 PeV. This we define as the validity range of the presented limits.

Flux limit map for the northern sky

A flux limit can also be specified for each grid center investigated in the grid search of the full northern sky. We present these limits here as color coded maps (Hammer-Aitoff and linear projections) shown in figure 9.15. The same spectrum and identical units are used as for the candidate source catalog. Only the limit on the muon neutrino flux is presented. From this map it is easy to obtain neutrino flux upper limits for arbitrary point like objects on the northern hemisphere.

Flux limits for the high states of Markarian 421 and Cygnus X-3

The number of neutrinos found in selected periods of high X-ray flux from Markarian 421 and periods of high radio flux from Cygnus X-3 was compatible with the expectations from atmospheric neutrino background. Therefore we derive an upper limit on the neutrino flux in the selected high states. With 90% confidence we can exclude a differential $\nu_\mu + \overline{\nu}_\mu$ flux of:

$$E^2 \, \frac{d\Phi_{90}^{\mathrm{lim}}}{dE} \;=\; 1.7 \cdot 10^{-7}\ \mathrm{GeV\ cm^{-2}\ s^{-1}} \ ,$$

in the 141 effective days selected as high states for Markarian 421 and a flux of:

$$E^2 \, \frac{d\Phi_{90}^{\mathrm{lim}}}{dE} \;=\; 3.4 \cdot 10^{-7}\ \mathrm{GeV\ cm^{-2}\ s^{-1}} \ ,$$

in the 114 effective days selected as high states for Cygnus X-3. For both limits a neutrino spectrum of $d\Phi/dE \propto E^{-2}$ was assumed.

Source name	RA[h]	Dec[$\circ$]	N_{obs} / N_{bg}	μ_{90}	$N_{\nu_\mu}^{(\mathrm{sig})}$ / $N_{\nu_\tau}^{(\mathrm{sig})}$	$\mathbf{\Phi_0^{\nu_\mu}}$	$\Phi_0^{\nu_\tau}$	$\mathbf{\Phi_0^{\nu_\mu+\nu_\tau}}$
TeV Blazars								
Markarian 421	11.1	38.2	6 / 7.37	4.1	0.97 / 0.15	**4.2**	27.8	**7.4**
1ES 1426+428	14.5	42.7	5 / 5.52	4.8	0.90 / 0.13	**5.4**	36.6	**9.4**
Markarian 501	16.9	39.8	8 / 6.39	7.9	0.93 / 0.14	**8.5**	57.2	**14.7**
1ES 1959+650	20.0	65.1	5 / 4.77	5.6	0.71 / 0.11	**7.8**	52.2	**13.5**
1ES 2344+514	23.8	51.7	4 / 6.18	3.1	0.89 / 0.15	**3.5**	20.9	**5.9**
GeV Blazars								
QSO 0219+428	2.4	42.9	5 / 5.52	4.9	0.89 / 0.13	**5.5**	37.6	**9.6**
QSO 0235+164	2.6	16.6	7 / 6.12	6.7	1.03 / 0.14	**6.5**	46.8	**11.4**
QSO 0528+134	5.5	13.4	4 / 6.08	3.2	1.06 / 0.14	**3.0**	22.8	**5.3**
QSO 0716+714	7.4	71.3	1 / 4.20	1.2	0.70 / 0.13	**1.8**	9.2	**3.0**
QSO 0954+556	9.9	55.0	2 / 6.26	1.4	0.91 / 0.15	**1.6**	9.2	**2.7**
3C273	12.5	2.1	8 / 4.72	9.6	0.96 / 0.10	**10.0**	94.3	**18.0**
QSO 1611+343	16.2	34.4	6 / 6.96	4.5	0.95 / 0.15	**4.8**	30.5	**8.3**
QSO 1633+382	16.6	38.2	9 / 7.37	8.1	0.97 / 0.15	**8.4**	55.0	**14.6**
other AGN								
NGC 1275	3.3	41.5	4 / 6.75	2.7	0.95 / 0.14	**2.9**	19.7	**5.0**
M87	12.5	12.4	6 / 6.08	5.3	1.07 / 0.14	**4.9**	38.6	**8.7**
Microquasars & Neutron star binaries								
LSI +61 303	2.7	61.2	5 / 4.81	5.6	0.75 / 0.13	**7.4**	44.0	**12.6**
CI Cam	4.3	56.0	9 / 6.34	9.4	0.91 / 0.14	**10.3**	65.7	**17.8**
GRO J0422+32	4.4	32.9	9 / 6.72	9.0	0.94 / 0.14	**9.6**	63.7	**16.7**
AO 0535+26	5.7	26.3	7 / 6.48	6.4	0.99 / 0.14	**6.5**	45.4	**11.3**
XTE J1118+480	11.3	48.0	3 / 7.05	1.5	0.97 / 0.14	**1.6**	10.7	**2.8**
SS433	19.2	5.0	4 / 6.14	3.1	1.16 / 0.13	**2.7**	23.6	**4.8**
GRS 1915+105	19.3	10.9	7 / 6.07	6.8	1.08 / 0.14	**6.3**	50.5	**11.2**
Cygnus X-1	20.0	35.2	8 / 7.01	7.3	0.95 / 0.15	**7.7**	48.4	**13.2**
Cygnus X-3	20.5	41.0	7 / 6.48	6.4	0.95 / 0.14	**6.8**	46.7	**11.8**
Supernova Remnants & Pulsars								
PSR J0205+6449	2.1	64.8	1 / 4.68	1.3	0.72 / 0.11	**1.8**	11.8	**3.1**
Crab Nebula	5.6	22.0	10 / 6.74	10.1	0.98 / 0.15	**10.2**	68.9	**17.8**
Geminga	6.6	17.9	3 / 6.23	2.0	1.01 / 0.14	**2.0**	14.0	**3.5**
SGR 1900+14	19.1	9.3	5 / 5.65	4.8	1.09 / 0.13	**4.4**	35.6	**7.8**
PSR 1951+32	19.9	3.3	4 / 6.72	2.7	0.94 / 0.14	**2.9**	19.0	**5.0**
Cassiopeia A	23.4	58.8	5 / 6.00	4.4	0.86 / 0.13	**5.1**	33.2	**8.9**
AGASA UHECR Multiplets								
Multiplet 1	1.3	20.4	5 / 6.29	4.1	0.99 / 0.15	**4.1**	28.0	**7.1**
Multiplet 2	11.3	56.9	7 / 5.91	6.9	0.89 / 0.14	**7.8**	49.2	**13.4**
Unidentified high energy gamma-ray sources								
3EG J0450+1105	4.8	11.4	8 / 5.94	8.4	1.08 / 0.14	**7.8**	61.6	**13.8**
TeV J2032+4131	20.5	41.5	7 / 6.75	6.1	0.95 / 0.14	**6.4**	43.8	**11.2**

Table 9.8: *Flux upper limits for the sources in the catalog of potential neutrino emitters. From left to right are given the source name, its sky position, the number of observed and expected events, the event upper limit at 90% confidence level* μ_{90}*, the expected number of events from muon neutrino* $N_{\nu_\mu}^{(sig)}$ *and tau neutrino interaction* $N_{\nu_\tau}^{(sig)}$ *for a differential flux of* $E^2\ d\Phi/dE = 10^{-8}\ GeV\ cm^{-2}\ s^{-1}$ *and the resulting upper limit* Φ_0^{ν} *on the normalization constant of such a flux. Upper limits are presented for the muon neutrino flux, the tau neutrino flux and the combined flux in both channels.*

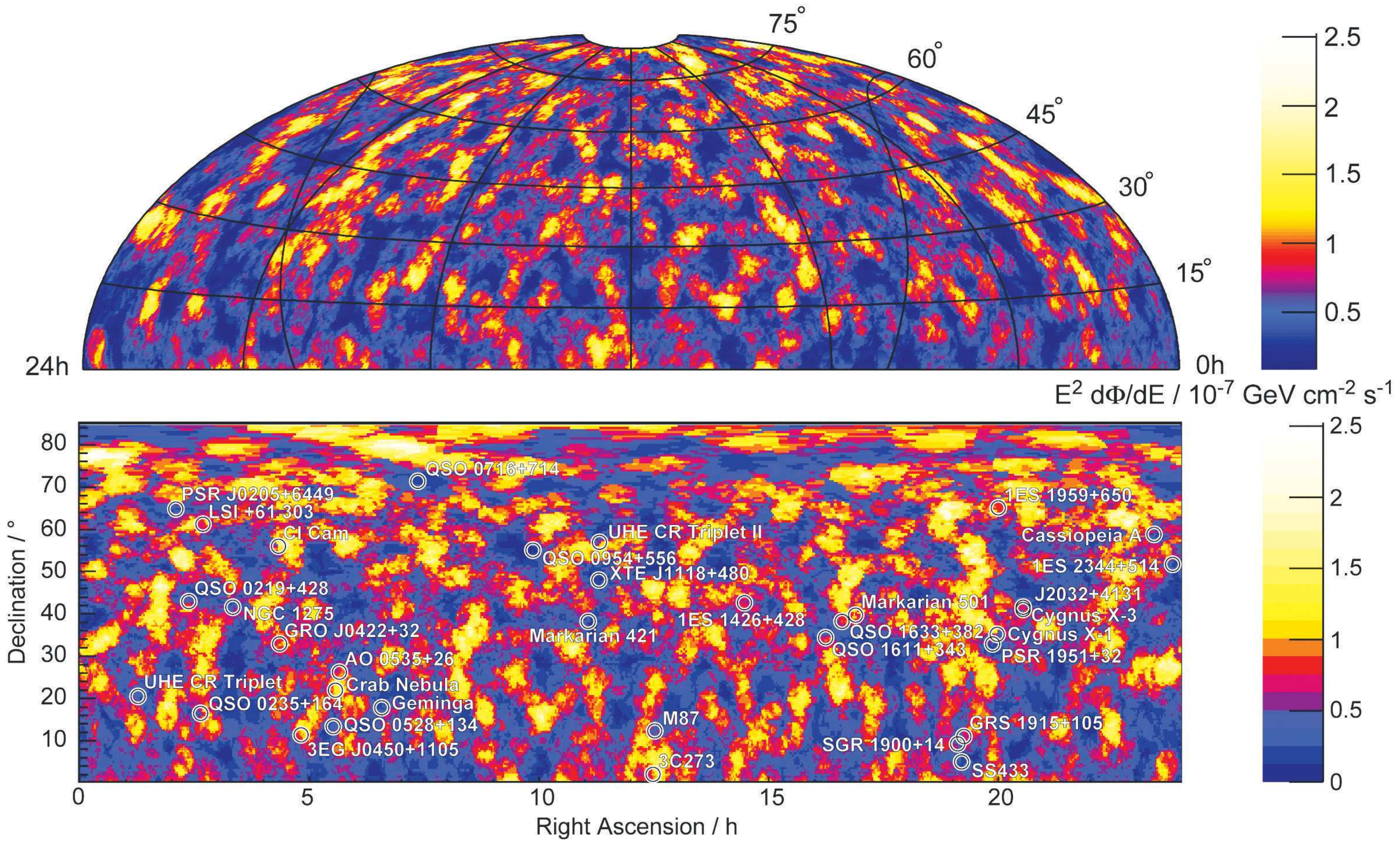

Figure 9.15: *Maps of the neutrino flux limits for the northern sky obtained by this analysis in Hammer-Aitoff and linear projections. The same units as in table 9.8 are used. The curved line on the upper map symbolizes the galactic plane. The circles with source names display the sky positions of the sources in the candidate catalog.*

Chapter 10

Discussions and Summary

10.1 Neutrino flux limits in comparison to other experiments

The limits derived in this analysis currently represent the most stringent upper limits on neutrino fluxes from point-sources on the northern hemisphere. The limits have improved on average by a factor of 3.8 compared to a former published analysis of AMANDA-II data [A^+04d] based on 197 effective days of data taken in the year 2000. A second point source analysis based on a different event selection, was developed in AMANDA-II in parallel to this work [A^+05a]. It is based on 607 effective days taken in the years 2000-2002. In comparison to [A^+05a], the analysis presented in this thesis provides on average a factor of 1.5 more stringent limits.

In figure 10.1 we show a comparison of the sensitivity and the flux limits (for a neutrino spectrum $d\Phi/dE \propto E^{-2}$) obtained in this analysis with other experiments and former AMANDA-II point source analyses. The most stringent published neutrino flux limits from a different experiment are [A^+01b] using the MACRO detector[1]. Due to its location on the northern hemisphere it is mainly sensitive to southern hemisphere sources. Experiments currently under construction are ANTARES in the Mediterranean Sea and the km^3-sized IceCube at the South Pole. We present the expected sensitivities for 1 year of ANTARES [Hei04] and 1 year of IceCube [A^+04e] operation.

10.2 Limits to specific neutrino source models

As the last point we want to compare the flux limits obtained in this work to specific theoretical models of neutrino production in astrophysical sources. Many current models exhibit energy cut-offs as well as broken power law spectra with spectral indices in the range from $\gamma = 3$ to $\gamma = 0$. Therefore it is impossible to simply compare the numbers in table 9.8 to the fluxes predicted by these models. One has to recalculate the limits based on a simulation of the actual spectrum of the model as mentioned in section 9.4. The limits in 9.8 are only valid for a spectrum following a power law with an index of $\gamma = 2$, derived from the general assumption that the neutrino spectrum follows the spectrum of hadrons accelerated in the source.

It is not meant to be a complete comparison covering all existing models, but rather a

---

[1] MACRO published integrated flux limits above $E_\nu > 1$ GeV based on a spectral index of $\gamma = 2.1$. The limits have been adjusted to differential limits for $\gamma = 2$ delivering the same integral flux.

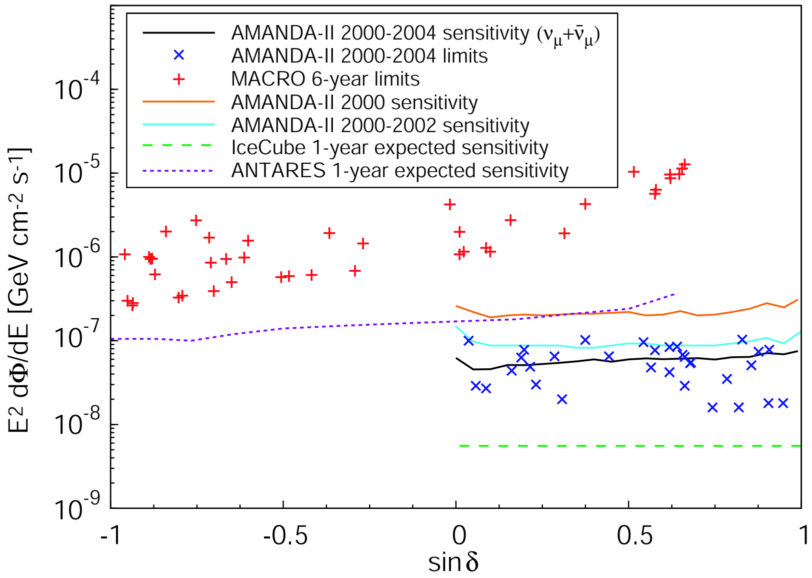

Figure 10.1: *Upper limits and sensitivities to the neutrino flux from point sources for different experiments. See text for references.*

subjective selection including predictions for sources from each generic source class introduced in section 2.3. For each flux prediction we give the "Model Rejection Factor" (MRF), which is the ratio between the flux this analysis can exclude and the flux anticipated by theoretical considerations. A MRF of 10 therefore means that we can exclude a flux 10 times higher than the predicted one. Considering the uncertainties involved in the modeling of astrophysical sources we will call a MRF<10 "in the range" of the model. Flux limits with such MRFs can already constrain its parameter space. In the following we always compare the predictions for the $\nu_\mu + \nu_\tau$ flux at Earth (including anti-particles) to the corresponding limit from this analysis. A flavor ratio of $\nu_\mu + \nu_\tau = 1:1$ is assumed according to the standard scenario for neutrino production and oscillation.

10.2.1 Active Galactic Nuclei

The predicted neutrino flux from the TeV-visible Blazars is rather low. The left picture in figure 10.2 displays the anticipated neutrino fluxes from Markarian 421 by [M$^+$03]. For comparison we show also the gamma-ray flux from this source measured by the WHIPPLE air shower Čerenkov telescope (taken from [DK05]) during different states of activity. The dotted lines in the figure present the limits from this analysis to a neutrino flux $d\Phi/dE$ following the measured gamma-ray spectrum and following the prediction in [M$^+$03]. For the latter we find a MRF$\approx 10^6$, so even a much larger telescope than AMANDA-II could not detect such a source. For the former case we cannot specify a MRF[2] due to the variability of the source. Since the observation time of Čerenkov telescopes is very short, we do not know the total time the source emitted a gamma-ray flux corresponding to each of the levels shown in the plot. Also the observed gamma-ray flux does not correspond to the intrinsic one, but is attenuated by the interaction of the gamma-rays with the extragalactic background light (see [DK05] for a detailed discussion). So we just note, that the AMANDA-II limit on the neutrino flux is close to the observed gamma-ray flux in a high state of Markarian 421.

On the right picture of figure 10.2 the predictions for the neutrino flux from the EGRET

---

[2] The model in this case would be that the neutrino flux is identical to the gamma-ray flux.

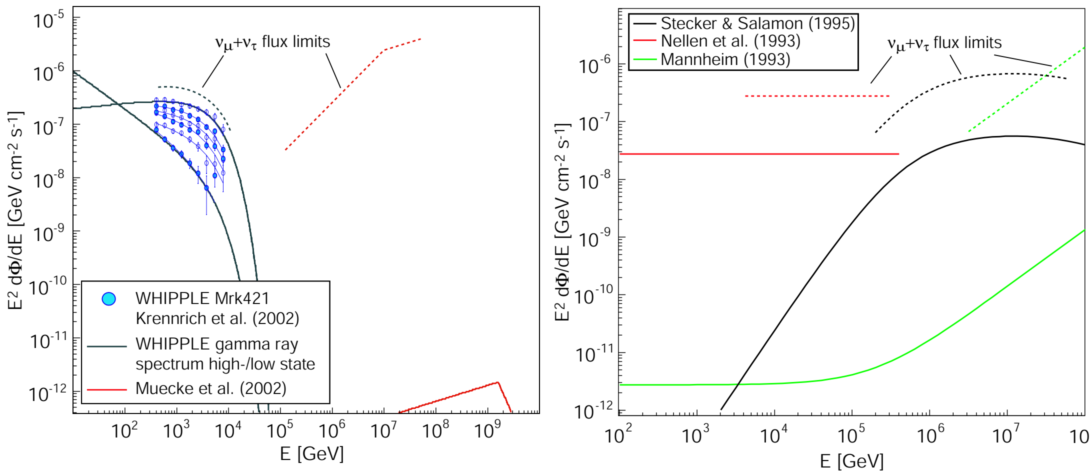

Figure 10.2: *Model predictions (solid lines) for neutrino fluxes from Markarian 421 (left) and 3C273 (right) compared to upper limits (dashed lines) derived from this analysis. The energy range covered by the limit is indicated by the length of the dashed line.*

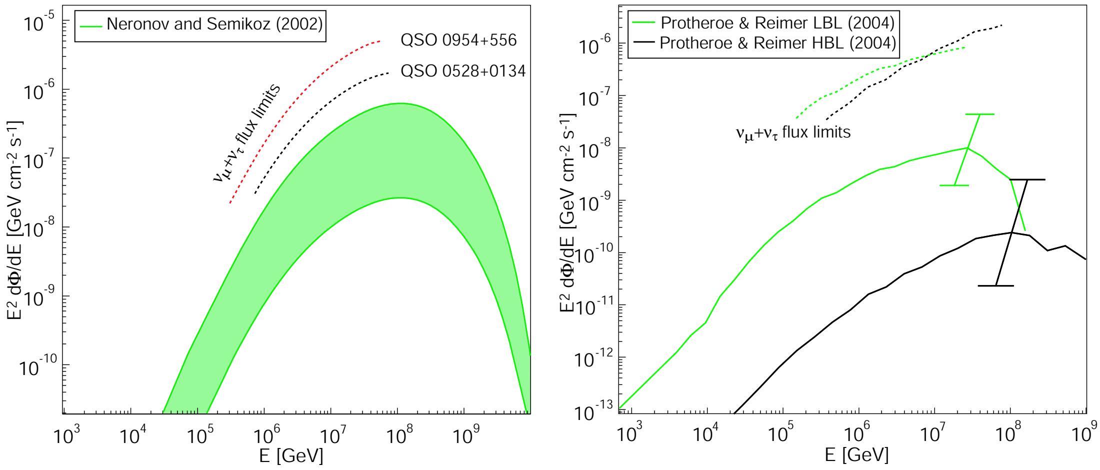

Figure 10.3: *Model predictions (solid lines) for neutrino fluxes from a generic "neutrino-loud" Blazar defined in [NS02] (left) and M87 (right) compared to upper limits (dashed lines) derived from this analysis. See text for the meaning of the different curves within the models.*

Blazar 3C273 by the models in [NMB93, Man93, SS96] are shown together with the corresponding limits from this analysis. The MRF values are 11.9 (Stecker and Salamon), 11.1 (Nellen et al.) and 877 (Mannheim). For [NMB93, SS96] these limits are an order of magnitude above the fluxes anticipated. However, the predictions on a diffuse neutrino flux derived from the two models have already been ruled out by AMANDA-II [Hod05].

The limits obtained for two other EGRET Blazars are compared to the generic model [N$^+$02, NS02] for neutrino emission from GeV-Blazars in figure 10.3 (left picture). These sources have been mentioned there as favoured neutrino emitters. A range is given for the anticipated neutrino flux depending on the relativistic beaming angle. For QSO 0528+0134 we find a MRF=3.0 to the most optimistic model prediction, while the limit is more than a factor of three worse for QSO 0954+556. This source is at high declination and considering the hard spectrum proposed, neutrino absorption in the Earth attenuates a possible signal.

A similarly hard spectrum is proposed for the neutrino emission from M87, assuming that it is a mis-aligned BLLac object. From the spectral energy distribution it is not clear if

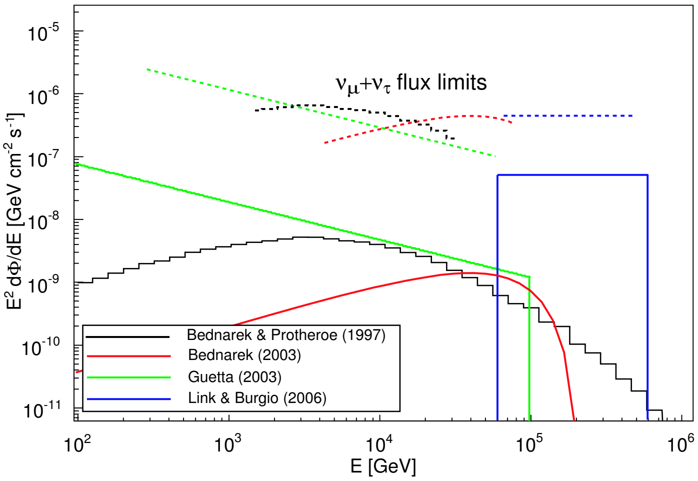

Figure 10.4: *Neutrino flux predictions (solid lines) for the Crab Nebula compared to the flux upper limits (dashed lines) derived from this analysis.*

this source belongs to the HBL or LBL class, therefore [PDR03] predict the neutrino flux for both hypotheses. The flux together with the limits from this analysis are presented on the right side of figure 10.3. The unknown doppler factor of the jet is responsible for the large error bars on both flux predictions. The limit from this analysis is about two orders of magnitudes higher than the anticipated flux in the LBL case. Only next generation detectors (i.e. IceCube) will be in the range of the fluxes proposed in this model.

10.2.2 Pulsars wind nebulae

Figure 10.4 shows upper limits obtained in this analysis for predictions of neutrino fluxes from the most famous Pulsar wind nebula, the Crab Nebula. The models [GA03, BP97, Bed03, LB05] have already been mentioned in section 2.3.3. All predictions are far below the flux that AMANDA-II is able to exclude, with exception of the neutrino fluxes calculated by [LB05] (MRF=8.6). An interesting aspect of this model is that it predicts pulsed emission. So a future analysis of the arrival times of the neutrinos with respect to the pulsar phase could help to verify or falsify the proposed neutrino production mechanisms.

10.2.3 X-ray binaries

The limits from this analysis are more exciting, when compared to the predictions of neutrino fluxes from X-ray binaries, particularly from Microquasars. Figure 10.5 shows the predictions for a neutrino flux produced in the jet of SS433 [D$^+$02] and neutrinos produced in the accretion disk and companion star of Cygnus X-3 [Bed05].

For SS 433 the MRF equals to 0.4, excluding the neutrino flux calculated in [D$^+$02]. An average of 7.8 neutrinos would have been expected from SS 433 according to that model in our final data sample. But also for the fluxes predicted by [Bed05] the limit is in the range of the model, being the MRF equal to 3.1 (accretion disk) and 4.7 (companion star) respectively.

However due to the low-energy neutrino flux ($E < 1$ TeV) expected from the accreting Neutron Star AO 0535+625 [A$^+$03c] the limit from this analysis is far from the predictions (MRF=53.5). The effective area is too small at such low energies.

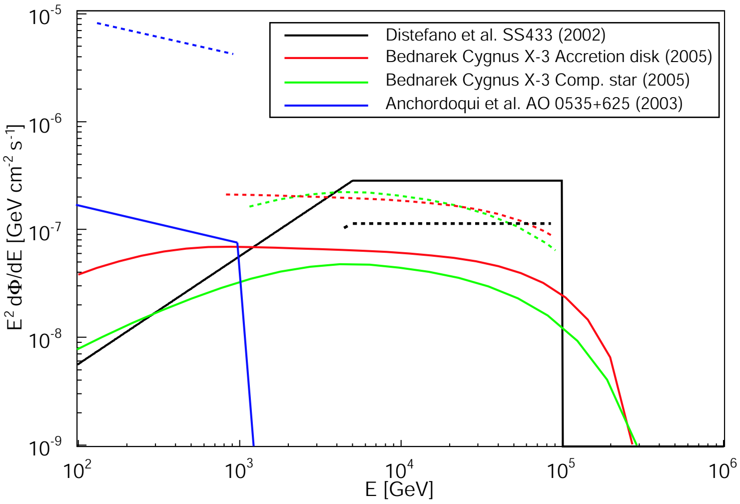

Figure 10.5: *Neutrino flux predictions (solid lines) for various X-ray binaries compared to the flux upper limits (dashed lines) derived from this analysis.*

10.3 Outlook

With a total of 9 strings deployed in the winter 2005/2006, the successor to AMANDA-II, IceCube, is now the largest neutrino detector in the world. If deployment plans for the upcoming winter are successful, a sensitivity can be reached in one year of operation with the then 21 strings of IceCube, which is at least comparable to the sensitivity of this analysis based on 5 years of AMANDA-II data. For this reason, the search for neutrino point sources will focus on the analysis of IceCube data in the near future. Apart from its physical size, the complete recording of waveforms, the prospect of higher overall stability due to a digital module readout, a dead-time free data acquisition and an improved angular resolution, promise considerable improvements for the next generation of point source analysis. The expected sensitivity of the full IceCube detector – to be completed in 2011 – reaches neutrino flux levels predicted for several classes of objects. Then, hopefully, a positive detection of a neutrino source can be reported. The techniques introduced here to enhance the detection chance for objects with time variable emission patterns might help considerably for a significant detection of a source: the GLAST satellite to be launched next year as well as neutrino triggered observations of Čerenkov telescopes currently discussed can provide abundant light curves on high energy gamma-ray fluxes from many sources. Based on these light curves the definition of active states should be possible for many potential neutrino sources considerably reducing the background from atmospheric neutrinos.

10.4 Summary and Conclusions

In this work data collected in 1001 effective days of AMANDA-II operation was analyzed for a signal from cosmic point-like sources of high energy neutrinos.

For about 10^{10} triggered events, an event selection has been developed to separate neutrino induced events from the background caused by down-going muons generated in cosmic ray interactions in the atmosphere. For this selection, a newly developed event reconstruction method (JAMS) as well as new signal-background discrimination parameters (Resolution, Flariness) have been used to improve the upper limit setting power of the analysis by 15% compared to a previous analysis (for identical observation time). A numerical procedure has been applied to find a set of event selection cuts, which optimize the upper limit setting capability in this analysis, independently for a simulated neutrino source with a hard spectrum and a neutrino source with a soft spectrum. Afterwards, a common set of selection cuts was derived from the two optimizations being optimal for both spectra.

4282 events reconstructed with up-going tracks passed the selection criteria. Comparisons to a simulation of the atmospheric neutrino flux showed good agreement in numbers as well as in the distributions of event parameters. On this sample several searches for neutrino point sources were performed. A catalog of preselected candidate neutrino sources was scanned, looking for a statistically significant localized excess of events over the isotropic background of atmospheric neutrinos from the directions of these sources. No excess incompatible with fluctuations of the background was found in this search. Next, a grid scan of the northern sky was performed in steps of 0.5°, looking for unknown sources of neutrinos. Also here no significant excess of events was found. Accordingly, upper limits on the neutrino fluxes compatible with this observation have been calculated. The average flux upper limit achieved in this analysis for a ν_μ+ν_τ flux with a spectrum of $d\Phi/dE \propto E^{-2}$ is $E^2 d\Phi/dE = 1.0 \cdot 10^{-7}$ GeV cm^{-2} s^{-1} assuming a flavor ratio of 1 : 1. For the northern sky a flux upper limit map has been created. A test of the angular correlations of event pairs has been performed, which is sensitive to a cumulative signal from several hidden sources, too weak to be individually detected. It has been found that the angular distribution of event pairs is compatible with randomly distributed events, like expected from a sample of atmospheric neutrinos.

Besides the searches for a signal in the integrated observation time, special methods have been developed to enhance the detection chance for a signal from sources which are suspected to be highly variable neutrino emitters. A selection of periods of active states has been performed for two sources, Markarian 421 and Cygnus X-3, based on their light curves at X-ray and radio frequencies respectively. No enhanced neutrino event rate has been found in these periods for the two sources and a limit on the neutrino flux in active states has been set. Additionally, a search for neutrino flares from a selection of 13 known variable sources with a sliding window has been conducted. Also here, no event multiplicity has been discovered incompatible with fluctuations of the atmospheric neutrino background. However, an interesting correlation was found between the arrival time of neutrinos from the direction of the Blazar 1ES 1959+650 and a series of large TeV gamma-ray flares observed from this source. Since this correlation was found “a-posteriori”, i.e. without a pre-defined statistical test on a possible correlation, the significance of such an observation cannot be evaluated and no conclusion can be drawn about the atmospheric or cosmic origin of these neutrinos.

Finally, the systematic uncertainty of the analysis from limited accuracy in detector calibration and signal simulation has been investigated. A new analysis of the uncertainty in the light collection efficiency of the Optical Module developed here improved the corresponding systematic error from 30% to about 10%. The total systematic error on the signal efficiency depends on the assumed spectrum of the signal neutrino. For a flux $d\Phi/dE \propto E^{-2}$ we find an uncertainty of $+9/-14\%$.

The upper limits presented on neutrino fluxes from point-like sources on the northern hemisphere in this thesis are the most stringent limits currently available. The limit improvement with respect to a former analysis of AMANDA-II data collected in 197 effective days of detector operation in the year 2000 corresponds to a factor of 3.8. A comparison to predicted neutrino fluxes shows that these limits are in the range of fluxes anticipated by several models of neutrino emission from Microquasars. In particular, a flux prediction for the Microquasar SS 433 is 2.5 times higher than the flux that can be excluded on 90% confidence level.

List of Figures

List of Tables

Bibliography

[A^{+}94] Anselmann, P.; et al.: GALLEX results from the first 30 solar neutrino runs. In: *Physics Letters B*, volume 327:p. 377, 1994.

[A^{+}00a] Andres, E.; et al. (The AMANDA Collaboration): The AMANDA neutrino telescope: principle of operation and first results. In: *Astroparticle Physics*, volume 13:p. 1, 2000.

[A^{+}00b] Atoyan, A.M.; et al.: On the gamma-ray fluxes expected from Cassiopeia A. In: *Astronomy & Astrophysics*, volume 355:p. 211, 2000.

[A^{+}01a] Aharonian, F.; et al.: Evidence for TeV gamma ray emission from Cassiopeia A. In: *Astronomy & Astrophysics*, volume 370:p. 112, 2001.

[A^{+}01b] Ambrosio, M.; et al.: Neutrino Astronomy with the MACRO Detector. In: *Astrophysical Journal*, volume 546:p. 1038, 2001.

[A^{+}02] Aharonian, F.; et al.: A unidentified TeV source in the vicinity of Cygnus OB2. In: *Astronomy & Astrophysics*, volume 393:p. L37, 2002.

[A^{+}03a] Aharonian, F.; et al.: Detection of TeV Gamma-Rays from the BL Lac 1ES1959+650 in its low states and during a major outburst in 2002. In: *Astronomy & Astrophysics*, volume 406:p. L9, 2003.

[A^{+}03b] Aharonian, F.; et al.: Is the Giant Radio Galaxy M87 a TeV Gamma-Ray Emitter? In: *Astronomy & Astrophysics*, volume 403:p. L1, 2003.

[A^{+}03c] Anchordoqui, L.; et al.: Neutrinos from Accreting Neutron Stars. In: *Astrophysical Journal*, volume 589:p. 481, 2003. `astro-ph/0211231`.

[A^{+}04a] Aharonian, F.; et al.: High-energy particle acceleration in the shell of a supernova remnant. In: *Nature*, volume 432:p. 75, 2004.

[A^{+}04b] Ahrens, J.; et al. (The AMANDA Collaboration): Calibration and survey of AMANDA with the SPASE detectors. In: *Nucl. Instrum. Meth. A*, volume 522:p. 347, 2004.

[A^{+}04c] Ahrens, J.; et al. (The AMANDA Collaboration): Muon track reconstruction and data selection techniques in AMANDA. In: *Nucl. Instrum. Meth. A*, volume 524:p. 169, 2004.

[A^{+}04d] Ahrens, J.; et al. (The AMANDA Collaboration): Search for extraterrestrial point sources of neutrinos with AMANDA-II. In: *Physical Review Letters*, volume 92(071102), 2004.

[A^{+}04e] Ahrens, J.; et al. (The AMANDA Collaboration): Sensitivity of the IceCube Detector to Astrophysical Sources of High Energy Muon Neutrinos. In: *Astroparticle Physics*, volume 20:p. 507, 2004.

[A^{+}05a] Ackermann, M.; et al. (The AMANDA Collaboration): Search for extraterrestrial point sources of high energy neutrinos with AMANDA-II using data collected in 2000-2002. In: *Physical Review D*, volume 71(077102), 2005.

[A^{+}05b] Aharonian, F.; et al.: A New Population of Very High Energy Gamma-Ray Sources in the Milky Way. In: *Science*, volume 307:p. 1938, 2005.

[A$^+$05c] Aharonian, F.; et al.: Discovery of Very High Energy Gamma Rays Associated with an X-ray Binary. In: *Science*, volume 309:p. 746, 2005.

[A$^+$05d] Aharonian, F.; et al.: Serendipitous discovery of the unidentified extended TeV gamma-ray source HESS J1303-631. In: *Astronomy & Astrophysics*, volume 439:p. 1013, 2005.

[A$^+$06a] Achterberg, A.; et al. (The IceCube Collaboration): On the selection of AGN neutrino source candidates for a source stacking analysis with neutrino telescopes, 2006. Accepted by Astroparticle Physics.

[A$^+$06b] Achterberg, A.; et al. (The IceCube Collaboration): Search for astrophysical neutrinos from individual and stacked point sources in the northern sky using the AMANDA-II neutrino telescope, 2006. To be published.

[A$^+$06c] Ackermann, M.; et al. (The AMANDA Collaboration): Optical properties of deep glacial ice at the South Pole. In: *Journal of Geophysical Research*, volume 111(D13203), 2006.

[A$^+$06d] Albert, J.; et al.: Variable Very-High-Energy Gamma-Ray Emission from the Microquasar LS I +61 303. In: *Science*, volume 312:p. 1771, 2006.

[AJY00] Athar, H.; Jezabek, M.; Yasuda, O.: Effects of neutrino mixing on high-energy cosmic neutrino flux. In: *Physical Review D*, volume 62(103007), 2000. `hep-ph/0005104`.

[AMH02] Alvarez-Muniz, J.; Halzen, F.: Possible High-Energy Neutrinos from the Cosmic Accelerator RX J1713.7-3946. In: *Astrophysical Journal*, volume 576:p. L33, 2002.

[B$^+$87] Bionta, R.M.; et al.: Observation of a neutrino burst in coincidence with supernova 1987A in the Large Magellanic Cloud. In: *Physical Review Letters*, volume 58:p. 1494, 1987.

[B$^+$03a] Bernloehr, K.; et al.: The optical system of the H.E.S.S. imaging atmospheric Cherenkov telescopes. In: *Astroparticle Physics*, volume 20:p. 111, 2003.

[B$^+$03b] Butt, Y.M.; et al.: Chandra/Very Large Array Follow-up of TeV J2032+4131, the Only Unidentified TeV Gamma-Ray Source. In: *Astrophysical Journal*, volume 497:p. 494, 2003.

[B$^+$05a] Berger, E.L.; et al. (The CTEQ Collaboration): 2005. URL, `www.phys.psu.edu/~cteq/`.

[B$^+$05b] Blazejowski, M.; et al.: A Multi-wavelength View of the TeV Blazar Markarian 421: Correlated Variability, Flaring, and Spectral Evolution. In: *Astrophysical Journal*, volume 630:p. 130, 2005. `astro-ph/0505325`.

[B$^+$05c] Bramall, N.E.; et al.: A deep high-resolution optical log of dust, ash, and stratigraphy in South Pole glacial ice. In: *Geophysical Research Letters*, volume 32:p. L21815, 2005.

[Bed03] Bednarek, W.: Neutrinos from the pulsar wind nebulae. In: *Astronomy & Astrophysics*, volume 407:p. 1, 2003. `astro-ph/0305430`.

[Bed05] Bednarek, W.: TeV neutrinos from microquasars in compact massive binaries. In: *Astrophysical Journal*, volume 631:p. 466, 2005. `astro-ph/0505547`.

[Bir00] Biron, A.: Reconstruction uncertainties due to time calibration errors. AMANDA internal report 20001101, DESY Zeuthen, 2000.

[Bir02] Biron, A.: *Search for Atmospheric Muon-Neutrinos and Extraterrestric Neutrino Point Sources in the 1997 AMANDA-B10 Data*. Ph.D. thesis, Humboldt-Universität, Berlin, 2002.

[Boe04] Boettcher, M.: Coordinated Multiwavelength Observations and Spectral Variability Modeling of Gamma-Ray Blazars. In: *Proceedings of the 5th INTEGRAL Workshop*. Munich, Germany, 2004. `astro-ph/0403589`.

[Boe05] Boettcher, M.: A hadronic synchrotron mirror model for the "orphan" TeV flare in 1ES 1959+650. In: *Astrophysical Journal*, volume 621:p. 276, 2005.

[BP97] Bednarek, W.; Protheroe, R.J.: Gamma Rays and Neutrinos from the Crab Nebula Produced by Pulsar Accelerated Nuclei. In: *Physical Review Letters*, volume 79:p. 2616, 1997.

[BPV03] Berezhko, E.; Pühlhofer, G.; Völk, H.: Gamma-ray emission from Cassiopeia A produced by accelerated cosmic rays. In: *Astronomy & Astrophysics*, volume 400:p. 971, 2003.

[BSK00] Bugaev, E.; Sokalski, I.; Klimushin, S.: Simulation accuracy of long range muon propagation in medium: analysis of error sources, 2000. `hep-ph/0010323`.

[Bur78] Burnham, R.: *Burnham's Celestial Handbook: An Observer's Guide to the Universe Beyond the Solar System*. Dover Publications, Mineola, USA, 1978.

[BV06] Berezhko, E.; Völk, H.: Theory of cosmic ray production in the supernova remnant RX J1713.7-3946, 2006. Accepted by Astronomy & Astrophysics, `astro-ph/0602177`.

[BW00] Biron, A.; Wissing, H.: Impact of varied OM sensitivities on the AMANDA-B10 analysis. AMANDA internal report 20001202, DESY Zeuthen, 2000.

[C^+97] Cantanese, M.; et al.: Multiwavelength observations of a Flare from Markarian 501. In: *Astrophysical Journal*, volume 487:p. L143, 1997.

[C^+98] Cantanese, M.; et al.: Discovery of Gamma-Ray Emission above 350 GeV from the BL Lacertae Object 1ES 2344+514. In: *Astrophysical Journal*, volume 501:p. 616, 1998.

[C^+03] Conrad, J.; et al.: Including systematic uncertainties in confidence interval construction of Poisson statistics. In: *Physical Review D*, volume 67:p. 012002, 2003.

[CH01] Cowen, D.; Hanson, K.: Time Calibration of the AMANDA Neutrino Telescope with Cosmic Ray Muons. In: *Proceedings of the 27th ICRC*. Hamburg, Germany, 2001.

[CHR85] Cheng, K.S.; Ho, C.; Ruderman, M.: Energetic radiation from rapidly spinning pulsars. In: *Astrophysical Journal*, volume 300:p. 500, 1985.

[Con03] Conrad, J.: *A Search for Neutrinos from Cosmic Point Sources using AMANDA-B10 with Emphasis on Limit Calculation Techniques*. Ph.D. thesis, Uppsala Universitet, 2003.

[CR01] Chirkin, D.; Rhode, W.: Muon Monte Carlo: a new high precision tool for muon propagation through matter. In: *Proceedings of the 27th ICRC*. Hamburg, Germany, 2001.

[D^+02] Distefano, C.; et al.: Neutrino flux predictions for known Galactic microquasars. In: *Astrophysical Journal*, volume 575:p. 378, 2002. `astro-ph/0202200`.

[DA81] Dziewonski, A.; Anderson, D.: Preliminary reference Earth model. In: *Physics of the Earth and Planetary Interiors*, volume 25:p. 297, 1981.

[DH02] DeYoung, T.; Hill, G.: Application of Bayes theorem to muon track reconstruction in AMANDA. In: *Proceedings Advanced Statistical Techniques in Particle Physics*. Durham, United Kingdom, 2002.

[DK05] Dwek, E.; Krennrich, F.: Simultaneous Constraints on the Spectrum of the Extragalactic Background Light and the Intrinsic Tev Spectra of Mrk 421, Mrk 501, and H1426+428. In: *Astrophysical Journal*, volume 618:p. 657, 2005. `astro-ph/0406565`.

[DRS00] Dutta, S.I.; Reno, M.H.; Sarcevic, I.: Tau Neutrinos Underground: Signals of Muon to Tau Neutrino Oscillations with Extragalactic Neutrinos. In: *Physical Review D*, volume 62(123001), 2000. `hep-ph/0005310`.

[E^+04] Eidelman, S.; et al.: Review of Particle Physics. In: *Physics Letters*, volume B592:p. 1, 2004. `http://pdg.lbl.gov`.

[FC98] Feldman, G.; Cousins, R.: A Unified Approach to the Classical Statistical Analysis of Small Signals. In: *Physical Review D*, volume 57:p. 3873, 1998. `physics/9711021`.

[Fer49] Fermi, E.: On the Origin of the Cosmic Radiation. In: *Physical Review*, volume 75:p. 742, 1949.

[G^+96] Gandhi, R.; et al.: Ultrahigh-Energy Neutrino Interactions. In: *Astroparticle Physics*, volume 05:p. 81, 1996. `hep-ph/9512364`.

[G^+06] Galassi, M.; et al.: *GNU Scientific Library Reference Manual*. ISBN 0954161734. The Free Software Foundation, 2nd edition, 2006.

[GA03] Guetta, D.; Amato, E.: Neutrino flux predictions for Galactic plerions. In: *Astroparticle Physics*, volume 19:p. 403, 2003. `astro-ph/0209537`.

[Gai90] Gaisser, T.: *Cosmic Rays and Particle Physics*. Cambridge University Press, 1990.

[GH02] Gaisser, T.; Honda, M.: Flux of Atmospheric Neutrinos. In: *Annu. Rev. Nucl. Part. Sci.*, volume 52:p. 153, 2002.

[Ghi98] Ghisellini, C.: A theoretical unifying scheme for gamma-ray bright blazars. In: *Mon. Not. Roy. Astron. Soc.*, volume 303:p. 451, 1998.

[GJ69] Goldreich, P.; Julian, W.H.: Pulsar electrodynamics. In: *Astrophysical Journal*, volume 157:p. 869, 1969.

[GK05] Gazizov, A.; Kowalski, M.: ANIS: High Energy Neutrino Generator for Neutrino Telescopes. In: *Comput. Phys. Commun.*, volume 172:p. 203, 2005.

[GPT99] Gregory, P.C.; Peracaula, M.; Taylor, A.R.: Discovery of Periodic Phase Modulation in LS I +61 303 Radio Outbursts. In: *Astrophysical Journal*, volume 520:p. 376, 1999. `hep-ph/9512364`.

[Gre66] Greisen, K.: End to the Cosmic-Ray Spectrum? In: *Physical Review Letters*, volume 16:p. 748, 1966.

[GS02] Gaisser, T.; Stanev, T.: Cosmic Rays. In: *[E^+04]*. 2002.

[H^+87] Hirata, K.S.; et al.: Observation of a neutrino burst from the supernova SN1987A. In: *Physical Review Letters*, volume 58:p. 1490, 1987.

[H^+90] Hirata, K.S.; et al.: Results from one thousand days of real-time, directional solar-neutrino data. In: *Physical Review Letters*, volume 65:p. 1297, 1990.

[H^+95] Honda, M.; et al.: Calculation of the Flux of Atmospheric Neutrinos. In: *Physical Review D*, volume 52:p. 4985, 1995. `hep-ph/9503439`.

[H^+98] Heck, D.; et al.: CORSIKA: A Monte Carlo code to simulate extensive air showers. Tech. Report 6019, Forschungszentrum Karlsruhe, 1998.

[H^+99] Hartman, R.C.; et al.: The Third EGRET Catalog of High-Energy Gamma-Ray Sources. In: *Astrophys. J. Suppl. Ser.*, volume 123:p. 79, 1999.

[H^+02a] Hill, G.; et al.: Ice property investigations with muons and implications for AMANDA analyses, 2002. Contribution to the AMANDA Collaboration Meeting, Berkeley.

[H^+02b] Horan, D.; et al.: Detection of the BL Lacertae Object H1426+428 at TeV Gamma-Ray Energies. In: *Astrophysical Journal*, volume 571:p. 753, 2002.

[H^+03] Holder, J.; et al.: Detection of TeV Gamma Rays from the BL Lacertae Object 1ES 1959+650 with the Whipple 10 Meter Telescope. In: *Astrophysical Journal*, volume 583:p. L9, 2003.

[Hau04] Hauschildt, T.: *Search for neutrino point sources with the AMANDA detector*. Ph.D. thesis, Humboldt-Universität, Berlin, 2004.

[Hei04] Heijboer, A.J.: *Track Reconstruction and Point Source Searches with ANTARES*. Ph.D. thesis, Universiteit van Amsterdam, The Netherlands, 2004.

[Hes12] Hess, V.F.: Über Beobachtungen der durchdringenden Strahlung bei sieben Freiballonfahrten. In: *Phys. Z.*, volume 13:p. 1084, 1912.

[HH05] Halzen, F.; Hooper, D.: High Energy Neutrinos from the TeV Blazar 1ES 1959+650. In: *Astroparticle Physics*, volume 23:p. 537, 2005.

[Hil96] Hill, G.: *Experimental and Theoretical Aspects of High Energy Neutrino Astrophysics*. Ph.D. thesis, University of Adelaide, Australia, 1996.

[Hil01] Hill, G.: Bayesian event reconstruction and background rejection in neutrino detectors. In: *Proceedings of the 27th ICRC*. Hamburg, Germany, 2001.

[HJ81] Hjellming, R.M.; Johnston, K.J.: Structure, strength, and polarization changes in radio source SS433. In: *Nature*, volume 290:p. 100, 1981.

[Hod05] Hodges, J.: Search for Diffuse Flux of Extraterrestrial Muon Neutrinos using AMANDA-II Data from 2000 to 2003. In: *Proceedings of the 29th ICRC*. Pune, India, 2005.

[Hoe03] Hoerandel, J.: On the knee in the energy spectrum of cosmic rays. In: *Astroparticle Physics*, volume 19:p. 193, 2003.

[Hoe04] Hoerandel, J.: Models of the Knee in the Energy Spectrum of Cosmic Rays. In: *Astroparticle Physics*, volume 21:p. 241, 2004.

[HP98] He, Y.D.; Price, P.B.: Remote sensing of dust in deep ice at the South Pole. In: *Journal of Geophysical Research*, volume 103:p. 17041, 1998.

[Hue06] Huelss, J.P.: *Search for Signatures of Extra-Terrestrial Neutrinos with a Multipole Analysis of the AMANDA-II Sky Map*. Diploma thesis, Universität Wuppertal, 2006.

[Hun99] Hundertmark, S.: AMASIM Neutrino Detector Simulation Program. In: Spiering, C., editor, *Proceedings of the Workshop on Simulation and Analysis Methods for Large Neutrino Telescopes*. Zeuthen, Germany, 1999. `DESY-Proc-1999-01`.

[Jac96] Jackson, J.D.: *Classical Electrodynamics*. Wiley, New York, USA, 3rd edition, 1996.

[JR03] Japaridze, G.; Ribordy, M.: Photon arrival time distribution convoluted to a gaussian time measurement uncertainty. AMANDA internal report 20031201, 2003.

[K$^+$04] Krawczynski, H.; et al.: Multiwavelength observations of strong flares from the TeV-Blazar 1ES 1959+650. In: *Astrophysical Journal*, volume 604:p. 151, 2004.

[Kar99] Karle, A.: Monte Carlo Simulation of Photon Transport and Detection in Deep Ice: Muons and Cascade. In: Spiering, C., editor, *Proceedings of the Workshop on Simulation and Analysis Methods for Large Neutrino Telescopes*. Zeuthen, Germany, 1999. `DESY-Proc-1999-01`.

[Kay05] Kayser, B.: Neutrino mass, mixing, and flavor change. In: *[E$^+$04]*. 2005.

[Kow04] Kowalski, M.: *Search for Neutrino-Induced Cascades with the AMANDA-II Detector*. Ph.D. thesis, Humboldt-Universität, Berlin, 2004.

[KW05] Kashti, T.; Waxman, E.: Astrophysical Neutrinos: Flavor Ratios Depend on Energy. In: *Physical Review Letters*, volume 95(181101), 2005.

[Lan05] Lang, R.: *Search for point sources of high-energy neutrinos with the AMANDA detector*. Diploma thesis, Universität Ulm, 2005.

[LB05] Link, B.; Burgio, F.: TeV mu Neutrinos from Young Neutron Stars. In: *Physical Review Letters*, volume 94(181101), 2005. `astro-ph/0412520`.

[LB06] Link, B.; Burgio, F.: Flux predictions of high-energy neutrinos from pulsars, 2006. Submitted to Mon. Not. Roy. Astron. Soc., `astro-ph/0604379`.

[Lev04] Levine, A.: RXTE ASM lightcurve download page, 2004. Web page, `http://xte.mit.edu/`.

[Lip93] Lipari, P.: Lepton spectra in the earth's atmosphere. In: *Astroparticle Physics*, volume 1:p. 195, 1993.

[LM00] Learned, J.; Mannheim, K.: High-Energy neutrino Astrophysics. In: *Ann. Rev. Nucl. Part. Sci*, volume 50:p. 679, 2000.

[Low97] Lowry, W.: *Fundamentals of Geophysics*. Cambridge University Press, 1997.

[LS91] Lipari, P.; Stanev, T.: Propagation of multi-TeV muons. In: *Physical Review D*, volume 44, 1991.

[LW01] Levinson, A.; Waxman, E.: Probing Microquasars with TeV Neutrinos. In: *Physical Review Letters*, volume 87(171101), 2001. `hep-ph/0106102`.

[M$^+$03] Muecke, A.; et al.: BL Lac Objects in the Synchrotron Proton Blazar Model. In: *Astroparticle Physics*, volume 18:p. 593, 2003. `astro-ph/0206164`.

[Mag97] Magnussen, N.: The MAGIC Telescope Project for Gamma Astronomy above 10 GeV. In: *Proc. 36th ELOISATRON Workshop on New Detectors*. Erice, Italy, 1997. `astro-ph/9805184`.

[Man93] Mannheim, K.: Gamma Rays and Neutrinos from a Powerful Cosmic Accelerator. In: *Physical Review D*, volume 48:p. 2408, 1993. `astro-ph/9306005`.

[Man98] Mannheim, K.: Possible Production of High-Energy Gamma Rays from Proton Acceleration in the Extragalactic Radio Source Markarian 501. In: *Science*, volume 279:p. 684, 1998. `astro-ph/9803241`.

[Mil69] Miller, S.L.: Clathrate hydrates of air in Antarctic ice. In: *Science*, volume 165:p. 489, 1969.

[Mio01] Miocinovic, P.: *Muon energy reconstruction in the Antarctic Muon And Neutrino Detector Array (AMANDA)*. Ph.D. thesis, University of California, Berkeley, USA, 2001.

[MR99] Mirabel, I.F.; Rodriguez, L.F.: Sources of Relativistic Jets in the Galaxy. In: *Annual Reviews of Astronomy & Astrophysics*, volume 37:p. 409, 1999. `astro-ph/9902062`.

[MR04] Mioduszewski, A.; Rupen, M.P.: CI Cam: A Shell-shocked X-ray Nova. In: *Astrophysical Journal*, volume 615:p. 432, 2004. `astro-ph/0407277`.

[N$^+$02] Neronov, A.; et al.: Large scale extragalactic jets powered by very-high energy gamma rays. In: *Physical Review Letters*, volume 89(051101), 2002. `astro-ph/0201410`.

[N$^+$03] Nolan, P.; et al.: Variability of EGRET Gamma-Ray Sources. In: *Astrophysical Journal*, volume 597:p. 615, 2003. `astro-ph/0307188`.

[Nah05] Nahnhauer, R.: 2005. Private communication.

[NAS02] NASA: Rossi X-Ray Timing Explorer (RXTE), 2002. Web page, `http://heasarc.gsfc.nasa.gov/docs/xte/XTE.html`.

[NAS05] NASA: The CGRO Mission, 2005. Web page, `http://cossc.gsfc.nasa.gov/docs/cgro/index.html`.

[Neu03] Neunhöffer, T.: *Entwicklung eines neuen Verfahrens zur Suche nach kosmischen Punktquellen mit dem AMANDA-Neutrinoteleskop*. Ph.D. thesis, Johannes Gutenberg-Universität, Mainz, 2003.

[Neu06] Neunhöffer, T.: Estimating the angular resolution of tracks in neutrino telescopes based on a likelihood analysis. In: *Astroparticle Physics*, volume 25:p. 220, 2006.

[NMB93] Nellen, L.; Mannheim, K.; Biermann, P.L.: Neutrino production through hadronic cascades in AGN accretion disks. In: *Physical Review D*, volume 47:p. 5270, 1993. `hep-ph/9211257`.

[NS02] Neronov, A.; Semikoz, D.: Which blazars are neutrino loud? In: *Physical Review D*, volume 66(123003), 2002. `hep-ph/0208248`.

[OW01] Olbrechts, P.; Wiebusch, C.: On the angular sensitivity of optical modules in the ice. AMANDA internal report 20010102, DESY Zeuthen, 2001.

[P$^+$02a] Price, P.B.; et al.: Temperature profile for glacial ice near the south pole. In: *Proc. Nat. Acad. of Sci.*, volume 99:p. 7847, 2002.

[P$^+$02b] Pumplin, J.; et al.: New Generation of Parton Distributions with Uncertainties from Global QCD Analysis. In: *Journal of High Energy Physics*, volume 07, 2002. `hep-ph/0201195`.

[Pan96] Pandel, D.: *Bestimmung von Wasser- und Detektorparametern und Rekonstruktion von Myonen bis 100 TeV mit dem Baikal-Neutrinoteleskop NT-72.* Diploma thesis, Humboldt-Universität Berlin, 1996.

[PB97] Price, P.B.; Bergström, L.: Optical properties of deep ice at the South Pole: scattering. In: *Appl. Opt.*, volume 36:p. 4181, 1997.

[PD99] Palanque-Delabrouille, N.: Measurement of the water transparency in the ANTARES site. In: *Proceedings of the 26th ICRC*. Salt Lake City, USA, 1999.

[PDR03] Protheroe, R.; Donea, A.-C.; Reimer, A.: TeV gamma rays and cosmic rays from the nucleus of M87, a mis-aligned BL Lac object. In: *Astroparticle Physics*, volume 19:p. 559, 2003. `astro-ph/0210249`.

[PM05] Picozza, P.; Morselli, A.: The science of PAMELA space mission. In: *Proceedings of the 12th Lomonosov Conference on Elementary Particle Physics*. Moscow, Russia, 2005.

[Poh04] Pohl, A.: *A Statistical Tool for Finding Non-Particle Events from the AMANDA Neutrino Telescope.* Ph.D. thesis, Uppsala Universitet, 2004.

[Poo04] Pooley, G.: 2004. Data from the RYLE telescope were provided by G. Pooley.

[PTVF97] Press, W.; Teukolsky, S.; Vetterling, W.; Flannery, B.: *Numerical Recipies in C.* Cambridge University Press, Cambridge, UK, 2nd edition, 1997.

[PW01] Price, P.B.; Woschnagg, K.: Role of Group and Phase Velocity in High-Energy Neutrino Observatories. In: *Astroparticle Physics*, volume 15:p. 97, 2001. `hep-ex/0008001`.

[RBP05] Reimer, A.; Böttcher, M.; Postnikov, S.: Neutrino emission in the hadronic Synchrotron Mirror Model: the "orphan" TeV flare from 1ES 1959+650. In: *Astrophysical Journal*, volume 630:p. 186, 2005.

[Ree84] Rees, M.J.: Black Hole Models for Active Galactic Nuclei. In: *Annual review of Astronomy & Astrophysics*, volume 22:p. 471, 1984.

[Rib02] Ribordy, M.: AMANDA-II/2000 data statistics, OM selection and retriggering procedure. AMANDA internal report 20020601, DESY Zeuthen, 2002.

[RS75] Ruderman, M.; Sutherland, P.G.: Theory of pulsars - Polar caps, sparks, and coherent microwave radiation. In: *Astrophysical Journal*, volume 196:p. 51, 1975.

[Sch02] Schmidt, T.: *Aufbau und Funktionsnachweis eines Optischen Moduls mit optisch-analoger Pulsübertragung für den AMANDA-II- und IceCube-Detektor.* Ph.D. thesis, Humboldt-Universität Berlin, 2002.

[Sch03] Schlickeiser, R.: *Cosmic Ray Astrophysics.* Springer Verlag, Berlin, Germany, 2nd edition, 2003.

[Sch05] Schmidt, F.: *Search for Pulsed TeV Gamma-Ray Emission from Pulsars with H.E.S.S.* Diploma thesis, Humboldt-Universität Berlin, 2005.

[SS96] Stecker, F.W.; Salamon, M.H.: High Energy Neutrinos from Quasars. In: *Space Sci.Rev.*, volume 75:p. 341, 1996. `astro-ph/9501064`.

[Ste02] Steffen, P.: Direct Walk II (Improved version of Direct Walk). AMANDA internal report 20020201, DESY Zeuthen, 2002.

[Ste05] Steffen, P.: SLJAMS.cc, 2005. Source code inside the SIEGLINDE cvs code archive, `pub.icecube.wisc.edu/net/local/cvsroot`.

[Sud01] Sudhoff, P.: Transmission measurements with AMANDA glass and evaluation for IceCube. AMANDA internal report 20010701, DESY Zeuthen, 2001.

[Tab02] Taboada, I.: *Search for High Energy Neutrino Induced Cascades.* Ph.D. thesis, University of Pennsylvania, State College, USA, 2002.

[TGG96] Thunman, M.; G.Ingelman; Gondolo, P.: Charm Production and High Energy Atmospheric Muon and Neutrino Fluxes. In: *Astroparticle Physics*, volume 5:p. 309, 1996.

[Tlu03] Tluczykont, M.: *Beobachtung und Nachweis von Aktiven Galaktischen Kernen und Suche nach Galaktischen Objekten im TeV-Energiebereich mit den HEGRA-Cherenkov-Teleskopen sowie Modellierung eines Photonspektrums durch den Zerfall neutraler Pionen aus schockbeschleunigten Hadronen.* Ph.D. thesis, Universität Hamburg, Hamburg, 2003.

[U$^+$00] Uchihori, Y.; et al.: Cluster analysis of extremely high energy cosmic rays in the northern sky. In: *Astroparticle Physics*, volume 13:p. 151, 2000.

[UP95] Urri, C.M.; P.Padovani: Unified Schemes for Radio-Loud Active Galactic Nuclei. In: *Publ. Astron. Soc. Pac.*, volume 107:p. 803, 1995.

[Voi05] Voigt, B.: 2005. Private communication.

[Wie95] Wiebusch, C.: *The Detection of Faint Light in Deep Underwater Neutrino Telescopes.* Ph.D. thesis, RWTH Aachen, 1995.

[Wos99] Woschnagg, K.: Matching/combining laser/drill geometries. AMANADA internal note, 1999. `http://icecube.berkeley.edu/kurt/interstring/matchgeo.html`.

[Wos00] Woschnagg, K.: Preliminary (Non-Optical) Position Calibration of Strings 14 to 19. AMANDA internal report 20001002, 2000.

[Z$^+$03] Zhang, B.; et al.: High energy neutrinos from magnetars. In: *Astrophysical Journal*, volume 590:p. 346, 2003.

[ZK66] Zatsepin, G.T.; Kuz'min, V.A.: In: *Sov. Phys. JETP Lett.*, volume 4:p. 78, 1966.

Acknowledgements

I would like to thank Prof. Dr. Hermann Kolanoski for taking the responsibility for this thesis and Dr. Christian Spiering, who gave me the opportunity to work in the IceCube group in Zeuthen and supported me exceptionally during the whole time I have been here. I also want to express my gratitude to Dr. Stefan Schlenstedt who had an open door for all of my problems and made it possible that I went three times to Antarctica.

In particluar my thanks go to Dr. Elisa Bernardini, the inofficial co-supervisor of my thesis and a great colleague and friend for lots of help, fruitful discussions, good advice and guidance from which I and this thesis have benefitted greatly.

I am especially greatful to Dr. Tonio Hauschildt and Dr. Marek Kowalski who introduced me to AMANDA analysis and supplied me with all the undocumented expert knowledge so important in AMANDA as well as to Dr. Matthias Leuthold who initiated and designed with me an unified data filtering, from which this analysis profited a lot. Also I would like to thank Dr. Elisa Resconi for the good team work in the development of strategies to search for time-variabe neutrino sources.

I appreciated very much the innumerous discussions on Physics and the life besides it with my fellow graduate students Sebastian Boeser, Stefan Klepser, Oxana Tarasova, Bernhard Voigt and Henrike Wissing as well as the post-docs and staff of the Zeuthen group, Dr. David Boersma, Dr. Julien Bolmont, Dr. Rolf Nahnhauer, Damian Pieloth, Dr. Peter Steffen, Dr. Martin Tluczykont, Dr. Mike Walter and Dr. Ralf Wischnewski. They are also responsible for creating a nice working atmosphere, which I have enjoyed much. A special thanks to the proof-readers of my thesis Sebastian, Bernhard, Martin, Marek, Stefan and Elisa.

The weeks at South Pole have been some of the best during the last three years. Most of the time I spent there with Timo Messarius and Dr. Wolfgang Wagner. Thank's to them for making this time not only hard work but also much fun. And of course, thank's to all the other members of the big IceCube collaboration, with whom I spent lots of time discussing during collaboration meetings and conferences, in particular Dr. Thomas Becka, Johan Lundberg, Prof. Dr. Lutz Koepke and Prof. Dr. Christopher Wiebusch.

And finally, thank you, Pamela, for keeping my spirits up in all our years together and especially during the last month of writing this thesis.

Selbständigkeitserklärung

Hiermit erkläre ich, die vorliegende Arbeit selbständig ohne fremde Hilfe verfasst und nur die angegebene Literatur und Hilfsmittel verwendet zu haben.

Berlin, den 01.08.2006

Markus Ackermann